Dislocation electron tomography : applications and association to continuum mechanics and dislocation dynamics

Timmo Weidner

Université de Lille

Unité Matériaux Et Transformation École Doctorale n°104 :

Sciences de la Matière, du Rayonnement et de l'Environnement

Thèse de doctorat

Spécialité : Physique (Milieux denses, matériaux et composants)

Dislocation electron tomography - Applications and association to continuum mechanics and dislocation dynamics

-

Tomographie électronique des dislocations – Applications et associations à la mécanique des milieux continus et à la dynamique des dislocations

---

Thèse préparée par :

Timmo WEIDNER

pour obtenir le grade de Docteur en Physique

Soutenue publiquement le 25 avril 2024 devant le jury composé de :

Pr Ovidiu ERSEN	Univ. Strasbourg	Rapporteur
DR Fabien ONIMUS	CEA Saclay	Rapporteur
Pr Karine MASENELLI-VARLOT	INSA Lyon	Président du Jury
CR Jonathan AMODEO	Univ. Aix-Marseille	Examinateur
MCF HDR Alexandre MUSSI	Univ. Lille	Directeur
Pr Patrick CORDIER	Univ. Lille	Co-Directeur
MCF Karine GOURIET	Univ. Lille	Co-Encadrante

Acknowledgement

First of all, I would like to thank Patrick Cordier for providing me with the opportunity to undertake this project and for coordinating the work in Lille. His guidance, support, and wisdom not only brought passion back to me, when I felt a bit down, but I also admire the fruitful discussions with him, which lead to new ideas.

I owe immense gratitude to Alexandre Mussi, who supervised me and told me so much in regarding the TEM. Sometimes he had to be patient with me, when not everything worked as planned. And he held a clear eye on everything, whenever I made a mistake and helped me whenever I needed help.

I want to thank Karine Gouriet, for her co-supervision of my work. Her assistance especially with the modelling and the trust she placed in me were invaluable. Her gestures, like bringing cakes to lighten the mood, and assistance with French matters, were immensely appreciated.

I want to thank Ahmed, who helped me improve my sample preparation and helped me out at the TEM, whenever a problem occurred and also always had a smile on his face, even when I sometimes messed up. He helped me to keep calm, even when I though I made a disaster at the microscope. Further thanks go to Sylvie, who told me the importance of olivine.

I want to thank Vincent and Laurent, who were both patient, enthusiastic and helpful collaborates. They gave me both a warm welcome when I stayed with them to improve our work.

I want to thank Valentin and Jean who were amazing office mates and always assisted with French language challenges, creating a pleasant atmosphere throughout my time. Additionally, they helped me take breaks now and then, for example, by playing volleyball together.

Contents

1 Introduction **1**

2 State of the Art - Plasticity - Dislocations **5**

2.1 Dislocations in Continuum Mechanics 5

2.1.1 Burgers Circuit and Burgers Vector 5

2.1.2 Nye Tensor 7

2.1.3 Strain Energy in Linear Elastic Theory 8

2.1.4 Core Models 11

2.2 Visualization of Dislocations in TEM 13

2.2.1 Image Contrast 13

2.2.1.1 Diffraction Mode 14

2.2.1.2 Image Mode 14

2.2.2 Ewald's Sphere 15

2.2.3 Extinction Distance 16

2.2.4 Weak Beam Dark-Field 18

2.2.5 Dislocation contrast in TEM 19

2.2.6 Tomography in TEM 21

2.2.6.1 History 21

2.2.6.2 Dislocation Electron Tomography 22

2.3 Dislocation Dynamics 23

2.3.1 Glide Mechanism 23

2.3.2 Thermal Regimes 24

2.3.2.1 Low Temperature Regime 24

2.3.2.2 Athermal Regime 25

2.3.2.3 High Temperature Regime 26

2.3.3 Dislocation Interactions 26

2.3.4 Climb Mechanism 28

2.3.4.1 Climb as Recovery Mechanism 29

2.3.4.2 Climb as Strain producing Mechanism 31

3 Methodology **35**

3.1 Dislocation Electron Tomography . . . 35

3.1.1 TEM Analysis . . . 35

3.1.1.1 Sample holder . . . 35

3.1.1.2 Tilt Series Acquisition . . . 36

3.1.1.3 Precession . . . 37

3.1.1.4 Postprocessing . . . 38

3.1.2 Reconstruction . . . 40

3.1.2.1 Weighted Back Projection Algorithm (WBP) . . . 40

3.1.2.2 Reconstructed Dislocation Improvement . . . 41

3.1.2.3 Characterization of habit planes . . . 42

3.1.3 Dislocation electron tomography for a beam sensitive material . . . 43

3.1.4 Burgers vector indexation - Ishida method . . . 44

3.2 Field Dislocation Mechanics . . . 47

3.2.1 Associate with Tomography - Transform tomography data . . . 49

3.2.2 Nye'zation . . . 50

3.3 Discrete Dislocation Dynamic simulations . . . 53

3.3.1 Historical development . . . 54

3.3.2 Discrete dislocation dynamics with NUMODIS . . . 55

3.3.3 Association with Tomography . . . 57

3.3.4 2.5D-Dislocation Dynamics . . . 58

4 Results - General Applications of Dislocation Electron Tomography **63**

4.1 Quartz - Evidence of Mixed Climb . . . 63

4.1.1 Introduction . . . 63

4.1.2 Materials and Methods . . . 65

4.1.2.1 Specimens . . . 65

4.1.2.2 Dislocation electron tomography . . . 70

4.1.2.3 Plastic strain associated with dislocation segments . . . 71

4.1.2.4 Estimation of the local loading conditions . . . 72

4.1.3 Results . . . 73

4.1.3.1 Quantitative analysis of the microstructure . . . 76

4.1.3.2 Glide Mechanism . . . 82

4.1.3.3 Climb Mechanism . . . 85

4.1.3.4 Strain analysis from electron tomography data . . . 88

4.1.4 Discussion . . . 89
4.1.4.1 Slip systems . . . 89
4.1.4.2 Mixed climb . . . 89
4.1.4.3 Inferring stress loading . . . 92
4.1.4.4 Limitations . . . 96
4.1.5 Conclusion . . . 99
4.2 Olivine - Evidence of Mixed Climb . . . 100
4.2.1 Results . . . 100
4.2.2 Discussion . . . 102

5 Results - Dislocation Electron Tomography - An Association to Field Dislocation Mechanics 103
5.1 Materials and Deformation Experiments . . . 103
5.2 Results and Discussion . . . 104
5.2.1 Dislocation Microstructure . . . 104
5.2.2 Simulation Results . . . 105
5.3 Discussion . . . 109
5.4 Conclusion . . . 112

6 Results - Dislocation Electron Tomography - An Association to Discrete Dislocation Dynamics 113
6.1 Implementation . . . 113
6.1.1 Time and length scales . . . 113
6.1.2 Simulation Parameters . . . 115
6.1.3 Velocity law . . . 117
6.1.4 Material . . . 117
6.1.5 Refinements . . . 118
6.2 Results . . . 119
6.3 Discussion . . . 122
6.4 Conclusion . . . 124

7 Side Project - Modeling creep in periclase (MgO) under lower mantle conditions 127
7.1 Periclase deforms slower than bridgmanite at lower mantle conditions . . . 127
7.1.1 Diffusion coefficients . . . 128
7.1.2 Modelling dislocation creep of periclase . . . 129
7.1.3 Laboratory versus nature . . . 131

8 General Discussion **135**

8.1 Dislocation Electron Tomography 135

8.1.1 Analysis Possibilities 135

8.1.2 Advanced characterization with DET 136

8.2 DET: Association with Continuum Mechanics and Dislocation Dynamics . . . 137

8.2.1 Association of DET with Continuum Mechanics at the Grain Scale . . 137

8.2.2 Association of DET with Continuum Mechanics at the Scale of WBDF Resolution 138

8.2.3 Association of DET with Time by Dislocation Dynamics 139

9 Conclusion: Advancing Dislocation Analysis through Electron Tomography **143**

9.1 On the Importance of Climb in Geodynamics 143

9.2 An Association with Continuum Mechanics and Dislocation Dynamics 145

9.3 Perspectives 146

A Appendix **149**

A.1 Analysis on straight line dislocations 149

Bibliography **153**

1 Introduction

This thesis delves into the intricate dynamics of mineral deformation, with a particular focus on the role of dislocations under various environmental conditions, such as high temperatures and low strain rates. Dislocations, or linear defects within a crystal lattice, are pivotal in understanding the mechanisms behind plastic deformation in materials. These defects are characterized by specific properties such as Burgers vectors, line vectors, and habit planes, encompassing both slip and climb planes. The movement of these dislocations, promoted by applied stress, enables materials to deform plastically without necessitating the breaking of atomic bonds across the entire lattice plane. This fundamental process not only responds to applied stress but also dictates the material's capacity for strain and, consequently, its mechanical properties. Central to our study is the differentiation between glide and climb movements of dislocations. Glide refers to the conservative dislocation movement along dense crystallographic planes, whereas climb is driven by atomic diffusion, permitting dislocations to move perpendicular to their glide planes. This distinction is crucial for a comprehensive analysis of how materials undergo deformation. To observe these phenomena at the microscopic scale, Transmission Electron Microscopy (TEM) has been instrumental, despite its limitation to projected images, which can sometimes lead to interpretative errors.

To overcome these limitations and advance our understanding of dislocation microstructures, Dislocation Electron Tomography (DET) has been employed. The third dimension facilitates the observation of dislocation structures, offering a more precise interpretation of their configurations. My thesis work has significantly contributed to enhancing DET technology. By going beyond reconstruction, we have performed quantitative analyses and applied this information to other fields. Among the mechanisms of dislocation movement, mixed climb—representing a complex configuration between glide and climb—has emerged as a focal point of our research. This mechanism suggests a balance in the mobility of dislocations across both glide and climb, a phenomenon especially noticeable in microstructures with high lattice friction at elevated temperatures. In general, the importance of climb stands out significantly. A simplified dislocation dynamics (DD) approach to to study the deformation of the lower mantle has seen the importance of climb, both as a mechanism for controlling the rate of deformation and as a mechanism for producing deformation.

By utilizing DET, we have characterized the 3D microstructures of dislocations in natural samples of quartz and olivine, uncovering the presence of the mixed climb mechanism. This finding not only adds a new dimension to our understanding of dislocation behavior but also challenges previous notions of material deformation. Building upon DET's capabilities, my research has explored the integration of tomography with continuum mechanics. We have estimated the strain tensor of a grain in a natural quartz sample, taking into account the lengths of dislocation segments and their orientations. We found that a significant portion of dislocation lengths was in mixed climb configuration. This observation, coupled with the hypothesis that mixed glide and climb activation could involve the contribution of unusual glide planes, necessitates further empirical and theoretical investigation. We've demonstrated that glide alone can account for the observed strain, meeting the von Mises-Taylor criterion, yet climb's contribution is substantial, challenging the exclusive reliance on glide for deformation analysis.

To further extend the scope of our study we incorporated DET-derived microstructures with continuum mechanics by using a field dislocation mechanics (FDM) approach, bridging the gap between localized dislocation behavior and the broader framework of material deformation, unveiling significant local variations in stress fields and Resolved Shear Stresses (RSSs) in olivine. This approach has not only advanced our understanding of plastic anisotropy and dislocation slip system activation but also facilitated the exploration of phenomena like kinematic hardening at the nanoscale. Additionally, we integrated a DET microstructure into Dislocation Dynamics (DD) simulations for dynamic modeling. This approach, facilitated by the NUMODIS nodal DD software, developed at CEA Saclay has allowed us to simulate dislocation behavior based on actual microstructures instead of relying on virtual dislocations. While still in the proof-of-concept stage and requiring further development, this approach should allow us at some point to simulate complex dislocation interactions under stress This comprehensive study bridges macroscopic geophysical processes and nanometer-scale observations, illuminating the complexities of material deformation. Through advanced imaging techniques, detailed microstructural analysis, and theoretical modeling, this work offers valuable insights to the geosciences and materials science communities, enhancing our understanding of the fundamental processes governing material deformation.

In the sections to come, I will embark on a detailed exploration of dislocations, beginning with their conceptualization within the framework of continuum mechanics.

Subsequently, I will delve into the visualization and analysis of dislocations through Transmission Electron Microscopy (TEM), and then go into more detail on dynamics of dislocation and their interactions. Next follows a description of all the relevant methods needed to achieve

this work. The core of this thesis presents the findings from various studies. Starting with direct application of DET to different minerals and unveiling the occurrence of mixed climb in them. Then I move over to association to other models, illustrating how integrating DET data with FDM enhances our understanding of stress and strain fields at the dislocation level. Followed by a work that explores how combining DET with DDD simulations provides access to interactions and evolution over time, with a real dislocation microstructure. In the last part I will write about a 2.5D DD approach that helped us study the deformation in the lower earth's mantle. Each study will be presented with its respective results, followed by a discussion and conclusion, offering a thorough examination of the findings within the context of the broader scientific discourse. The thesis will culminate in a general discussion that synthesizes all the findings, drawing connections between the individual studies. Finally, I will conclude with a summary that encapsulates the key discoveries and insights derived from this research, while also outlining future prospects and potential areas for further exploration.

2 State of the Art - Plasticity - Dislocations

2.1 Dislocations in Continuum Mechanics

The topic of dislocations had its origins in the early 20th century. The start for this field was laid with the groundbreaking work on the theory of elasticity by Volterra (1907). Initially, Volterra's work was not directly connected to dislocations but served as a conceptual mathematical framework within continuum mechanics. His work described different types of deformations in cut-open, homogeneous, and isotropic cylinders (see Figure 3).
The connection between this theoretical framework and the physical phenomenon of dislocations began to emerge with the work of Frenkel (1926). Frenkel observed a significant discrepancy between theoretical predicted shear strength and shear strength of measurements. He proposed a model for the shear-stress-shear-displacement relation, which assumed that a crystal undergoing plastic shearing on a plane would pass through configurations of equivalent energies at intervals defined by the magnitude of a simple lattice-translation vector, **b**. This model, however, overlooked the minor end effects arising from the formation of surface steps due to shear. Despite the elegance of this model, the experimentally observed values for the maximum resolved shear stress necessary to initiate plastic flow in metals were orders of magnitude lower than Frenkel's predictions. This disparity could only be resolved through the introduction of dislocations into the theoretical framework. In 1934, Orowan, Polanyi and Taylor (Orowan 1934; Polanyi 1934; Taylor 1934) independently postulated the existence of edge dislocations as sources of plastic deformation.
Their collective insight laid the foundation for comprehending the role of dislocations in the mechanical behavior of crystalline materials.

2.1.1 Burgers Circuit and Burgers Vector

Following the foundational insights by Orowan, Polanyi, and Taylor on the existence of dislocations as the primary sources of plastic deformation, a deeper understanding of dislocation mechanics is facilitated by the concept of the Burgers vector. If we look at an edge dislocation inside a crystal lattice, it is characterized by a disruption of the regular lattice along

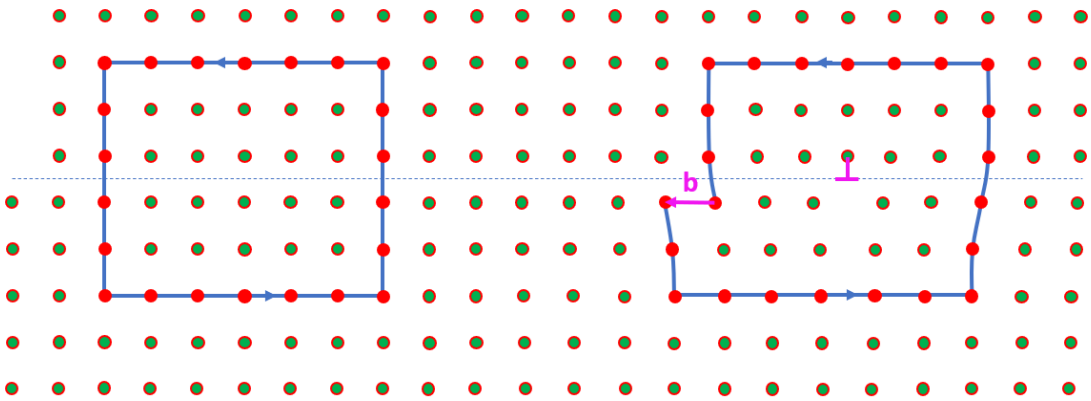

Figure 1: Burgers circuit : On the left, one can see a closed path around an undistorted enclosing of the lattice. On the right, one can see the same path around the region close to the dislocation. The purple vector indicating the missing displacement by the Burgers vector **b**. The dislocation line **t** is also indicated in purple and is pointing towards us. The glide plane containing **b** and **t** is indicated by the dotted line.

a line t. This disruption can be introduced by looking at a closed loop in an undistorted region of a crystal. If we form the same loop around the edge dislocation the loop can only be closed by an additional vector, which is the Burgers vector **b** (see Figure 1). The Burgers vector characterizes both the magnitude and direction of the lattice distortion created by the dislocation. The line direction is not always edge on, but itself can be described by a vector **t**, called the line vector and can be in an arbitrary angle to the Burgers vector.
If the line vector and the Burgers vector are normal to each other as in Figure 1, the dislocation is called edge, if they are parallel, it is called a screw dislocation, any other configuration is called a mixed dislocation.

Since a dislocation line is the boundary of an area over which slip displacement has occurred, a dislocation line cannot terminate within the body, it ends either at another dislocation, or in itself by forming a loop or at a crystal boundary. Those boundaries can be the surface of a crystal or grain boundaries. When dislocations end at another dislocation, this intersection is called a dislocation node. At a node, the sum of all Burgers vectors remains zero to conserve the Burgers vector, providing a critical constraint that governs their behavior.

2.1.2 Nye Tensor

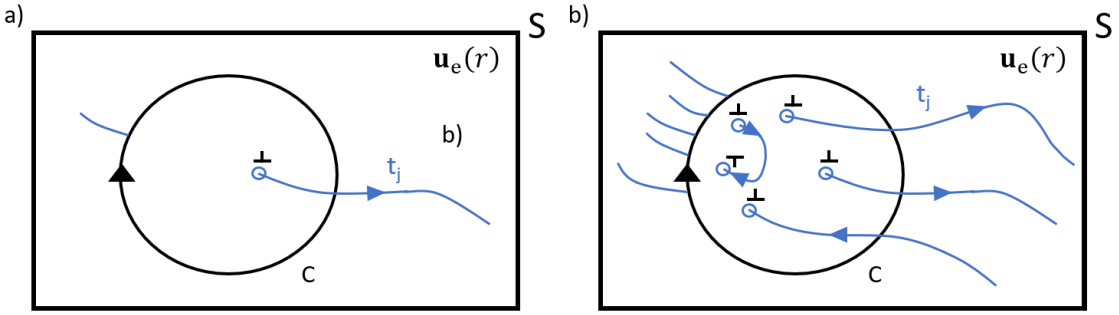

Figure 2: Nye tensor calculation: (a) A single dislocation colored in blue, that is cut by a surface S, on which we define our displacement field $\boldsymbol{u_e}$. The orientation of the components t_j of the dislocation lines is given by the blue lines with arrows. The black circle indicated the integration path to get the Nye tensor. (b) Identical sketch for a dislocation network.

To enhance our understanding of the lattice distortion caused by dislocations within the framework of continuum mechanics, we introduce the concept of the Nye tensor. Revisiting the Burgers circuit allows us to directly link the distortion to the Burgers vector by integrating along such a closed path (Figure 2(a)):

$$\mathbf{b} = \oint_C \mathbf{U}_e d\mathbf{r} \tag{2.1}$$

Here $\mathbf{U}_e$ is the elastic distortion induced by the dislocation and $d\mathbf{r}$ represents the differential path length along the closed loop. The Nye tensor $\boldsymbol{\alpha}$, introduced by Nye (1953) incorporates both the line direction and the magnitude and direction of the Burgers vector, and it is associated with incompatible elastic distortions. The Nye tensor, as shown below, shows that the presence of dislocations alters the local structure of the crystal lattice and induces elastic distortions. It can be setup component wise as follows:

$$\alpha_{ij} = \frac{b_i}{\Delta S} t_j \tag{2.2}$$

Where ΔS represents the area enclosed by our path integral. The components of the Nye tensor α_{ij} can be related to the dislocations with total Burgers vector length along direction i per unit surface ΔS, with line vector along direction j. When analyzing multiple dislocations intersecting our surface (Figure 2(b)), the Nye tensor portrays the cumulative distortion from all dislocations within this area. Components from dislocations of opposite signs or line directions, for example, may neutralize each other, while similar distortions add up, we

speak of geometrically necessary dislocations. Utilizing Stokes' theorem, we can now directly connect the line integral of the Burgers vector to the Nye tensor:

$$\mathbf{b} = \iint_S \nabla \times \mathbf{U}_e \cdot \boldsymbol{n}\, dS = \iint_S \alpha \cdot \boldsymbol{n}\, dS \tag{2.3}$$

In the above equation, one can skip the surface integrals and directly relate the Nye tensor to the curl of the elastic distortion. Thus, the Nye tensor effectively maps how the presence of dislocations alters the local structure of the crystal lattice, causing elastic distortions. This tensor is crucial to link the gradient of displacement and the strain fields around a dislocation (see Section 3.2), making it easier to understand the effects of dislocations on the material.

2.1.3 Strain Energy in Linear Elastic Theory

After discussing the Nye tensor, we now turn to linear elastic theory to understand the impact of dislocations on strain energy, using the Volterra framework as our guide. For a broader perspective, we will also touch upon the analysis of dislocation networks, which is covered in Section 3.2.

In the Volterra dislocation concept, a cylinder contains a dislocation line parallel to its axis. The dislocation induces elastic distortions inside the cylinder. To remove the elastic distortions, a cut is made along the cylinder, parallel to its axis. The two created surfaces are then allowed to move with respect to each other, to relax the elastic distortion within the cylinder. The way the surfaces move with respect to each defines the nature of the dislocation Burgers vector and as such of the nature of the dislocation. If the two surfaces show a jump of displacement parallel to the dislocation line, it is a screw dislocation. If it is perpendicular, it is an edge dislocation. Such a concept was also used for defining disclinations. Hence, the nature of the displacement and distortion fields around these dislocations characterizes the stress state of the material and its mechanical response to applied forces. The displacement vector $\mathbf{u}$ represents the displacement of points in the material from their original, undeformed positions, to their new positions in the deformed state. It is a vector field that varies from point to point in the strained material, indicating both the direction and magnitude of the displacement. The strain itself is the change or derivative of the displacement and is linearly approximated as:

$$\epsilon = \frac{1}{2}\left((\nabla \mathbf{u})^T + \nabla \mathbf{u}\right) \tag{2.4}$$

The resulting stress, denoted as σ and is governed by Hooke's law:

$$\sigma = \mathbf{C} : \epsilon \tag{2.5}$$

Here, : represents the inner product, $\mathbf{C}$ is the elastic stiffness tensor, which depends on material properties and can be composed of up to 21 independent components. The symmetry of a structure can reduce the amount of components. Olivine as example has an orthorhombic structure, which reduces the amount of independent components to 9. In the assumption of an isotropic medium, we are left which two components, called elastic moduli, for instance the two Lame constants, λ and μ (with μ also known as the shear modulus).
The increase in internal energy of a strained material is associated with strain energy, which can be calculated as:

$$\frac{dE_e}{dV} = \frac{1}{2}\sigma\epsilon \tag{2.6}$$

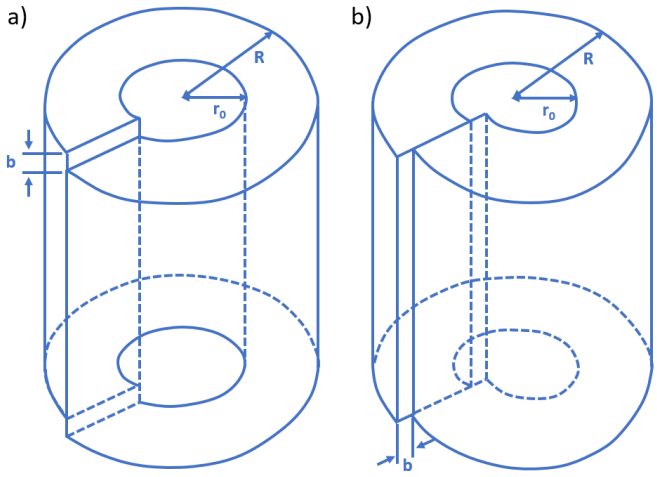

Figure 3: Volterra distortion cylinders (for calculating the elastic strain energy): (a) screw dislocation; (b) edge dislocation

The total strain per unit length (E_{total}) contains both the energy contained in the elastic field E_e and the core energy E_{core}. In the Volterra's description, the abrupt transition from zero displacement to the Burgers vector upon crossing the dislocation line results in a singularity along the line, causing the associated fields to diverge. In the context of linear elasticity, we circumvent this, by excluding a cylindrical region around the dislocation line. From there we can calculate the elastic strain of a straight screw dislocation. Utilizing the concepts introduced earlier and applying it to the displaced cylinder (Figure 3(a)), we derive the

elastic strain energy for a screw dislocation as follows:

$$E_e(screw) = \frac{\mu\, b^2}{4\,\pi} \int_{r_0}^{R} \nabla \times \frac{dr}{r} = \frac{\mu\, b^2}{4\,\pi} ln\left(\frac{R}{r_0}\right) \tag{2.7}$$

Here r_0 is the cut-off core radius (below which classical elasticity is not valid anymore) and R the outer radius for integration. The term $\mu\, b^2$ is related to the product of the stress and strain components. For an edge dislocation, we obtain (Figure 3(b)):

$$E_e(edge) = \frac{\mu\, b^2}{4\,\pi(1-\nu)} \int_{r_0}^{R} \nabla \times \frac{dr}{r} = \frac{\mu\, b^2}{4\,\pi(1-\nu)} ln\left(\frac{R}{r_0}\right) \tag{2.8}$$

Here ν is the Poisson ratio. To calculate the strain energy of a mixed dislocation, we superimpose the cases for screw and edge dislocations since, as demonstrated in the Nye section, it involves a composite of both elements:

$$E_e(mixed) = \frac{\mu\, b^2\,(1-\nu\, cos^2\theta)}{4\,\pi(1-\nu)} \ln\left(\frac{R}{r_0}\right) \propto \mu\, b^2 \tag{2.9}$$

Where θ is the angle between edge and screw. This demonstrates that the elastic energy associated with any type of dislocation scales with the square of the Burgers vector $\mathbf{b}$, making smaller lattice translation vectors favorable.

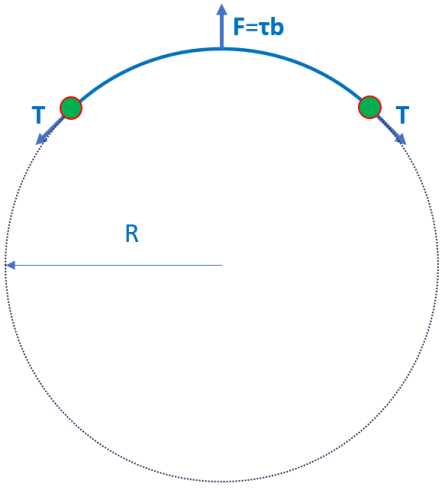

Figure 4: Sketch of a pinned dislocation segment that bow out under applied resolved shear stress τ. Pinning points are indicated in green.

The total elastic energy of a dislocation U, is the elastic strain energy over the dislocation's length L. The dislocation length is therefore minimized to reduce energy, which result in dislocations tend to have the shortest possible length and align as straight as possible. When

we consider the curvature of a dislocation, it reflects a balance between the elastic energy, striving to keep the dislocation as short as possible, and the force ($\mathbf{F} = \tau\mathbf{b}$) associated with the applied stress (τ) on the dislocation. This can be approximated as (Friedel 1964):

$$R = \frac{\mu\mathbf{b}}{\tau} \tag{2.10}$$

Here, R represents the radius of curvature. This relationship is visualized in Figure 4. Another important consequence of the high energy associated with a dislocation is that knots with more than three dislocations are prone to splitting into two knots with three dislocations and an intermediate dislocation to reduce line tension.

2.1.4 Core Models

To describe the mobility of a dislocation, it's crucial to consider the core region, which was previously simplified by excluding it. The Peierls-Nabarro (PN) model, proposed by Peierls (1940), offers a more regularized understanding of the dislocation core. It considers the balance between elastic forces and inelastic forces arising from atomic misfit within the core region. As a result, the shear profile associated with the dislocation spreads within the core (see Figure 5 (b)). However, the PN model primarily addresses dislocations spreading along a single plane, making it suitable for analyzing planar core structures but less effective for complex core configurations.

To capture the complexities of dislocation cores more accurately, further models have been

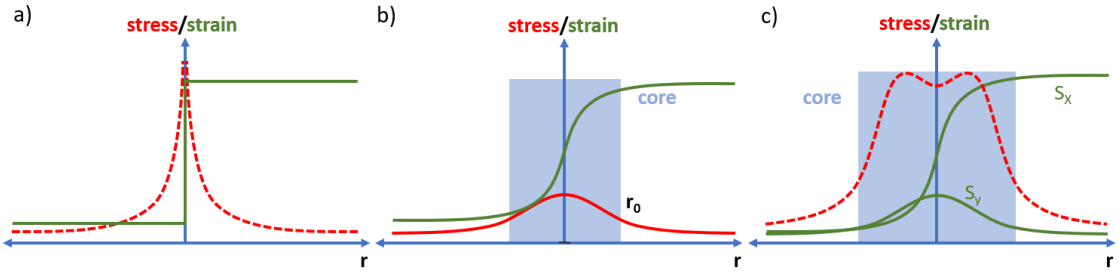

Figure 5: Stress (red) and strain (green) profiles around a dislocation line for different core models: (a) Volterra/Linear elasticy, abrupt jump at the dislocation line results in a divergent stress field; (b) PN model spreads the strain field around the core, resulting a smoother stress field. Blue region indicate the core region, define by a cut-off core radius r_0; (c) PNG model for a non-collinear core , showing a different strain field in x-direction (S_x) and y-direction (S_y) (example shows a camel-hump potential in the presented plane, could be a different shape in a different plane).

developed. The Generalized Stacking Fault (GSF) model, demonstrated by Vitek (1968), introduces the concept of shearing along a plane with the restoring force being the gradient of the GSF energy. This approach provides insights into whether a dislocation core will

exhibit simple behavior or undergo dissociation, like it can be seen in olivine (Durinck et al. 2007a), where the dislocation transforms into partial dislocations, each characterized by Burgers vectors smaller than any lattice repetition. These partial dislocations are separated by a stacking fault.

A more generalized approach is found in the Peierls-Nabarro-Galerkin (PNG) model, which accommodates multiple glide planes and complex core structures, including non-collinear (see Figure 5(c)) and three-dimensional cores. The PNG model uses a three-dimensional displacement field $\mathbf{u}(r)$ for continuous deformation around the core and a two-dimensional displacement discontinuity field $\mathbf{f}(r)$ for displacement jumps across planes. This dual-field approach allows for a detailed examination of the core structure by minimizing elastic energy and interplanar potential.

2.2 Visualization of Dislocations in TEM

Until the 1950s, dislocations remained hypothetical entities, based on theoretical concepts. It was only through the TEM experiments conducted by Hirsch et al. (1956) that dislocations were first directly visualized. Hirsch employed a diffraction contrast method to visualize dislocations, a technique we will also utilize in this work.

In diffraction contrast, we do not directly image the dislocations themselves but rather the strain field that surrounds them. The bending of the crystal lattice around a dislocation core creates lattice distortions and generates observable contrast.

Before delving into the specifics of diffraction contrast and its application to dislocation visualization, let's first explore the fundamental concepts of imaging in a TEM.

2.2.1 Image Contrast

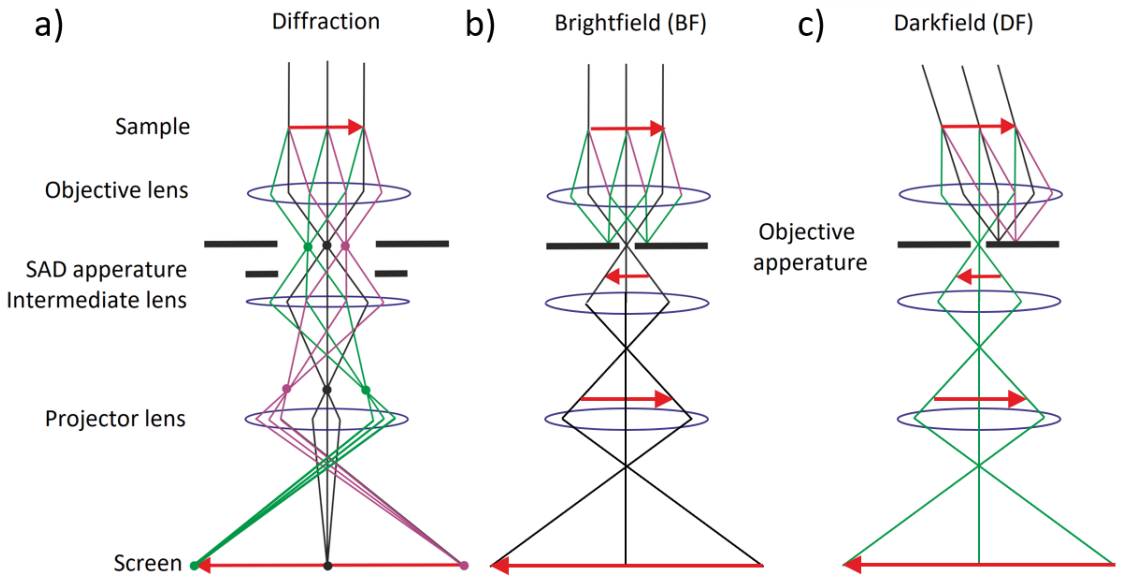

Figure 6: Sketch of ray paths in TEM: (a) Diffraction condition; (b) Brightfield condition; (c) Darkfield condition.

In a conventional TEM, the imaging process relies on a parallel and non coherent electron beam that passes through a thin specimen, primarily undergoing forward scattering interactions. To manipulate this electron beam for imaging, a series of electromagnetic lenses, similar in function to those in a light microscope, are employed. These lenses include an objective lens, an intermediate lens, and projector lenses.

TEM operation is typically divided into two primary modes: the diffraction mode and the image mode.

2.2.1.1 Diffraction Mode

In the diffraction mode, the electron beam's interaction with the crystalline lattice of the specimen reveals lattice periodicity through diffracted spots in reciprocal space. The diffracted electron beams are brought into focus in the back focal plane of the objective lens, which corresponds to the plane of the diffraction pattern. Subsequent lenses magnify this diffraction pattern and project it onto a phosphorescent screen or a CCD detector, yielding critical insights into the crystallographic structure of the specimen.
A selected area aperture, placed before the intermediate lens, can be used to limit the observation to a specific region of interest within the specimen. A full schematic ray path for the diffraction mode is illustrated in Figure 6(a)).

2.2.1.2 Image Mode

In the image mode, the goal is to obtain a magnified view of the specimen. The focus of the intermediate lens is therefore adjusted to create an intermediate image of the image plane on to the projection lens that then further magnifies the image on to the detector.
By default, in image mode, the image may exhibit a faint contrast due to multi-scattering effects. To address this, specific electron beams can be selected and manipulated. For this an objective aperture is inserted in the back focal plane of the objective lens.
When the direct beam is selected, the background appears bright, while strongly diffracted regions, such as those near defects, appear dark. This mode is therefore referred as **bright-field imaging** (BF), and the corresponding ray path is illustrated in Figure 6(b).
To isolate a diffracted beam, the electron beam can be shifted accordingly. This shift results in a dark-field image, where specific diffraction events are highlighted and the undiffracted parts appear dark. The ray path for **dark-field imaging** (DF) is illustrated in Figure 6(c).

2.2.2 Ewald's Sphere

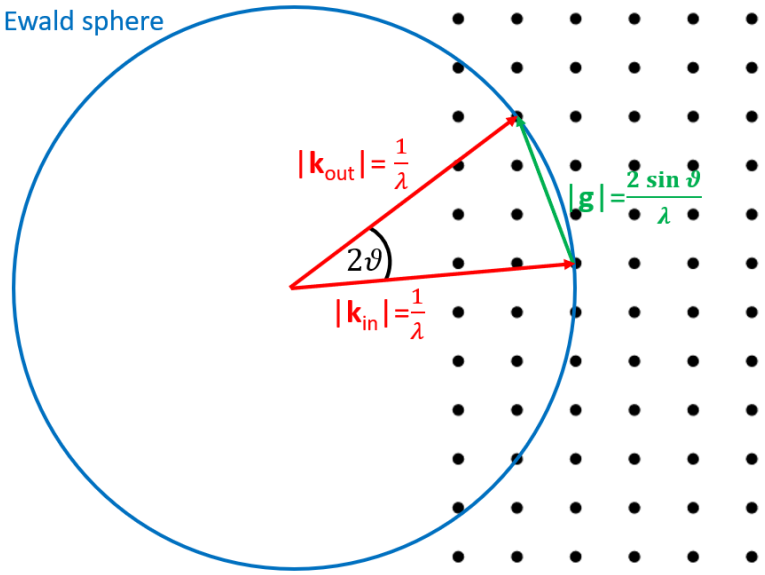

Figure 7: Ewald sphere construction in 2D. Indicating the incident wave vector $\mathbf{k}_{in}$ and diffracted wave vector $\mathbf{k}_{out}$ in red and the diffraction vector $\mathbf{g}$ in green.

Diffraction contrast arises from the coherent elastic scattering of electrons at specific angles, known as Bragg angles. To achieve robust diffraction contrast, the sample is typically tilted in such a way that only one diffracted beam is excited, this condition is called "two-beam condition". This phenomenon can be understood through the Bragg-Laue condition (Laue 1913), which plays a central role in diffraction contrast:

$$\mathbf{k}_{out} - \mathbf{k}_{in} = \mathbf{g}_{hkl} \tag{2.11}$$

Here, $\mathbf{k}_{out}$ represents the wave vector of the diffracted electron beam, $\mathbf{k}_{in}$ is the wave vector of the incident beam, and $\mathbf{g}_{hkl}$ denotes the reciprocal lattice vector associated with the crystal lattice's orientation, also known as the diffraction vector. This equation essentially states that for diffraction to occur, the difference between the incident and diffracted wave vectors must be equal to a reciprocal lattice vector. This concept can be visually grasped through the Ewald sphere construction, where a sphere with a radius of $1/\lambda$ (where λ is the wavelength of the incident electrons) represents all possible reflections. Where the Ewald sphere intersects with reciprocal lattice nodes, the diffraction condition for constructive interference is satisfied. A 2D representation of the Ewald construction can be seen in Figure 7. This construction reveals that the magnitude of $\mathbf{g}$ is $2sin\vartheta/\lambda$, where ϑ is the angle between incident and diffracted beam. This aligns with Bragg's law:

$$\lambda = 2d_{hkl}sin\vartheta \tag{2.12}$$

Here, d_{hkl} represents the inter-planer spacing. When aligning a zone axis with the electron beam, where "zone axis" denotes a high-symmetry orientation of a crystal with multiple lattice rows parallel to a specific direction, the Laue condition theoretically predicts the absence of diffracted spots for central region (in the zero order Laue zone). However, in practice we can observe diffraction patterns with multiple diffracted spots at these orientations. This inconsistency can be explained by the excitation error s. The reciprocal lattice nodes, which are essentially sinc functions in cross-section, and extend in mainly in z direction (direction of the electron beam) and are therefore called reciprocal lattice rods (relrods). The deviation s from the ideal diffraction condition, then results in an adjusted Laue condition:

$$\mathbf{k}_{out} - \mathbf{k}_{in} = \mathbf{g}_{hkl} + \mathbf{s} \tag{2.13}$$

Which later will become relevant when talking about a refined contrast in weak beam dark field (Section 2.2.4).

2.2.3 Extinction Distance

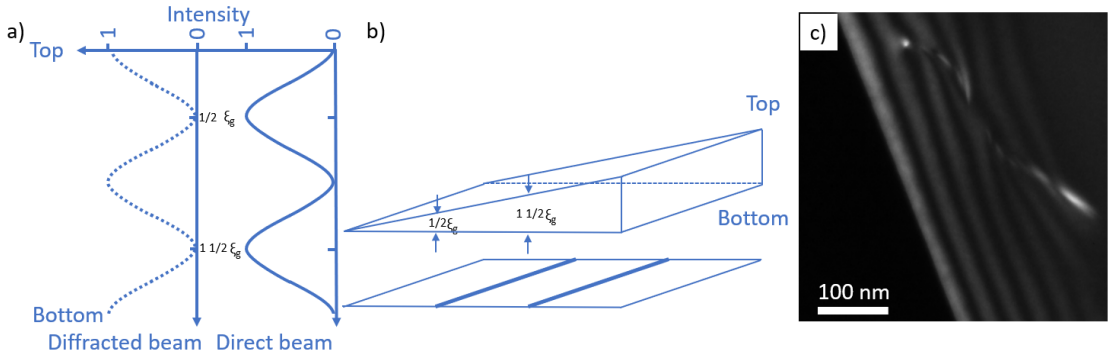

Figure 8: Illustration of the effect of the extinction distance ξ_g on wedge shaped specimens: (a) Intensity profile of diffracted and direct beam; (b) Sketch of a wedge in BF contrast indicating the corresponding thickness fringes in dark blue; (c) Weak Beam Dark-Field (WBDF) micrograph showing thickness fringes at the wedge.

Another effect that must be considered is linked with the phase of the electron beam. As electrons cross the specimen, the direct and diffracted beams behave like a coupled pendulum, oscillating back and forth in amplitude. The frequency at which the intensity changes can be

described by the extinction distance ξ_g (see Williams and Carter 2009, p. 223):

$$\xi_g = \frac{\pi V_c \cos \vartheta_B}{\lambda \cdot |\mathbf{F}_g|} \tag{2.14}$$

Here, V_c represents the unit cell volume, ϑ_B is the Bragg angle, and F_g is the structure factor. This dynamic interaction manifests in various effects, one of which is occurrence of thickness fringes in wedge-shaped samples (illustrated in Figure 8). It also creates an oscillating contrast of inclined dislocation. The corresponding intensity of the diffracted beam I_g (see Williams and Carter 2009, p. 228) is given by:

$$I_g = |\Phi_g|^2 = \left(\frac{\pi h}{\xi_g}\right)^2 \frac{sin^2(\pi h s_{eff})}{(\pi h s_{eff})^2} \tag{2.15}$$

Here, Φ_g is the amplitude of the diffracted beam, h is the specimen thickness, and s_{eff} represents the effective excitation error, relating to the extinction distance ξ_g and the excitation error s:

$$s_{eff} = \sqrt{s^2 + \frac{1}{\xi_g^2}} \tag{2.16}$$

2.2.4 Weak Beam Dark-Field

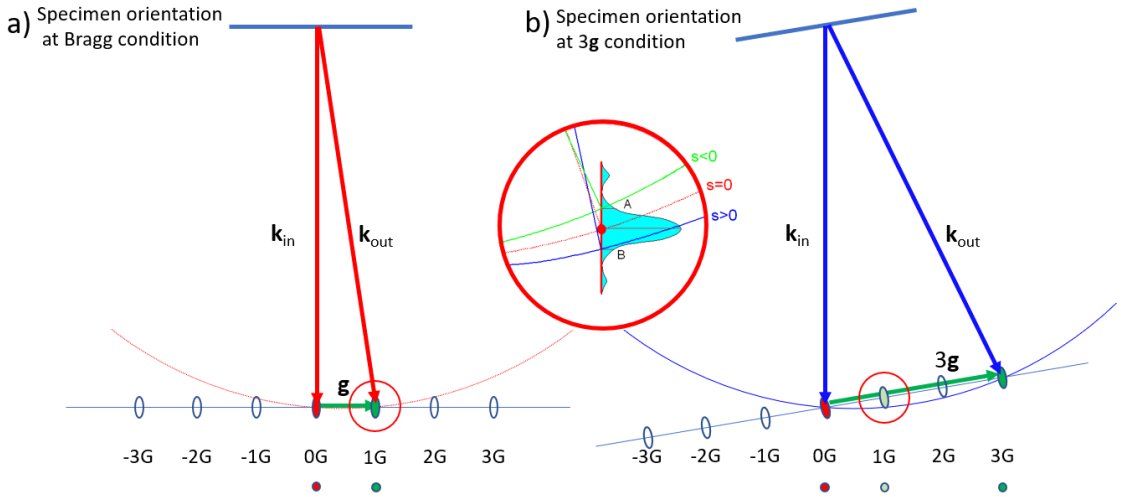

Figure 9: WBDF imaging: Ewald sphere construction shows the intersection with the reciprocal lattice rods and the resulting spot intensity for different diffraction vectors. (a) Bragg condition; (b) Tilted specimen in WBDF condition, with maximal excitation of the 3G diffraction vector. Weak intensity for selected diffraction vector circled in red. Red circle in the center shows different s value condition; G inside Ewald sphere → s positive and G outside Ewald sphere → s negative.

Shifting focus from the intricacies of electron beam interaction, we will now describe the image technique as Weak Beam Dark-Field (WBDF) imaging. WBDF imaging, was developed in 1969 by D.J.H. Cockayne, I.L.F. Ray, and Whelan (Cockayne et al. 1969). This technique is used to significantly improve the spatial resolution of dislocation imaged in the TEM. It starts by setting up a two-beam condition, then the specimen is delicately tilted away from this state, causing a stronger excitation of a higher-order diffraction vectors. This is done till most of the time the 3**g** diffraction vector is brought into Bragg condition (s=0). Due to the deviation parameter, a narrow but weak signal persists for the 1**g** diffraction spot with a high *s* value. This diffraction vector is then selected as the diffracted spot for the dark field imaging (this process is illustrated in Figure 9). It results in a narrow signal for the dislocation lines. However, the weakened signal necessitates longer exposure times to increase the signal to noise ratio, which requires a high stage stability.

2.2.5 Dislocation contrast in TEM

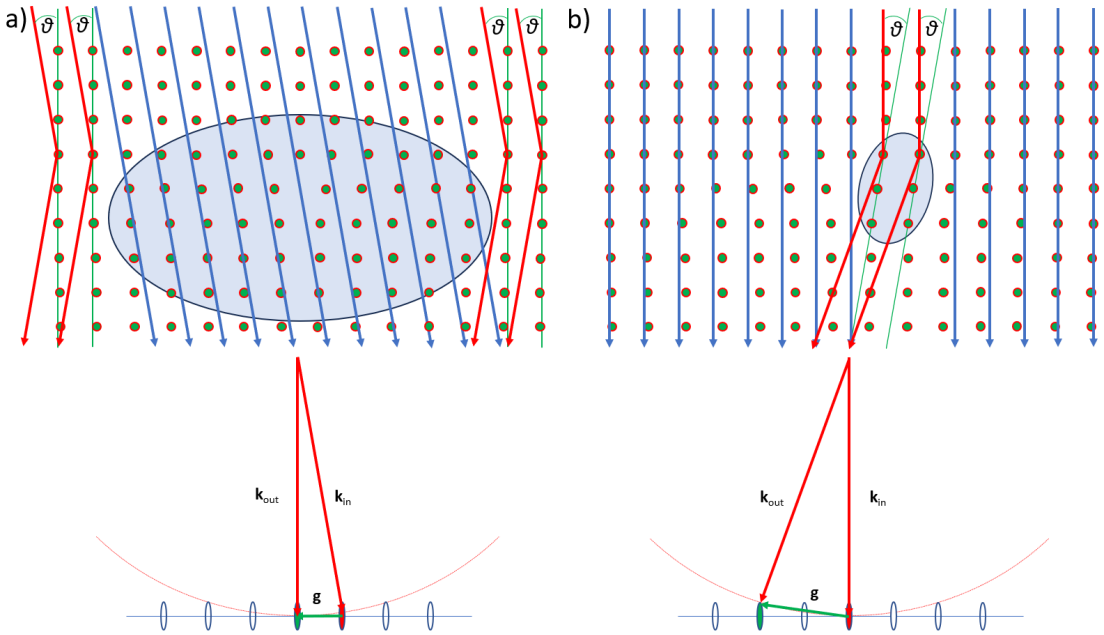

Figure 10: Diffraction of electron beam on the crystal lattice surrounding a dislocation and the corresponding Ewald construction; blue area indicates region of contrast, red vectors indicate diffracted electron beam: (a) Bragg condition and (b) WBDF condition.

Let's consider a straight edge dislocation lying perpendicular to the optical axis. To image the dislocation, a slight tilt away from the Bragg condition (see Figure 10(a)) is applied, ensuring that only the distorted planes on the right side of the dislocation line will satisfy the Bragg condition (see Figure 10(b)).

It is the WBDF technique, as described in the previous section. Contrast is derived solely from the strongest strained part close to the dislocation core. Physically, this corresponds to the diffraction of the planes which are bent just enough to bring them back into the extended Bragg condition, which also shifts the signal closer to the core position.

Due to the high s value, this scenario can be described within the kinematic approximation ($s >> \xi_g^{-1}$), where only the interaction between the direct and a single diffracted beam gets considered, excluding any interferences with other diffractions. For dislocation contrast this framework was introduced by Hirsch and Whelan (1960). In this approximation, the amplitude Φ_g of the electron wave at a certain depth z is determined by integrating the scattering from distorted region in a thin column parallel to the incoming beam direction. The key assumption is that there is no dispersion of the beam outside this column (it is also referred as column approximation). While the scattered wave crosses through the faulted region (characterized by a displacement field $\mathbf{u}$), it undergoes a phase change $\alpha = 2\pi\mathbf{g} \cdot \mathbf{u}$. The amplitude Φ of the scattered wave at the bottom surface of the TEM specimen is then

described by:

$$\Phi_g = \int_{column} \exp(i\,\alpha) \exp(i2\pi s z)\, dz \tag{2.17}$$

The intensity I_g is therefore $\sim |\mathbf{g} \cdot \mathbf{b}|^2$. The corresponding intensity profiles were initially derived for perfect screw dislocations parallel to the TEM specimen surface by Hirsch and Whelan (1960) and were later extended to pure edge dislocations by Gevers (1962). These profiles are illustrated in Figure 11.

In the case of screw dislocations, the displacement of the peak from the exact dislocation position is approximately the width of the image contrast. The intensity profiles are notably influenced by the $n = \mathbf{g} \cdot \mathbf{b}$ factor. For $n = 3$ and 4, an additional maximum appears on the side of the dislocation. Intensity profiles for edge dislocations exhibit a broader shape, about twice as wide as those for corresponding screw dislocations. The displacement of the image contrast of an edge dislocation is also approximately double that of the screw line. It's essential to note that the actual line profiles for edge dislocations are contingent on their Poisson ratios. Gevers (1962) calculations presented in Figure 11 assume a Poisson ratio of $\nu = 1/3$.

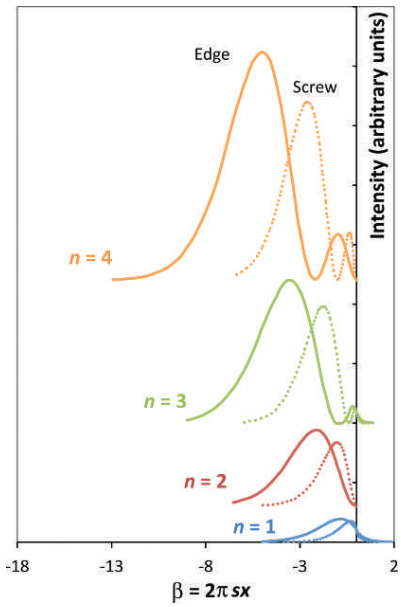

Figure 11: Kinematic intensity profiles in DF imaging for screw (dotted lines) and edge (solid lines) dislocations (Gevers 1962), which depend on: $n = \mathbf{g} \cdot \mathbf{b}$ and $\beta = 2\pi s x$, with s representing the excitation error and x indicating the distance to the dislocation core (the center of the dislocation is positioned at $x = 0$). Illustrations for values of n ranging from 1 to 4 are presented, each offset vertically for clearer distinction. Figure from Cordier 2013.

2.2.6 Tomography in TEM

2.2.6.1 History

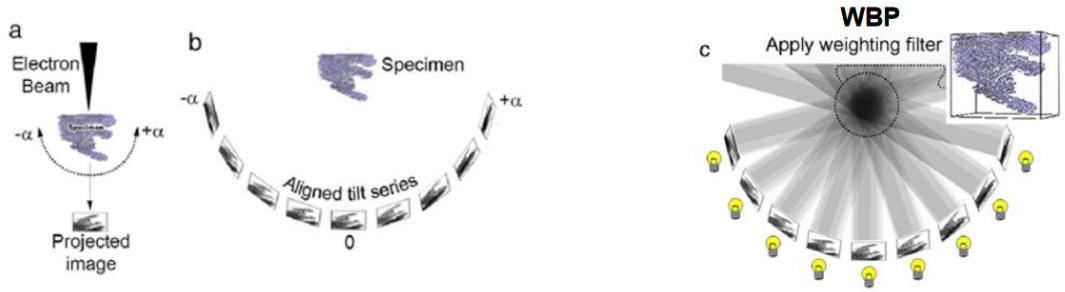

Figure 12: Sketch illustrating the main steps of electron tomography; (a) Image acquisition at different angles; (b) forming a tilt series that has to be aligned; (c) of which a 3D volume of the structure gets created by applying a reconstruction algorithm (WBP, see section 3.1.2.1). Sketch from Liu et al. (2014, Figure 1)

TEM images are inherently limited to two-dimensional projections of thin three-dimensional objects. Electron tomography represents a powerful technique capable of transcending this inherent limitation. An overview of the main steps for an electron tomography are shown in Figure 12.

The evolution of tomography in TEM has historical roots across various scientific domains. Its inception traces back to the field of biology, with the pioneering work accomplished by De Rosier and Klug (1968), relying on mass-thickness contrast. Over time, tomography extended its reach into the domain of material science, as demonstrated by Koster et al. (2000), who successfully reconstructed a metal/zeolite crystal. Further exploration of this field can be found in a comprehensive review by Friedrich et al. (2009).

In the context of dislocation microstructures, which is our focus, the concept of characterization planes of dislocation traces back to early ideas based on stereo projection, an approach initially proposed by Miller (1839). Practical application of these ideas emerged by Basinski and Basinski (1964) who studied dislocation networks in plastically deformed single-crystal copper. The first three-dimensional reconstruction was done using stereo pairs, employing electron microscopy or X-ray topography (Lang 1959). In this method, two images are captured at the same reflection angle, while the sample underwent a slight tilt around an axis parallel to the reflection. These paired images are then observed through a stereo viewer to generate a basic 3D representation. Newer studies improved the stereo pair technique and applied it to the TEM (Jácome et al. 2018), with further work done by Eftink et al. (2017), and Oveisi et al. (2018). In the same time, X-ray stereo pair topography, developed by Ludwig et al. (2001), evolved into X-ray topo-tomography. This technique recorded a tilt

series while rotating the sample by 180° in the X-ray beam, maintaining a constant imaging reflection, as initially proposed by Haruta (1965). The resulting reconstruction successfully resolved dislocations with separations on the order of 100 µm in a diamond sample. The implementation of tomography at the TEM for dislocation microstructure took until 2006 (Barnard et al. 2006), using the technique applied in our approach, known as Dislocation Electron Tomography (DET). A more detailed exploration of DET will be provided in the subsequent paragraph.

2.2.6.2 Dislocation Electron Tomography

DET is a powerful technique that relies on diffraction contrast, making it strongly orientation dependent. This technique can reconstruct with high quality 3D dislocations microstructures. It can extract numerous geometric parameters, including dislocation length, density, spacing and radius of curvature. Additionally, it provides valuable crystallographic parameters such as dislocation character, habit planes and line directions. The origins of DET can be traced back to the pioneering work of Barnard et al. (2006). It is worth noting a considerable time gap since the initial implementation of TEM tomography in 1968. This delay can be attributed to the challenge of maintaining consistent diffraction conditions throughout the extensive angular range required for tomography. This demands precise alignment of the tilt axis, typically within a tenth of a degree. Since then, the technique has been applied to various scenarios, including analyses near cracks (Tanaka et al. 2008 and Sharp et al. 2008), investigations on subgrain boundaries (Kacher et al. 2011) and their interactions with grain boundaries (Kacher and Robertson 2014), as well as DET studies on dislocation-precipitate interactions (Liu and Robertson 2011).

DET has also found applications in the field of mineralogy, with the first on olivine by Mussi et al. (2014), with subsequent studies done in 2015 (Mussi et al. 2015a,b). Those studies also form the basis for the implementation into Dislocation Dynamics (DD), shown in this work. Furthermore, DET has been extended to beam-sensitive materials, such as quartz, where reconstruction is achieved using only a few projected images (Mussi et al. 2021c). Additional insights and reviews on DET are provided in works by Hata et al. (2020b) and Feng et al. (2020).

Recent advancements in DET have incorporated machine learning to facilitate the reconstruction process. For example, Altingövde et al. (2022) combines neural network and stereo pair in STEM mode to perform tilt-less DET, while Sills and Medlin (2022) employ a semi-automated object-based approach, using the fact that dislocations are 1D objects. Moreover, advancements have been made towards achieving 4D reconstructions, including the dimen-

sion of time. Notably, a quasi-4D tomography, as demonstrated by Kacher and Robertson (2012), in which dislocations are observed in real-time in 2D during in situ straining experiments, followed by post-mortem tomography to retrieve 3D microstructural information; or the first implementation of a real 4D tomography by Mussi et al. (2021b), where they utilizes electron radiation to make dislocations climb. These developments showcase the versatility and continuous innovation within the realm of DET.

In our study we take a different approach to examining the 4D evolution of microstructures. This is accomplished by incorporating microstructural data from DET into Dislocation Dynamic Modeling (DDD). In the subsequent sections, I will provide a deeper exploration of the dynamics of microstructures in a more general context.

2.3 Dislocation Dynamics

The motion of defects controls the transport of shear in solid material and therefore its plastic deformation. Dislocations are the defects that mainly contributes to the strain, only in a high temperature regime point defects take over.

2.3.1 Glide Mechanism

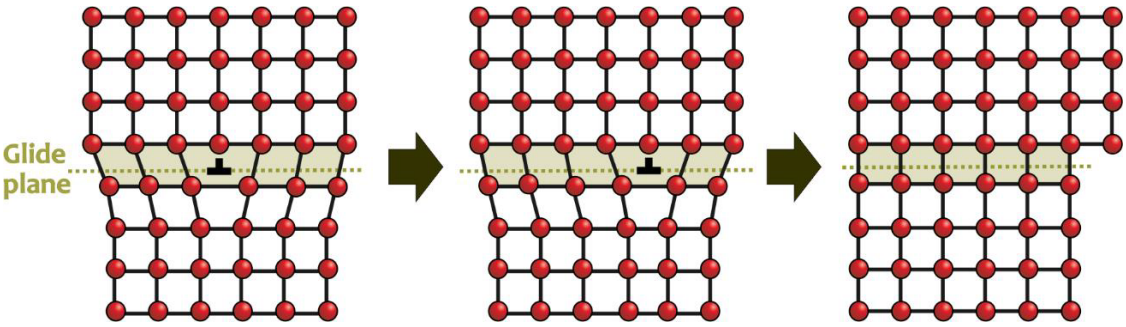

Figure 13: Movement of an edge dislocation via glide motion due to applied stress, courtesy A. Goryaeva.

Under applied stress, dislocations are allowed to move via a conservative glide motion. The motion of a dislocation occurs on a plane containing its dislocation line and its Burgers vector. A glide process of an edge dislocation is shown in Figure 13. The stress needed to activate a glide plane depends on the lattice friction. Due to the stress fields surrounding the core (see Section 5), dislocations encounter an energy barrier known as the Peierls potential, which must be overcome to enable glide. The stress required at absolute zero temperature to overcome this barrier is the Peirls stress. The activation of glide systems typically prioritizes

the densest atomic packing within the crystal lattice.

To connect this microscopic understanding to a macroscopic stress analysis, we introduce the concept of resolved shear stress (RSS) using the Schmid tensor. The Schmid tensor $\mathbf{S}$ is a representation of the slip system's orientation, derived from the outer product of the slip direction represented by the Burgers vector $\mathbf{b}$ and the slip plane normal vector $\mathbf{n}$. This tensor is essential in determining the RSS, which is the component of the applied stress tensor σ_{app} that acts along the slip direction on the slip plane:

$$\mathbf{S} = \mathbf{b} \otimes \mathbf{n} \tag{2.18}$$

The resolved shear stress τ_{RSS} is then calculated by projecting the applied stress tensor onto the slip system through the Schmid tensor:

$$\tau_{RSS} = \sigma_{app} : \mathbf{S} \tag{2.19}$$

In practice, the minimum stress required to surpass the Peierls potential and initiate glide along a specific slip direction is termed the critical resolved shear stress (CRSS), denoted as τ_{CRSS}. It is important to note, that this parameter remains constant for each unique slip system within a given crystal structure and a given temperature.

2.3.2 Thermal Regimes

Up to this point, we only considered flow at absolute zero temperature. However, in practice that is not the case. Therefore, in the following sections, we will delve into the evolution of flow across a range of temperature regimes, as illustrated in Figure 14. This exploration will provide a more comprehensive understanding of how material deformation varies under different thermal conditions.

2.3.2.1 Low Temperature Regime

At absolute zero temperature, dislocations remain immobile unless the applied stress exceeds the Peierls stress. However, at finite temperatures, thermal fluctuations allow dislocations to move. This occurs through the localized thermal agitation of atoms, enabling specific portions of the dislocation to overcome the motion energy barrier. As a result, kink pairs are formed along the dislocation line, as depicted in Figure 15. Subsequently, these kinks propagate within the Peierls valley until the entire dislocation line has transitioned into the

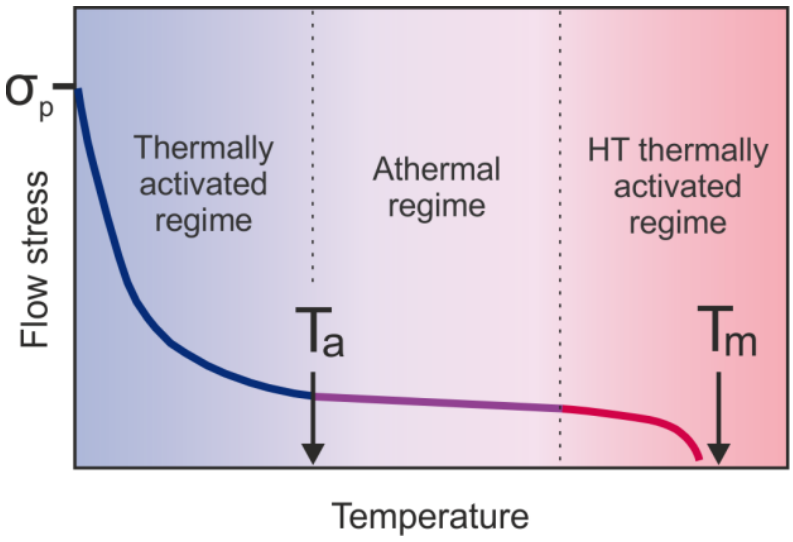

Figure 14: Thermal glide regimes, where T_a denotes the athermal temperature and T_m is the melting temperature; courtesy A. Goryaeva.

new valley. This cyclic process repeats itself. The velocity of dislocation motion in this temperature regime can be described by Kocks' law (Kocks et al. 1975):

$$v = \frac{\omega_D L b^2}{l_c^2} \exp\left(-\frac{\Delta H(\tau)}{k_B T}\right) \tag{2.20}$$

Here ω_D is the Debye frequency, L is the length of the dislocation, b is the magnitude of the Burgers vector, l_c is the critical length of kink-pair nucleation, k_B the Boltzmann constant T the temperature and ΔH is the activation enthalpy.

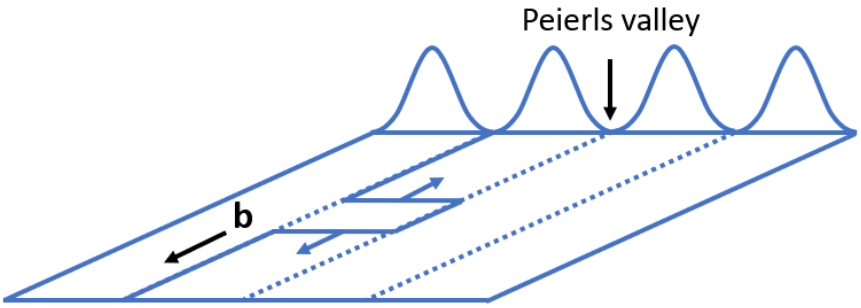

Figure 15: A sketch of a kink pair that just over come the Peierls barrier to reach the next low energy valley and now spreads.

2.3.2.2 Athermal Regime

As temperature increases, the likelihood of such events rises, resulting in an increase in their average velocity. When a sufficiently high temperature is reached, we enter a regime

where the previously mentioned kink-pair mechanism is no longer necessary. In this regime, dislocations can move more freely, it is known as the athermal regime. Here, the gliding velocity experiences a slowdown primarily due to interactions with the crystal lattice, which is quantified by a drag coefficient B. The velocity can be expressed as follows:

$$v_g = \frac{\tau_{eff}\mu}{B}\frac{T}{T_0} \tag{2.21}$$

Here $T_0 = 300K$ is the ambient temperature, T is the temperature of interest and τ_{eff} denotes the effective stress. When we look not at the glide velocity but at the collective velocity of a dislocation network, the velocity is controlled in this regime by dislocation interactions, which hinders their motion and is linked with recovery mechanism that resolve these interactions (see Section 2.3.4.1). This leads to a steady-state conditions, which is why we see a plateau in Figure 14.

2.3.2.3 High Temperature Regime

At even higher temperatures, approaching the melting point, diffusion becomes active promoting high temperature mechanisms, like climb, that can lead to recovery and possibly recrystallization. More details on some of these recovery processes will be given in Section 2.3.4 in the context of climb.

2.3.3 Dislocation Interactions

Up to this point, we have considered individual dislocations, but to accurately describe continuous deformation, we must also account for their interactions with one another. When analyzing the forces acting on dislocations, we need to consider not only the external forces (applied stress) but also the stress that arises from dislocations interacting with each other. The forces acting on each individual dislocation can be calculated using the Peach-Koehler force equation:

$$\mathbf{F}_{PK} = \mathbf{b} \cdot (\sigma_{app} + \sigma_{int}) \times \mathbf{t} \tag{2.22}$$

Here, $\mathbf{b}$ represents the Burgers vector, $\mathbf{t}$ is the dislocation line, σ_{app} denotes the applied stress, and σ_{int} is the stress field induced by the dislocation microstructure. This implies that the force acting on a dislocation is fully determined by the local stress on the dislocation, allowing us to calculate stress as a linear superposition of all occurring stresses.

We will now describe some of the interactions that dislocations can undergo when they encounter one another. We'll begin with the simplest interactions that occur between parallel dislocation segments. When two such segments approach each other, they can either repel or attract, depending on whether their Burgers vectors have the same or opposite signs. Overcoming this interaction requires external stresses to be greater than the interaction forces between them. When two dislocations in parallel planes, of opposite sign and identical Burgers vector get close to each other, they can create a dipole, which can annihilate if they are within a certain distance. This annihilation can occur via a climb mechanism, which we'll discuss further in the next section.

A special case has to be considered for pure screw dislocations. Since the Burgers vector of pure screw dislocations is parallel to their line direction, the slip plane is not uniquely defined. Consequently, pure screw dislocations can change their glide plane, a process known as "cross-slip". Hence, pure screw dislocations will annihilate through cross-slip. They will also cross-slip when encountering other obstacles.

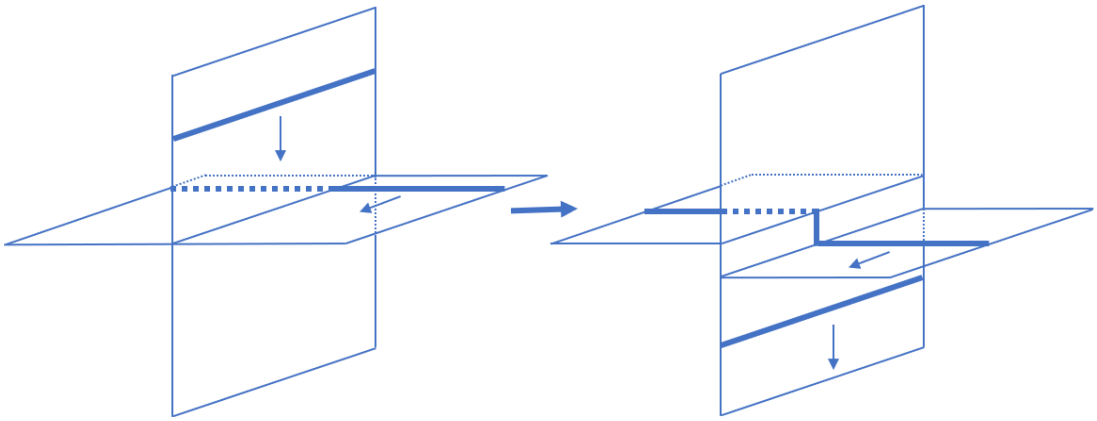

Figure 16: Jog formation: Intersection of edge dislocations with perpendicular Burgers vectors and planes.

One notable interaction between dislocations that cross paths through non-parallel gliding planes is the formation of "jogs". Those occur when edge dislocations with different Burgers vectors and perpendicular planes intersect, see Figure 16. A jog is a short section of the dislocation line, typically a Burgers vector distance after a single dislocation interaction, which lies outside the slip plane. Jogs affect dislocation mobility and contribute to work hardening, since they are sessile. The movement of jogs can leave a trail of point defects, and if they accumulate significantly, they can form dislocation loops.

Jogs can also arise through the absorption of point defects during dislocation climb, which we will explore in more detail in the following section.

The interaction between two dislocations with collinear Burgers vectors gliding in intersect-

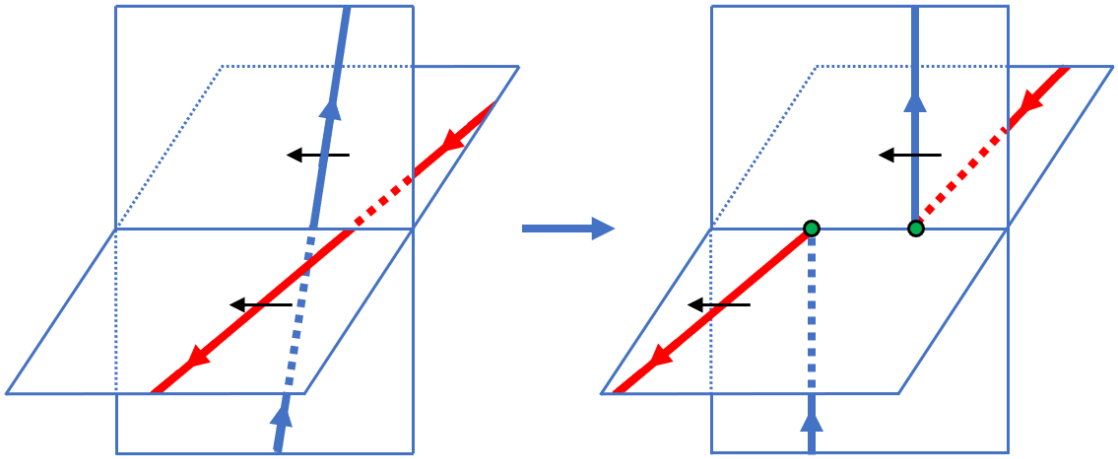

Figure 17: Collinear interaction between two dislocation with black arrows indication **b** and the colored lines are the dislocation lines. The nodes that remain with a reduced mobility, are indicated by the green circles.

ing slip planes is called a collinear interaction and can be seen in Figure 17. It results in an annihilated junction, corresponding to zero elastic energy. This interaction is the most stable of these reactions. They are among the strongest reactions between dislocations in face centered cubic (fcc) (Madec et al. 2003). The nodes of the two dislocations with different planes that remain have a reduced mobility.

Looking at an advanced state of deformation, more dislocation interaction will lead to more obstacles in the microstructure, be through the formation of sessile junction, collinear interactions, or the formation of jogs. Regions with such obstacles increase the likelihood of new dislocations becoming immobilized. Over time, these immobile dislocations aggregate and form clusters, a phenomenon known as "forest hardening". Sustaining deformation in the presence of forest hardening hinges on the dislocations capacity to either transition to alternative glide planes or undergo annihilation. For both processes climb plays a significant role.

2.3.4 Climb Mechanism

So far, we only considered the conservative motion along the glide planes. However, when glide becomes challenging or prohibited due to factors such as limited glide options or the presence of sessile dislocation clusters, a non-conservative motion called "climb" becomes significant if temperature is high enough to activate diffusion.

In climb, diffusion results in the absorption or emission of vacancies at an edge dislocation line. This action causes a short segment of the dislocation line to move away from the glide plane in a direction perpendicular to the Burgers vector, forming a jog (Mott 1951). The process can be seen in Figure 18.

One noteworthy characteristic of climb is that the plane normal and the Burgers vector are collinear. For an in-depth exploration of this subject, I recommend referring to the review paper by Carrez et al. (2024).

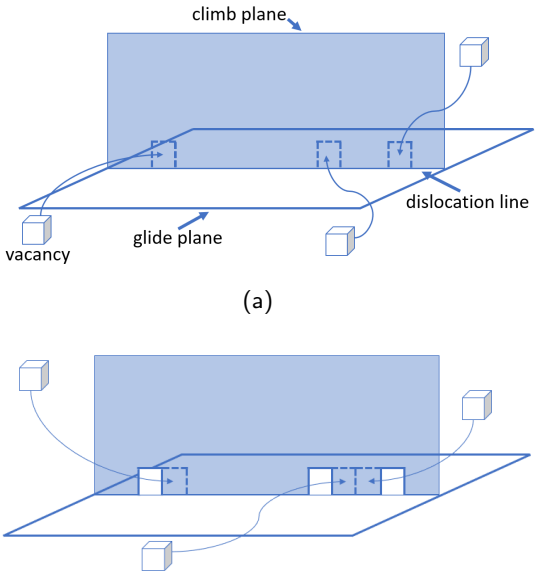

Figure 18: Jog formation due to the absorption of point defects. Vacancies diffuse towards the dislocation line and getting absorbed, creating jogs.

2.3.4.1 Climb as Recovery Mechanism

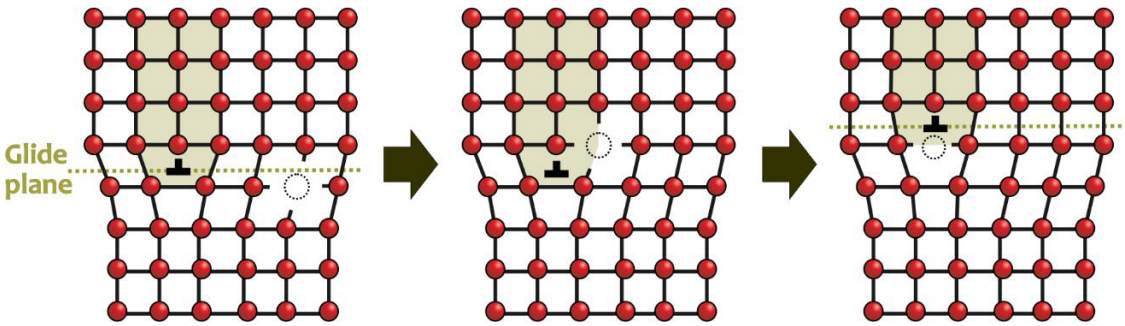

Figure 19: Sketch of a stuck dislocation which changes its glide plane via climb motion, courtesy A. Goryaeva.

Climb plays a crucial role in the recovery of materials subjected to plastic deformation. Such deformation is described using creep models, where creep describes a permanent deformation under a constant load over time at a fixed high temperature. There exist many creep models in literature, but what they have in common is the description of a steady-state deformation, where the material's response to the applied stress reaches a balance between hardening mechanisms and recovery processes, enabling continuous plastic deformation. The related strain rate can then be described by the Bailey-Orowan equation:

$$\dot{\varepsilon}_s = \frac{r}{h} \tag{2.23}$$

where r and h represent the recovery and strain hardening rates, respectively.

One of these creep models is "dislocation creep" which is characterized by the movement and multiplication of dislocations as the primary mechanism of plastic deformation. A key recovery process in dislocation creep is dislocation climb, which is essential for relieving stress concentrations and enabling dislocations to move out of their glide planes. It is requiring the absorption or emission of vacancies for a dislocation to move perpendicular to its slip plane (Figure 19). A model proposed by Weertman (1955) describe this behavior via the creation of dipoles resulting from the elastic interactions of blocked edge segments. These can then annihilate via climb, which then leads to further dislocation movement, creating a steady-state behavior. A general flow law can describe this behavior (Weertman 1955):

$$\dot{\varepsilon} = \dot{\varepsilon}_0 \sigma^n \exp\left(-\frac{\Delta H}{k_B T}\right) \tag{2.24}$$

In this equation, $\dot{\varepsilon}_0$ represents a mechanism-dependent constant, n denotes the stress exponent, and ΔH indicates the activation enthalpy. The velocity related to climb is covered by the diffusion behavior. An expression for the climb velocity can be given as (Caillard and Martin 2003):

$$v_c = \kappa \frac{D^{sd}}{b}\left[\exp\left(\frac{\tau^c \Omega}{k_B T}\right) - \frac{c_\infty}{c_0}\right] \tag{2.25}$$

Here κ is a geometric factor depending on the geometry of the flux field, D^{sd} is the self-diffusion coefficient and Ω is the corresponding atomic volume. Additionally, k_B stands for the Boltzmann constant, τ^c denotes the effective stress resolved in the climb direction, c_∞ signifies the vacancy concentration far from the dislocation lines, and c_0 represents the intrinsic vacancy concentration.

Furthermore, climb recovery is associated with the formation of subgrain boundaries, which i.e. is evidence for climb in minerals. The analysis of both, laboratory deformation mi-

crostructures (e.g. quartz, Cordier et al. 1989; Tullis and Yund 1989) and natural samples (e.g. quartz White 1977; olivine, Green 1976;-Kirby and Wegner 1978) has highlighted the activation of dislocation climb, marked by well-organized subgrain boundaries. Here the analysis via TEM plays an important role. An example of such subgrain formation can be seen in a study of olivine in Section 4.2. On a mesoscopic scale, recovery often results in patterning, characterized by cells with fewer dislocations separated by dislocation walls. This patterning encompasses the annihilation of dislocation pairs and the formation of subgrain boundaries. Both, laboratory experiments and dislocation dynamics (DD) modeling have played a pivotal role in validating the significance of climb in recovery mechanisms. Coupling DD simulations with vacancy diffusion has effectively reproduced the characteristics of Weertman creep, underscoring the necessity of climb for achieving steady-state deformation (Keralavarma et al. 2012, Boioli et al. 2015b). More details are given in Chapter 7, where we describe such a study to simulate the deformation of periclase at lower mantle conditions. These simplified models already reproduce the necessity of climb to reproduce a steady-state deformation. Recent advanced 3D DD models, like the ones Kohnert and Capolungo (2022) can give even further insights.

2.3.4.2 Climb as Strain producing Mechanism

In the recovery-controlled creep model, climb is generally not expected to make a significant contribution to the total strain. However, it's important to note that climb can also serve as a mechanism for producing strain in certain scenarios.

2.3.4.2.1 Pure Climb In scenarios where glide is prohibited, an alternative mechanism known as pure climb, proposed by Nabarro in his paper on steady-state diffusional creep Nabarro 1967, comes into play. This mechanism operates independently of grain boundaries and focuses on the role of dislocations as primary sources and sinks for vacancies.
The dislocation density increases through the operation of Bardeen-Herring sources and decreases as dislocations of opposite signs annihilate through climb motion. The strain rate resulting from this process can be described by the following flow law (Nabarro 1967):

$$\dot{\epsilon} = \frac{D^{sd}\mu b}{\pi k_B T}\left(\frac{\sigma}{\mu}\right)^3 / \ln\left(\frac{4\mu}{\pi\sigma}\right) \tag{2.26}$$

Here, D^{sd} represents the self-diffusion coefficient, μ stands for the shear modulus, b is the Burgers vector, σ represents the applied stress, k_B is the Boltzmann constant, and T denotes the temperature in Kelvin.

An experimental example illustrating the pure climb mechanism can be found in the work of Edelin and Poirier (1973), conducted on single crystals of magnesium at temperatures close to the melting point.
For the lower mantle modelling by Boioli et al. (2017) and Reali et al. (2019a) showed that pure climb creep is a very likely mechanism for the deformation of bridgmanite. This topic is further elaborated in Chapter 7, where we explore the rheology of the lower mantle in greater detail.

2.3.4.2.2 Mixed Climb Another relatively recently discovered strain-producing mechanism is known as mixed climb, which occurs when climb and glide velocities are of similar orders of magnitude. While many research groups have proposed a significant contribution of climb to the total strains, or at least considered it as a viable option, quantifying its exact impact remains challenging.

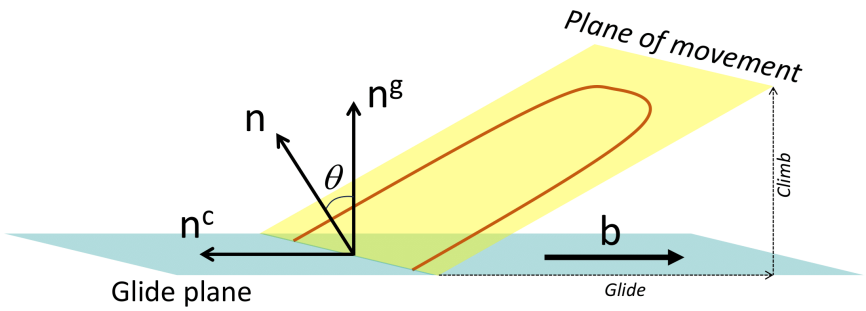

Figure 20: Geometry of a dislocation in mixed climb configuration, i.e., where the plane of movement (identified by its normal n) is intermediate between the glide plane and the climb plane. n_g is the normal of the dislocation glide plane, n_c is the normal of the dislocation climb plane. b is the Burgers vector.

In a recent TEM in-situ deformation study on TiAl at a temperature of $790°C$, Galy et al. (2023) revealed a similar velocities for both mechanisms. It is assumed that dislocations moving simultaneously by glide and climb follow undefined planes whose orientation lies intermediate between the glide plane and the pure climb plane (as depicted in Figure 20). This concept was initially proposed by Malaplate et al. (2004) and later supported by studies conducted by Couret (2010) and Voisin et al. (2016) on TiAl alloys. Mussi et al. (2021b) observed mixed climb in MgO within a helical dislocation under electron irradiation. In such cases, the glide velocity was reduced due to high lattice friction.
To precisely quantify this mechanism, advanced techniques are required to characterize the corresponding planes accurately. Dislocation electron tomography emerges as an ideal method

for studying mixed climb, as demonstrated in the examination of naturally deformed olivine and quartz in Chapter 4.

3 Methodology

In this chapter, I will provide a detailed description of the Dislocation Electron Tomography (DET) method and its implementation into the framework of static Field Dislocation Mechanics (FDM) and Discrete Dislocation Dynamics (DDD) modeling.

3.1 Dislocation Electron Tomography

This section will delve into the methodology of Dislocation Electron Tomography (DET) and will explain how we can extract all the dislocation characteristics needed for our simulations. The procedure outlined here is based on the work of (Mussi et al. 2017, 2014).

3.1.1 TEM Analysis

3.1.1.1 Sample holder

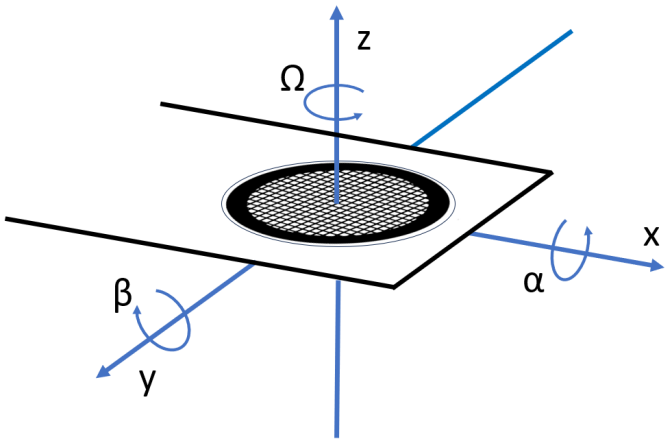

Figure 21: Sketch of a TEM sample holder indicating the three rotation axes.

To perform a tomography, we must choose a suitable sample holder. The sample stage is characterized by up to three angles (see Figure 21). The primary tilt angle, denoted as α, involves tilting along the principal axis of the sample holder. The second angle, Ω, corresponds to a rotation along the z-axis, aligned with the electron beam direction, and β defines

the remaining tilt axis perpendicular to the other two axes. Now we consider two optional sample holders. A triple-axes tomography holder, also called HATA sample holder (Hata et al. 2011), enables tilting around all three axes. It is offering a high angular range for primary tilt ($\pm 80°$), which is particularly advantageous when dealing with thin specimens and with a high dislocation density, since at high angles the electron signal gets weaker. It makes also precise orientation in Ω easier, since it is part of the system. The only downside is the low angular range for β ($\pm 7.5°$), which makes it harder to find a good orientation, especially in a single crystal specimens, where the orientation is fixed and therefore the orientation to perform tomography can be out of the limit. In this case a classical double tilt holder can be useful it has a high range in β ($\pm 30°$), but a smaller range for α ($\pm 60°$). It also has the downside, that it requires manual specimen rotation to adjust Ω.

3.1.1.2 Tilt Series Acquisition

Our objective is to identify a region within the specimen that satisfies specific criteria. We seek an area with an intermediate dislocation density, falling between $5.10^{12}\, m^{-2}$ and $5.10^{14}\, m^{-2}$. Additionally, we aim for an optimal thickness that strikes a delicate balance—thin enough to ensure electron transparency even at high angles and thick enough to reveal a more pronounced 3D dislocation microstructure.

An adequate diffraction vector **g** for our tomography has to be selected. It is essential that this vector possesses a high structure factor, to have a strong dislocation signal even at a high tilt angle. Then we carefully orientate the principal axis of the sample holder along the diffraction vector, a meticulous task requiring multiple extractions and insertions of the sample holder. This precision is crucial to maintaining consistent dislocation contrast throughout the entire tilt-series acquisition.

The next step involves acquiring a tilt-series under optimal WBDF conditions, capturing images every $2°$ within an angular range between $\pm 35°$ (totaling $70°$) and $\pm 80°$ (totaling $160°$). We meticulously maintain a constant s parameter, avoiding any sign changes at all costs (a change in sign would mirror the contrast of the dislocations to the opposite of the dislocation line, making an accurate 3D reconstruction impossible).

Due to the limited angular range, there exists a region where no image can be obtained, known as the "missing wedge." In this region, the reconstruction algorithm must extrapolate the dislocation positions.

While acquiring the tilt- series along a diffraction vector, we move through several zone axes. To later link the orientation of the tilt series to the specimen crystallographic orientation we acquire diffraction patterns corresponding to those zone axis (see Figure 22). The diffraction patterns are identified using the Electron-Diffraction software (Morniroli et al. 1994).

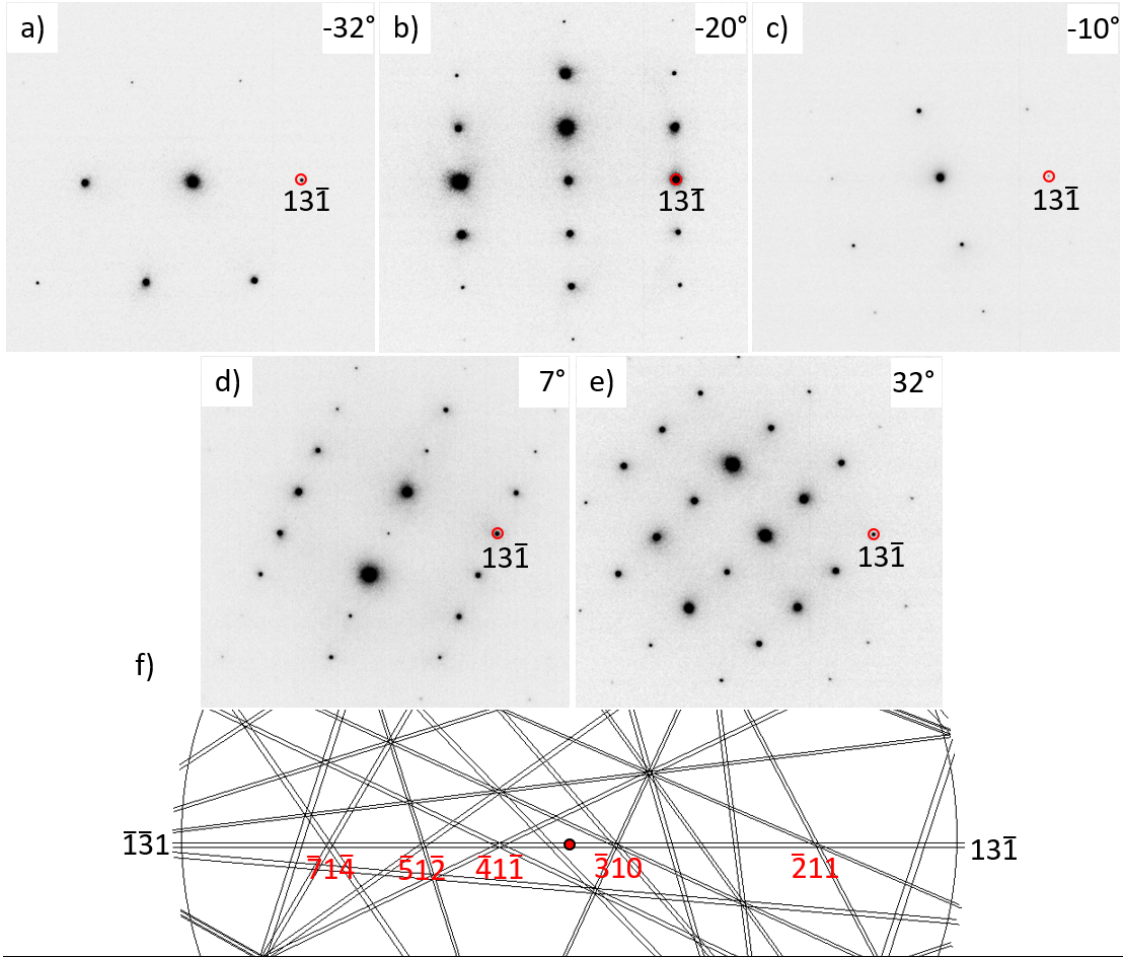

Figure 22: (a) - (e) Zone axis patterns along a tilt series taken with the $13\bar{1}$ diffraction vector. (f) Kikuchi map at 0° indication the different zone axes (red) from left (minus) to the right (plus).

3.1.1.3 Precession

To enhance the quality of our analysis, we implement a gentle electron beam precession (Vincent and Midgley 1994), typically set below 0.3°. This controlled precession mitigates multiple diffraction effects by oscillating the beam around the optical axis, resulting in a reduction of phase-related contrasts such as thickness fringes and dislocation oscillating contrasts. A high precession also allows for a broader illumination range, enabling the visibility of dislocations in areas with slightly different orientations. But, if the precession angle is too high, the signal will be masked by the objective aperture. Thus, the chosen precession angle

strikes a balance: it is sufficiently high to significantly diminish shadowing phase contrast and low enough to prevent masking by the objective aperture. Our approach is rooted in the methodology outlined by Rebled et al. (2011), where beam precession-assisted bright-field electron tomography was employed to reconstruct a precipitate in 3D. We utilize the "*Spinning Star*" precession module from the Nanomegas Company.

3.1.1.4 Postprocessing

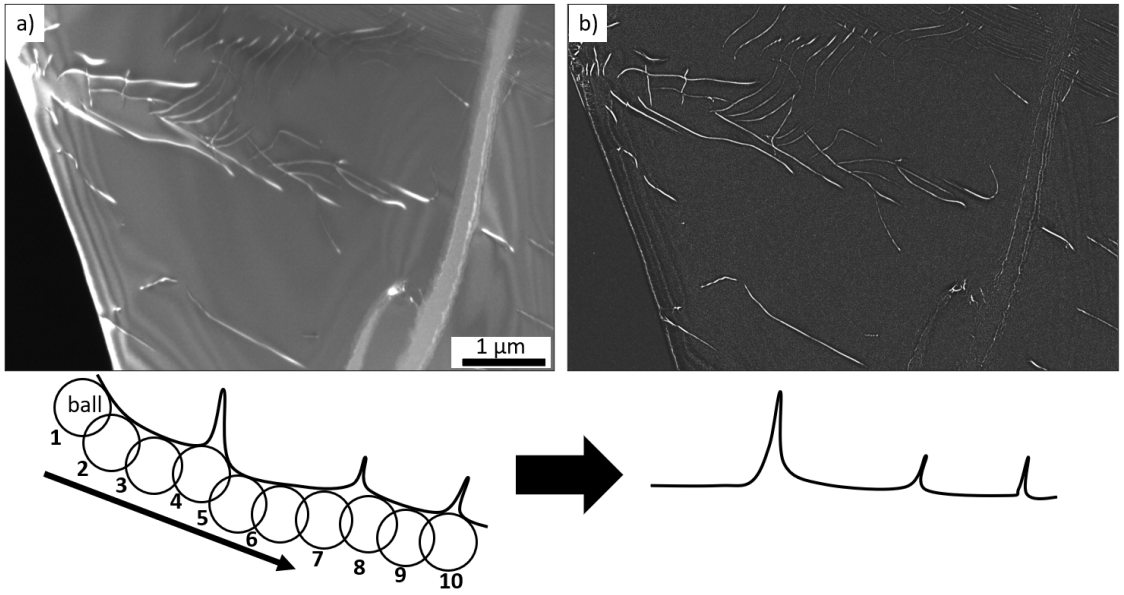

Figure 23: Removal of the background intensity by application of the "rolling ball" algorithm (accessible in the ImageJ software), applied to a WBDF mircograph. The sketch shows the change of an intensity profile before and after applying the algorithm.

3.1.1.4.1 Contrast refinement To further enhance dislocation contrast, we employ filtering techniques like Median filtering and background removal, including a "rolling-ball" algorithm of the ImageJ software package (Figure 23). In complex cases, manual redrawing of dislocation contrast may be necessary.

3.1.1.4.2 Tilt axis alignment To implement a tomography algorithm, precise alignment of the tilt-series to pixel accuracy is imperative. To eliminate translational shifts within the tilt series, we superimpose the contrast of each image and perform alignment using stable features that remain fixed, such as small loops or other stationary details (refer to Figure 24). To correctly reconstruct the volume, we need to know the angle between the tilt axis of the tilt series and the micrograph. This is achieved by examining an image stack of the tilt series sequentially, allowing for the observation of its rotation. Subsequently, we measure

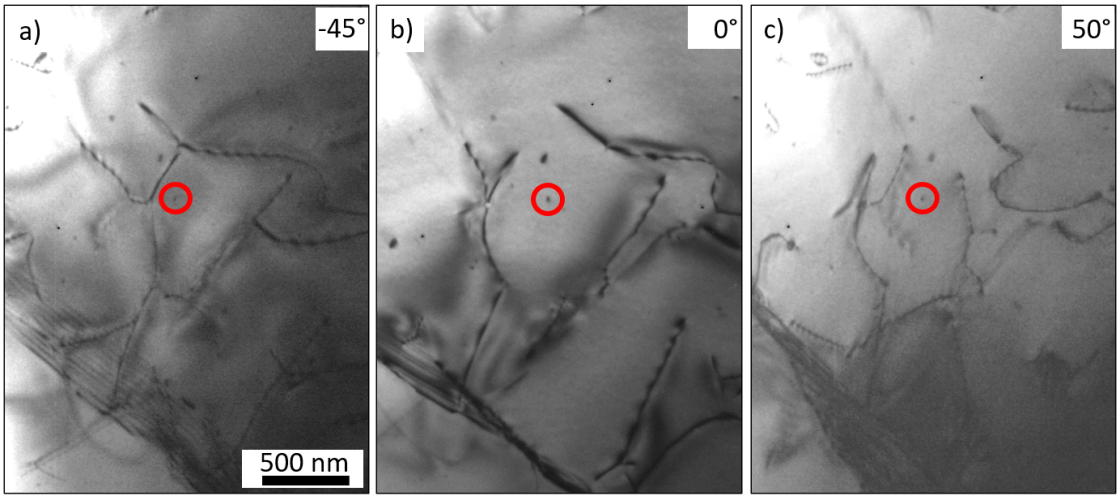

Figure 24: Three WBBF micrographs of a tilt series. Red circle indicates the alignment detail visible in all micrographs.

the angular shift by tracking the consistent horizontal shift of image details, as illustrated in Figure 25.

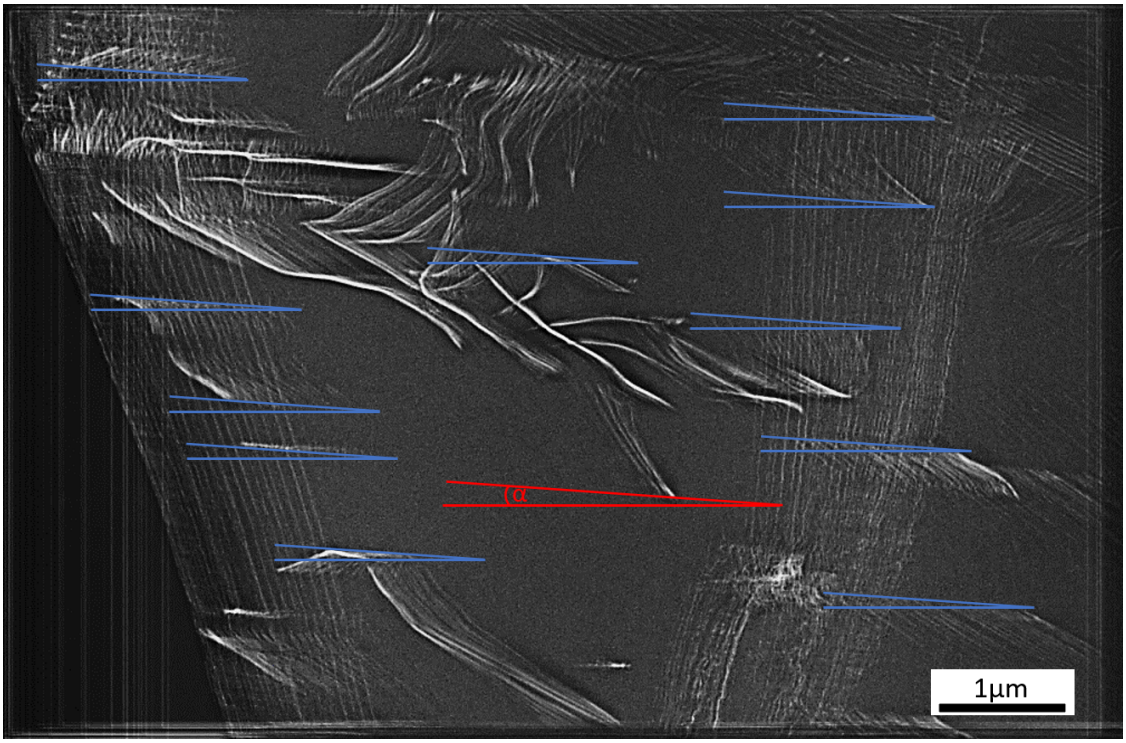

Figure 25: Superposition of all micrographs of a tilt series in WBDF condition. Highlighting in blue the angle between the perpendicular with the tilt axis and the horizontal line of the micrograph.

3.1.2 Reconstruction

3.1.2.1 Weighted Back Projection Algorithm (WBP)

For our reconstruction, we employ the Weighted Back Projection (WBP) algorithm (Herman et al. 1976), which is conveniently available within ImageJ through the TomoJ plugin (Messaoudil et al. 2007).
There are different types of tomography algorithms, iterative or non-iterative. Iterative methods, such as the Algebraic Reconstruction Technique (ART) and the Simultaneous Iterative Reconstruction Technique (SIRT), progressively refine images through iterations by leveraging both measured and predicted data. ART models data acquisition in tomography as a set of linear equations and is well-suited for sparse data, while SIRT simultaneously updates all pixel values, making it particularly effective for noisy data, commonly used in applications like computed tomography scan and positron emission tomography. The Discrete Algebraic Reconstruction Technique (DART) is tailored for objects with a few distinct compositions, each associated with a constant grey value in the reconstruction, it is a segmented contrast. It uses prior knowledge of gray values to enhance accuracy, especially in scenarios with limited data, noisy projections, and errors in gray value estimation. The Compressed Sensing technique (a signal processing method) aims to accurately reconstruct sparse or compressible signals from a reduced set of measurements. It offers advantages in terms of data acquisition efficiency, reduced sampling requirements, and enhanced robustness against noise and artifacts.
In comparison, the WBP algorithm (Herman et al. 1976) stands as a non-iterative approach. The choice of this algorithm depends on the specific needs of the application. We have used the WBP algorithm because it is a relatively simple, straightforward, and intuitive technique, making it ideal for initial image reconstruction without the need for complex mathematical modeling. WBP is computationally efficient, well-suited for real-time applications or situations requiring rapid results. It excels when object characteristics can be represented as sharp edges or lines and in scenarios characterized by black-and-white contrast. It is therefore ideally suited to reconstruct dislocations. A comparison of the algorithm to an iterative and a simple back-projection approach, reconstructing a simple object can be seen in Figure 26.
The WBP algorithm operates as follows. At first it collects 1D projections (sinograms) of the object from various angles, obtained through the Radon transform (Radon 1917). This transform capturing information about how an object, or a signal, varies along a specific direction, by integration of the signal along this direction.

The next step involves back projection onto an empty 2D grid dedicated to reconstructing the final 3D image. Each projection is back-projected onto this grid, marking potential radiation

origins based on angles (in our case the radiation is related to the transmitted electron beam). To enhance accuracy, the algorithm assigns weights to each data point within the projection, considering its distance from the grid points it contributes to. These weights are typically determined by the imaging system's geometry. Finally, the algorithm accumulates all the back-projected projections, progressively constructing the final 3D image.

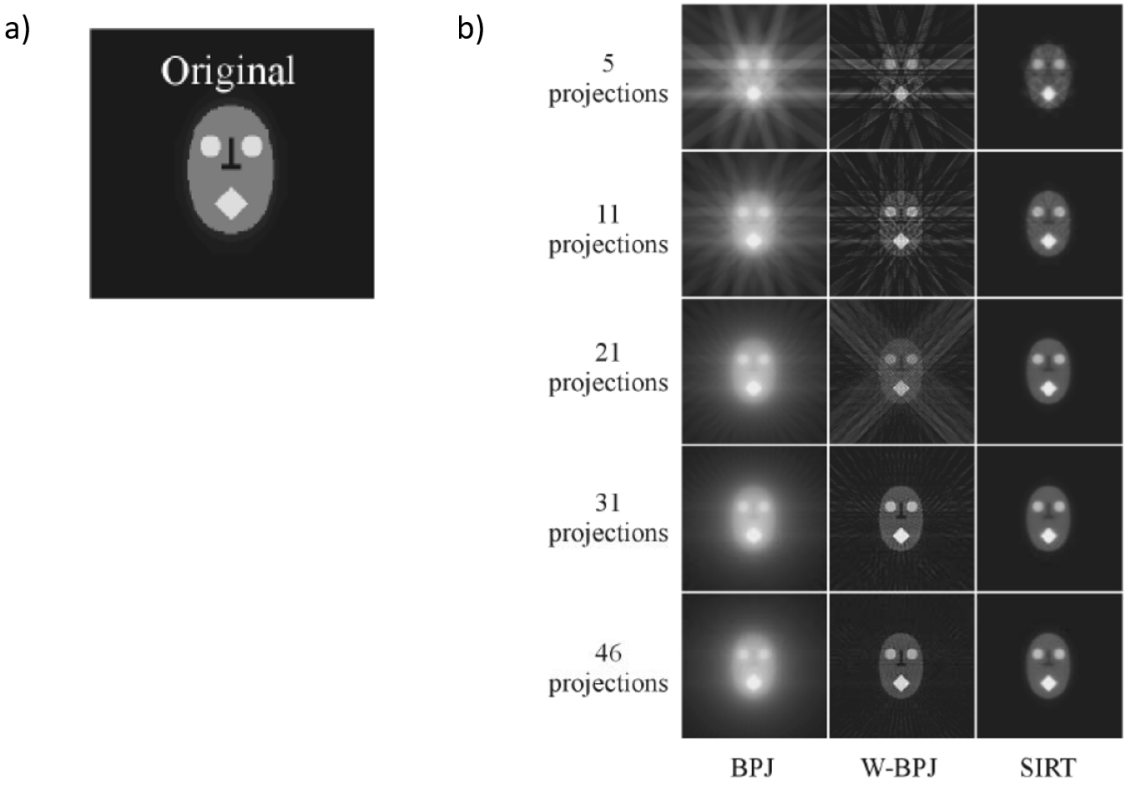

Figure 26: Comparison of tomography algorithms using a different number of projections, with (a) the original image and (b) showing the different reconstruction. Images taken from (Midgley and Weyland 2011)

3.1.2.2 Reconstructed Dislocation Improvement

As the reconstruction algorithm extrapolates dislocation positions in missing-wedges of the tilt-series, the resulting thickness of the reconstructed dislocations becomes greater in these angular regions. Consequently, the initial reconstructed dislocations manifest as ribbons (Figure 27 (a)), yet the distribution of intensity within these ribbons enables precise localization of the line position. Utilizing the UCSF Chimera software (Pettersen et al. 2004), it becomes possible to identify the highest gray value among the voxels where the dislocation core image is still discernible (refer to Figure 27) and subsequently redraw each dislocation within the raw reconstructed volumes . This process effectively restores the cylindrical geometries of the dislocations.

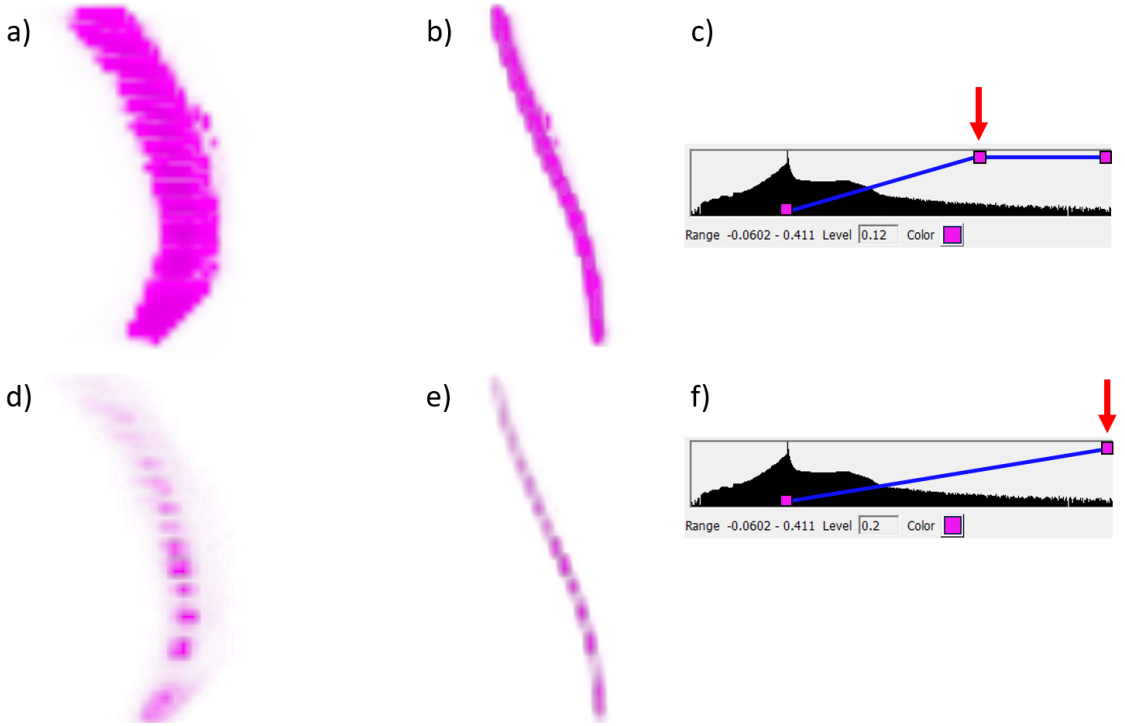

Figure 27: Contrast tracing of a dislocation using the Chimera software to improve the accuracy at the missing wedge. (a)-(c) Raw reconstructed volume at $90°$ and at $0°$ with a low grey level value indicated with the red arrow in (c). (d)-(f) Same reconstructed volume with the maximum grey level showing a reduced thickness of the ribbon.

To ensure the accuracy of the reconstruction, an iterative refinement of the reconstruction quality is followed by superimposing the reconstructed volume on top of the original tilt series. If a visible deviation, larger than the thickness of the dislocation, is observed, the reconstruction needs improvement. This refinement is particularly critical for high angles, where the quality of the tomography is compromised due to the extrapolation of the volume in the missing wedge. The final reconstruction is segmented, as markers are placed at fixed nodes, allowing the extraction of 3D coordinates of the dislocation microstructure, utilizing notes saved in 'pdb' data types.

3.1.2.3 Characterization of habit planes

To characterize the habit planes of the dislocations, we search the projection angles where each projection of dislocation segment becomes rectilinear while minimizing the number of planes required. This is accomplished by subtly rotating the reconstructed volume along α until the habit plane of the dislocation of interest is in an edge-on orientation, allowing for the indexation of the corresponding plane. One fundamental criterion is that the orientation of the trace of the habit plane must correspond to the orientation of the dislocation. This alignment

is crucial in ensuring that the projection of the dislocation is linear for the given projection angle α. In cases where dislocations exhibit a three-dimensional (3D) geometry, composed

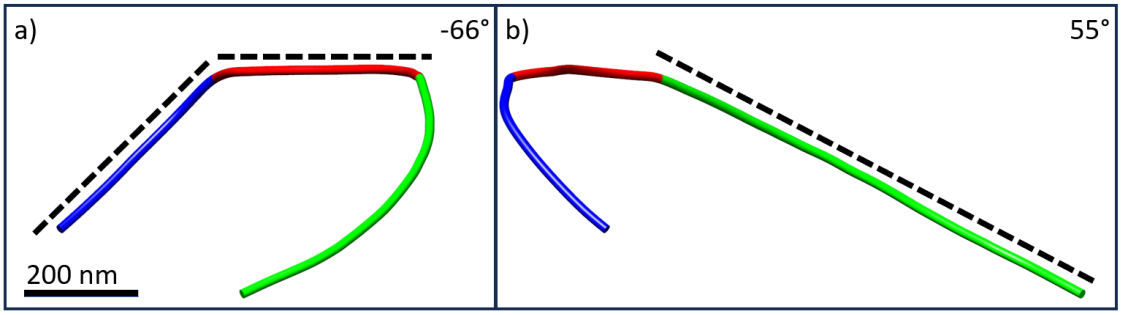

Figure 28: Reconstructed 3D dislocation in Chimera at two different projection angles, showing the different glide planes edge on. (a) Shows the blue and red dislocation segment where the habit plane is adjoined at $-66°$. (b) At $55°$ the green segment aligns with another habit plane.

of multiple dislocation segments, a specialized approach is employed. While consistent with the general method described above, it takes into account the plane where the dislocation segment is longest. This strategy ensures that the habit plane selected best represents the overall structure of the complex dislocation, ultimately aiming for accurate characterization (illustrated for an example dislocation in Figure 28).

In the case of quartz, an additional method was employed to identify the length and orientation of straight-line dislocations, which were initially excluded from the analysis due to a change in research focus. This approach, is similar to a stereo pair method and is detailed in the Appendix A.1.

3.1.3 Dislocation electron tomography for a beam sensitive material

When working with a beam-sensitive material like quartz, we consider procedure adjustments to preserve the specimen. These adjustments are described from a previous study by Mussi et al. (2021c).

First of all, we are using a small condenser aperture and a small spot size for TEM analyses to minimize the electron dose. In addition, we enhance the signal-to-noise ratio in WBDF micrographs, by binning the pixels four by four. Furthermore, we limit the number of projected images by increasing the angular gap between each image (in one case using intervals of $10°$ instead of the standard $2°$) to reduce electron exposure. To compensate for the fewer images, the dislocation contrast was redrawn manually for each image to enhance the black and white contrast, which is known to produce higher-quality volumes compared to continuous grey-level reconstructions. For the remaining analysis we follow the initial procedure.

3.1.4 Burgers vector indexation - Ishida method

To comprehensively characterize dislocations, obtaining information about the Burgers vector becomes crucial. The classical method for determining the Burgers vector involves the use of invisibility criteria, expressed as:

$$\mathbf{g} \cdot \mathbf{b} = 0 \tag{3.1}$$

A zero dot product implies that the dislocation does not contribute to the diffraction intensity along a specific diffraction vector, resulting in a vanishing dislocation contrast. However, this technique requires at least three independent extinction conditions per Burgers vector. These criteria necessitate a robust two-beam condition and encounter challenges at the Bragg condition. Other problems emerge, particularly with residual contrast, in example when we characterize substantial edge components (small bending contours occur due to distortion of lattice planes). The impact of anisotropy further introduces complexities to the effectiveness of the invisibility criteria.

Addressing these challenges, an alternative and more robust approach uses the Large Angle Convergent Beam Electron Diffraction (LACBED) technique. This technique converges the electron beam into a small probe below the specimen, creating a superposition of image contrast and diffraction contrast, associated with a difference in z. In LACBED, dislocation lines intersecting Bragg lines display characteristic distortions and splitting. The Bragg line undergoes simultaneous rotation and separation into a system of fringes at the intersection with the dislocation line. The exact relationship resulting from this technique can be expressed by the Cherns and Preston rule (Cherns and Preston 1986):

$$\mathbf{g} \cdot \mathbf{b} = n \tag{3.2}$$

Here, n represents the number of subsidiary minima between the Bragg lines. Notably, this technique allows for the determination of the Burgers vector (including its sign and magnitude) without any a priori assumptions. An advantage of LACBED is, its suitability for beam-sensitive materials, thanks to the defocused beam. However, for excessively thick crystals, multiple scattering events become more pronounced, posing challenges in interpretation. Therefore, we employ an alternative method based on the termination of thickness fringes, a concept initially demonstrated by Ishida for x-ray analysis and subsequently extended to bcc and fcc structures at high voltage with additional specimen considerations (Ishida et al. 1976; Ishida et al. 1980). The relationship is the same as for the LACBED method:

$$\mathbf{g} \cdot \mathbf{b} = n$$

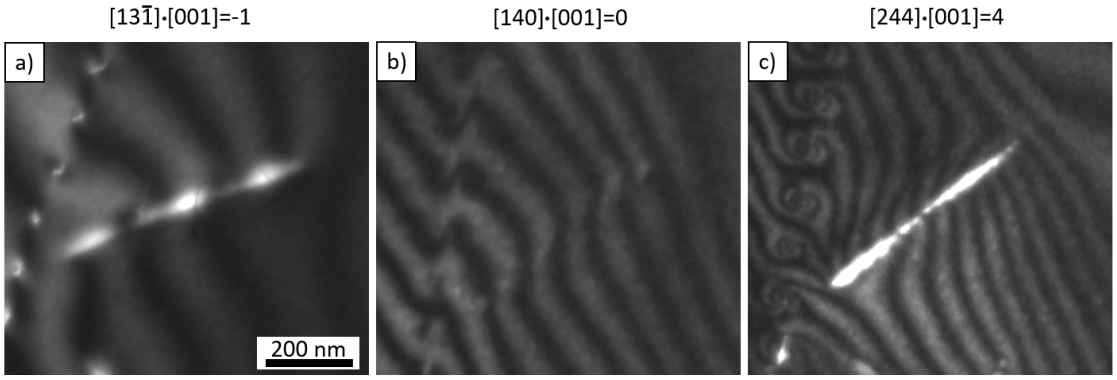

Figure 29: WBDF micrographs of a [001] dislocation taken with different diffraction vectors showing the terminating thickness fringes, to identify the dislocation with the Ishida method. (a) 1 thickness fringe terminates from the bottom at the the left end of the dislocation and 1 from top on the right end, resulting in $n = -1$. (b) 0 terminating thickness fringes, resulting in $n = 0$. Dislocation is out of contrast, but bending of the fringes is still visible. (c) 4 thickness fringes terminate each from top left and bottom right, resulting in $n = 4$.

But this time n signifies the count of terminating thickness fringes at the extremity of a dislocation (an example characterization is depicted in Figure 29). Importantly, this method requires any set of three independent conditions; zero is not a necessity. It necessitates the use of Weak Beam Dark Field (WBDF) without precession to achieve a small spacing of thickness fringes associated to a high s value.

This technique allows for the exact determination of both the magnitude and the sense of the Burgers vector. The sign is attributed to the termination direction of the fringes regarding the direction of the edge. The sign is positive, if top fringes, with respect to the edge, terminate on the right side and bottom fringes on the left side (Miyajima and Walte 2009).

An alternative approach to get the sign is linked to the asymmetry of the contrast intensity at dislocation extremities. This data can be cross-referenced with that acquired from the orientations of terminating thickness fringes (see Figure 30). By considering all these indicators collectively, we can successfully identify the signs of the majority of Burgers vectors.

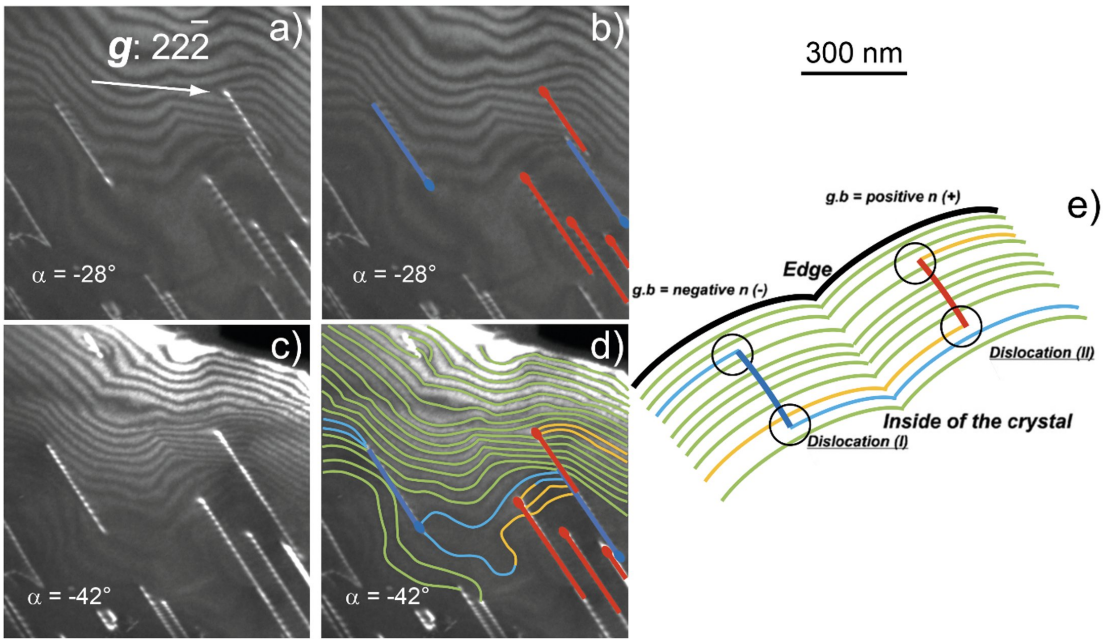

Figure 30: Association of the intensity of the dislocation extremities with the sign of the Burgers vector: (a) Raw micrograph in WBDF conditions, obtained with the $22\bar{2}$ diffraction vector (with a projection angle of $-28°$), where an intensity asymmetry of dislocation extremities is clearly seen; (b) arrows added on the raw micrograph of figure 30 (a), the arrow is oriented in the direction of the intense extremity of the dislocation; (c) raw micrograph of the same domain with a projection angle of $-42°$; (d) arrows and thickness fringes added and redrawn on the raw micrograph of figure 30 (c), where the thickness fringes are coloured in green when they are not terminated on the extremities of dislocations, in red at the extremities of the dislocations represented with arrows oriented on the opposite direction of the edge, and in blue at the extremities of the dislocation represented with an arrow oriented on the direction of the edge; (e) cartoon extracted from Miyajima and Walte (2009), where the method to get access to the $\boldsymbol{g} \cdot \boldsymbol{b}$ product is described, taking into account the signs of the Burgers vectors, following Ishida et al. (1980), with the same colour code and arrow direction code as figure 30 (d). A link between the intensity of the dislocation extremities and the sign of the Burgers vector is noticeably evident. Reprinted from Miyajima and Walte (2009), Copyright (2009), with permission from Elsevier.

3.2 Field Dislocation Mechanics

The general idea here is to get the equilibrated stress field in our thin foil volume, as well as the associated elastic displacements, strains, and rotations, based on the Nye tensor field resulting from our dislocation network. It is based on a linear approximation of the Field Dislocation Mechanics (FDM) model seen in Acharya (2001) and follows the work of Djaka et al. (2017). For nonlinear solution see also Acharya (2001). This adaptation and the general implementation are done in collaboration with V. Taupin (LEM3 Metz).

An application of the FDM model can be found in Ernould et al. (2022), where the stress field near a nanopipe dislocation in GaN is characterized with HR-EBSD and then compared to a modelling in elastic fields achieved using FDM. In this study we will apply FDM to a network of dislocation, with data from DET. In the following we describe the fundamental relationships regarding this work.

Let us consider an infinite isotropic body which is strained. This strain, is characterized by an elastic distortion $\boldsymbol{U_e}$ of the body. The elastic distortion can then be expressed as gradient of an elastic displacement vector $\boldsymbol{u_e}$, which relates each unstrained point, with its strained counterpart. We now look at a cut of the body along an arbitrary surface S. If we now take a closed integral over any possible path on that surface the integral will be equal to zero:

$$\oint_C \mathbf{U}_e \, dr = 0 \tag{3.3}$$

Due to the presence of dislocations we have discontinuities in the elastic displacement field. Consequently, Equation 3.3 is no longer applicable.
To overcome this issue, we use an approach similar as in electrostatic (see Sokolnikoff 1966, p. 408). We split the elastic distortion field $\boldsymbol{U_e}$ into a compatible part, which is our previous gradient of the elastic displacement field and into an incompatible part, due to the dislocation represented by a curl of a unique periodic tensor field χ:

$$\mathbf{U}_e = \mathbf{U}_e^{\parallel} + \mathbf{U}_e^{\perp} = \nabla \, \mathbf{u}_e + \nabla \times \chi \tag{3.4}$$

The former integral becomes now:

$$\oint_C \mathbf{U}_e dr = \mathbf{b}$$

Which is the Burger's vector $\mathbf{b}$, as defined in Eq. 2.1. Now we again use Stokes theorem to transform this integral to:

$$\mathbf{b} = \iint_S \nabla \times \mathbf{U}_e^{\perp} \cdot \boldsymbol{n}\, dS = \iint_S \boldsymbol{\alpha} \cdot \boldsymbol{n} dS$$

$\nabla \times \mathbf{U}_e^{\parallel}$ vanishes since $\nabla \times \nabla f = 0$. Which results in the incompatibility equation Kröner 1959:

$$\nabla \times \mathbf{U}_e = \boldsymbol{\alpha} \tag{3.5}$$

Here $\boldsymbol{\alpha}$ is the Nye tensor as we defined in Section 2.1.2. This time we look at continuous fields with a dislocation network, instead of a solution for straight single dislocation. We therefore have to go a bit deeper to get to a general solution. Starting by applying the identity $\nabla \times \nabla \times \mathbf{U}_e^{\perp} = \nabla\nabla \cdot \mathbf{U}_e^{\perp} - \nabla \cdot \nabla \mathbf{U}_e^{\perp}$, which leads to a Poisson type equation, since $\nabla\nabla \cdot \mathbf{U}_e^{\perp} = \nabla\nabla \cdot \nabla \times \chi = 0$:

$$\Delta\, \mathbf{U}_e^{\perp} = -\nabla \times \alpha \tag{3.6}$$

Which is again similar to electrostatics, where we have an electrostatic potential due to electric point charges, we now get a distortion potential due to the discontinuities at the dislocations. This is then solved for a given Nye tensor based on distribution of dislocation density in the volume by a fast Fourier transform (FFT) algorithms for more details see Djaka et al. 2017.

In the next step we look at the remaining compatible part that balance out the incompatibilities. If we account that for any periodic stress field, there is an equilibrium given as:

$$\nabla \cdot \boldsymbol{\sigma} = 0 \tag{3.7}$$

And in addition we consider Hooke's law:

$$\boldsymbol{\sigma} = \boldsymbol{C} : \boldsymbol{U}_e \tag{3.8}$$

Where **C** is the elastic stiffness tensor, this leads us to:

$$\nabla \cdot (\boldsymbol{C} : \boldsymbol{U}_e) = \nabla \cdot \left(\boldsymbol{C} : \boldsymbol{U}_e^{\parallel}\right) + \nabla \cdot \left(\boldsymbol{C} : \boldsymbol{U}_e^{\perp}\right) = 0 \tag{3.9}$$

Using the form of equation 3.4, this gives the expression:

$$\nabla \cdot (\boldsymbol{C} : \nabla \boldsymbol{u}_e) + \nabla \cdot \left(\boldsymbol{C} : \boldsymbol{U}_e^{\perp}\right) = 0 \tag{3.10}$$

From which we obtain the elastic displacement field $\boldsymbol{u}_e$. It can be again solved using a FFT solver (see Djaka et al. 2017). Once the elastic displacement is known, we calculate the compatible elastic distortion by taking the gradient of the displacement field. The total elastic distortion is then determined by combining it with the incompatible part. From this we finally achieve the balanced anisotropic stress field $\boldsymbol{\sigma}$ by multiplying it with the elastic stiffness tensor $\boldsymbol{C}$.

3.2.1 Associate with Tomography - Transform tomography data

To transform our tomography data from Chimera to an input file that can be used for the simulation, we developed a semi-automatic program written in C++.

In Chimera the dislocations are stored as interconnected nodes in a "pdb" format (see 3.1.2.2). Each node is assigned with a dislocation position in the reconstructed volume. In addition, the connectivity of the node to the connected nodes is stored. In the “pdb”-file the individual nodes are ordered according to the placement order used during the reconstruction, which is not linked with the line directions of the individual dislocations. In addition, we write a separate file ("input.dat"), which contains the Burgers vector and the number of nodes for each dislocation.

For the Nye'zation these nodes have to be divided into individual dislocations and then reordered according to their line directions. This reordering and splitting of nodes in individual dislocations is done using our program. Additionally, the code includes adjustments for scale variations observed between TEM analysis, Chimera software, and simulations, achieved through a scale factor. It also incorporates an option to accommodate orientation changes between the Chimera reference frame and the sample reference frame. The program combined the "pdb"-file of each dislocation with their Burgers vector file, and save the result (processed nodal list) in a final file.

To align the crystallographic orientation of our sample with the simulation box's reference frame, we compute Bunge Euler angles using the MTEX software package integrated into MATLAB (Bachmann et al. 2010).

To correlate the applied stress direction with the crystalline structure of our sample, we compute the associated metric tensor.

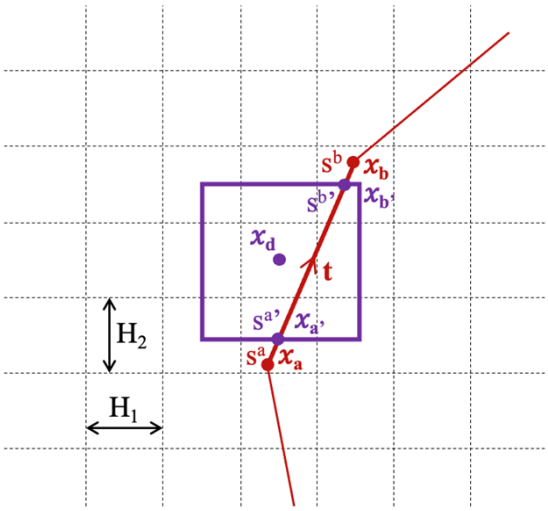

Figure 31: A 2D illustration of the method employed for assigning a Nye dislocation density to a voxel denoted as $\mathbf{x_d}$ based on a dislocation segment. Refer to the accompanying text for a comprehensive explanation.

3.2.2 Nye'zation

In the final step we setup our Nye tensor field in a continuous form using the approach of Bertin (2019).

To use the discrete dislocation line segments for the creation of a continuous field, it is crucial to smooth them across multiple voxels within our FFT grid. This process of assigning a Nye dislocation density to each voxel, we refer to as "Nye'zation" and the following description of it draws upon our paper published in Modelling and Simulation in Materials Science and Engineering[1]. In Figure 31, we illustrate a portion of a discrete dislocation line comprised of three straight segments, highlighted in red. Although the figure presents a two-dimensional representation for clarity, the calculations are conducted in three dimensions. Let's focus on the second (middle) dislocation segment, represented as a bold red line. This segment is defined by its starting point, $\mathbf{x}_a$, and its ending point, $\mathbf{x}_b$, following the direction of the segment's line vector, $\mathbf{t}$.

The thin dashed black lines mark off the grid voxels employed in the numerical algorithm utilized to solve the FDM equations. These voxels have dimensions H_1, H_2, and H_3 in the x_1, x_2, and x_3 directions. The position of the center of the voxel, denoted as d in Figure 31, is described by its position vector, $\mathbf{x}_d$. The volume of this voxel is represented as $\Omega_d = H_1 \times H_2 \times H_3 = H^3$, with $H_1 = H_2 = H_3 = H$ chosen as the voxel size.

[1] Weidner, T., V. Taupin, S. Demouchy, K. Gouriet, A. Guitton, P. Cordier, and A. Mussi (Nov. 2023). "From electron tomography of dislocations to field dislocation mechanics: application to olivine". In: *Modelling and Simulation in Materials Science and Engineering* 32.1, p. 015004. DOI: *10.1088/1361-651X/ad0a42*. URL: *https : //dx.doi.org/10.1088/1361-651X/ad0a42*.

For the voxel *d*, a surrounding box with dimensions $2H_1 \times 2H_2 \times 2H_3$ is centered at the point $\mathbf{x}_d$, illustrated with purple solid lines in the figure. If any part of a given dislocation segment falls within this box, a Nye dislocation density associated with that segment is assigned to this voxel. Here's how it is done:

If the start and/or end points, $\mathbf{x}_a/\mathbf{x}_b$, lie outside the box, the dislocation segment is adjusted to new start and/or end points, $\mathbf{x}_a{}'/\mathbf{x}_b{}'$. If they are within the box, they remain unchanged. Now, consider a point $\mathbf{x}$ along the dislocation segment. We define the vector $\mathbf{R}_d = \mathbf{x}_d - \mathbf{x}$, which translates points $\mathbf{x}$ on the segment to the center of voxel $\mathbf{x}_d$. The unit vector $\mathbf{t} = \frac{\mathbf{x}_b - \mathbf{x}_a}{\|\mathbf{x}_b - \mathbf{x}_a\|}$ represents the segment's tangent vector. The distance from the segment's supporting line to the point $\mathbf{x}_d$ is denoted as *d*, which is the norm of the vector $\mathbf{d} = \mathbf{R}_d - (\mathbf{R}_d \cdot \mathbf{t})\mathbf{t} = \mathbf{x}_d - \mathbf{x}_0$. Here, $\mathbf{x}_0$ is the starting point of the vector $\mathbf{d}$ on the segment's supporting line, and it ends at $\mathbf{x}_d$. With this information, one can parameterize the position $\mathbf{x}$ along the dislocation segment as $\mathbf{x} = \mathbf{x}_0 + s\mathbf{t}$, where s is a scalar value within the interval $[s_a, s_b]$. The two bounds, s_a and s_b, shown in Figure 31 (or s'_a and s'_b if the segment is cropped) are defined as $s_a = (\mathbf{x}_a - \mathbf{x}_0) \cdot \mathbf{t}$ and $s_b = (\mathbf{x}_b - \mathbf{x}_0) \cdot \mathbf{t}$.

From these definitions, we can finally express the position vector $\mathbf{R}_d = \mathbf{x}_d - \mathbf{x}$ as $\mathbf{R}_d = \mathbf{d} - s\mathbf{t}$. The dislocation density at voxel *d*, attributed to a specific dislocation segment, can be computed through the following line integral:

$$\alpha_{ij}(\mathbf{x}_d) = \frac{b_i\, t_j}{\omega_d} \int_{\mathbf{x}_a}^{\mathbf{x}_b} S(\mathbf{x}_d - \mathbf{x})\, dL(\mathbf{x}) = \frac{b_i\, t_j}{\omega_d} I(\mathbf{x}_d) \tag{3.11}$$

where the weight function S is taken to be a Cloud-In-Cell function defined by:

$$S(\mathbf{x}_d - \mathbf{x}) = \begin{cases} \prod_{i=1}^{3} \left(1 - \frac{\|x_i^b - x_i\|}{H_i}\right) \text{if } \|x_i^b - x_i\| < H_i \\ 0 \qquad\qquad\qquad\qquad \text{otherwise} \end{cases} \tag{3.12}$$

This integral can then be numerically evaluated to give us, for each voxel d, an assigned dislocation density, that then build up the simulation volume.

To assure stress balance inside the volume, a so called gas phase is used, with a 10^4 smaller stiffness for relaxation to remove stresses outside the volume and so create zero-traction boundary conditions. Consequently, the boundary between the thin foil and the gas phase is a free surface. Which allows a convergence of the FDM-FFT algorithm. An overview of the Nye'zation step for a vertical screw dislocation can be seen in Figure 32. For the visualization of data we use Paraview (Ahrens et al. 2005).

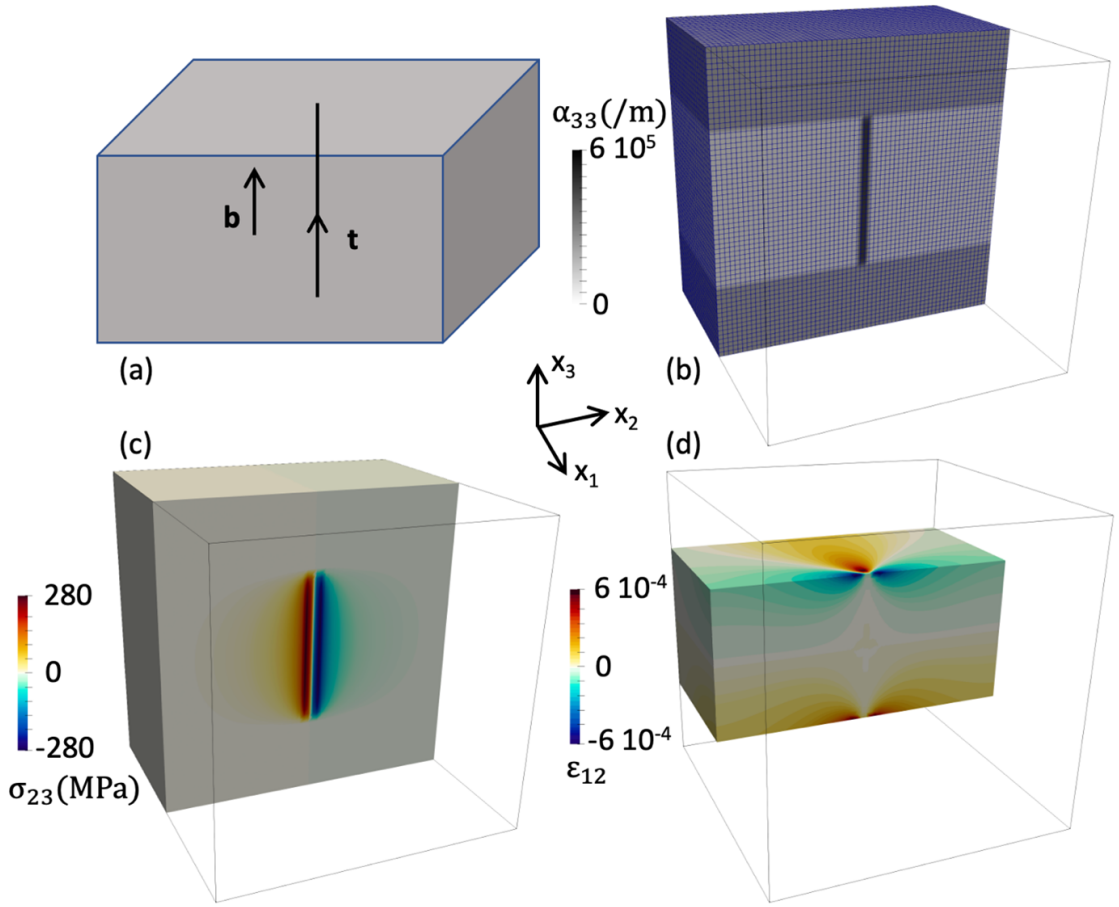

Figure 32: Numerical Approach for Modeling the Stress Field of Discrete Dislocation Lines Observed by Tomography in a Thin Foil. (a) Depiction of a thin foil with a single vertical threading screw dislocation line (represented by the black solid line, along with indications of the line and Burgers vectors). (b) Visualization of the Nye tensor screw component α_{33} on the 3D FFT grid (clipped). Bright voxels correspond to the thin foil, while dark voxels represent the gas phase. (c) Presentation of the internal shear stress field σ_{23}. (d) Illustration of the elastic strain field ε_{12}, generated in the vicinity of and on the free surfaces of the thin foil to counteract the internal stresses σ_{13} and σ_{23} at the free surfaces. The coordinate system used for figures (b), (c), and (d) is indicated at the center of the figure.

3.3 Discrete Dislocation Dynamic simulations

Discrete dislocation dynamics (DDD) is a mesoscale simulation technique used to simulate the behavior of dislocations (Bulatov and Cai 2006; Lepinoux and Kubin 1987). The general idea is to discretize the dislocations along their dislocation lines piecewise into segments. These segments are linked by nodes for which their velocities are calculated according external and internal stresses. The corresponding motion is then used to update the nodal positions at incremental time steps. So, it's not only discrete in space but also in time. This is described in more detail in Section 3.3.2.

A critical consideration in DDD is the choice between nodal and segment representations to track dislocations. In the segment representation, dislocation movement is tracked through the positions and orientations of line segments on the crystal lattice. While this representation is only composed of screw and edge dislocation segments (see Figure 33 (a)), it proves computationally efficient and easier to develop. In the nodal representation (see Figure 33 (b)), dislocation lines are depicted as a set of nodes connected by linear segments, with each segment attributed a Burgers vector and a glide plane. Notably, the nodes in nodal representation are free to move within the dislocation glide plane. The nodal representation results in smoother dislocation lines, offering better representation of topological constraints like curvature and core structure but at the cost of increased complexity and computational demands.

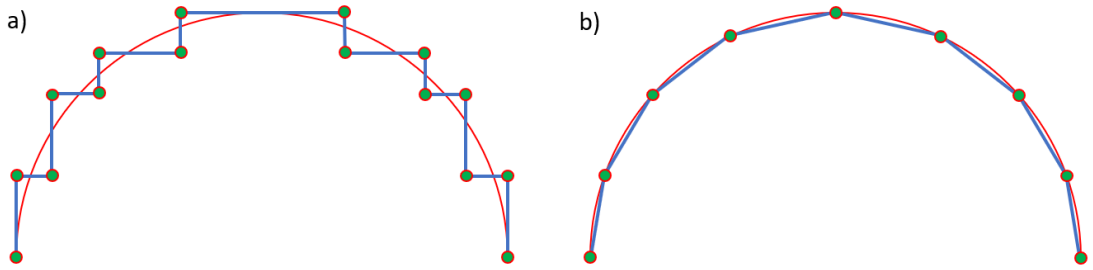

Figure 33: Comparison of a segment representation (a) and a nodal representation (b). The fine red line shows the actual dislocation line, the green points show the nodes, and the blue lines represents the line segments.

The choice between nodal and segment-based approaches in dislocation simulation is primarily dictated by the objectives and scales of the study. Nodal codes excel in capturing the exact morphology of dislocations over extended distances, offering a more accurate representation of dislocation shapes. This accuracy is particularly valuable when the continuous aspects of dislocations are under scrutiny. However, it's essential to note the challenges associated

with segment codes at smaller scales. Despite their preference for detailed examination of dislocation interactions in areas of high stress gradients, segment representations can struggle to accurately depict small-scale phenomena. This limitation can lead to spurious effects, especially in contexts involving climb where curvature representation at small scales is critical. Additionally, nodal codes have an advantage in implementing complex junction reactions more straightforwardly, enhancing their utility for certain detailed analyses. Despite these considerations, segment codes maintain a distinct advantage in terms of computational efficiency, simplicity, and robustness, making them a faster and more straightforward option for many applications. This efficiency is particularly notable on equivalent computing resources, although nodal codes may offer more detailed and accurate representations under certain conditions.

3.3.1 Historical development

The computational cost pave the way of history in DDD, a struggle between accuracy on the one hand and complexity and computational power on the other hand.
The first implementation was done by Foreman and Makin (1966), it was nodal but in 2D and looked at fcc metal to study the effect of hardening using random arrays of obstacles. It took till 1987 to perform the first 2.5 D approach done by Lepinoux and Kubin (1987), a simplified version where only straight edge segments are used and therefore line tension and other 3D behavior are neglected. In addition, it needs the application of local rules to account for the interaction between the dislocation as well as artificial multiplication. The authors showed the formation of slip bands, a similar approach is used in this work to study rheology of MgO with climb in the lower mantle which can be seen later. With fast increase in computing power and easier accessibility of data centers in the 90s, the first 3D approaches were realized by Devincre (1993) starting with fcc, and Moulin et al. (1997) who first implemented on a simple cubic lattice. The first application to earth science in the form of forsterite was then done by Durinck (2005) at Lille University were most of our study will be compared to.
This discussion leads us to the most recent developments in the field of Dislocation Dynamics (DD), focusing on nodal codes initially developed by Kukta and Freundt (1998), particularly ParaDis, developed at the Lawrence Livermore National Laboratory, and NUMODIS, developed in France at CEA (Saclay) which will be used in our study. These nodal codes have been extensively applied in various studies. For instance, others have employed NUMODIS to investigate loop interactions, as exemplified by Li et al. (2018). ParaDis has been for example utilized in simulations of dislocation interactions with low-angle grain boundaries, demonstrated by Liu et al. (2012). However, it's worth noting that these nodal codes have

certain limitations, such as the assumption of an infinite elastic field and the absence of nucleation, although nucleation can be incorporated when coupled with other codes. Furthermore, the contemporary trend in the field emphasizes the coupling of various codes to leverage their respective advantages. Recent projects in the DD community have explored areas like vacancy clusters using modified ParaDis, as seen in Wu et al. (2022), as well as the investigation of dislocation-induced hardening, a topic explored by Madec et al. (2003). An ongoing project called EL-NUMODIS involves the coupling of NUMODIS with FEM (Finite Element Method) to accommodate surface stresses and Monte Carlo simulations for nucleation, led by Gonzalez-Joa et al. (2023). Additionally, first studies delved into the mechanics of dislocation climb, with work on diffusion climb loops conducted by Bakó et al. (2011) using NUMODIS, or the coupling of climb mechanisms with ParaDis and Monte Carlo simulations by McElfresh et al. (2022). Also first attempts to implement cross-slip in an fcc structure were achieved by Longsworth and Fivel (2021) using NUMODIS. While these developments are crucial, our primary focus lies in directly comparing our modeling results with experimental data. NUMODIS was recently used to investigate the influence of irradiation-induced defects in zirconium alloys with comparison to MD simulations and experimental data by Drouet et al. (2014). In a study from Pollock and LeSar (2013), the authors compared data obtained from DET studies by Hata et al. (2011) and DDD simulations. They highlighted the importance of bridging the gap between these two fields, to provide a better validity from both sides. Our goal is to establish a direct comparison between modeling and real microstructures, utilizing the latter as input. However, this endeavor presents challenges, as experiments are inherently non-idealized. Therefore, we start this work with a relatively simple microstructure whereas many parameters as possible are known. Additionally, as a proof of concept, we limit ourselves to an unmodified version of NUMODIS, which excludes cross-slip.

3.3.2 Discrete dislocation dynamics with NUMODIS

NUMODIS which stands for Numerical Modelling of Dislocation, is a nodal DDD code similar to ParaDis, where a particular focus was given on node splitting. Node splitting allows physical multi-arm nodes to split into multiple new nodes connected by new segments, which improves the handling of junctions. It was developed in France at CEA (Saclay) in collaboration with CNRS (Grenoble and Thiais) and INRIA (Bordeaux).

The choice of NUMODIS is supported by its nodal nature, which enables it to directly trace dislocation lines, facilitating a seamless transition from tomography data to simulation. Additionally, it has been adapted to accommodate orthorhombic structures, specifically

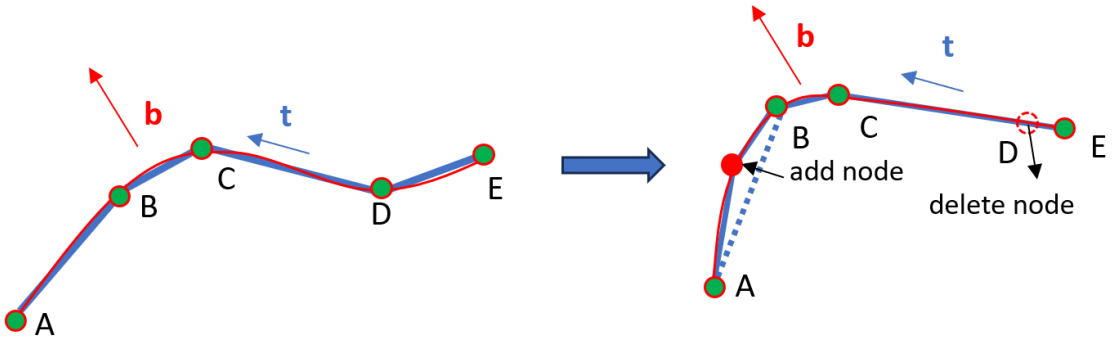

Figure 34: Discretization in NUMODIS. Fine red line shows the actual dislocation line, the green points show the nodes and the blue lines represents the line segments. In addition Burgers vector **b** and the line direction **t** are indicated. The illustration on the right showcases the evolution of the system after a certain duration and the corresponding remeshing. The dotted blue line highlights the line segment between nodes A and B, which no longer follows the dislocation line, therefore a new node has to be added. At the same time node D becomes obsolete to and gets removed, since not C and D are enough to discretice the line.

for forsterite simulations. This adaptation and the general implementation are done in collaboration with L. Dupuy (CEA Saclay), the leading developer of the code.

In the following, I will outline the general scheme of the code. The initial step involves the discretization of dislocation lines into segments, which are interconnected by nodes (see figure 34). Each segment is assigned a Burgers vector and a glide plane normal.
Since NUMODIS assumes linear elasticity, the stress at each point x can be calculated by:

$$\sigma(x) = \sigma_{app}(x) + \sum_{seg} \sigma_{seg}(x) \tag{3.13}$$

Here, σ_{app} represents the applied stress from an external field, and σ_{seg} denotes the stress arising from each segment and represents the stress created between the individual segments, due to the microstructure. However, it's worth noting that this method involves calculating interactions not only with direct neighbors but with all segments in the system, resulting in a scaling complexity of $O(N^2)$. That means the the running time of the algorithms scales quadratic with the number of input elements N.

To account for the divergence of the stress field at the dislocation line we rely on a non-singular continuum isotropic elasticity model by Cai et al. (2006). This method uses a spreading parameter, a_0, to avoid infinite stress at the dislocation line, similar to the Peierls-Nabarro model (see chapter 2.1.4).

Nodal forces acting at each end of discrete dislocation segments arise from the long-range elastic distortion field (stress) and from the dislocation core energy. The elastic forces are computed using the Peach-Koehler formula, as defined in equation 2.22 using the analytic expression from Arsenlis et al. (2007).

However, the non-singular model applies elasticity uniformly, necessitating an "energy correction term" (E^c_{NS}) to capture both the actual energy of a dislocation and ensure numerical stability. This term acts similarly to core energy but is distinct in that it includes elastic contributions within the core radius, underscoring its role as an energy correction rather than merely a core energy substitute. This correction term is derived by the approach of DeWit and Koehler (1959).

Moving on to the velocity calculation, where in the simplest scenario, a linear relationship is assumed:

$$v = \frac{F^{el}(x)}{B} \tag{3.14}$$

where B stands for a dragging coefficient, which reflects the viscosity/resistance of the lattice plane and can be adjusted for individual slip systems. In the next step discrete events take place such as junction formation, node splitting, or annihilation.
Finally, the process returns to the initial step, where the mesh is updated with new positions. This step also allows for remeshing, which can involve coarsening certain parts of the mesh by removing unnecessary nodes or refining it by adding nodes, as depicted in Figure 34.

The simulation box is set up to mimic the surfaces of the thin foil. With NUMODIS, we employee free surface boundary conditions. When dislocations approach the surface, mirror forces come into play, prompting us to extend the box for our final simulations, a topic elaborated further in section 6.

3.3.3 Association with Tomography

After the initial transformation of the tomography data (see Section 3.2.1), our code underwent specific adjustments tailored to meet the unique demands of Dislocation Dynamics (DDD) datasets. Initially, all previously ordered data was converted into the structure and format (XML) required for the NUMODIS input file. Additionally, the slip system planes were previously obtained from tomography for each dislocation. Then, we manually completed the information in a file, which is read by the program for comprehensive analysis. For dislocations which are in multiple planes, the dislocation get divided into separate dislocations

connected by one node, located at the intersection of the corresponding glide planes. The program was then enhanced to enable a back transformation of the DDD dataset into Nye input data, to analyse the stress field evolution. We have also created an option to extend straight segments, to the surface of the simulation box. To get the mechanical response of a bulk crystal instead of the thin foil.

3.3.4 2.5D-Dislocation Dynamics

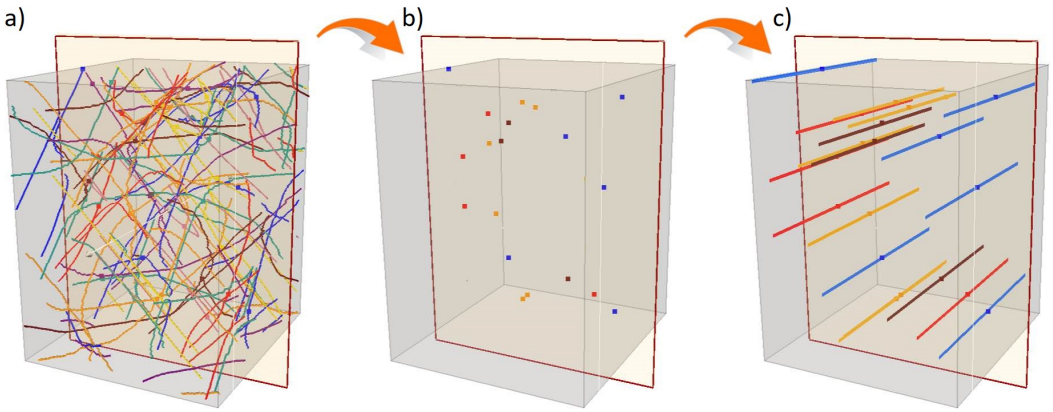

Figure 35: Scheme of the reduction from a 3D DD simulation box to a 2.5D DD simulation box. (a) 3D microstructure with the indication of the cutting plane; (b) Intersection point of the dislocation on the plane (2D); (c) edge on extension into the volume (2.5D). Courtesy F. Boioli.

To model creep in periclase under mantle conditions, we employ a 2.5D Dislocation Dynamics (DD) simulation approach, rather than opting for a full 3D approach. This approach has already been benchmarked for periclase at ambient pressure (Reali et al. 2017). The reason behind this simplification is to account for the climb mechanism. In the context of scales, it is currently challenging to integrate both the climb and glide behaviors into a single simulation. Climb mechanisms operate through the diffusion of single point defects, while glide occurs in fixed planes. Additionally, another complicating factor is that the timescales associated with these mechanisms can differ by multiple orders of magnitude. Given our objective of achieving significant strains, employing a coupled approach, as seen in McElfresh et al. (2022), may not be feasible.

The idea is to examine a cross-section of a 3D dislocation structure and represent each dislocation as an edge dislocation that extends in a straight line throughout the 3D environment (see Figure 35), which is why our approach is referred as 2.5D. This results in discrete simulation points rather than 2D objects embedded in a 3D space, inevitably leading to the exclusion of certain effects related to 3D interactions, in example the limitation to a single slip plane.

To enable this simplification, it is essential to possess a comprehensive understanding of the underlying elementary processes that occur within the material. To incorporate these processes, we implement local rules (junction formation strengthening and dislocation multiplication). One of the primary considerations is accounting for the formation of junctions and the subsequent increase in dislocation density.

During plastic flow, dislocations arrange themselves into great patterns of dislocation-rich and dislocation-poor regions, creating cells which get denser when the stress is increased. This phenomenon is called the "principle of similitude" (Gómez-Garcıa et al. 2006). The inter-dislocation spacing diminishes with increasing stress, leading to an overall rise in dislocation density. This increase in dislocation density is governed by the Taylor relation and remains valid for strain rates below $10s^{-1}$ (Gómez-Garcıa et al. 1999). Since this study is focused on the lower mantle where the strain rates are of the order $10^{-16}s^{-1}$, where are far below that threshold. It is given as follows (Sauzay and Kubin 2011):

$$\rho \propto \left(\frac{\sigma}{b\mu}\right)^2 \tag{3.15}$$

Another consequence of the "principle of similitude" is that the stress field that is usually proportional to the inverse distance from the dislocation line, now concentrates within a specific cutoff distance corresponding to the mean inter-dislocation length. This means only short range interactions are included and it is not accounted for dislocation interactions of the whole network like it is done in DDD. To avoid the formation of artificial patterns from the similitude principle, the cut off distance is allowed to vary a bit. 3D simulations done by Devincre et al. (2011) reproduced those behaviors.

A consequence of this simplification is a significant reduction in the computational cost required for force calculations, shifting from an $O(N^2)$ complexity (as described in Devincre et al. 2011) to a more efficient $O(N)$ algorithm (as outlined in Gómez-Garcıa et al. 1999). This computational optimization enables us to tackle larger scales with considerably less computational effort. An additional point that has to be discussed is that, since we solely account for edge dislocations, we omit screw dislocations that typically stabilize dislocation tangles in 3D. An effect that can be ignored in 2D. However, screw dislocations also allow a continuous movement of dislocations via cross-slip, which is accounted for in the annihilation rules. Another consideration is the multiplication of dislocations via Frank-Read sources. In a 2D dislocation structure, this multiplication is not possible, as it requires a 3D dislocation structure. To address this, they are added artificially, with a multiplication rate of $m = 10^{-15}\, m^{-2}$, taken from 3D simulations in fcc crystals by Madec et al. (2002). Here m is the rate at which the dislocation density increases with the plastic strain. However, adding

dislocations at the same locations multiple times can lead to spurious annihilations due to interactions with their replicas. To solve this, dislocations are randomly added to the simulation box, providing that their effective stress is in the direction of the applied shear stress as outlined in Gómez-García et al. (2006). In order to stabilize the stresses and dislocation fluxes at the boundaries of each simulation box, we employ periodic boundary conditions. Otherwise, the dislocations tend to accumulate in the center of the boxes. In addition to validate the local rules, the simulation is tested at low and intermediate time scales against results from three dimensional DD simulations and experiments (Amodeo et al. 2011; Appel and Wielke 1985; Sato and Sumino 1980; Srinivasan and Stoebe 1974).

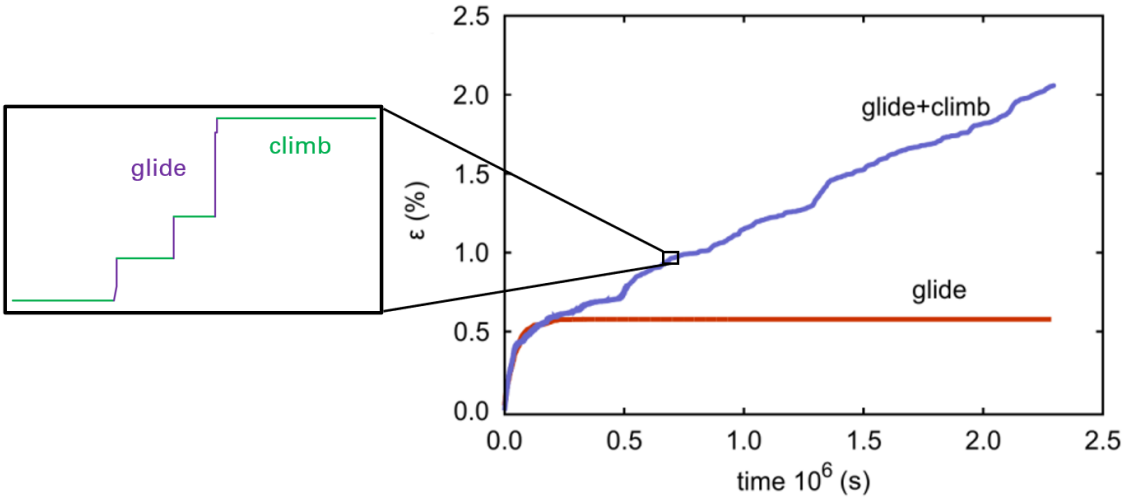

Figure 36: Strain ϵ evolution over time t, with glide only (red) and with glide and climb combined (blue). Zoom shows the strain contribution of glide and climb in the the combined simulation, indicating that glide mainly contributes to the strain.

To account for the timescale difference between glide and climb mechanism we separate these two processes into individual regimes. Initially, we initiate the glide regime, which persists until a quasi-equilibrium configuration is reached where dislocations cease to glide. This is monitored by looking at the strain saturation, by calculating a floating average strain of the last 400 simulation steps. When the difference in strain between the first 200 steps and the second 200 steps becomes smaller than a certain value, in our case 10^{-23}, we identify this as reaching equilibrium. At this point, we switch to the climb regime, with significantly longer time steps and employ a different velocity law (see equation 2.25). Once a displacement equivalent to a full Burgers vector is achieved through climbing, we revert to the glide regime. This cycle of switching between glide and climb is repeated iteratively throughout the entire simulation to maintain a continuous deformation with a constant strain rate (see Figure 36). Finally let's briefly outline the simulation steps employed in this 2.5D approach. Initially, we

calculate the forces acting on each dislocation using the Peach-Koehler force (equation 2.22). Subsequently, dislocation velocities are computed using equation 2.21 in the glide regime and equation 2.25 during the climb regime. Following this, the signals are time-integrated to update the positions of the dislocations. In the subsequent step, all the contributions of individual segments are summed to obtain the total strain. Finally, the local rules are applied, and the simulation cycles back to the initial step.

4 Results - General Applications of Dislocation Electron Tomography

4.1 Quartz - Evidence of Mixed Climb

This section draws from a paper published to Journal of Geophysical Research[1] In this project, my primary role involved acquiring the DET data in collaboration with my PhD supervisor A. Mussi. Subsequently, I conducted post-treatment on the data to facilitate its transformation into a quantitative analysis. This entailed setting up statistical analyses and making adjustments to enhance data interpretation. Additionally, I focused on improving data visualization to ensure clarity. In this study, we apply DET to characterize 3D dislocation microstructures in two highly sheared quartz mylonite specimens from the Moine and Main Central thrusts which were deformed extensively by dislocation creep in the presence of water.

4.1.1 Introduction

Quartz is one of the major constituents, by volume, of the Earth's crust. Above ca. 300°C (corresponding to depths beyond 10 km, Stipp et al. 2002b), quartz is ductile and it appears to be one of the weaker minerals in naturally deformed rocks of the continental crust. The plasticity of quartz is thus important to the description of the rheology of the lower crust. Many studies over the last 60 years have been devoted to the plasticity of quartz. Still, the plastic behaviour of this mineral is only partially understood, even in the laboratory. Our understanding of the crystal plasticity of this mineral under natural conditions, and its control of crustal rheology, is far from resolved. The simple question of how quartz deforms by glide of dislocations is not straightforward. In this trigonal mineral, glide of <a> dislocations ($1/3\langle 2\bar{1}\bar{1}0\rangle$) in the basal plane is expected (Baeta and Ashbee 1969). It was indeed observed experimentally very early on and is complemented at higher temperatures by glide

[1] Weidner ,T., A. Mussi, O. Castelnau, A. Kronenberg, R. Law and P. Cordier. (2024)" Evidence of Dislocation Mixed Climb in Quartz from the Moine and Main Central Thrusts: an Electron Tomography Study". In: *Journal of Geophysical Research: Solid Earth*, 129, e2024JB029083. *https://doi.org/10.1029/2024JB029083*.

of $[c]$ ($[0001]$) dislocations in prismatic planes (Blacic 1975). However, these slip systems by themselves are insufficient to satisfy the von Mises-Taylor criterion for general strains with arbitrary non-zero components (Mises 1928; Taylor 1938;Ball and White 1978). Activating <c+a> glide can potentially satisfy the remaining strain components (Baeta and Ashbee 1969; Trépied and Doukhan 1982): however, this mechanism seems to have been neglected for several years. As far as deformation involving dislocation motion is concerned, conservative glide is not the only process contributing to creep. Additional degrees of freedom to deformation may be facilitated by dislocation climb as point defects become mobile through diffusion. Strains may also be satisfied by cracking at low effective stresses or sliding at grain boundaries (Behrmann and Mainprice 1987; Fliervoet et al. 1997; Fukuda et al. 2018; Rutter and Brodie 2004; Tokle et al. 2019). Beyond the fundamental questions about intracrystalline deformation mechanisms that apply to all minerals (and crystalline solids in general), dislocation creep of quartz and its mechanical properties depend on impurities, particularly those derived from water (such as hydroxyls at structural sites of the crystalline structure and dislocations). Owing to the three-dimensional network of strong Si-O bonds, dry quartz is very strong, and almost undeformable by dislocation motions in the laboratory. In contrast, quartz deformed at tectonic strain rates in the presence of water (at temperatures greater than 300 °C) is ductile and appears to be one of the weakest minerals of quartzo-feldspathic crustal rocks.

The phenomenon of water (or hydrolytic) weakening was discovered by Griggs and Blacic (1965) and interpreted to result from hydrolysis of strong Si-O-Si bonds, to form weak hydrogen-bonded SiOH groups at dislocation cores (Griggs 1967, 1974). Hydrous defects were originally thought to be transported to dislocation cores by volume diffusion. However, alternative water weakening models have since been proposed, including potential effects of hydrogen impurities on other charged point defects that facilitate climb (Hobbs 1984; Hobbs 1981), and effects of hydrogen impurities on concentrations (and mobilities) of dislocation kinks and jogs (Hirsch 1981). All of these models have been challenged, though, by the discovery that solubilities of OH defects within the quartz structure are low (Cordier et al. 1989; Cordier and Doukhan 1991; Doukhan and Paterson 1986; Kronenberg et al. 1986), limiting the predicted changes in point defect chemistry of crystalline quartz and the delivery of OH to dislocations cores by radial volume diffusion to dislocation cores. Ab initio models of hydrous molecular structures and dislocation kinks in quartz indicate that hydrous defects are stable at dislocation cores, particularly at dislocation kinks (Heggie and Jones 1986; Heggie et al. 1985). Hydrous defects are therefore thought to gain access to dislocation cores by pipe

diffusion from grain boundaries or fluid inclusions (Bakker and Jansen 1990, 1994; Cordier et al. 1989; Cordier et al. 1988; Cordier and Doukhan 1991; Heggie 1992).

Hydrolytic weakening has only been observed when measured OH concentrations are super-saturated with respect to hydrous defect solubilities (Cordier et al. 1989; Kekulawala et al. 1978, 1981; Kirby and McCormick 1979). Initial transient creep rates of OH-supersaturated quartz have been explained by mechanisms of dislocation nucleation at non-equilibrium water clusters and fluid inclusions with further dislocation multiplication facilitated by pipe diffusion of hydrous defects (Cordier et al. 1989; Gerretsen et al. 1989; McLaren et al. 1989). Most relevant to the present study is the role of hydrous defects in facilitating dislocation climb during plastic deformation of quartz.

Dislocation climb is usually regarded as a recovery mechanism rather than a strain-producing mechanism (Tullis and Yund 1989). However, activation of the climb mechanism proposed by Nabarro (1967) was suggested by Ball and White (1978) and Ball and Glover (1979) to apply to quartz single crystals experimentally compressed along the $[0001]$ direction. The activity of dislocation climb in quartz also has implications for the onset of dynamic recrystallization (Hirth and Tullis 1992). In the absence of significant contributions from dislocation climb at low temperature, recrystallization involves strain-induced grain boundary migration (GBM), or bulging. At higher temperature, when dislocation climb is enhanced, recrystallization may occur by progressive subgrain rotation (Hirth and Tullis 1992).

In a recent study, an analytical method was applied to quartz using electron tomography of dislocation microstructures to determine the components of the plastic strain tensor (Mussi et al. 2021c) resulting from the displacement of these dislocations. This study revealed the unexpected activation of <c+a> dislocation climb. The present study was undertaken to learn whether climb of <c+a> dislocations is important to the plastic deformation of quartz in natural shear zones. Quartz mylonite specimens were selected for electron tomography from the Moine and Main Central thrusts, both of which deformed extensively by dislocation creep in the presence of water. TEM tomography of dislocations presented in this study is applied to determine the relative mobilities of dislocations by glide and climb.

4.1.2 Materials and Methods

4.1.2.1 Specimens

Two highly sheared quartz mylonite specimens have been selected for this study, exhibiting optical microstructures and crystallographic preferred orientations indicative of dislocation creep and dynamic recrystallization. Both mylonites come from major shear zones associated

with collisional tectonic boundaries, one from the Main Central Thrust of Northwest India, related to the southward-directed Oligocene-Miocene extrusion of the Greater Himalayan slab (Hodges 2000), and the other from the Moine Thrust of Northwest Scotland, associated with Caledonian shortening of the foreland continental margin during closure of the Iapetus Ocean (Strachan et al. 2002). The Main Central Thrust mylonite specimen S-09-35a (hereafter referred to as MCT) was taken from a quartz-rich horizon of Greater Himalayan orthogneisses in the western part of the Sutlej Valley, at a structural distance of 71 meters above the Main Central Thrust (Law et al. 2013). The Moine Thrust mylonite specimen SG-10 (hereafter referred to as MT) was collected from Cambrian quartzites in the footwall at the Stack of Glencoul, just 4.6 m below the thrust contact with overlying Neoproterozoic Moine schists (Law et al. 1986, 2010).

The MCT specimen is made up of highly sheared quartz horizons within a sheared matrix of mixed quartz and layer silicates (Figure 37). Almost all quartz horizons of this specimen have been recrystallized, but the TEM observations made here are for larger residual quartz grains whose deformation gives them the grain shapes of augen (Figure 37). These quartz augen exhibit patchy undulatory extinction and well-developed subgrain walls. Fine recrystallized quartz grains appear within the larger grains and at their margins, with microstructures that indicate that recrystallization occurred predominantly by subgrain rotation (SGR) with subordinate grain boundary migration (GBM) (Law et al. 2013; Stipp et al. 2002a). The mean recrystallized grain size measured in quartz-rich layers is $\sim 45\,\mu$m (Francsis 2012). Crystallographic c-axes of recrystallized quartz-rich horizons show distinctly asymmetric cross-girdle patterns due to internal shear in the fault transport direction, with high c-axis densities defining a great circle consistent with oblique grain shape alignments subparallel to lineation and top-to-the SW (thrust) shear (Law et al. 2013).

Using the Faleiros et al. 2016 opening angle thermometer, the temperature of deformation for MCT is estimated to be $515\,^{\circ}$C, based on a measured c-axis fabric opening angle of 68° (Law et al. 2013). In contrast to the differences in crystal fabric and petrologically based temperatures of Moine thrust specimens at the Stack of Glencoul, estimates of peak deformation and metamorphic temperatures, based on c-axis patterns and coexisting garnet and muscovite compositions of mylonites collected from the Sutlej Valley, are in close agreement. Peak pressures estimated for mylonites $\sim 1100\,$m structurally above MCT are of the order of $800\,$MPa (Supplementary file in Law et al. 2013). The differential stress estimated from the mean recrystallized grain size of MCT and the modified Stipp et al. (2006) grain size piezometer is $\sim 24\,$MPa (Francsis 2012; Law et al. 2013). The strain rate predicted by the Hirth et al. (2001) flow law at these conditions is $\sim 10^{-12}\,$s^{-1}. Other than our own pre-

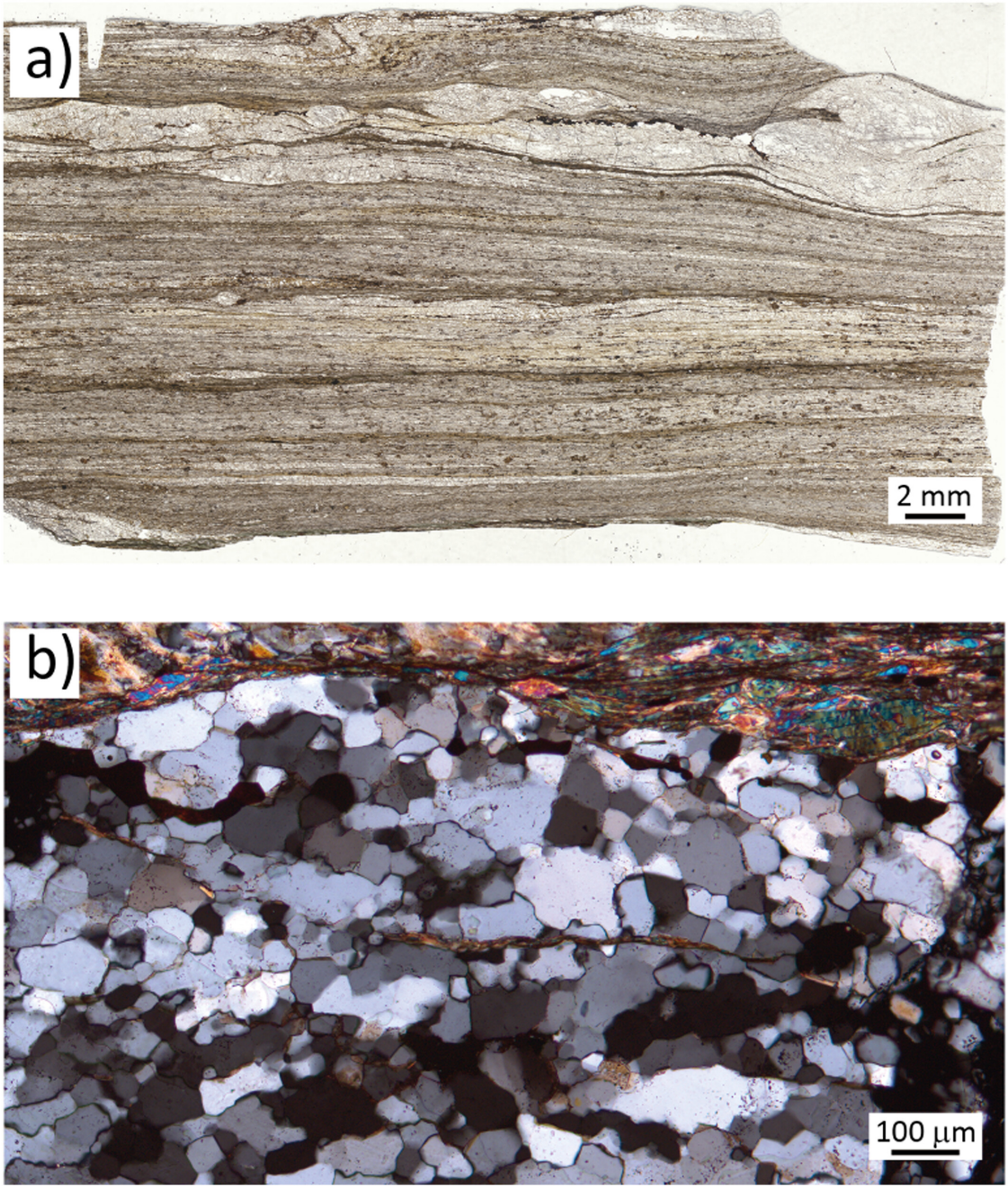

Figure 37: Low magnification optical micrographs of specimen Main Central Thrust (MCT) (S-09-35a) from hanging wall orthogneisses of the MCT, collected from the western part of the Sutlej Valley, NW India (Law et al. 2013): (a) Plane light image of XZ section prepared perpendicular to foliation (horizontal in this image) and parallel to lineation (in foliation), nearly parallel to the fault transport direction (top to the left), with sheared quartz horizons within a matrix of quartz and layer silicates. (b) Deformation and recrystallization microstructures of quartz horizon in cross-polarized light.

liminary TEM of MCT samples, we are not aware of any previous studies of dislocations by electron microscopy of high strain rocks from the Sutlej Valley. Undulatory extinction and subgrains of the MCT sample at the optical scale correspond to dislocations and subgrain walls at the TEM observational scale. Infrared absorption measurements of OH bands reveal large but variable OH contents of large augen quartz grains with mean molar OH contents of 3010 ± 2780 ppm (Kronenberg et al. 2017). These bands are due to intragranular molecular water, and preliminary TEM shows that fine fluid inclusions routinely decorate dislocations.

The MT specimen consists of sheared ribbon (high aspect ratio) quartz grains with smooth undulatory extinction observed in conventional thin sections, and well-developed subgrain walls that are apparent in ultra-thin sections ($\sim$5 μm) (Kronenberg et al. 2020), consistent with optical microscopy of etched sections and TEM of nearby mylonitic Cambrian quartzites (Ord and Christie 1984; Weathers et al. 1979). Ribbon quartz grains are recrystallized at their margins, with microstructures due to grain boundary bulging (BLG) and subordinate subgrain rotation (SGR) (Law 2014; Stipp et al. 2002a); over 70 % of this specimen consists of recrystallized grains (with a 21 μm mean size; Kronenberg et al. 2020; Weathers et al. 1979) but the new TEM observations of this study are from original ribbon quartz grains (Figure 38). Crystallographic c-axes of ribbon and recrystallized quartz grains exhibit nearly symmetric crossed-girdle patterns aligned with respect to grain shape foliation and lineation (Law et al. 2010), consistent with significant plane-strain foliation-normal shortening by glide on multiple slip systems with Burgers vectors parallel to <a> and to [c] (and other crystallographic slip vectors with components in a and c).

The temperature of deformation for the leading edge of the MT, based on crystallinity of white micas, is relatively low, $300 - 350\,^{\circ}$C (Johnson et al. 1985), while temperature estimates for the MT specimen based on opening angles of quartz c-axis fabrics measured on ribbon detrital quartz grains (53°) and matrix recrystallized quartz grains (69°) are as large as $415\,^{\circ}$C and $525\,^{\circ}$C respectively (Faleiros et al. 2016; Law et al. 2010 opening angle thermometer). Peak lithostatic pressures during mylonitization have not been determined. The differential stress estimated from the mean recrystallized grain size ($21\,\mu$m) of MT and the modified Stipp et al. (2006) recrystallized grain size piezometer (with the adjustment of Holyoke III and Kronenberg 2010) is ~ 44 MPa, and strain rates based on this stress, temperature estimates of $350 - 400\,^{\circ}$C, and the quartzite flow law of Hirth et al. (2001) are between $10^{-14}\,s^{-1}$ and $10^{-13}\,s^{-1}$.

Preliminary TEM observations of MT corroborate earlier observations of dislocation microstructures (Ord and Christie 1984; Weathers et al. 1979 and intimate dislocation-fluid inclusion relationships suggest that hydrogen defects had direct access to the cores of dis-

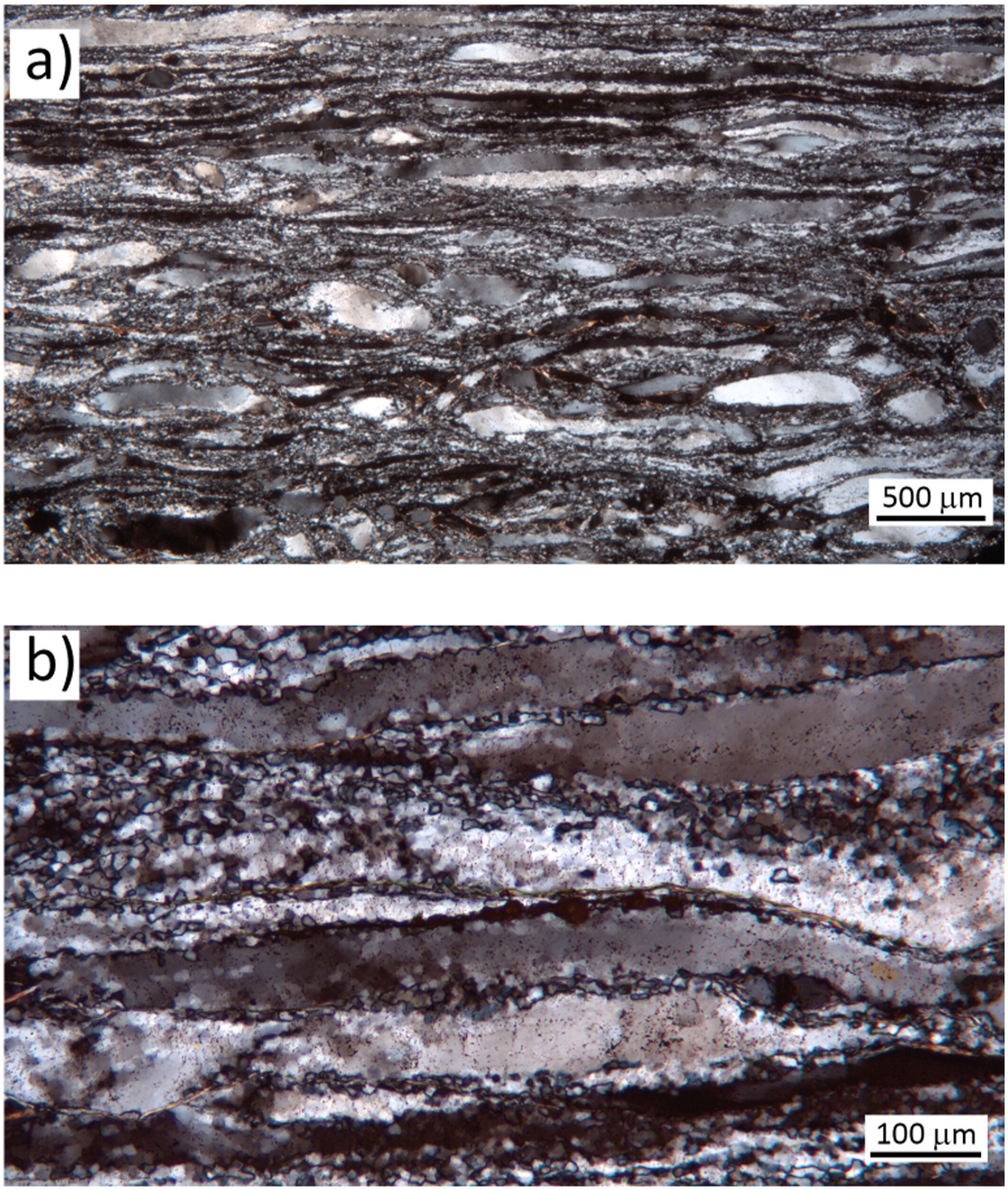

Figure 38: Optical micrographs of specimen Moine Thrust (MT) (SG-10) from footwall quartz mylonites of the MT collected at the Stack of Glencoul, NW Scotland (Christie et al. 1964; Law 2014; Law et al. 1986, 2010): (a) Cross-polarized image of XZ section prepared perpendicular to foliation (horizontal in this image) and parallel to lineation (in foliation) and fault transport direction (top to the left) shows highly sheared (high aspect ratio) ribbon quartz grains and extensive dynamic recrystallization. (b) Larger ribbon quartz grains show smoothly undulatory extinction with serrated grain boundaries at their margins, of similar dimensions as recrystallized quartz grains.

locations. Infrared absorption measurements of OH bands of original ribbon quartz grains of MT are large, varying from one grain to another, with molar OH/Si concentrations of 2400 ± 700 ppm ($H/10^6$ Si) (Kronenberg et al. 2020).

While the inferred temperatures, pressures, differential stresses and strain rates of the two mylonite specimens investigated in this study vary, the overall crystallographic fabrics are remarkably similar. With their similar quartz cross-girdle c-axis fabrics and fabric opening angles for the MT and MCT specimens (68° for recrystallized grains in MCT, and 53° and 69° measured for deformed detrital and recrystallized grains, respectively, in MT), we might expect similar dislocation slip systems to be important with similar proportions of slip vector components in the a and c directions.

Temperature estimates for these specimens correspond well with the temperature ranges for dynamic recrystallization of quartz by BLG, SGR, and GBM mechanisms (Stipp et al. 2002a); subgrain rotation recrystallization appears to be important for both mylonites, with the implication that dislocation climb is important in both tectonic settings and deformation conditions. In addition to SGR recrystallization, the MCT specimen has grain boundaries characteristic of some GBM recrystallization, while the MT specimen exhibits evidence for BLG recrystallization as well as the SGR mechanism (Kronenberg et al. 2020, 2017).

4.1.2.2 Dislocation electron tomography

DET was employed to analyze the dislocation populations in specimens from the MCT of the Himalayas (specimen S09) and the MT zone at the Stack of Glencoul (specimen SG10). The high-structure factor $11\bar{2}2$ and $1\bar{1}01$ diffraction vectors were used for the MCT and MT specimens, respectively. Considering the electron beam sensitivity of quartz, precautions were taken into account based on the techniques described in chapter 3.1.3. To account for this we used a condenser aperture with a diameter of $100\,\mu m$ and a spot size of $11.3\,nm$.

For the MCT specimen, WBDF micrographs were acquired at 5° intervals, covering angles from -55° to 70°. This tilt-series comprised a total of 26 projected images. For the MT specimen, Weak Beam Bright-Field (WBBF) micrographs were acquired every 10° from -50° to 50°, and additionally from -45° to 35°. These tilt-series consisted of 11 and 9 projected images, respectively. The WBBF technique was used for the second sample due to phase contrast issues.

4.1.2.3 Plastic strain associated with dislocation segments

Most of the dislocation segments observed in this study lie out of their glide planes. This configuration is discussed in section 4.1.4.2. These dislocation segments must be analysed, recognizing that they must have moved by a combination of glide and climb, mixed climb. In the following, we express the strain that can be generated by the displacement of the dislocation segments present in the specimen, taking into account their movement plane. We denote $\mathbf{n}$ the unit vector normal to the plane containing the dislocation line (referred to as the movement plane), and $\mathbf{n}^g$ the unit vector normal to the glide plane (index g stands for 'glide'). The Burgers vector $\mathbf{b}$ is thus perpendicular to $\mathbf{n}^g$ (Figure 20). The unit line vector of the dislocation, denoted $\mathbf{t}$, is in the movement plane and is therefore perpendicular to $\mathbf{n}$. For the part of a segment that is edge oriented, the line vector, denoted $\mathbf{t}^e$ (index e stands for 'edge') is also perpendicular to the Burgers vector. Therefore, it can be expressed as:

$$\mathbf{t}^e = \frac{\mathbf{b} \times \mathbf{n}}{\|\mathbf{b} \times \mathbf{n}\|} \tag{4.1}$$

where '$\times$' is the cross product. The normal $\mathbf{n}^g$ of the dislocation glide plane is perpendicular to both the line vector $\mathbf{t}^e$ and the Burgers vector $\mathbf{b}$ and can thus be written:

$$\mathbf{n}^g = \frac{\mathbf{t}^e \times \mathbf{b}}{\|\mathbf{t}^e \times \mathbf{b}\|} \tag{4.2}$$

The dislocation (edge or screw) gliding in that plane produces a plastic strain-rate proportional to its Schmid tensor $\mathbf{S}^g$, according to the Orowan equation:

$$\dot{\varepsilon}^g_{ij} = \rho b v^g S^g_{ij} \tag{4.3}$$

with $S^g_{ij} = \frac{1}{2}(n^g_i \hat{b}_j + n^g_j \hat{b}_i)$, where $\hat{\mathbf{b}}$ is the unit vector parallel to $\mathbf{b}$, ρ is the density of mobile dislocations and v^g is their glide velocity. The inclination θ between the dislocation plane and the glide plane (Figure 20) can be calculated from $\cos\theta = \mathbf{n}^g \cdot \mathbf{n}$. For non-zero values of θ, climb must be involved. The kinematics of the climb of an edge dislocation is a little more complicated as diffusion may not produce an isochoric strain (see Lebensohn et al. 2010 and Yuan et al. 2018). However, considering geological time scales, we assume that the density of point defects that affect climb achieve equilibrium concentrations (i.e., constant with time) at a given temperature. Thus, no volume change is expected due to climb. The strain-rate tensor produced by climb is proportional to the 'climb Schmid tensor' $\mathbf{S}^c$ (index c stands for climb)

$$\dot{\varepsilon}^c_{ij} = \rho b v^c S^c_{ij} \quad (4) \tag{4.4}$$

where v^c is the climb rate of the segment and $\mathbf{S}^c$ is given by $S^c_{ij} = \hat{b}_i\hat{b}_j - \frac{1}{3}\hat{b}_k\hat{b}_k\delta_{ij}$. As indicated in Tables 4.1 and 4.2, several dislocation segments and movement planes have been identified in the two grains investigated. Grain deformation can be investigated by summing-up the contributions of glide and/or climb of one or more dislocation segments, and the number of the associated independent deformation systems can be computed as explained in Cotton et al. (1991) and Castelnau et al. (2020) for any crystal symmetry.

4.1.2.4 Estimation of the local loading conditions

Here we attempt to infer the local stress that acted *in situ* on the investigated grain to produce the observed dislocation microstructure. We assume a power law constitutive relation for glide and for climb to estimate the dislocation velocity for glide and climb. These velocities, which depend on the local stress, are linked together by the angle θ shown in Figure 20.

4.1.2.4.1 Glide Mechanism We start with the Orowan equation (eq. 4.3), written for a specific slip system and consider a standard power-law (Morales et al. 2011) to describe the shear-rate at the slip system scale:

$$\dot{\gamma} = \dot{\gamma}_0 \left|\frac{\tau}{\tau_0}\right|^{n_g-1} \frac{\tau}{\tau_0} \tag{4.5}$$

where $\dot{\gamma}_0$ is a reference strain-rate, τ_0 is the corresponding reference stress, n_g gives the stress sensitivity for glide, and τ is the shear stress resolved on the glide plane given by:

$$\tau = n^g_i \hat{b}_j \sigma'_{ij} \tag{4.6}$$

The dislocation glide velocity is thus given by:

$$v_g = \frac{\dot{\gamma}_0}{\rho b} \left|\frac{\tau}{\tau_0}\right|^{n_g-1} \frac{\tau}{\tau_0} \tag{4.7}$$

4.1.2.4.2 Climb Mechanism Here we use the Orowan equation (eq. 4.4) adapted to climb, following Lebensohn et al. (2010). As for glide, we consider a standard power-law to describe the longitudinal strain-rate:

$$\dot{\epsilon} = \dot{\gamma}_0 \left|\frac{\sigma'}{\sigma_0}\right|^{n_c-1} \frac{\sigma'}{\sigma_0} \tag{4.8}$$

where $\dot{\gamma}_0$ is a reference strain-rate (which can be taken as the same as for glide), σ_0 is the corresponding reference stress, n_c gives the stress sensitivity for climb, and σ' is the deviatoric

stress given by:

$$\sigma' = \hat{b}_I \hat{b}_j \sigma'_{ij} \tag{4.9}$$

The dislocation climb velocity is thus given by:

$$v_c = \frac{\dot{\gamma}_0}{\rho b} \left| \frac{\sigma'}{\sigma_0} \right|^{n_c - 1} \frac{\sigma'}{\sigma_0}. \tag{4.10}$$

4.1.2.4.3 Estimation of the Local Stress The velocities v_c and v_g are related by the angle θ between the normal to the plane of movement and the normal to the glide plane. This can be expressed as

$$(v_g \hat{\mathbf{b}} + v_c \mathbf{n}^g) \cdot \mathbf{n} = 0 \tag{4.11}$$

where $\cos\theta = \mathbf{n}^g \cdot \mathbf{n}$. To find a stress state compatible with the observed dislocation structure, we must solve for a system of nonlinear equations formed by one condition (12) for each observed dislocation segment. We adopt a minimization procedure in order to find the stress tensor that best matches the observations. We construct the following objective function

$$\sum_s l_s^k (\theta_s^{\text{mod}} - \theta_s^{\text{obs}})^2 \tag{4.12}$$

where θ^{mod} is the θ angle computed from the above equations and θ^{obs} is the observed angle. The difference in θ angles is weighted by the dislocation length l in order to force a better match for longer dislocation segments (here, we used a value for $k = 4$). The objective function is the sum over all observed dislocation segments s, minimized by the Nelder-Mead method.

4.1.3 Results

The dislocation microstructures of the MCT and MT specimens are comparable. Dislocation densities are $3 \times 10^{12}\,\text{m}^{-2}$ and $4 \times 10^{12}\,\text{m}^{-2}$ respectively (with densities measured directly from the reconstructed volumes). Sub-grain boundaries due to recovery are observed in both specimens (Figures 39 and 40).

In this section, the quantitative analysis of the microstructure is described, followed by a detailed characterization of slip systems, and then climb systems for each specimen. From these analyses, Schmid tensors and associated equivalent strain and stress tensors of each specimen are estimated.

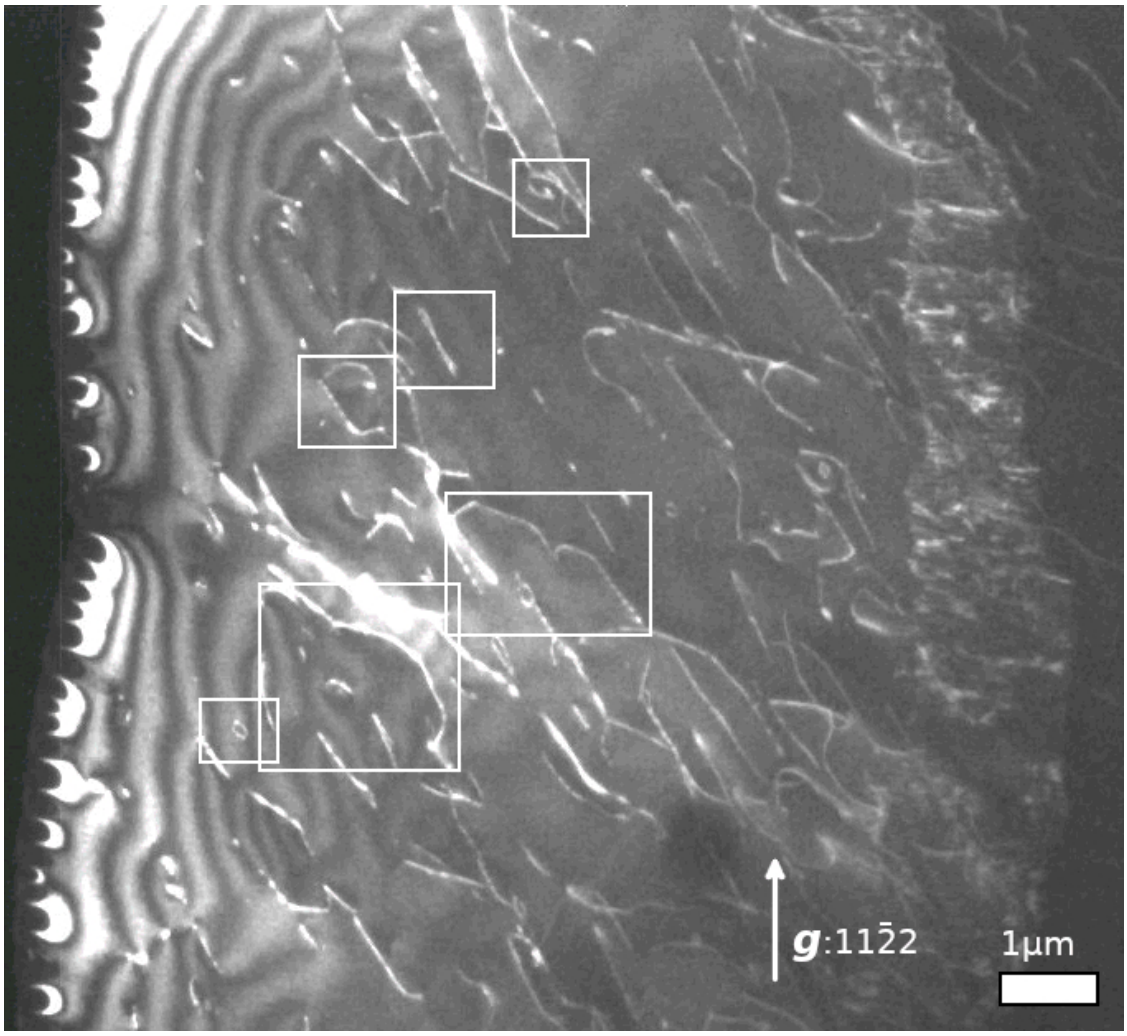

Figure 39: Global microstructure of the specimen from the MCT: Micrograph in WBDF condition obtained with the $11\bar{2}2$ diffraction vector (the white rectangles are analysed in detail in this study), where one sub-grain can be observed.

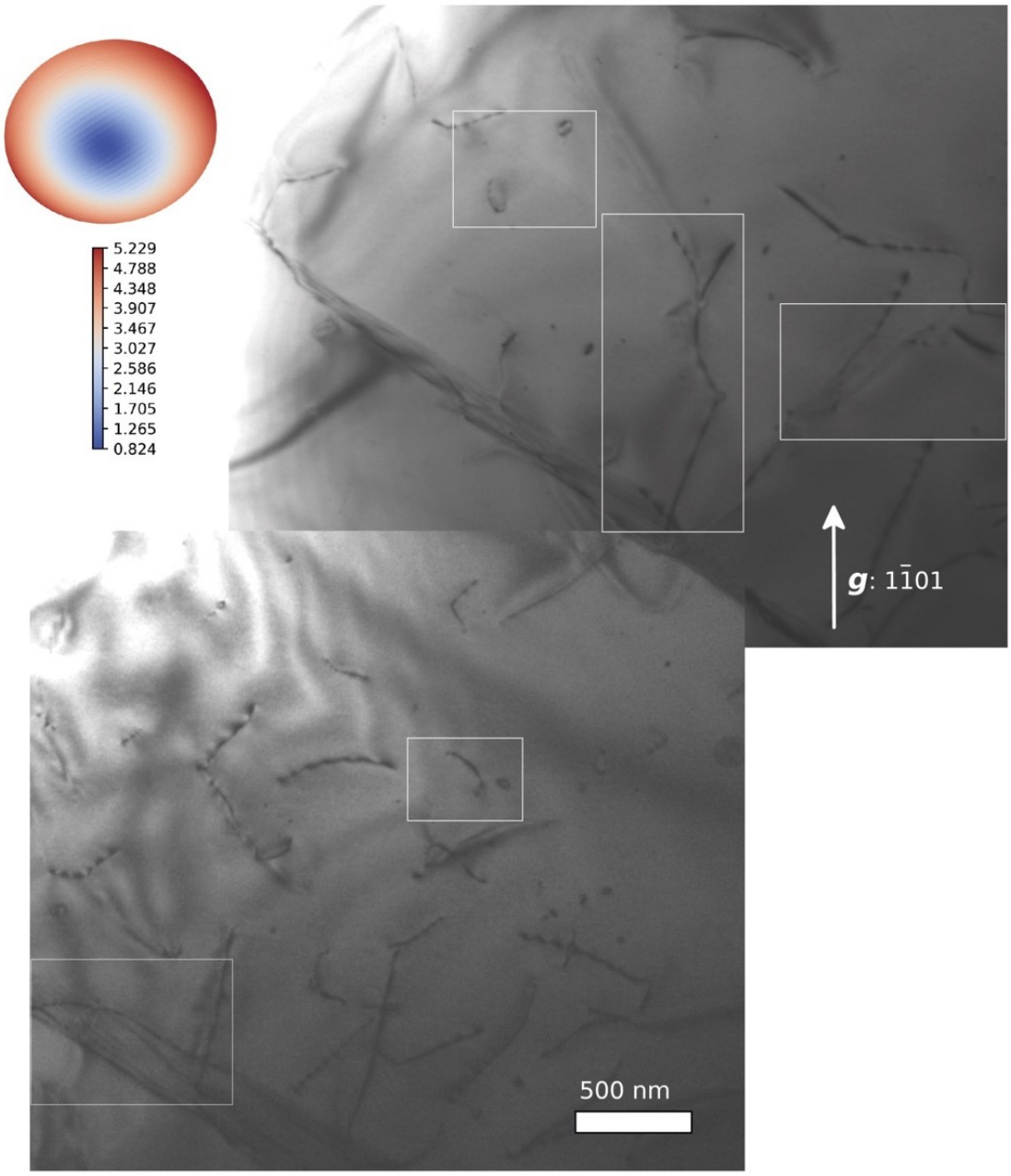

Figure 40: Global microstructure of specimen from the MT: Micrograph in WBBF condition obtained with the $1\bar{1}01$ diffraction vector (the white rectangles are analyzed in detail in this study) where two sub-grains can be observed. In the top left corner is the stress ellipsoid inferred from the present analysis (see discussion, Figure 49).

4.1.3.1 Quantitative analysis of the microstructure

The characterization of dislocation glide and/or climb relies on determination of the plane of movement of dislocation, which can only be achieved for curved dislocations. In this study, however, we have sought to take into account the contribution of rectilinear dislocations to the microstructure. Lattice friction is high in quartz under the deformation conditions of our specimens Doukhan and Trépied (1985). Consequently, it is highly likely that rectilinear dislocations are in glide configurations. Following the characterization of direction lines of rectilinear dislocations with known Burgers vectors, it is possible to infer their glide planes (provided that they are not pure screw in character). In order to optimize the quantification of the dislocation glide and climb contributions, we have only considered the dislocations whose Burgers vectors could be unambiguously determined, keeping in mind that indexing of Burgers vectors has previously been optimized. However, DET has been conducted for each specimen with only one diffraction vector which does not allow identification of all dislocation segments. More precisely, the DET study of the MCT specimen has been conducted with the $11\bar{2}2$ diffraction vector, where all dislocations ($\langle a \rangle$, $[c]$ and $\langle c+a \rangle$) are in contrast except $c+a_3$ dislocations. Our DET study of the MT specimen has been conducted with the $11\bar{0}1$ diffraction vector where all dislocations are in contrast except a_3, $c+a_2$ and $c-a_1$. A complete list of the characterized dislocation segments of both specimen is given in Tables 4.1 and 4.2.

Table 4.1: List of dislocations where Burgers vector and habit planes have been characterized in the MCT specimen (Figures 41 to 43). The last column reports the angle between the normal of those planes and the Burgers vector $\mathbf{b}$.

Dislocation ($\mathbf{b}$)	Segment no.	Length (nm)	Plane	$\angle(n,b)$
$\frac{1}{3}[\bar{2}110]$	1 (no.1)	398	$(31\bar{4}0)$	$44°$
$\frac{1}{3}[\bar{2}110]$	1 (no.2)	1409	$(31\bar{4}1)$	$45°$
$\frac{1}{3}[\bar{2}110]$	1 (no.3)	1215	$(2\,\overline{12}\,10\,\overline{11})$	$52°$
$\frac{1}{3}[\bar{2}110]$	1 (no.4)	527	$(\bar{2}021)$	$36°$
$\frac{1}{3}[1\bar{2}10]$	2 (no.1)	1327	$(10\bar{1}0)$	$90°$
$\frac{1}{3}[1\bar{2}10]$	2 (no.2)	619	$(1\bar{3}20)$	$11°$

Continued on next page

Table 4.1 continued from previous page

Dislocation $(\mathbf{b})$	Segment no.	Length (nm)	Plane	$\angle(n, b)$
$\frac{1}{3}[1\bar{2}10]$	2 (no.3)	943	$(12\bar{3}2)$	$56°$
$\frac{1}{3}[1\bar{2}10]$	3 (no.1)	1116	$(11\,1\,\bar{1}\bar{2}\,3)$	$86°$
$\frac{1}{3}[1\bar{2}10]$	3 (no.2)	430	$(1\bar{5}4\bar{2})$	$27°$
$\frac{1}{3}[1\bar{2}10]$	3 (no.3)	987	$(35\bar{8}1)$	$52°$
$\frac{1}{3}[1\bar{2}10]$	4	1187	$(10\bar{1}0)$	$90°$
$\frac{1}{3}[1\bar{2}10]$	5 (no.1)	611	$(01\bar{1}0)$	$30°$
$\frac{1}{3}[1\bar{2}10]$	5 (no.2)	756	$(31\bar{4}0)$	$76°$
$\frac{1}{3}[1\bar{2}10]$	5 (no.3)	352	$(02\bar{2}3)$	$56°$
$\frac{1}{3}[1\bar{2}10]$	6	388	$(42\bar{6}\bar{1})$	$71°$
$\frac{1}{3}[1\bar{2}10]$	7 (no.1)	493	$(\bar{1}\bar{1}\,6\,5\,4)$	$59°$
$\frac{1}{3}[1\bar{2}10]$	7 (no.2)	542	$(4\bar{5}1\bar{1})$	$21°$
$\frac{1}{3}[1\bar{2}10]$	7 (no.3)	334	$(22\bar{4}\bar{3})$	$66°$
$\frac{1}{3}[1\bar{2}10]$	8	1126	$(\bar{1}011)$	$90°$
$\frac{1}{3}[1\bar{2}10]$	9	1069	$(10\bar{1}0)$	$90°$
$\frac{1}{3}[1\bar{2}10]$	10	1125	$(10\bar{1}0)$	$90°$
$\frac{1}{3}[1\bar{2}10]$	11	937	$(10\bar{1}0)$	$90°$
$\frac{1}{3}[1\bar{2}10]$	12	1141	$(10\bar{1}0)$	$90°$
$\frac{1}{3}[11\bar{2}0]$	13	878	$(\bar{3}120)$	$49°$
$\frac{1}{3}[11\bar{2}0]$	14 (no.1)	297	$(40\bar{4}\bar{3})$	$42°$
$\frac{1}{3}[11\bar{2}0]$	14 (no.2)	656	$(12\bar{3}4)$	$51°$

Continued on next page

Table 4.1 continued from previous page

Dislocation ($\mathbf{b}$)	Segment no.	Length (nm)	Plane	$\angle(n, b)$
$\frac{1}{3}[11\bar{2}0]$	15	1141	$(35\bar{8}1)$	$10°$
$\frac{1}{3}[11\bar{2}0]$	18	274	$(11\bar{2}0)$	$0°$
$\frac{1}{3}[11\bar{2}0]$	19	438	$(5\bar{1}\bar{4}2)$	$44°$
$\frac{1}{3}[11\bar{2}0]$	20 (no.1)	370	$(01\bar{1}0)$	$30°$
$\frac{1}{3}[11\bar{2}0]$	20 (no.2)	619	$(21\bar{3}1)$	$20°$
$\frac{1}{3}[11\bar{2}0]$	21 (no.1)	551	$(1\bar{5}4\bar{2}))$	$44°$
$\frac{1}{3}[11\bar{2}0]$	21 (no.2)	716	$(\bar{7}431)$	$65°$
$\frac{1}{3}[11\bar{2}0]$	21 (no.3)	375	$(2\bar{6}41)$	$50°$
$\frac{1}{3}[11\bar{2}0]$	22 (no.1)	759	$(\bar{6}241)$	$50°$
$\frac{1}{3}[11\bar{2}0]$	22 (no.2)	1024	$(41\bar{5}\bar{1})$	$21°$
$\frac{1}{3}[11\bar{2}0]$	23 (no.1)	1486	$(21\bar{3}0)$	$11°$
$\frac{1}{3}[11\bar{2}0]$	23 (no.2)	696	$(11\bar{2}1)$	$25°$
$\frac{1}{3}[11\bar{2}0]$	23 (no.3)	683	$(1\bar{2}1\bar{1})$	$63°$
$\frac{1}{3}[11\bar{2}0]$	23 (no.4)	1086	$(4\bar{5}1\bar{1})$	$79°$
$\frac{1}{3}[11\bar{2}0]$	24 (no.1)	480	$(\bar{2}021)$	$36°$
$\frac{1}{3}[11\bar{2}0]$	24 (no.2)	483	$(\bar{1}102)$	$90°$
$\frac{1}{3}[11\bar{2}0]$	25 (no.2)	600	$(16\bar{7}2)$	$26°$
$\frac{1}{3}[11\bar{2}0]$	25 (no.3)	733	$(31\bar{4}0)$	$16°$
$\frac{1}{3}[11\bar{2}0]$	25 (no.4)	407	$(\bar{2}110)$	$60°$
$\frac{1}{3}[11\bar{2}0]$	26 (no.1)	1146	$(5\,9\,\bar{1}\bar{4}\,\bar{6})$	$23°$

Continued on next page

Table 4.1 continued from previous page

Dislocation ($\mathbf{b}$)	Segment no.	Length (nm)	Plane	$\angle(n, b)$
$\frac{1}{3}[11\bar{2}0]$	26 (no.2)	409	$(4\,\bar{1}4\,10\,1)$	$46°$
$\frac{1}{3}[11\bar{2}0]$	27	405	$(10\bar{1}0)$	$30°$
$\frac{1}{3}[11\bar{2}0]$	28	422	$(02\bar{2}3)$	$56°$
$\frac{1}{3}[11\bar{2}0]$	29	625	$(1\bar{1}00)$	$90°$
$\frac{1}{3}[11\bar{2}0]$	30	880	$(1\bar{1}01)$	$90°$
$\frac{1}{3}[11\bar{2}0]$	31	839	$(1\bar{1}00)$	$90°$
$\frac{1}{3}[11\bar{2}0]$	32	481	$(1\bar{1}00)$	$90°$
$\frac{1}{3}[\bar{2}113]$	33 (no.1)	403	$(31\bar{4}2)$	$42°$
$\frac{1}{3}[\bar{2}113]$	33 (no.2)	964	$(31\bar{4}\bar{4})$	$83°$
$\frac{1}{3}[\bar{2}113]$	33 (no.3)	304	$(10\bar{1}0)$	$54°$
$\frac{1}{3}[1\bar{2}13]$	34 (no.1)	304	$(\bar{4}221)$	$81°$
$\frac{1}{3}[1\bar{2}13]$	34 (no.2)	246	$(10\bar{1}0)$	$90°$
$\frac{1}{3}[1\bar{2}13]$	35 (no.1)	640	$(10\bar{1}0)$	$90°$
$\frac{1}{3}[1\bar{2}13]$	35 (no.2)	211	$(10\bar{1}2)$	$51°$
$\frac{1}{3}[1\bar{2}13]$	36	1430	$(5\,\bar{1}2\,7\,1)$	$44°$
$\frac{1}{3}[1\bar{2}13]$	37	856	$(4\bar{5}1\bar{1})$	$60°$
$\frac{1}{3}[1\bar{2}13]$	38 (no.1)	592	$(1\,\bar{1}4\,13\,3)$	$44°$
$\frac{1}{3}[1\bar{2}13]$	38 (no.2)	772	$(1\bar{3}20)$	$49°$
$\frac{1}{3}[1\bar{2}13]$	39 (no.1)	234	$(\bar{2}110)$	$70°$
$\frac{1}{3}[1\bar{2}13]$	39 (no.2)	803	$(11\bar{2}2)$	$75°$

Continued on next page

Table 4.1 continued from previous page

Dislocation ($\mathbf{b}$)	Segment no.	Length (nm)	Plane	$\angle(n, b)$
$\frac{1}{3}[1\bar{2}13]$	39 (no.3)	290	$(\bar{2}110)$	$70°$
$[0001]$	40 (no.1)	423	$(02\bar{2}1)$	$68°$
$[0001]$	40 (no.2)	260	$(40\bar{4}1)$	$79°$
$[0001]$	40 (no.3)	778	$(1\bar{2}1\bar{3})$	$36°$
$[0001]$	41	923	$(14\bar{5}3)$	$63°$

Table 4.2: List of dislocations where Burgers vector and habit planes have been characterized in the MT specimen (Figures 42 and 44). The last column reports the angle between the normal of those planes and the Burgers vector $\mathbf{b}$.

Dislocation ($\mathbf{b}$)	Segment no.	Length (nm)	Plane	$\angle(n, b)$
$\frac{1}{3}[\bar{2}110]$	1	137	$(10\bar{1}\bar{3})$	$71°$
$\frac{1}{3}[\bar{2}110]$	2	155	$(01\bar{1}1)$	$90°$
$\frac{1}{3}[\bar{2}110]$	3	132	$(01\bar{1}\bar{2})$	$90°$
$\frac{1}{3}[\bar{2}110]$	4	289	$(\bar{7}251)$	$16°$
$\frac{1}{3}[\bar{2}110]$	5 (no.1)	671	$(\bar{1}2\bar{1}\bar{2})$	$68°$
$\frac{1}{3}[\bar{2}110]$	5 (no.2)	568	$(5\bar{3}\bar{2}1)$	$12°$
$\frac{1}{3}[\bar{2}110]$	5 (no.3)	962	$(1\bar{3}25)$	$80°$
$\frac{1}{3}[\bar{2}110]$	6	248	$(0\bar{1}\bar{1}2)$	$90°$
$\frac{1}{3}[\bar{2}110]$	7 (no.1)	326	$(4\bar{3}\bar{1}1)$	$20°$
$\frac{1}{3}[\bar{2}110]$	7 (no.2)	397	$(\bar{3}211)$	$20°$
$\frac{1}{3}[\bar{2}110]$	8	438	$(\bar{2}110)$	$0°$
$\frac{1}{3}[\bar{2}110]$	9	203	$(6\bar{5}\bar{1}3)$	$31°$

Continued on next page

Table 4.2 continued from previous page

Dislocation $(\mathbf{b})$	Segment no.	Length (nm)	Plane	$\angle(n, b)$
$\frac{1}{3}[\bar{2}110]$	10	388	$(52\bar{7}\bar{6})$	$56°$
$\frac{1}{3}[11\bar{2}0]$	11	266	$(\bar{5}\,6\,\bar{1}\,\bar{1}\,1)$	$60°$
$\frac{1}{3}[1\bar{2}10]$	12	312	$(\bar{1}011)$	$90°$
$\frac{1}{3}[1\bar{2}10]$	13	273	$(1\bar{3}20)$	$11°$
$\frac{1}{3}[1\bar{2}10]$	14	414	$(15\bar{6}\bar{3})$	$44°$
$\frac{1}{3}[1\bar{2}10]$	15 (no.1)	493	$(1\bar{1}01)$	$47°$
$\frac{1}{3}[1\bar{2}10]$	15 (no.2)	227	$(\bar{1}\bar{2}33)$	$61°$
$\frac{1}{3}[1\bar{2}10]$	15 (no.3)	130	$(13\bar{4}\bar{2})$	$49°$
$\frac{1}{3}[1\bar{2}10]$	16	245	$(\bar{5}7\bar{2}1)$	$16°$
$\frac{1}{3}[1\bar{2}10]$	17	75	$(\bar{2}02\bar{1})$	$90°$
$\frac{1}{3}[1\bar{2}10]$	18	435	$(\bar{1}01\bar{1})$	$90°$
$\frac{1}{3}[1\bar{2}10]$	19	883	$(5\bar{8}32)$	$15°$
$\frac{1}{3}[11\bar{2}0]$	20	999	$(1\bar{1}0\bar{1})$	$90°$
$\frac{1}{3}[11\bar{2}0]$	21	244	$(2\bar{2}0\bar{1})$	$90°$
$\frac{1}{3}[11\bar{2}0]$	22	349	$(1\bar{1}0\bar{2})$	$90°$
$\frac{1}{3}[11\bar{2}0]$	23	812	$(1\bar{1}0\bar{1})$	$90°$
$\frac{1}{3}[11\bar{2}0]$	24	467	$(2\bar{2}0\bar{1})$	$90°$
$\frac{1}{3}[\bar{2}113]$	25	517	$(2\bar{3}10)$	$64°$
$\frac{1}{3}[\bar{2}113]$	26 (no.1)	450	$(\bar{2}\bar{2}43)$	$74°$
$\frac{1}{3}[\bar{2}11\bar{3}]$	26 (no.2)	413	$(13\bar{4}3)$	$52°$

Continued on next page

Table 4.2 continued from previous page

Dislocation $(\mathbf{b})$	Segment no.	Length (nm)	Plane	$\angle(n, b)$
$\frac{1}{3}[\bar{2}11\bar{3}]$	26 (no.3)	240	$(\bar{2}7\bar{5}3)$	$85°$
$\frac{1}{3}[\bar{2}11\bar{3}]$	26 (no.4)	826	$(11\bar{2}\bar{1})$	$90°$
$\frac{1}{3}[11\bar{2}3]$	27 (no.1)	504	$(1\bar{1}01)$	$63°$
$\frac{1}{3}[11\bar{2}3]$	27 (no.2)	876	$(4\bar{3}\bar{1}1)$	$72°$
$\frac{1}{3}[11\bar{2}3]$	28	345	$(\bar{1}01\bar{1})$	$90°$
$\frac{1}{3}[11\bar{2}3]$	29	286	$(4\bar{1}\bar{3}1)$	$81°$
$[0001]$	30	249	$(31\bar{4}1)$	$78°$
$[0001]$	31	1124	$(2\bar{1}\bar{1}0)$	$90°$
$[0001]$	32	101	$(1\bar{1}00)$	$90°$

4.1.3.2 Glide Mechanism

4.1.3.2.1 MCT specimen In this specimen, we found evidence of $\langle a\rangle$ and $\langle c+a\rangle$ glide in prismatic $\{1\bar{1}00\}$ planes, and also of $\langle a\rangle$ glide in pyramidal $\{1\bar{1}01\}$ planes and in a $(1\bar{1}02)$ pyramidal plane. An example of tomographic reconstruction of a typical domain is shown in Figure 41. The Burgers vector indexing shows the presence of dislocations with $\frac{1}{3}[1\bar{2}10]$ (or a_2) and $\frac{1}{3}[1\bar{2}13]$ (or $c-a_2$) Burgers vectors, drawn in light and dark green, respectively. The reconstructed dislocation volumes can be tilted to view the planes containing these dislocations edge-on. Figures 41(a)-(c), show an a_2 dislocation lying near the prismatic $(10\bar{1}0)$ plane. This demonstrates activation of the $\frac{1}{3}[1\bar{2}10](10\bar{1}0)$ slip system. A slightly more complex configuration is detailed in Figures 41(d)-(f). Part of this dislocation is in the $(10\bar{1}0)$ glide plane. Moreover, a collinear interaction (Madec et al. 2003; Mussi et al. 2015a) with an a_2 sessile dislocation loop can be clearly identified. The plane of this loop is edge-on for a projection angle of $-18°$ (Figure 41(f)). The 3D geometry of this dislocation is due to this interaction. From Figures 41(g)-(i), we also characterize the $\frac{1}{3}[1\bar{2}13](10\bar{1}0)$ slip system.

4.1.3.2.2 MT Specimen The MT specimen also shows dislocations in glide configurations. We found evidence for glide of $\langle a\rangle$, $[c]$ and $\langle c+a\rangle$ dislocations. In this specimen, no prismatic

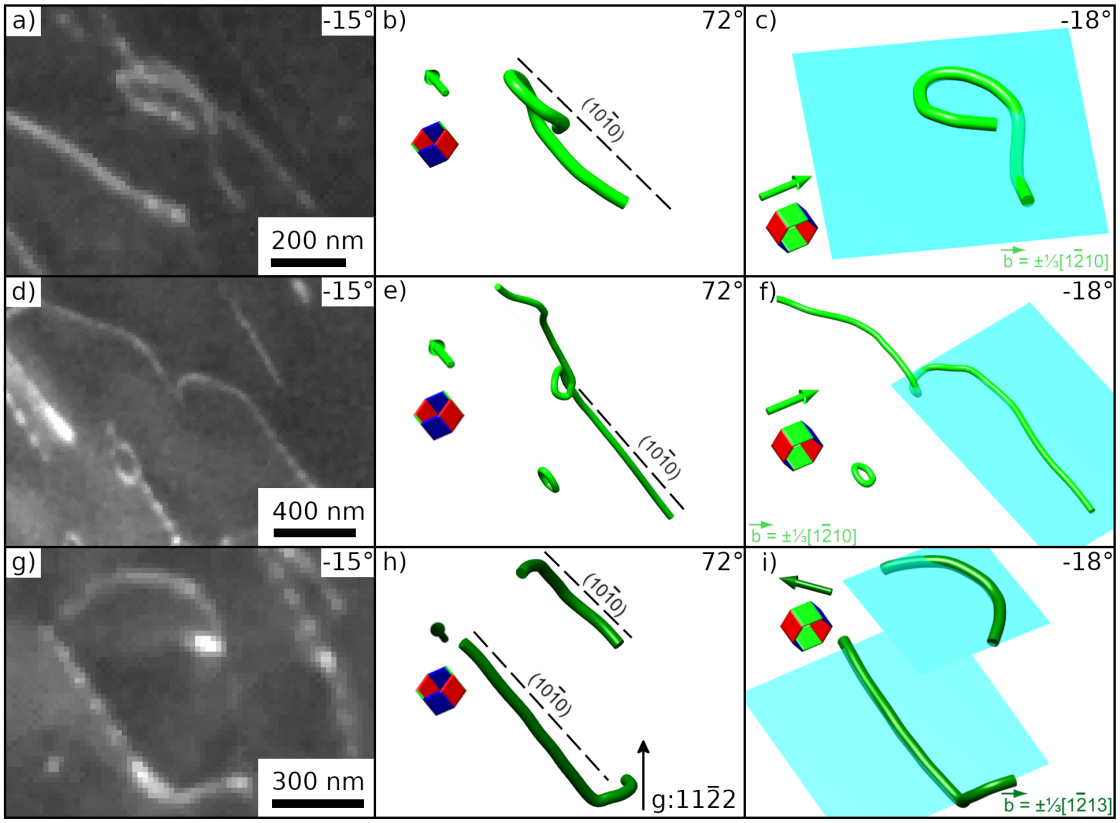

Figure 41: Slip system characterizations by dislocation electron tomography for the MCT specimen, obtained with the $11\bar{2}2$ diffraction vector: (a) Raw WBDF micrograph of an a_2 dislocation observed along a projection angle of $-15°$; (b) reconstructed volume of this dislocation (coloured in green) for a projection angle of $72°$ where the prismatic $(10\bar{1}0)$ plane is edge-on; (c) same reconstructed dislocation with a projected angle of $-18°$; (d) raw WBDF micrograph of two a_2 dislocations (a dislocation loop and a complex 3D dislocation) observed along a projection angle of $-15°$; (e) reconstructed volume of these dislocations for a projection angle of $72°$; (f) same reconstructed dislocations with a projected angle of $-18°$; (g) raw WBDF micrograph of 3D $c - a_2$ dislocations observed along a projection angle of $-15°$; (h) reconstructed volume of these dislocations (coloured in dark green) for a projection angle of $72°$; (i) same reconstructed dislocations with a projected angle of $-18°$. The $\frac{1}{3}[\bar{1}2\bar{1}0](10\bar{1}0)$ and $\frac{1}{3}[1\bar{2}13](10\bar{1}0)$ slip systems have been characterized in this figure.

glide has been observed for $\langle a \rangle$ and $\langle c+a \rangle$ dislocations; only $[c]$ dislocations in $(1\bar{1}00)$ and $(\bar{2}110)$ glide planes have been characterized. $\langle a \rangle$ dislocations appear to glide predominantly in $\{1\bar{1}01\}$ pyramidal planes. We have also noted evidence for $\langle a \rangle$ glide in $\{1\bar{1}02\}$ and $\{2\bar{2}01\}$, and $\langle c+a \rangle$ glide in $\{\bar{1}01\bar{1}\}$, $\{11\bar{2}\bar{1}\}$, $\{11\bar{2}2\}$ and $\{21\bar{3}\bar{1}\}$. Glide in $\{1\bar{1}01\}$ represents approximately $3/7$ of all glide in this specimen. An example of a slip system characterization is shown in Figures 42(a)-(d). The pyramidal $(11\bar{2}\bar{1})$ plane is edge-on with a projection angle of $14°$. The direction of the trace of this plane corresponds to the direction of the dislocation line with a projection that is rectilinear, as its movement plane is edge-on (Figure 42(b)). The $\frac{1}{3}[2\bar{1}\bar{1}3](11\bar{2}\bar{1})$ slip system has been identified given that the Burgers vector of this dislocation is $c+a_1$. We have also identified the $[0001](2\bar{1}\bar{1}0)$ slip system (Figures 42(e)-(h)).

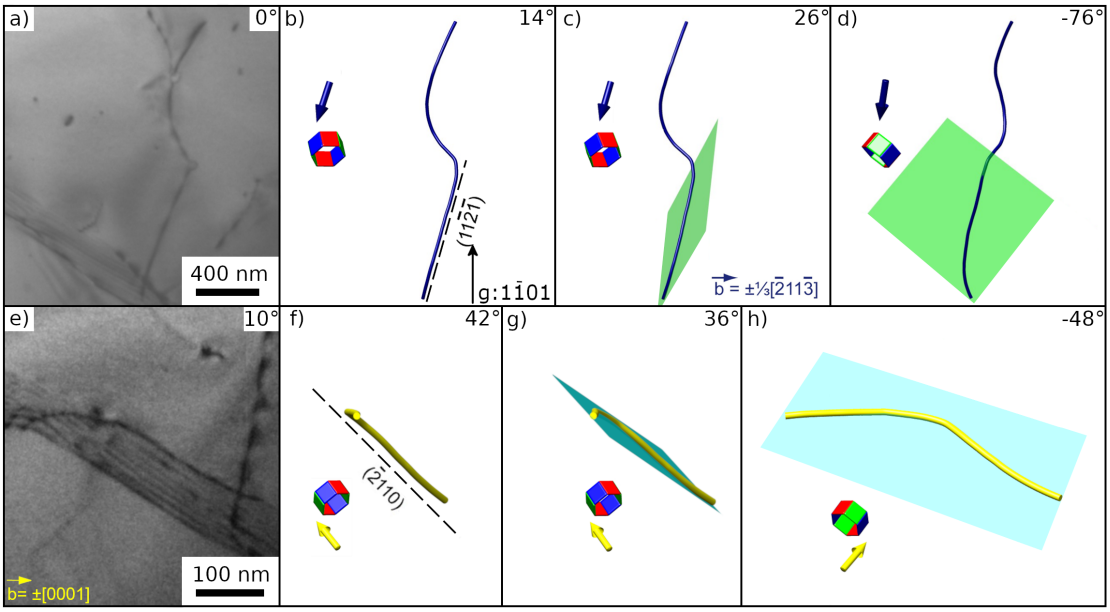

Figure 42: Slip system characterizations revealed by dislocation electron tomography, obtained with the $1\bar{1}01$ diffraction vector, in the MT specimen: (a) Raw WBDF micrograph of a $c+a_1$ dislocation observed along a projection angle of $0°$; (b) reconstructed volume of this dislocation (colored in dark blue) for a projection angle of $14°$ where the pyramidal $(11\bar{2}\bar{1})$ plane is nearly edge-on; (c) same reconstructed dislocation with a projected angle of $26°$ (green plane shows the habit plane of the dislocation segment); (d) same reconstruction with a projected angle of $-76°$ (the normal to the pyramidal plane is edge-on); (e) raw WBDF micrograph of a $[c]$ dislocation observed along a projection angle of $10°$; (f) reconstructed volume of this dislocation (colored in yellow) for a projection angle of $42°$ where the prismatic $(\bar{2}110)$ plane is edge-on; (g) same reconstructed dislocations with a projected angle of $36°$; (h) same reconstruction with a projected angle of $-48°$ (the normal to the prismatic plane is edge-on). The $1/3[\bar{2}11\bar{3}](11\bar{2}\bar{1})$ and $[0001](\bar{2}110)$ slip systems have been characterized in this figure.

4.1.3.3 Climb Mechanism

4.1.3.3.1 MCT Specimen A significant proportion of the dislocation population cannot be interpreted as resulting from glide (i.e., lying in a plane which contains the Burgers vector). For instance, Figures 43(a)-(c) show a $1/3[11\bar{2}0]$ dislocation (a_3) in a $(11\bar{2}0)$ plane. This corresponds to a prismatic loop in pure climb configuration. A complex 3D dislocation (Figures 43(d)-(f)) has been analysed where one of its segments is practically in pure climb configuration (Figure 43(f)) and three other segments are neither in pure climb nor in pure glide configurations. In other words, the Burgers vector of this dislocation makes an angle with the plane containing each segment under consideration with values between 0 and 90° (such as in Figure 20). These configurations are characterized as mixed climb, as kinematically described in section 4.1.2.3. We also note that this dislocation shows colinear climb interaction with a prismatic loop. Figures 43(g)-(i) show an example of mixed climb, which involves a $c - a_2$ dislocation. Of all dislocations analyzed in the MCT specimen, approximately $3/5$ are of mixed climb character (considering the lengths of the dislocation segments).

4.1.3.3.2 MT Specimen We find the same results for the MT specimen as for the MCT specimen, with a significant proportion, around half of dislocations in mixed climb configurations. (Figures 44(d)-(f) and 44(g)-(i)). An example of a small dislocation loop in a pure climb configuration has also been found (Figures 44(a)-(c)).

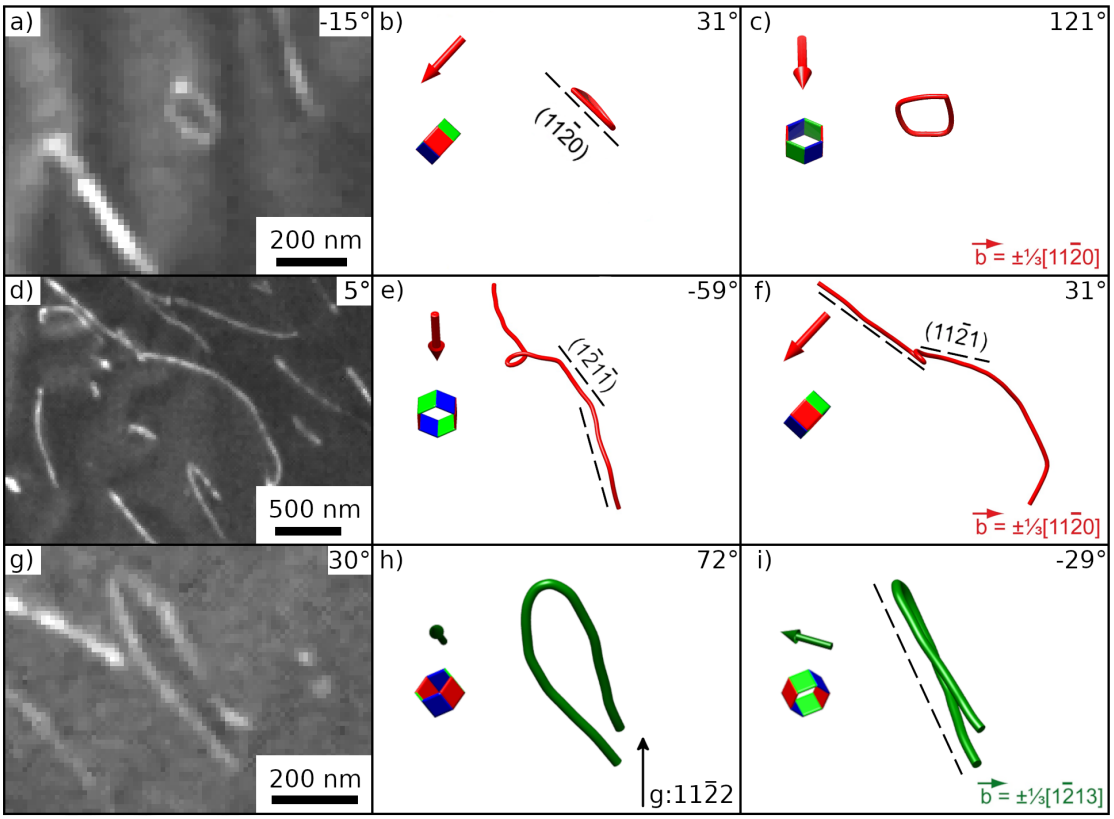

Figure 43: Climb characterizations revealed by dislocation electron tomography, obtained with the $11\bar{2}2$ diffraction vector, for specimen MCT: (a) Raw WBDF micrograph of a a_3 dislocation observed along a projection angle of $-15°$; (b) reconstructed volume of this dislocation (colored in red) for a projection angle of $31°$ where the prismatic $(11\bar{2}0)$ plane is edge-on; (c) same reconstructed dislocation with a projected angle of $121°$; (d) raw WBDF micrograph of another geometrically complex a_3 dislocation observed along a projection angle of $5°$; (e) reconstructed volume of this dislocation for a projection angle of $-59°$ where the pyramidal $(1\bar{2}1\bar{1})$ plane is edge-on; (f) the same dislocation with a projected angle of $31°$ where the pyramidal $(11\bar{2}1)$ plane is edge-on; (g) raw WBDF micrograph of a $c - a_2$ dislocation observed along a projection angle of $30°$; (h) the reconstructed volume of this dislocation (colored in dark green) for a projection angle of $72°$; (i) the same reconstructed dislocation with a projected angle of $-29°$ for which its plane is edge-on. The $1/3[11\bar{2}0](11\bar{2}0)$ pure climb system and the $1/3[11\bar{2}0](11\bar{2}1)$ and $1/3[11\bar{2}0](1\bar{2}1\bar{1})$ mixed climb systems have been characterized in this figure.

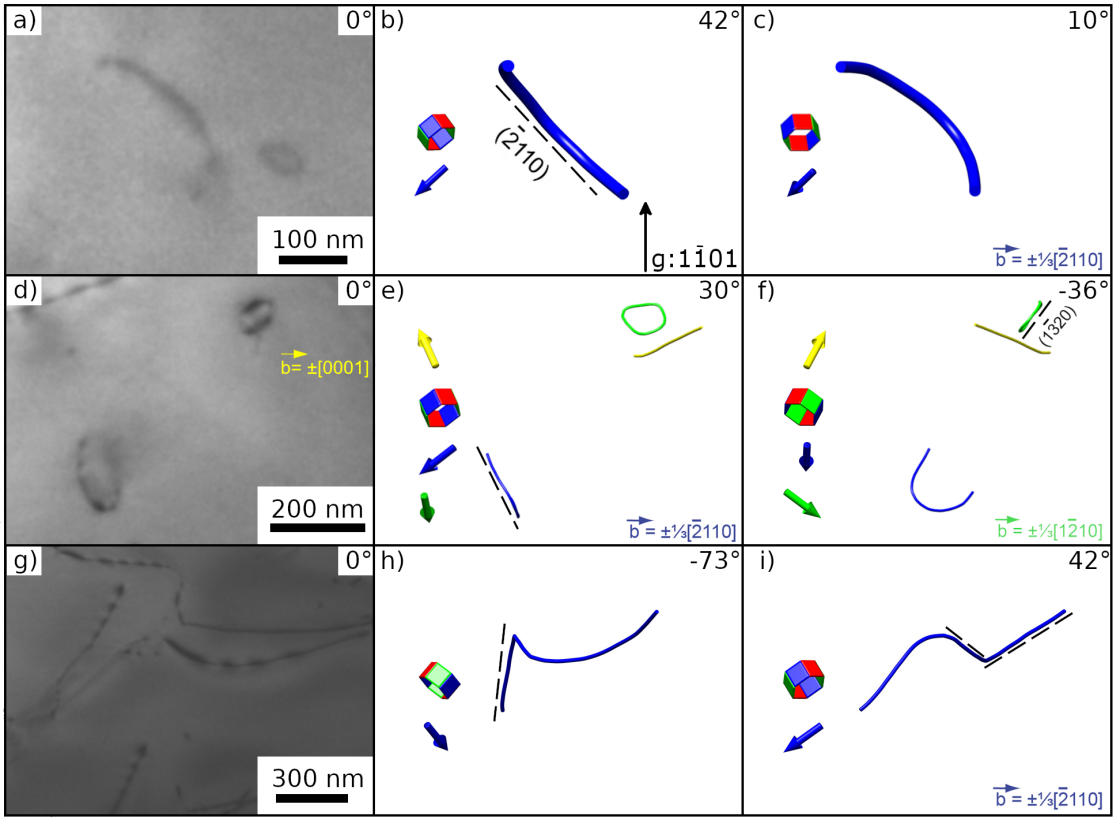

Figure 44: Characterizations of dislocation climb revealed by dislocation electron tomography, obtained with the $1\bar{1}01$ diffraction vector, for the MT specimen: (a) Raw WBDF micrograph of a a_1 dislocation observed along a projection angle of $0°$; (b) reconstructed volume of this dislocation (colored in blue) for a projection angle of $42°$ for which the prismatic $(\bar{2}110)$ plane is edge-on; (c) same reconstructed dislocation with a projected angle of $10°$; (d) raw WBDF micrograph of a_1, a_2 and c dislocations observed along a projection angle of $0°$; (e) reconstructed volume of these dislocations (colored in blue, green, and yellow respectively) for a projection angle of $30°$ where the habit plane of the a_1 dislocation loop is edge-on; (f) same reconstructed dislocations with a projected angle of $-36°$ where the prismatic $(1\bar{3}20)$ plane is edge-on (corresponding to the habit plane of the a_2 dislocation loop); (g) raw WBDF micrograph of a $\langle c-a_2\rangle$ complex dislocation observed along a projection angle of $0°$; (h) reconstructed volume of this dislocation for a projection angle of $-73°$ where the habit plane of a part of this dislocation is edge-on; (i) same reconstructed dislocation with a projected angle of $42°$ where the last two parts of this dislocation are edge-on. The $1/3[\bar{2}110](\bar{2}110)$ pure climb system and the $1/3[1\bar{2}10](1\bar{3}20)$ mixed climb system have been characterized in this figure.

4.1.3.4 Strain analysis from electron tomography data

The plastic strain inferred for the motion of each dislocation segment has been calculated based on the relations provided in section 4.1.2.3. We have considered, for each specimen, (1) the segments that correspond to pure glide ($\theta = 0$) only, (2) the segments in pure climb configurations ($\theta = 90°$) only, (3) all glide components of the segments (i.e., including pure glide segments and the glide contribution of segments in mixed climb configurations), and (4) all climb components (i.e., pure climb segments and the climb contributions of segments in mixed climb configurations). In all cases except in the case of pure climb, the set of available dislocations is sufficient to provide five independent strain components at the grain scale. Thus, the observed dislocation microstructure can accommodate any deformation. The Schmid tensors, either for glide or for climb, are full matrices in which no specific component dominates. As an illustrative example, we provide below the sum of all glide or climb individual Schmid tensors weighted by their corresponding relative dislocation length. This gives, expressed in crystal axes:

For SG10:

$$\bar{\mathbf{S}}^g = \begin{bmatrix} -0.061 & -0.042 & 0.152 \\ -0.042 & 0.067 & 0.090 \\ 0.152 & 0.090 & -0.006 \end{bmatrix}$$

$$\bar{\mathbf{S}}^c = \begin{bmatrix} 0.158 & -0.067 & 0.014 \\ -0.067 & -0.052 & -0.006 \\ 0.014 & -0.006 & -0.106 \end{bmatrix}$$

For S09:

$$\bar{\mathbf{S}}^g = \begin{bmatrix} -0.090 & 0.035 & -0.007 \\ 0.035 & 0.044 & 0.010 \\ -0.007 & 0.010 & 0.046 \end{bmatrix}$$

$$\bar{\mathbf{S}}^c = \begin{bmatrix} -0.058 & 0.113 & -0.021 \\ 0.113 & 0.301 & 0.094 \\ -0.021 & 0.094 & -0.243 \end{bmatrix}$$

The associated equivalent Schmid tensors, $\bar{S}^g_{eq} = (\bar{S}^g_{ii})^{1/2}$ for all glide contributions and $\bar{S}^c_{eq} = (\bar{S}^c_{ii})^{1/2}$ for all climb contributions, have similar values, about 0.2 for MT for both glide and climb. Somewhat smaller values are obtained for glide (≈ 0.1) than for climb (≈ 0.4) for the MCT specimen.

4.1.4 Discussion

4.1.4.1 Slip systems

In our specimens, dislocations observed are mostly of the $\langle a \rangle$ and $\langle c+a \rangle$ types with only a few $[c]$ dislocations observed in the MT specimen. Active slip systems in quartz have been constrained by many experimental studies (Baeta and Ashbee 1969; Hobbs 1968; Morrison-Smith et al. 1976) and their activities have been shown to depend strongly on temperature. Below 700°C, $\langle a \rangle$ basal glide dominates. Above 700°C, glide becomes progressively more active in pyramidal $\{1\bar{1}0n\}$ with $n = 0, 1, 2, 3$, and then on prismatic planes. Above 750°C, $\langle c+a \rangle$ dislocations are activated which glide in $\{1\bar{1}01\}$ and $\{11\bar{2}n\}$ with $n = 1, 2$ and then $[c]$ glide on prism planes. Under geological conditions of strain-rate and deviatoric stress, the same sequence is assumed to be valid with the activation of $[c]$ glide starting at 600-650°C (Mainprice et al. 1986; Okudaira et al. 1995). Mainprice et al. (1986) also point out that the activation of $[c]$ glide is favoured by wet conditions, which is the case in our specimens. Our observations are thus consistent with this transition sequence where $\langle a \rangle$ basal glide is not active, $[c]$ glide is of marginal importance, and $\langle a \rangle$ slip occurs predominantly on pyramidal and prismatic planes. The only remarkable observation is the widespread activation of $\langle c+a \rangle$ glide in the $\{10\bar{1}0\}$, $\{10\bar{1}1\}$, $\{11\bar{2}n\}$ ($n = 1, 2$) and even $\{21\bar{3}1\}$ (not previously reported) planes. Glide along $\langle c+a \rangle$ is generally expected at high temperatures (Baeta and Ashbee 1969). However, while $\langle c+a \rangle$ glide is reported in the literature, it has been the subject of far fewer detailed observational studies than $\langle a \rangle$ and $[c]$ glide, particularly in natural specimens. $\langle c+a \rangle$ dislocations were previously observed in a Bohemian granulite (Mussi et al. 2021c). Yet in many studies that depend on extracting geometrically necessary dislocation densities from EBSD measurements (Wallis et al. 2019) or modelling crystal preferred orientations (e.g., Keller and Stipp 2011; Morales et al. 2011), $\langle c+a \rangle$ glide has been neglected. General strains can be explained by assuming activation of other systems, but such suppositions are contrary to the results of this study.

4.1.4.2 Mixed climb

The most important observation of this study is the significant activation of climb over a wide range of middle to deep crustal temperatures and tectonic strain rates. Besides some evidence for dislocations in pure climb configuration, we found pervasive evidence of mixed climb (Carrez et al. 2024) of $\langle a \rangle$ and $\langle c+a \rangle$ dislocations. The long-standing problem of achieving general strains and satisfying the von Mises-Taylor criterion can be solved for quartz either by

activation of $\langle c+a \rangle$ glide, or climb. We show here that both operate together with $\langle c+a \rangle$ dislocations that exhibit mixed climb geometries. Moreover, we show that the contribution of glide produced by the observed microstructures is sufficient to accommodate any arbitrary strain. Hence, activation of climb is not necessary to provide additional strain components. However, we show that climb provides an additional contribution to strain comparable to that of glide.

Activation of dislocation climb in quartz has been recognized for many decades (White 1977), especially under wet conditions when internal water contents exceed the solubility limit of water-related defects (Cordier et al. 1989; Kirby and McCormick 1979; McLaren et al. 1989). Climb is generally inferred by the absence of apparent lattice friction (curved and entangled dislocations) and by the presence of sub-grain boundaries (Baeta and Ashbee 1973; Ball and Glover 1979), as found in our two specimens. It is always considered a recovery mechanism (Tullis and Yund 1989). Indeed, dislocation creep is usually described within the framework of Weertman (1968) creep where the strain is produced by dislocation glide whose resulting hardening is counterbalanced by a recovery mechanism, generally involving dislocation climb. It is implicit that dislocation glide produces most of the strain, while climb produces little strain but controls the strain-rate. This means that the glide velocity is supposed to be much greater (several orders of magnitude greater) than the climb velocity. On this basis, Boioli et al. (2015a) modelled creep in olivine above 1400 K with a glide velocity more than a thousand times faster than the climb velocity under low stress.

Our observation of pervasive mixed glide and climb with movement planes taking any orientation between pure glide and pure climb in quartz mylonites of the MCT and MT (Figure 45) suggests that velocities of dislocation glide and climb were comparable. In this case, climb and glide are both strain-producing mechanisms. Such mixed climb motions may be difficult to recognize without the characterization of both Burgers vectors and dislocation lines. However, we may well wonder whether this mechanism can be inferred from less detailed observations.

Early studies of deformation lamellae in quartz deformed in laboratory experiments (Blacic 1975; Christie et al. 1964; Hobbs 1968; Tullis et al. 1973) and under natural, crustal conditions (e.g., McLaren and Hobbs 1972; Sylvester 1969) were taken as evidence of slip on basal and prismatic planes. However, these planar optical features commonly occur at angles of up to $15-30°$C from rational crystallographic planes perpendicular and parallel to c (Christie and Ardell 1974; Heard and Carter 1968; Hobbs 1968; Tullis et al. 1973). Characterized optically by their anomalous refractive index, deformation lamellae observed by TEM were found to consist of lamellar zones of highly tangled dislocations rather than simple arrays of

free dislocations in their anticipated slip planes (Christie and Ardell 1976). Detailed TEM diffraction analysis of the tangled dislocations within these lamellae has not been possible. Nevertheless, Vernooij (2005) posed the hypothesis that orientations of deformation lamellae, like slip bands, reveal directions of dislocation motion, and therefore give relative velocities of glide within basal and prism planes, and climb out of these planes. Heard and Carter (1968) showed that non-basal deformation lamellae are favoured by high temperature (and low strain rate), as may be expected for higher climb velocities at higher temperatures. Misorientations of deformation lamellae may therefore result from some climb accompanying glide. Still, the tangled nature of dislocations within lamellar regions of early experiments indicates that climb was insufficient for significant recovery.

Much higher rates of dislocation climb and recovery are evident from the microstructures of MT and MCT quartzites and the DET analyses of this study. Compiling our results for these natural quartz shear zone specimens, Table 4.3 summarizes length-weighted proportions of dislocations found in glide, pure climb, and mixed glide-climb orientations.

Table 4.3: Proportion of dislocation segments in glide, pure climb and mixed climb configuration for each specimen.

	MCT specimen		MT specimen	
% Glide (without straight dislocation segments)	9		16	
% Pure Climb (without straight dislocation segments)	1	91	3	84
% Mixed Climb (without straight dislocation segments)	90		81	
% Glide (with straight dislocation segments)	38		51	
% Pure Climb (with straight dislocation segments)	1	62	2	49
% Mixed Climb (with straight dislocation segments)	61		47	

Glide-producing dislocation lines constitute approximately 38% of the total in the MCT specimen and approximately 50% for the MT specimen. More than half of the total dislocation line lengths analyzed involve some climb (pure or mixed) component in both specimens. Considering the length of each dislocation segment and measuring the angle between the Burgers vector and normal vector to each plane of motion ($(\hat{n,b})$), histograms can be plotted for all dislocation segments to quantify the climb contribution for each kind of Burgers vector. The $(\hat{n,b})$ angle ranges from 0° for pure climb to 90° for glide configurations (see Figure 45). Figures 45(a) and 45(c) describe the climb distribution of the MCT specimen without and

with rectilinear dislocation segments, respectively. Similarly, Figures 45(b) and 45(d) show the climb distributions for MT specimens without and with rectilinear dislocation segments, respectively. These histograms show no significant difference between dislocation microstructures in specimens MCT and MT. $\langle a \rangle$ dislocations are found most often in climb or mixed climb orientations.

Our calculations (section 4.1.3.4) for both MT and MCT specimens indicate that plastic strains produced by climb are of the same order of magnitude (possibly larger for the MCT specimen) as produced by glide. This is an important observation, as it bears on interpretations of Crystallographic Preferred Orientation (CPO) of rock deformed by dislocation creep. In recent studies, deformation is taken to be due to glide on the $\langle a \rangle$ basal system, then $\langle a \rangle$ prismatic/pyramidal slip, and then $[c]$ prismatic slip with increasing temperature (Keller and Stipp 2011; Morales et al. 2014, 2011; Okudaira et al. 1995; Tokle et al. 2019). Changes in proportions of different slip systems activated at different temperatures and strain rates are presumably reflects in c-axis fabrics of quartz mylonites, with opening angle about the normal to foliation for pure shear that constitute a balance between slip systems that rotate c-axes towards the maximum compressive stress (normal to foliation) and those that rotate c-axes towards foliation. Conceptual and numerical models of CPO development (e.g., Lister and Hobbs 1980; Tullis et al. 1973; Wenk et al. 1989; Wenk et al. 2019) are based on varying proportions of dislocation glide on $\langle a \rangle$ basal, $\langle a \rangle$ prism, $\langle a \rangle$ pyramidal, $[c]$ prism, and $\langle c+a \rangle$ pyramidal systems, but we know of no models that incorporate $\langle c+a \rangle$ prism glide or climb as a strain mechanism. Revisions in our interpretation of CPO will need to include the additional slip system with displacement vector $\langle c+a \rangle$. Kinematically, adding $\langle c+a \rangle$ glide will alter the proportions of $\langle a \rangle$ and $[c]$ glide. Moreover, if only glide is considered, we will miss a significant fraction of strains during dislocation creep. Deformation thermometers such as the quartz c-axis fabric opening angle thermometers of Kruhl (1996) and Faleiros et al. (2016) do not explicitly take into account the separate potential influences of glide and climb on fabric development. However, the interpretation of these empirically based thermometers will depend on activation of slip systems at varying temperature, strain rate and action of hydrous defects. Relations between glide-induced CPO and total strain will further depend on how much strain is accomplished by glide and by climb.

4.1.4.3 Inferring stress loading

Sylvester (1969) suggested that deviations of deformation lamellae orientations from rationale crystallographic planes tend towards planes of high shear stress, potentially offering a tool to reconstruct internal stresses. Here, we explore this hypothesis further. To do this, we

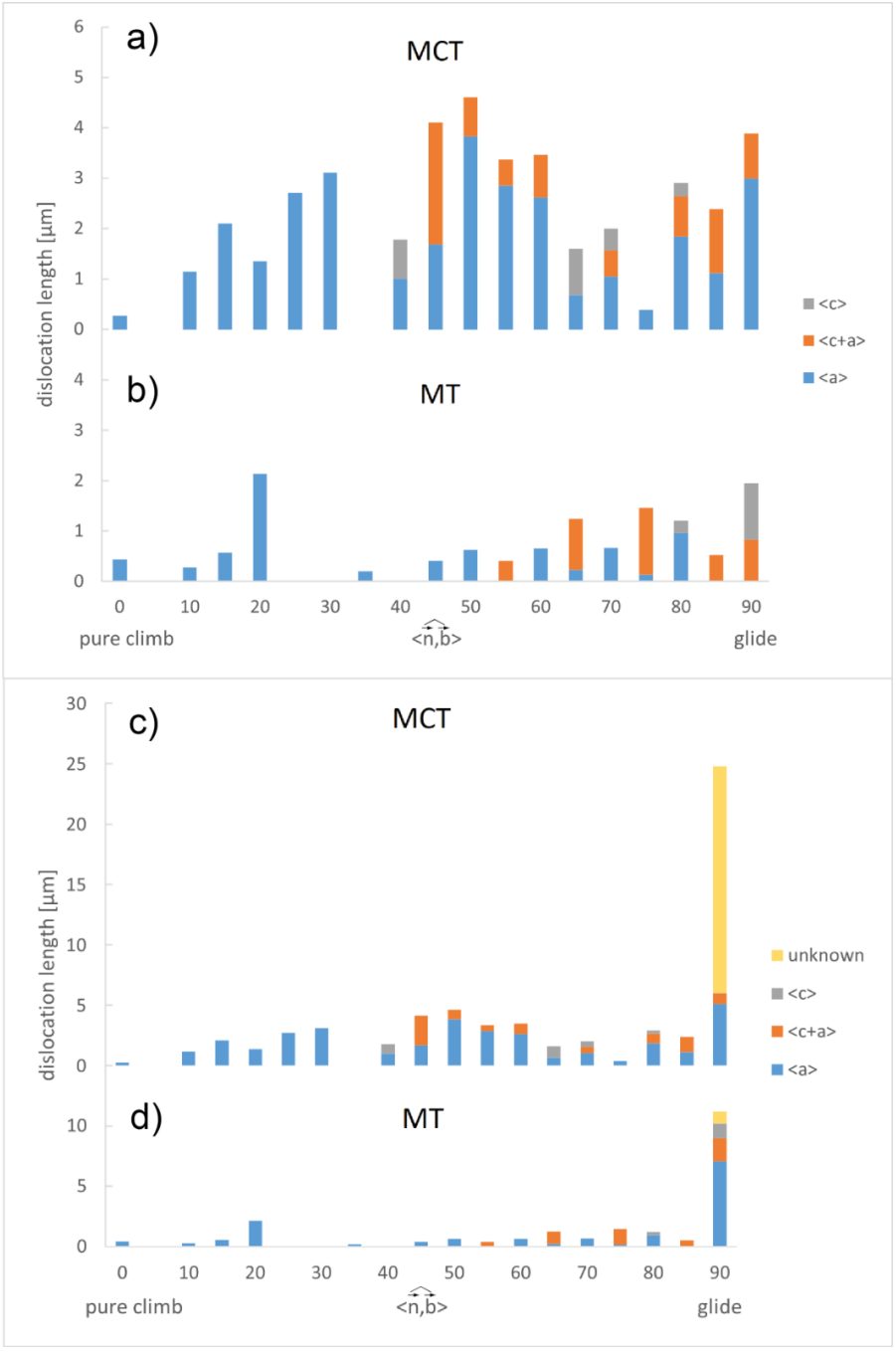

Figure 45: Histograms quantifying the climb contribution in quartz of $\langle c \rangle$, $\langle c+a \rangle$, and $\langle a \rangle$ dislocations: (a) Histogram of the evolution of the angle between Burgers vectors and normal vectors to habit planes $(\widehat{(n,b)})$ normalized for dislocation segment lengths for the MCT specimen; (b) histogram for the MT specimen; (c) MCT specimen: histogram where the lengths of straight-line dislocation segments are included, considering these segments are in a glide configuration; (d) MT specimen: histogram where the lengths of straight-line dislocation segments are included. From these histograms, more than 50% of the dislocation length is found in climb configurations.

represent on Figure 46 the different systems (glide or climb) on a stereographic projection for quartz with positive vertical $[0001]$ (upper hemisphere). Figure 46(a) summarizes our observations for the different types of dislocations, color-coding the contribution of climb. From this stereographic projection (Figure 46(b)), we can see that the orientation of the grain analysed in the MCT specimen strongly enhances activation of the $\frac{1}{3}[1\bar{2}10](10\bar{1}0)$ glide system. As a result, there is little climb of $\frac{1}{3}[1\bar{2}10]$ dislocations. In contrast, glide of $\frac{1}{3}[11\bar{2}0]$ dislocations is less favourable (Figure 46(c)) increasing the tendency to climb. In Figure 46(d), we extract the glide components of the mixed climb planes of $\frac{1}{3}[1\bar{2}10]$ dislocations into the pure climbing plane normal (along the $[11\bar{2}0]$ direction), but also on the glide plane normal depicted in Figure 20.

This analysis reveals the strain contributions of two easy slip systems: $\frac{1}{3}[11\bar{2}0](\bar{1}100)$ and $\frac{1}{3}[1\bar{2}10](\bar{1}101)$ and, to a lesser extent, of $\frac{1}{3}[1\bar{2}10](\bar{1}10n)$ as well as some other unexpected planes. Such evidence of glide in planes that have not been reported for quartz raises questions. Dislocation motion in these planes does not correspond to pure glide, but is associated with mixed climb. This observation is in line with the interpretation made by Malaplate et al. (2004) of mixed climb in TiAl alloys. According to them, dislocation motion in mixed climb planes may be facilitated by reduced lattice friction during pure glide (probably linked to specific dislocation core structures). We hypothesize that activation of mixed glide and climb may allow activation of glide on additional planes. This hypothesis, based as it is on preliminary observations, requires further observational and theoretical investigation.

We have also applied the method described in section 4.1.2.4 to learn whether the stress state that acted *in situ* can be inferred. Several minimization attempts have been carried out, and slightly better results have been obtained when allowing different slip resistances τ_0 for dislocations with $\langle a\rangle$, $\langle c+a\rangle$, and $[c]$ Burgers vectors. Results (Figure 47 for MT) show a good match between the observed and computed θ values. In the minimization procedure, we had to optimize not only the stress state but also the rheological parameters. Best results are obtained for a nearly linear behavior for both glide and climb ($n_g \approx n_c \approx 1$) and slip resistance for $\langle c+a\rangle$ and $[c]$ dislocations just half the slip resistance for $\langle a\rangle$ dislocations.

The stress state obtained in this way for the MT specimen (Figure 48) indicates that the larger normal stress (promoting climb) was along directions close to $\langle c+a\rangle$ and that the maximum shear stress (promoting glide) appeared to be on planes close to $\{10\bar{1}0\}$ or to (0002). Another graphical representation of the stress state inferred in the MT specimen is the stress ellipsoid (Figure 49). It exhibits an oblate shape, two principal stresses having similar absolute values (-4.4 and 5.2) while the third one is significantly smaller (0.8). The stress ellipsoid, oriented along the TEM view direction, is represented in Figure 39.

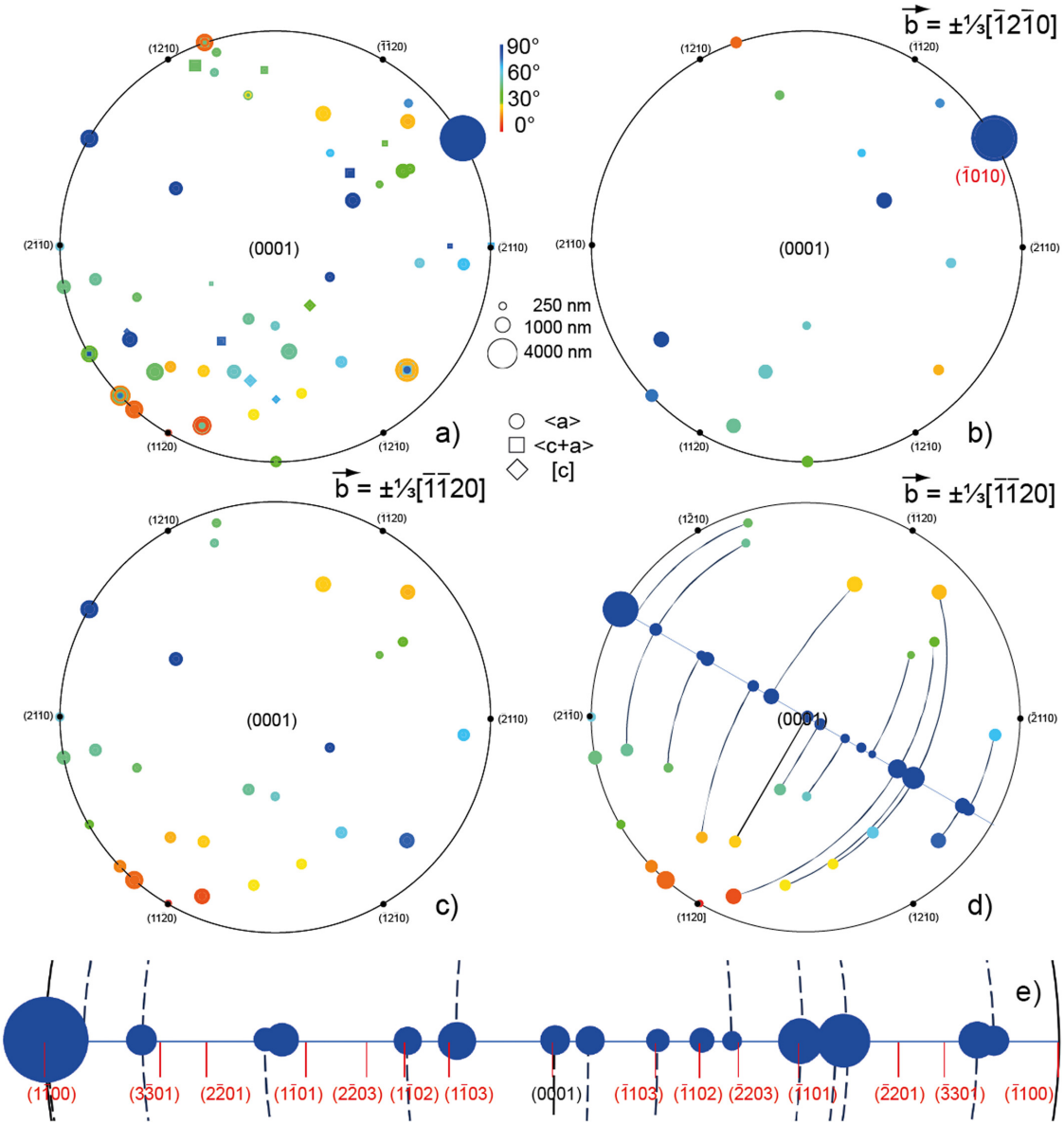

Figure 46: (0001) stereographic projection (upper hemisphere) of the normal to the habit planes of dislocations characterized in the MCT specimen. The rainbow colour code is associated with the angle between the habit plane normal and the Burgers vectors ($0°$ in red for pure climb and $90°$ in blue for glide) and the symbol sizes correspond to the lengths of dislocations using a non-linear scale illustrated by three examples: 250, 1000 and 4000 nm. (a) All Burgers vectors are represented ($\langle a \rangle$ dislocations are represented by circles, $\langle c+a \rangle$ by squares and $[c]$ by diamond); (b) Projections of the habit plane normals for a_2 dislocations (a high proportion of dislocations found in the $(\bar{1}010)$ glide plane); (c) Projections of habit plane normal for a_3 dislocations (a few in glide planes and many in mixed climb configurations); (d) Stereographic projection for a_3 dislocations where the glide components of the mixed climb planes are extracted and added. These glide components are linked to their parent mixed climb plane by a solid line. (e) enlargement of the great cirle of (d) showing glide planes normal to this plane. Labeled Miller indices of these planes show the diversity of glide components involved.

While this estimation of the local stress state acting *in situ* does not take into account changes in stress during the plastic deformation history, it is, to our knowledge, the first estimation of *in situ* stress state based on observed dislocation structures. Moreover, the rheological coefficients thus obtained for MCT and MT shear zones correspond to *in situ* conditions and extremely slow geological strain-rates.

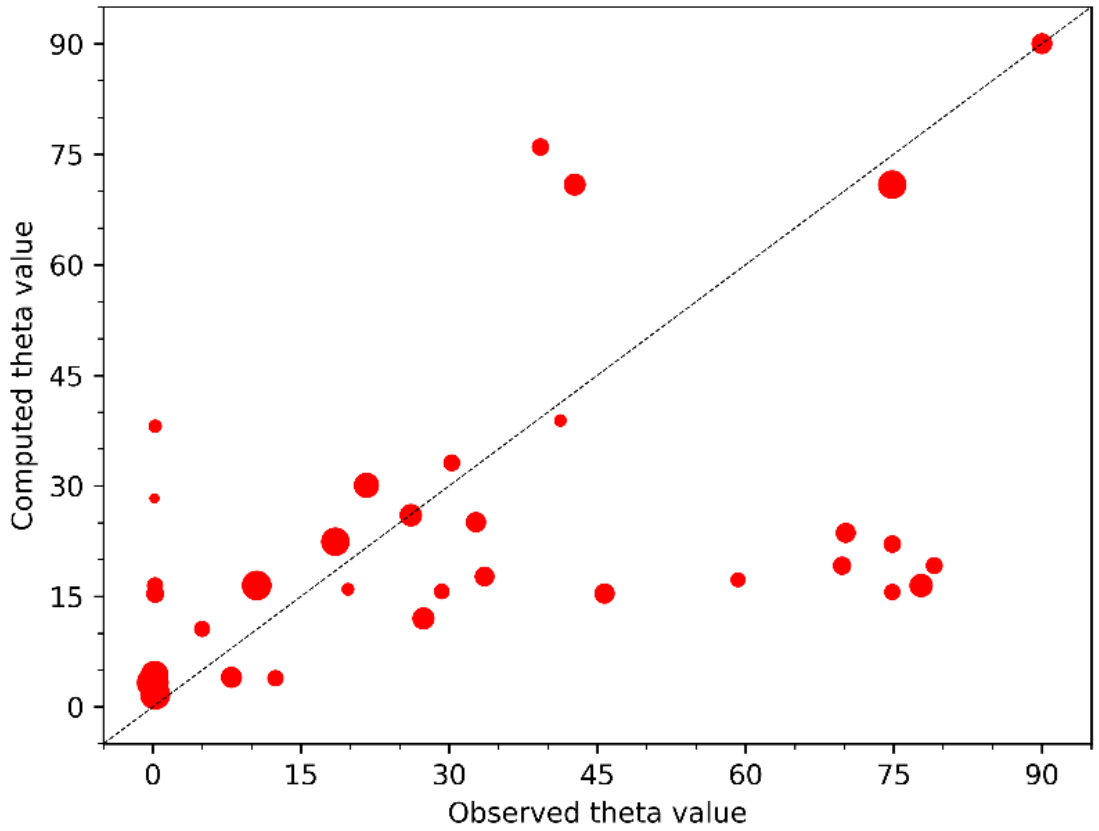

Figure 47: Computed θ^{mod} angles vs. observed θ^{obs} angles after minimizing the objective function (4.12) to find the stress state that is most consistent with the observations, for specimen MT. Each symbol corresponds to a different dislocation segment, and their size is proportional to the segment length.

4.1.4.4 Limitations

Detailed TEM characterization of a mineral as electron-beam sensitive as quartz necessarily leads to a limited number of characterizations. Although statistical evaluation is difficult to apply, the validity of the results can be discussed from several points of view. While the analysis of the deformation microstructures of natural samples is of prime importance, it is not without its difficulties. The first is that these samples are the product of a long and complex history. We assume implicitly that the dislocations available for study at the end of deformation are comparable to (potentially exactly the same systems as) dislocations that

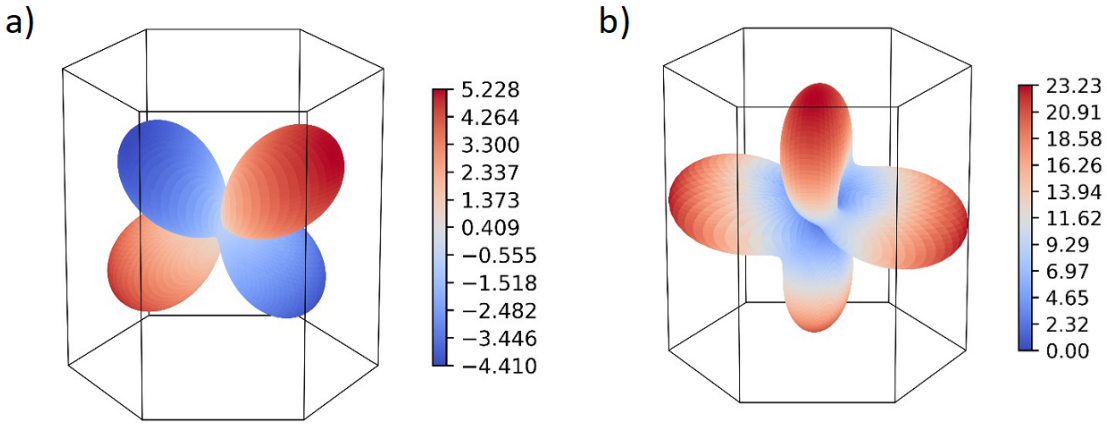

Figure 48: Stress state obtained for specimen MT after minimization of (4.12), plotted with respect to the hexagonal crystal lattice. (a) Norm of the normal stress acting on specific crystallographic planes, for any possible plane orientation. (b) Norm of the shear stress acting on those crystallographic planes. Stress values are relative, and adimensional, normalized by the critical shear stress corresponding to $\langle a \rangle$ glide.

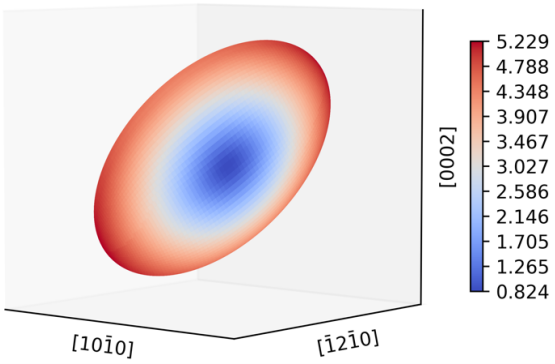

Figure 49: Stress ellipsoid for specimen with respect to crystallographic directions of the quartz grain of the MT specimen. Among the three principal stresses, two have similar absolute values -4.4 and 5.2 while the third one is significantly smaller 0.8, resulting in an oblate shape. Stress values are relative, and adimensional, normalized by the critical shear stress corresponding to $\langle a \rangle$ glide. See also Supplementary movie.

were present and mobile during peak metamorphic and deformation conditions. For simple thermal histories, this assumption can be made as the exponential dependence of dislocation creep leads to an effective temperature when dislocation mobilities slow down and dislocations are left within the crystalline interior, much as the exponential dependence of diffusion can lead to effective closure temperatures that govern geochemical age determinations. In the case of this study, we do not seek to link microstructures or mechanisms to any particular moment of the sample deformation histories.

The question remains as to whether the microstructure active during deformation was erased by a late episode of recovery at low or negligible deviatoric stress, particularly since evidence of recovery (subgrain boundaries) is present. With regard to the major results of this study, specifically the widespread activation of $\langle c + a \rangle$ glide and the importance of mixed climb to dislocation creep, our conclusions do not depend on demonstrating their activity at peak metamorphic-tectonic conditions or the statistics of large numbers of observations. For example, the development of a dislocation loop in a mixed plane can only be understood in terms of simultaneous and equivalent glide and climb displacements. Such a microstructure cannot be the result of two distinct and successive episodes of deformation and recovery.

A highly focussed study such as ours also raises the question of whether it samples a representative volume element (RVE) which is the smallest volume over which a measurement can be made that will yield a value representative of the whole. As our study is based on a very small volume and a small number of dislocations, it is important to discuss the validity of our observations without the support of statistical elements. With regard to the observation of mixed climb, we emphasize that two grains from two distinct samples (to which we can add the granulite sample of Mussi et al. 2021c) lead to the same observation. This suggests that the crystalline defects of our studied volumes are not exceptional and that the conclusions drawn from these limited observations are probably more general in their significance.

The other result is the completeness of the plastic strain tensor, which leads to the conclusion that the von Mises criterion is satisfied. The volume sampled is surely not large enough to provide a quantitative measure of the plastic strain tensor for either shear zone, but the scale of study is sufficient to demonstrate that the necessary slip systems required to accommodate any general plastic strain were indeed activated.

We have also tried to deduce, from dislocation microstructures, the mechanical loading conditions acting at the crystal scale that may have generated the microstructures. Here, we exploit the highly anisotropic nature of crystalline plasticity. In the case of the MCT sample, we can see the difference in responses of dislocations a_2 and a_3 (Figure 46). The minimization

of the objective function (eq. 4.12) gives the best results for the MT quartz grain, but it is unclear that this problem is uniquely solved. The local stress may include contributions from neighboring grains at the polycrystal scale, residual stresses of the dislocation network, and thermally derived stresses. Greater statistics would be required to capture the heterogeneity of stress in a polycrystalline rock over a much larger RVE.

4.1.5 Conclusion

Several important conclusions can be drawn from detailed 3D electron tomography of quartz specimens from the MCT and the MT, both of which were deformed extensively by dislocation creep in the presence of water. We show that $\langle a \rangle$ slip occurs predominantly on pyramidal and prismatic planes, that $\langle a \rangle$ basal glide is not active, and that $[c]$ glide is not significant under those conditions. A remarkable observation is the widespread activation of $\langle c+a \rangle$ glide in the $\{10\bar{1}0\}$, $\{10\bar{1}1\}$, $\{11\bar{2}n\}$ $(n = 1, 2)$ and even $\{21\bar{3}1\}$ (not previously reported) planes. Even more remarkable is the observation that more than approximately 60% of all dislocations involve climb in their motion. This was only possible thanks to the characterization of the three-dimensional microstructure of the dislocation lines by electron tomography. The simultaneous motion of dislocations by glide and climb, known as mixed climb in materials science, is apparently widespread in naturally deformed quartz shear zones. This mode of deformation is characterized by displacement of dislocations in intermediate planes between the glide and climb planes, with significant implications for relative glide velocity v_g and climb velocity v_c; v_g and v_c must have comparable magnitudes under natural strain rates. Our quantitative characterization of slip systems in these samples demonstrates that glide of the observed dislocations can accommodate any arbitrary strain without strains due to climb, grain boundary sliding or other intercrystalline mechanisms. On the other hand, the magnitudes of strains achieved include significant contributions due to dislocation climb. Plastic strains produced by climb are not subordinate to those of glide; rather, they are of the same order of magnitude as strains due to glide (and possibly larger for the MCT specimen than for the lower temperature MT specimen). Strain analysis based on the exclusive activation of glide systems does not therefore provide a satisfactory description of quartz deformation at natural strain rates.

4.2 Olivine - Evidence of Mixed Climb

This describes parts of a larger study published in Physics of the Earth and Planetary Interiors[2], where we investigated the microstructure of naturally deformed olivine, which had reached chemical equilibrium at a temperature of $1000°C$, using conventional transmission electron microscopy and electron tomography. The chosen peridotite sample, obtained from Oman ophiolite, exhibited a mylonitic microstructure characterized by the presence of residual, heavily deformed millimetric porphyroclasts, coexisting with newly formed, smaller olivine grains resulting from dynamic recrystallization.

Here I will focus on the tomography part, which constitutes my personal contribution to this research. Our electron tomography investigations uncovered several glide planes, closely resembling those observed in prior studies involving experimentally deformed polycrystalline olivine (Demouchy 2021; Green 1976; Gueguen and Darot 1980). More significantly, electron tomography allowed us to discern combinations of glide, climb, and mixed climb processes (as elaborated in the chapter 2.3.4.2.2). This study broadens our understanding of the various mechanisms responsible for the plastic deformation of olivine under lithospheric conditions.

4.2.1 Results

For the tomographic analysis, we chose the diffraction vector $13\bar{1}$, ranked as the third most intense structure factor within the olivine structure. This vector facilitated the visualization of both $[100]$ and $[001]$ dislocations. Employing the technique described in Section 3.1, we set a precession angle of $0.15°$. Tilt-series data was acquired at $2°$ intervals spanning from $-40°$ to $50°$ using a double-tilt sample holder.

In this particular study, we did not undertake an exhaustive characterization of all the habit planes present in the 3D reconstructed volume. However, we did identify several noteworthy configurations.

Our selection for tomographic analysis featured a representative sample volume, as depicted in Figure 50, encompassing both $[100]$ and $[001]$ dislocations. The area was imaged in WBDF mode (Figure 50(a)). Figures 50(b)-(g) present projections captured at various tilt angles. Further insights into the habit planes of select dislocations are provided in Figures 50(d)-(g). A comprehensive view of the reconstructed dislocation microstructure is presented in Figure 50(b).

[2] Demouchy, S., A. Mussi, T. Weidner, E. Gardés, and P. Cordier (2023a). "Dislocations in naturally deformed olivine: Example of a mylonitic peridotite". In: *Physics of the Earth and Planetary Interiors*, p. 107125

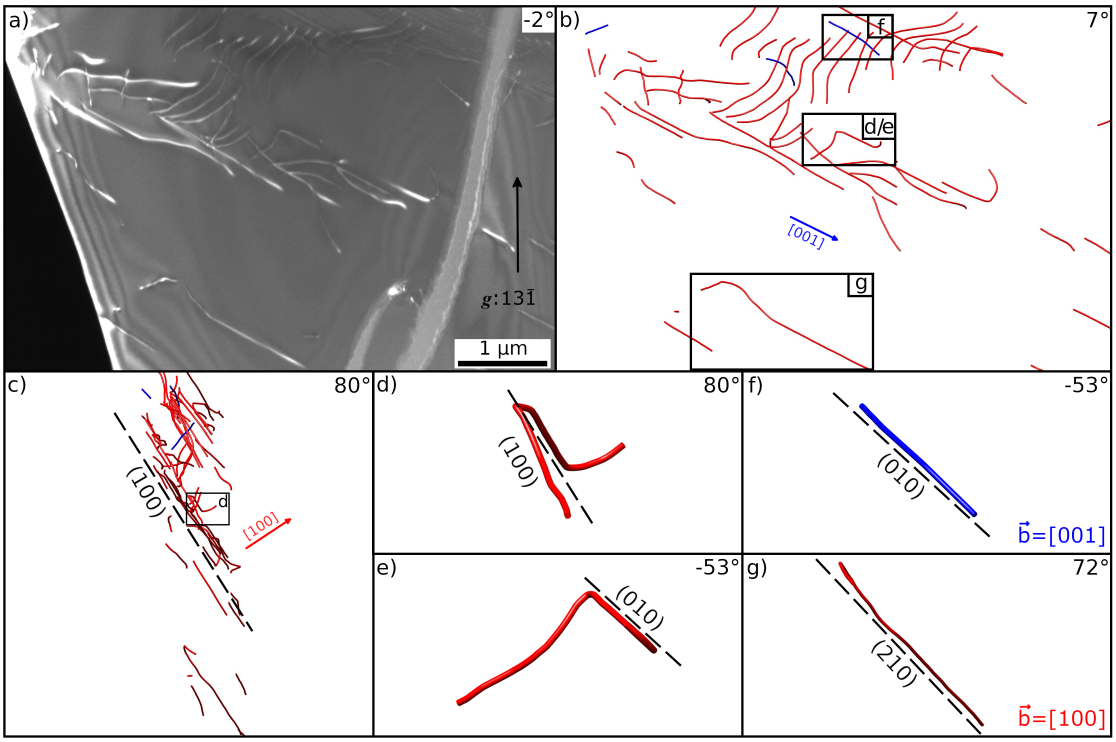

Figure 50: Dislocation electron tomography characterization: (a) weak-beam dark field micrograph taken with the $13\bar{1}$ diffraction vector at a projection angle of $2°$, showing $[100]$ and $[001]$ dislocations; (b) reconstructed tomographic volume viewed at $7°$ showing $[100]$ dislocations in red and $[001]$ dislocations in blue as well as the $[001]$ direction (black rectangles indicate dislocations which habit planes are edge-one in the corresponding subfigures); (c) reconstructed tomographic volume viewed with a projection angle of $80°$ showing the habit plane of the subgrain boundary edge-on, i.e. the (100) plane; (f) a $[001]$ dislocation in (010) in the reconstructed volume oriented with a projection angle of $53°$; (g) a $[100]$ dislocation in a mixed climb plane (210) viewed with a projection angle of $72°$; (d) and (e) characterization of a 3D $[100]$ dislocation where the upper part is in the (010) glide plane (seen at $53°$) and the lower part is in the subgrain boundary (here visualized at $80°$).

As observed in Figure 50(b), the quantity of $[100]$ dislocations (depicted in red) substantially surpasses that of $[001]$ dislocations (in blue). Additionally, $[100]$ dislocations appear to align closely with the $[001]$ direction. Short segments of both $[100]$ and $[001]$ dislocations (Figure 50(b) and (c)), gliding within the (010) plane (Figure 50(e) and (f)), bear witness to the activation of the $[100](010)$ and $[001](010)$ slip systems. The sub-grain boundary within the (100) plane (Figure 50(c)), positioned in the top left of Figure 50(a), is composed of $[100]$ dislocations. It's worth noting that indexation of the sub-grain boundary plane (Figure 50(c)) was only possible through tomography, as a tilt of $80°$ is physically unattainable within the TEM and can only be realized through a $3D$ reconstruction.

In Figure 50(d), a $[100]$ dislocation is situated near the (100) plane, indicative of a pure climb orientation. Figure 50(g) showcases a $[100]$ dislocation within a plane closely resembling (210), which neither conforms to a glide nor a climb plane but represents an intermediate

orientation, thereby shedding light on a mixed climb configuration. The contribution of dislocation climb is further elaborated upon in the subsequent discussion section.

4.2.2 Discussion

The dislocations commonly found in the studied peridotite are in perfect agreement with previous studies on mantle-derived and naturally deformed samples for lithospheric temperatures ($\sim 1000°$C) as well as with experimentally deformed olivines at similar transition homologous temperatures (e.g., Demouchy et al. 2014, 2013; Green 1976; Phakey et al. 1972). Both $[100]$ and $[001]$ dislocations coexist, but with little evidence of interaction between the dislocations from the different slip systems. This observation was also reported in previous studies (e.g., Durham et al. 1985).

Our observations have provided several pieces of evidence for the activation of dislocation climb under the natural deformation conditions experienced by this peridotite. The presence of sub-grain boundaries (see Figure 50(b) and 50(c), and more can be seen in the full study) is a common argument for recovery, and we recall that it requires the activation of climb. Grain boundaries parallel to (001) are made of $[001]$ dislocations. In addition climb loops where found in other areas covered in the main study. Climb is also evidenced by the detailed analysis of a three-dimensional $[100]$ dislocation shown in Figures 50(d) and 50(e). One segment of this dislocation is in a gliding configuration in (010) (Figure 50(e)), but the rest of the dislocation lies in the sub-grain boundary plane, parallel to (100), and hence is in a climb configuration (Figure 50(d)). It remains impossible to determine, however, whether it is a $[100]$ dislocation initially gliding in (010) and then being absorbed by climb into the subgrain boundary, or whether it is a dislocation from the subgrain boundary being emitted by glide in (010). More remarkable is the configuration in Figure 50(g), which shows a $[100]$ dislocation moving in an intermediate plane between the plane of glide plane and the plane of pure climb. Moreover, in the quartz section and the general discussion on mixed climb, we propose that under certain conditions, relevant to the lithospheric mantle, the dislocation glide and climb velocities to be of the same order of magnitude. This closer match between glide and climb velocities is probably a consequence of natural deformation conditions involving low stresses, which reduce glide velocity, and very low strain rates, which favor climb.

5 Results - Dislocation Electron Tomography - An Association to Field Dislocation Mechanics

This section draws upon our paper published in Modelling and Simulation in Materials Science and Engineering[1].

Here I propose a new procedure to extract information from electron tomography and use them as an input in a field dislocation mechanics. DET is an experimental technique that provides three-dimensional (3D) information on dislocation lines and Burgers vectors within a thin foil. The characterized 3D dislocation lines are used to construct the spatial distribution of the equivalent Nye dislocation density tensor. The model dislocation lattice incompatibility equation and stress balance equation are solved with a spectral code based on fast Fourier transform algorithms. As an output of the model, one obtains the 3D distribution of mechanical fields, such as strains, rotations, stresses, resolved shear stresses (RSSs) and energy, inside the material. To assess the potential of the method, we consider two regions from a previously compressed olivine sample. Our results reveal significant local variations in local stress fields and RSSs in various slip systems, which can impact the strong plastic anisotropy of olivine and the activation of different dislocation slip systems. It also evidences the built-up of kinematic hardening down to the nanometer scale.

5.1 Materials and Deformation Experiments

This study was conducted on an olivine sample (PoEM9) experimentally deformed by Demouchy et al. (2013) which had previously undergone TEM microstructural investigations (Mussi et al. 2015a,b). The axial compression experiments were performed on a cylinder specimen (length 6.32 mm; diameter 4.19 mm) extracted from a large, gem-quality, single crystal of San Carlos olivine ($(Mg_{0.91}Fe_{0.09}Ni_{0.003})_2SiO_4$). The sample PoEM9 (Demouchy

[1]Weidner, T., V. Taupin, S. Demouchy, K. Gouriet, A. Guitton, P. Cordier, and A. Mussi (Nov. 2023). "From electron tomography of dislocations to field dislocation mechanics: application to olivine". In: *Modelling and Simulation in Materials Science and Engineering* 32.1, p. 015004. DOI: *10.1088/1361-651X/ad0a42*. URL: *https : //dx.doi.org/10.1088/1361-651X/ad0a42*.

et al. 2013) was deformed along $[502]$ (see Figure 57) in a high-resolution gas-medium high-pressure apparatus (Paterson 1990) at $806°C$, with a constant strain rate of 5.1×10^{-5} s^{-1}, under a gaseous (Ar) confining pressure of 300 MPa (deformed cylinder and thin foil orientation can be seen in Figure 57). The finite strain reached was $\varepsilon_{\text{Total}} = 10.1\%$ (determined post-mortem), and the maximum differential stress was 754 MPa.

5.2 Results and Discussion

5.2.1 Dislocation Microstructure

To obtain an overview of the dislocation microstructure of PoEM9, six tilt-series (obtained with the $22\bar{2}$ diffraction vector) were acquired at low magnification, covering an analyzed total area of approximately 30 μm^2 (Mussi et al. 2015b), with an average angular range from -52° to 48°.

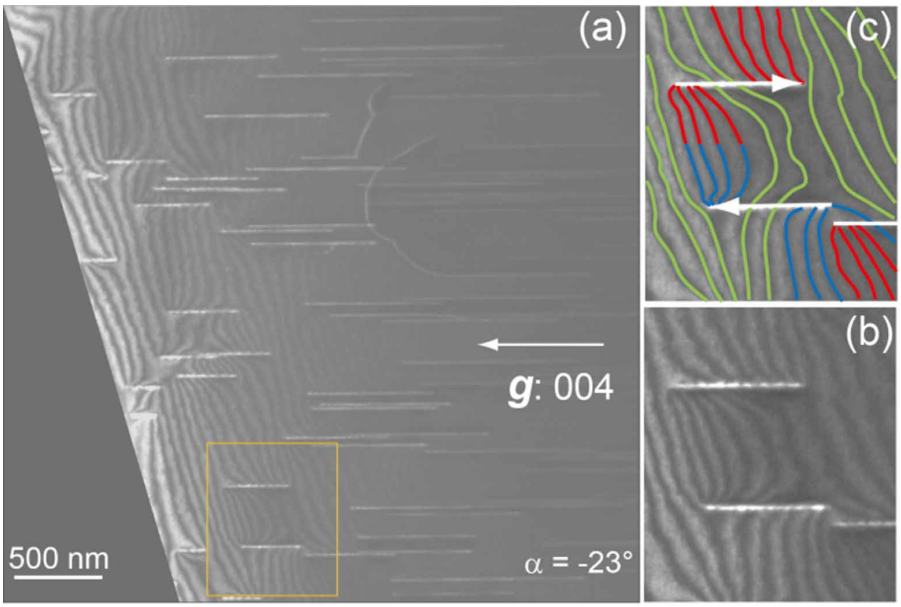

Figure 51: WBDF micrograph obtained with the 004 diffraction vector: (a) global micrograph where thickness fringes are clearly seen; (b) enlargement of a dislocation dipole pointed out by an orange rectangle on figure 1(a); (c) enlargement of the dipole where the unterminated thickness fringes are coloured in green, the terminated thickness fringes are coloured in red at the extremities of the dislocations represented with arrows oriented on the opposite direction of the wedge, and the terminated thickness fringes are coloured in blue at the extremities of the dislocation represented with an arrow oriented on the direction of the wedge (the directions of the arrows are linked with the signs of the Burgers vectors).

Burgers vector indexations were performed using the thickness fringes technique (see Section 3.1.4) with the 004 and $22\bar{2}$ diffraction vectors (Figures 51 and 30 respectively). These indexations revealed that the microstructures are predominantly composed of dislocations with

$[001]$ Burgers vectors, mostly exhibiting straight screw dislocation characters. An example of the dislocation microstructure obtained in WBDF conditions with the 004 diffraction vector is shown in Figure 51. Electron tomography revealed a predominance of $\{110\}$ and (100) glide planes, with few cross-slip configurations and collinear interactions (Mussi et al. 2015b). The reconstructed volumes also facilitated access to $(\boldsymbol{u}, \boldsymbol{b})$ doublets for each dislocation segment, aiding in the calculation of the Nye tensor and simulation of the continuous distribution of stress field.

Two specimen domains of PoEM9 were studied in detail: zone 1 (Figures 52(a)-(d)) and zone 2 (Figures 52(e)-(h)). Tilt-series composed of 51 micrographs (acquired every 2° with a tilt angle ranging from -48° to $+52^\circ$) and a second tilt-series of 54 micrographs (acquired every 2° with a tilt angle ranging from -56° to $+50^\circ$) were obtained in WBDF conditions with the $22\bar{2}$ diffraction vector (zones 1 and 2 respectively). Micrographs from Figures 52(a) and (e) are from these two tilt-series for a projection angle of 0°. Electron tomography reconstructions facilitated the characterization of the (110), $(1\bar{1}0)$, and (100) slip systems, identified by their colors: white, light grey, and black respectively, as in Mussi et al. (2015b). Neither the slip systems of the pure screw straight dislocations (coral pink-colored) nor the habit plane of the red sessile dislocation segment in Figure 52(f) could be indexed. Consequently, the reconstructed volumes were projected along the $[001]$ direction to orient the pure screw dislocations in an edge-on position (Figures 52(c) and (g)), providing optimal viewing conditions for studying the continuous stress distributions.

5.2.2 Simulation Results

The dislocation internal stresses in the thin foil are rotated to be presented in the olivine crystal reference frame. The x_1, x_2, and x_3 directions are now aligned with the a, b, and c directions of the olivine orthorhombic unit cell, respectively. In addition to this internal stress, we add the macroscopic stress applied experimentally during the compression test (754 MPa) and also rotated in the crystal reference frame. This is possible since we know the angle between the normal of the thin foil $[17\,\bar{5}\,12]$ and the compression axis $[502]$ (approximately 30°). The total stress field at every voxel in the thin foil is then $\sigma_{ij} = \sigma_{ij}^{\text{int}} + \Sigma_{ij}$, where σ_{ij}^{int} is the local internal stress field due to dislocations and Σ_{ij} is the macroscopic stress. It is then possible to project the total stress tensor at every voxel onto different slip systems using the associated Schmid tensor expressed in the olivine orthorhombic reference frame. In the following, we consider three slip systems, labeled 1, 2, and 3: $[001]\,(100)$, $[001]\,(110)$, and $[001]\,(1\bar{1}0)$ respectively. The resolved shear stress (RSS) for the three systems is denoted by

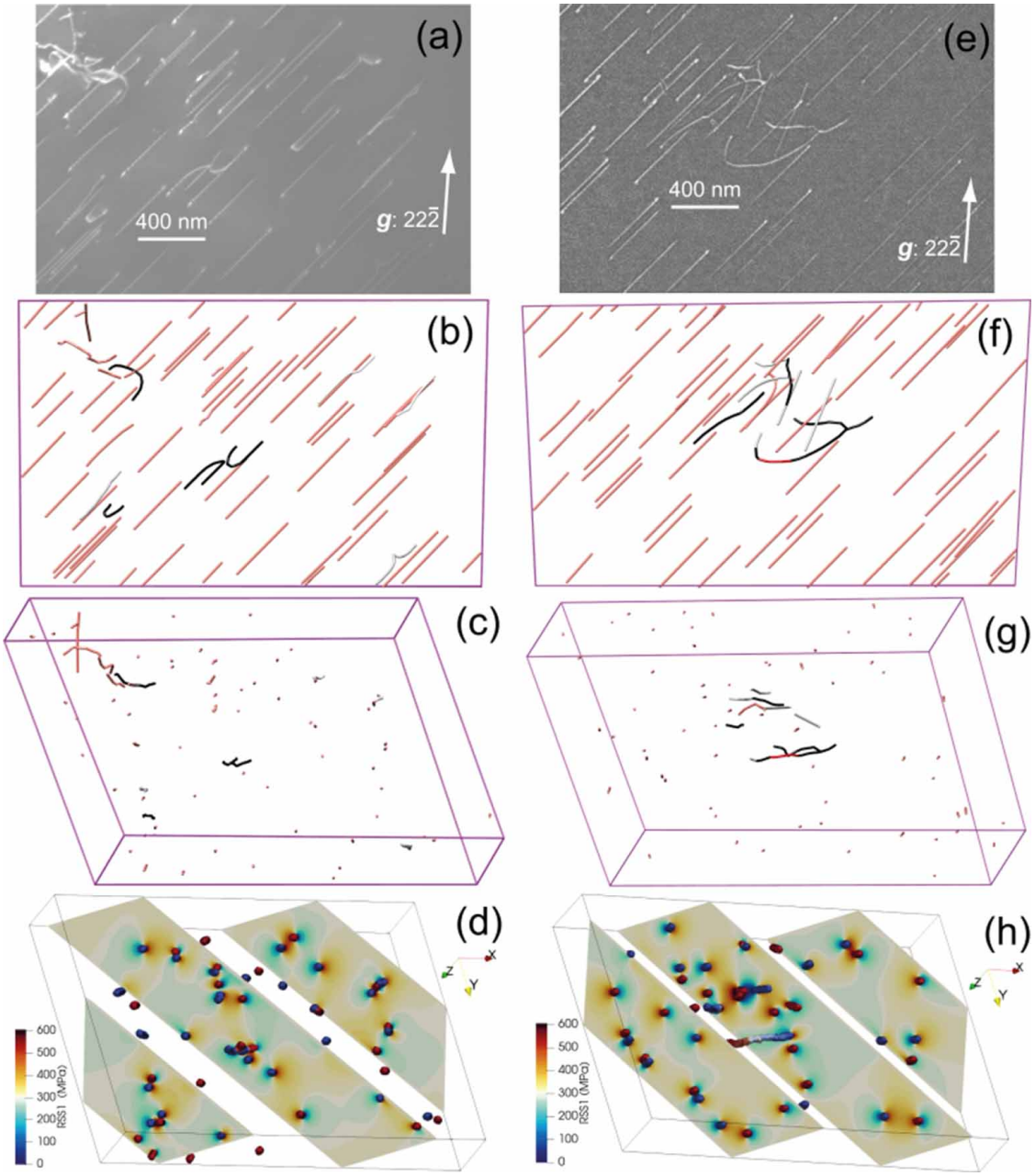

Figure 52: Link between DET and FDM: (a) Raw micrograph in WBDF conditions, obtained with the $22\bar{2}$ diffraction vector (with a projection angle of $0°$) of zone 1; (b) Reconstructed volume of the same domain with the same projected angle (the (110), $(1\bar{1}0)$ and (100) slip systems are respectively colored in white, light grey, and black as in Mussi et al. (2015b)); (c) Reconstructed volume of the same domain along the $[001]$ direction; (d) Spatial distributions (3 slices) of RSS1 in series 1 obtained along the same orientation as figure 52(c) located in the interaction between the two black dislocations in the middle of the micrograph in figures 52(a) and (b) (dislocation lines are also shown and colored with reference to their sign); (e) Raw micrograph in WBDF conditions, obtained with the $22\bar{2}$ diffraction vector (with a projection angle of $0°$) of zone 2; (f) Reconstructed volume of the same domain with the same projected angle (the $(1\bar{1}0)$ and (100) slip systems are respectively colored in light grey and black); (g) Reconstructed volume of the same domain along the $[001]$ direction; (h) Spatial distributions (3 slices) of RSS1 in series 5 obtained along the same orientation as figure 52(g) located in the red dislocation segment (dislocation lines are also shown and colored with reference to their sign).

RSS1, RSS2, and RSS3. They are equal to:

$$\begin{aligned}
\text{RSS}_1 &= \tau[001](100) = \sigma_{31} \\
\text{RSS}_2 &= \tau[001](110) = \frac{b}{\sqrt{a^2+b^2}}\sigma_{31} + \frac{a}{\sqrt{a^2+b^2}}\sigma_{32} \approx 90.63\%\sigma_{31} + 42.26\%\sigma_{32} \\
\text{RSS}_3 &= \tau[001](1\bar{1}0) = \frac{b}{\sqrt{a^2+b^2}}\sigma_{31} - \frac{a}{\sqrt{a^2+b^2}}\sigma_{32} \approx 90.63\%\sigma_{31} - 42.26\%\sigma_{32}
\end{aligned}$$

with a and b the directions of the olivine orthorhombic unit cell.

The macroscopic stress $\Sigma_{31} = \frac{10ac\sigma}{(5a)^2+(2c)^2} \approx 302.8$ MPa (with a and c the directions of the olivine orthorhombic unit cell and σ the applied stress) while $\Sigma_{32} = 0$. Figures 52 and 53 show the spatial distribution of the three RSSs on slices in the thin foil, for the two thin foil series. Dislocation lines are shown in Figure 52. They are removed in Figure 53 for a better comparison of RSS distributions in different slip systems. RSS1, RSS2, and RSS3 fields look similar, with local rotations of RSS patterns (lobes) near dislocations observed among the three RSS maps. The distribution of the internal elastic energy density $\frac{1}{2}\,\varepsilon^e_{ij}C_{ijkl}\varepsilon^e_{kl}$ is also shown in Figure 53, demonstrating elastic interactions between dislocations (interacting elastic fields between dislocations).

The mean internal elastic energy within the thin foil volume is calculated to be 51.6 kJ m^{-3} for series 1 and 52.2 kJ m^{-3} for series 5. Histograms of the RSS distributions in the thin foils are provided in Figures 54(a) and (b), showing a significant heterogeneity of the stress field within the thin foils. Notably, the mean value of RSS1 (302.8 MPa) is slightly larger than that of RSS2 and RSS3 (274.4 MPa), indicating preferential activation of system 1 due to the sample orientation. Strong variations in the stress values are observed, typically ± 400 MPa around the mean values. Regions with local stresses reaching 1 GPa are also observed, particularly nearby dislocation dipoles. Figure 54(c) shows cumulative distribution functions (CDFs) for RSS1, RSS2, and RSS3, for the two thin foil series, with RSS values extracted only at the dislocation lines (instead of taking values at all voxels in the thin foils). In doing so, we only consider dislocation driving stresses in the single crystal. The CDFs are centered about zero, with broad distributions and variations up to ± 400 MPa clearly evident, indicating significant local variations of the RSS values in the three systems considered due to the complexity of the 3D stress state.

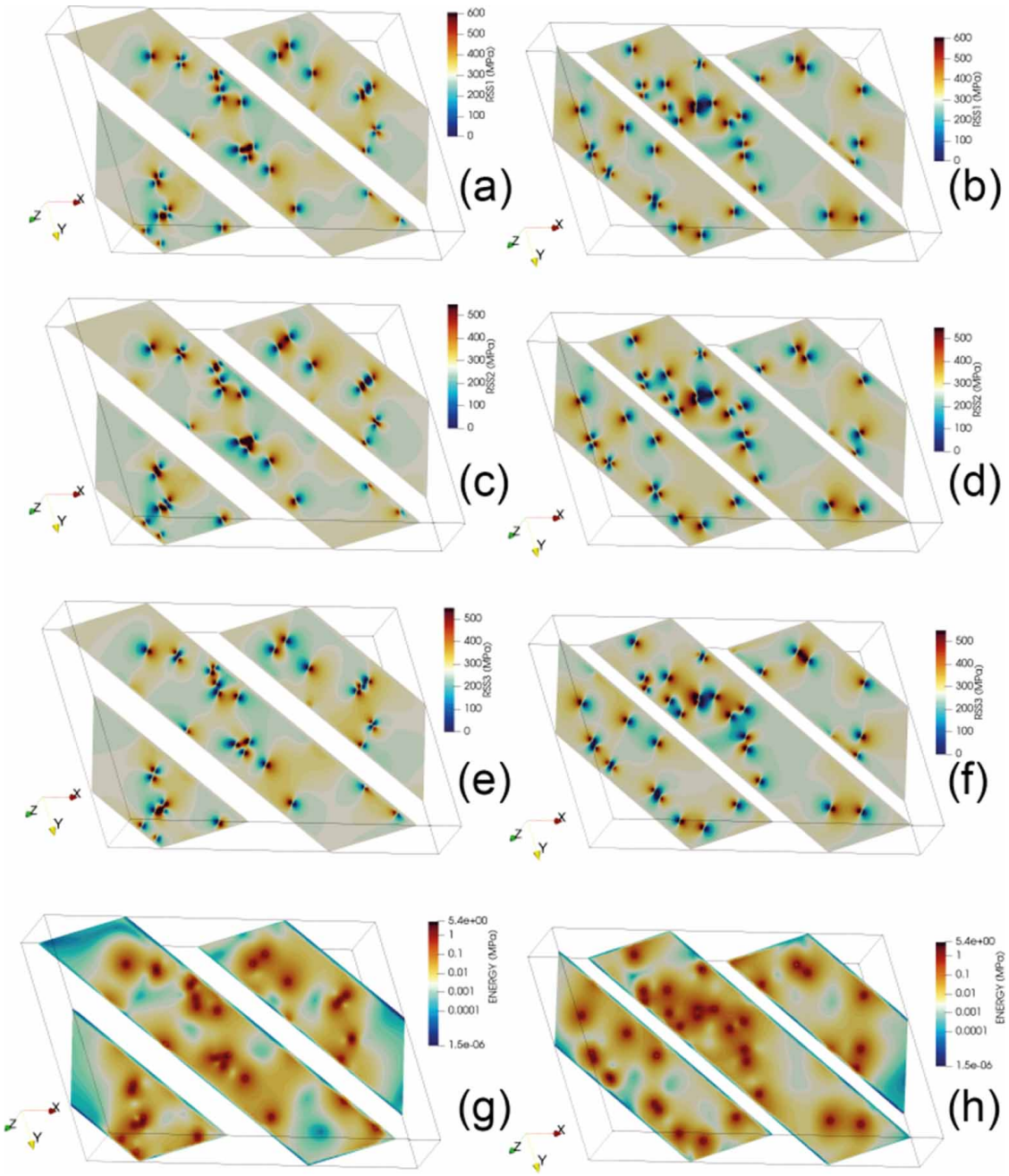

Figure 53: Spatial distributions (3 slices) of RSS1 (a), (b), RSS2 (c), (d), RSS3 (e), (f) and elastic energy density (g), (h) for series 1 (left column) and series 5 (right column).

5.3 Discussion

The present coupled electron tomography/FDM analysis allows obtaining for the first time a detailed, 3D, physical/mechanical description of dislocation networks in the studied thin foils. A physical description of dislocations (Burgers vectors, 3D arrangement of dislocation lines, junctions, dipoles, networks) is complemented by a mechanical description (strains, rotations, stresses, energy). In the present study, we specifically discuss two points, (1) the possible activation of different slip systems in olivine deformed at low temperature due to the complexity of the 3D stress state, and (2), the history of dislocation dynamics and the associated build-up of polarized internal stresses and kinematic hardening in single crystals at the nanometer scale.

1. Activation of slip systems: The POEM-9 specimen, from which thin foils have been extracted and analyzed here, was compressed along the $[502]$ direction, to preferentially activate the $[001](100)$ slip system (system 1 and RSS1). However, an uncertainty between the possible activated slip systems was mentioned Demouchy et al. (2013). Another system, $[001](110)$ was also proposed as a possible system. A third system could also be activated, $[001](1\bar{1}0)$. They correspond to system 2 and system 3 in the present study. Our distributions of RSS values in the thin foil indeed suggest that system 1 is only slightly favored as compared to systems 2 and 3, because the mean value of RSS1 is only slightly larger (difference of less than 30 MPa). However, in a recent work Mussi et al. (2015b), systems 2 and 3 are observed to be easier to activate (lower CRSS) than system 1, system 1 being the second easiest system to activate after system 2 and 3. As such it is not easy to say which one of system 1 or systems (2, 3) was preferentially activated in our studied sample. The distributions of the RSS values extracted only at dislocation lines are certainly more speaking. Indeed, the distributions show very similar features for all series and slip systems. More precisely, they are all broad and show significant local variations, $\pm$400 MPa. As such, the slight difference of the mean RSS between system 1 and systems (2, 3), less than 30 MPa, becomes negligible as compared to possible large local values of RSS. From this, we can conclude that, although POEM-9 was compressed in a way to favor slip system 1, the three systems can all be activated, because of the strong heterogeneity of the internal stress field.

2. Internal stresses and kinematic hardening: The simulated fields of RSS show a significant heterogeneity. Recently, an experimental work on deformed olivine single crystals and polycrystals using high-resolution-EBSD (HR-EBSD) revealed a pronounced het-

erogeneity in the in-plane elastic shear strains and shear stresses at the surface (Wallis et al. 2020, 2021). Variations up to ± 1 GPa around the mean value were reported in both polycrystals and single crystals (at low temperatures) at the micron scale. Such polarization and patterning of internal, intragranular and intergranular stresses, can be related to the build-up of geometrically necessary dislocation densities. Strong heterogeneity of internal stresses is to be associated with kinematic hardening. In the present study, we can look at the heterogeneity of internal stresses down to the scale of typical HR-EBSD map pixels, i.e. at the nanometer scale. Our results also reveal a significant heterogeneity of internal stresses at the nanometer scale in a single crystal containing dislocation networks. Distributions of RSS show broad profiles, with variations up to ± 400 MPa around the mean value. Interestingly, the histograms show a few negative RSS values. The results thus suggest that kinematic hardening has been built-up and is a signature of the past dynamics of dislocations observed.

The application of our electron tomography/FDM method brings valuable insights regarding the complexity of plastic flow in olivine. In a simple single crystal subjected to simple compression loading, it shows that plastic anisotropy and activation of dislocation slip systems can be significantly altered by the large fluctuations of the local mechanical fields. Furthermore, it evidences the built-up of kinematic hardening. This plastic behavior observed at the single crystal, nanometer scale, certainly has a strong impact on the rheology of olivine polycrystals within the Earth's mantle. More generally, our proposed analysis method can also be employed to investigate other mechanisms and defects typically investigated in the TEM for various crystals, such as subgrain boundaries, dislocation networks, dislocation grain boundary interactions, dislocation reactions, interactions between dislocations and pores/precipitates etc. Furthermore, as shown in Figure 55, the method also provides elastic fields in the vicinity of and at free surfaces, which allows making links between elastic fields measurements using experimental techniques such as precession electron diffraction (Cooper et al. 2015), HR-EBSD (high-resolution electron backscatter diffraction), HR-TKD (high-resolution transmission Kikuchi diffraction) (Ernould et al. 2022), ACOM (automated crystal orientation mapping) ASTAR®(Després and Veron 2023) and defects inside the material. It must be emphasized that, in addition to provide 3D anisotropic elastic fields, our approach allows a spatial resolution of 15 nm in routine use, extendable down to 5 nm. The method can also be used to assess the accuracy of HR-TKD, or ACOM/ASTAR methods, when measuring the elastic fields around dislocation structures.

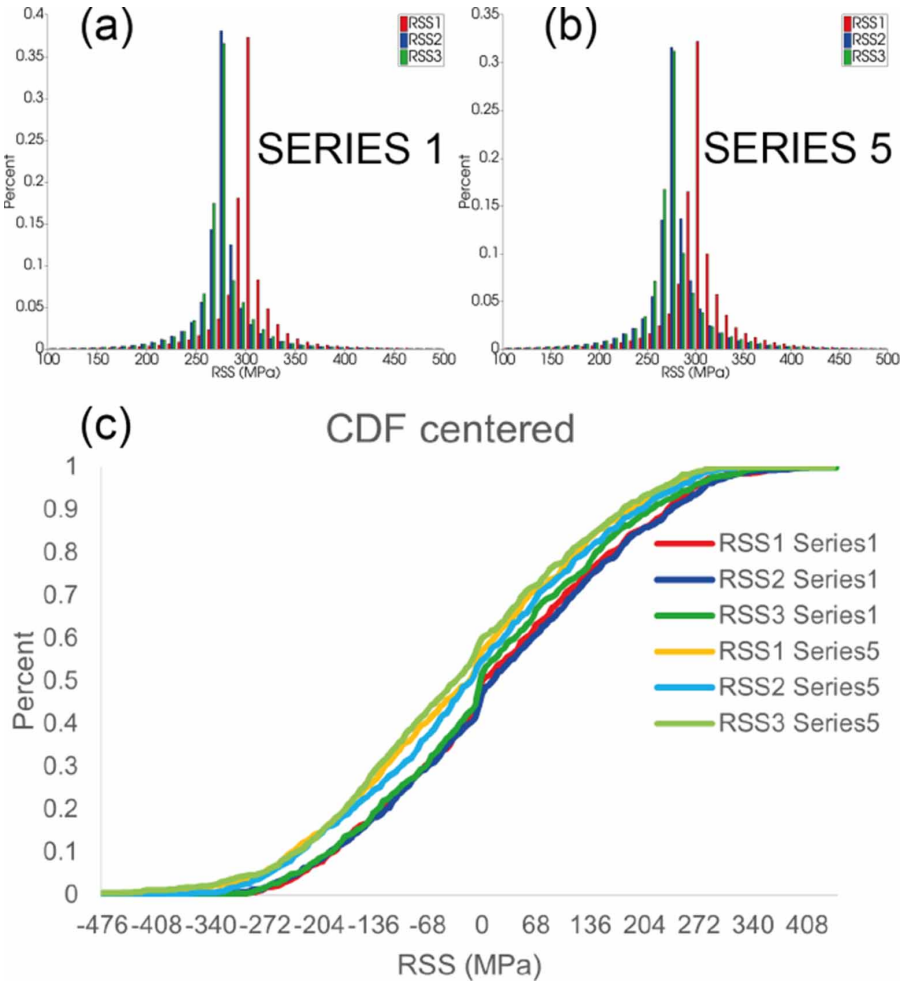

Figure 54: Distributions of RSS1, RSS2 and RSS3 for series 1 (zone 1) and series 5 (zone 2). (a)-(b) All RSS values in the thin foils are used. (c) Only RSS values at dislocation lines are used. All cumulative distribution functions (CDF) for the three slip systems and the two series are superimposed on the same figure.

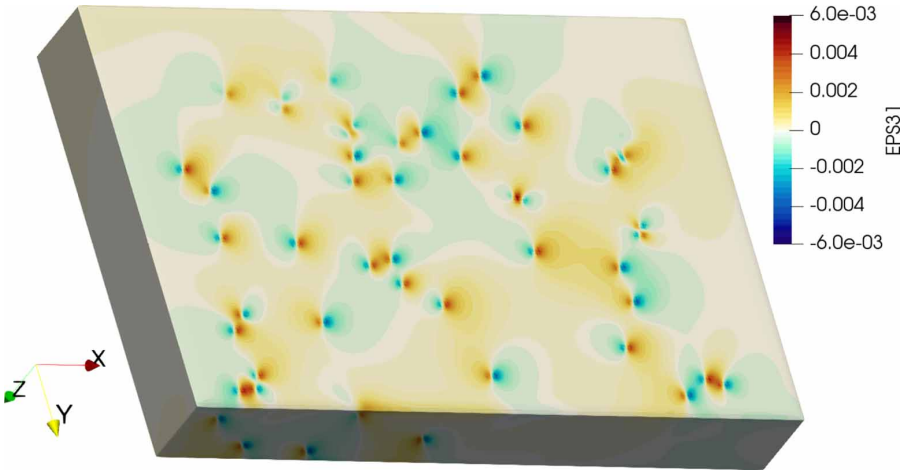

Figure 55: Elastic strain ε_{31} at the surface of the thin foil for series 1.

5.4 Conclusion

In this contribution, we propose an original experimental and theoretical characterization method for studying dislocation networks in crystalline materials. The method combines DET, which provides a 3D characterization of dislocation lines and Burgers vectors, to a FDM model, which provides the associated internal mechanical fields. To demonstrate the potential of our method, we have considered single crystal thin foils extracted from a compressed olivine single crystal. Our results have revealed significant local fluctuations in the local mechanical fields, particularly the RSSs in different slip systems, which certainly play a role in the strong anisotropy of olivine and the activation of different dislocation slip systems. Our first results have also evidenced the built-up of kinematic hardening at the nanometer scale in a single crystal. Our method has a considerable potential for studying various types of dislocation microstructures and plastic deformation mechanisms in different crystals.

6 Results - Dislocation Electron Tomography - An Association to Discrete Dislocation Dynamics

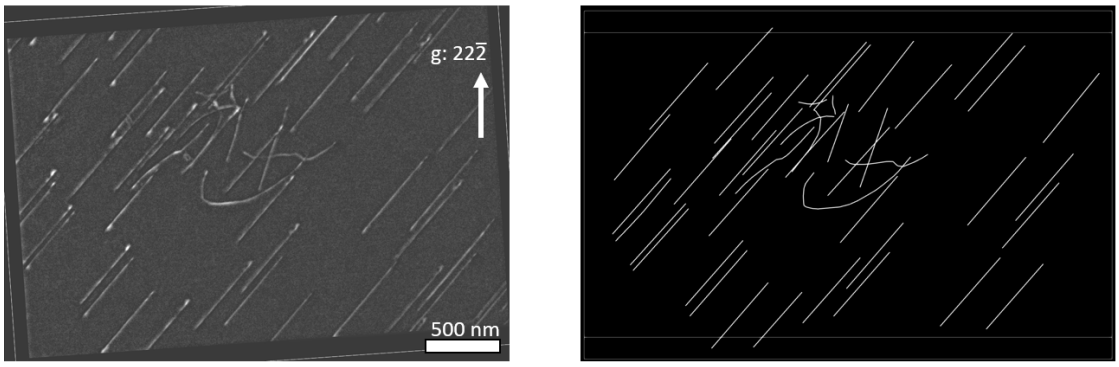

Figure 56: Dislocation microstructure at $0°$, actual micrograph on the left and reconstructed microstructure in NUMODIS on the right.

This study works as a proof of concept by implementing real dislocation microstructure extracted from DET into DDD, departing from the conventional use of artificially created microstructures. Employing DDD simulations via the NUMODIS framework, we aim to bridge the gap between experimental observation and computational modeling. This project utilizes the same olivine specimen as for the FDM analysis of the previous chapter. Limited to the microstructure of tilt series 5 within specimen PoEM9 (Demouchy et al. 2013). To run our simulations we leverage the high-performance computing (HPC) resources at the Mesocentre, equipped with a hybrid cluster boasting 340 Tflops and 244 nodes. An overview of the microstructure and its implementation in NUMODIS can be seen in Figure 56.

6.1 Implementation

6.1.1 Time and length scales

In preparation for our simulation, we had to adjust the simulation parameters according to the initial experiment. The sample, measuring 6.32 mm in length and 4.19 mm in diameter, under-went deformation at a strain rate of $\dot{\varepsilon} = 5.1 \times 10^{-5}\,\mathrm{s}^{-1}$ until reaching a total strain

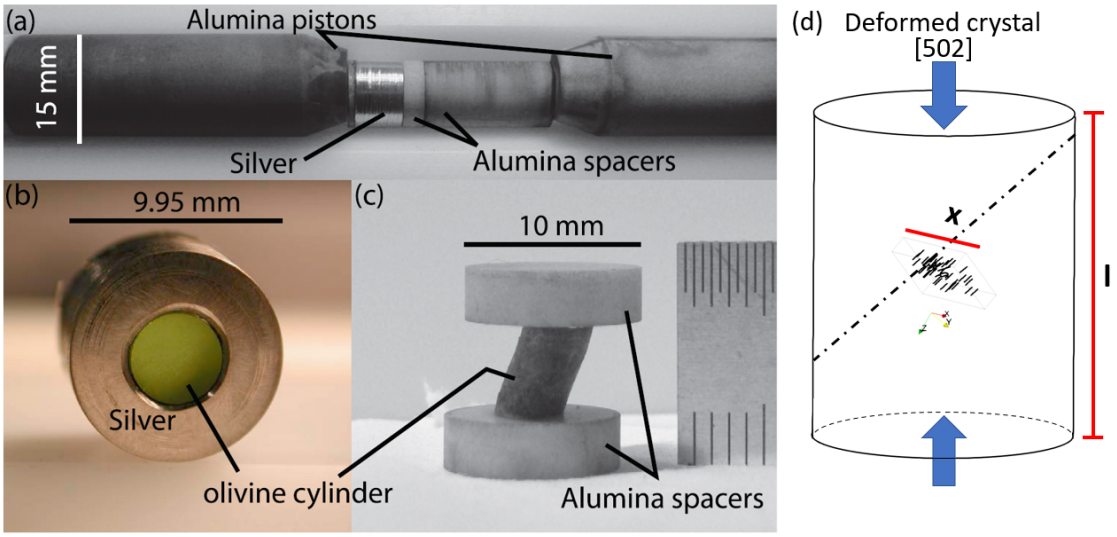

Experimental setup:

Figure 57: (a) High pressure assembly without iron jacket (b) Silver plug with a single crystal of olivine inside (c) A post-deformation olivine crystal (d) Sketch of the compressed cylinder with the compression direction and the orientation of the thin foil within the specimen (highly enlarge to make it visible). Axis grid indicates the orientation in the simulation box. Figure 57(a)-(c) from Demouchy et al. (2013, Figure 1)

of $\varepsilon_{\text{Total}} = 10.1\%$ and a maximum differential stress of 754 MPa. The principal axis of the sample was oriented along $[502]$. An overview of the sample, including scales and orientations, is shown in Figure 57. Considering the length of the cylinder and the strain rate, the resulting average deformation velocity can be approximated as:

$$v = l\dot{\varepsilon} \approx 3 \times 10^{-7}\,\text{m/s} = 3 \times 10^{-6}\,\text{Å/ns} \tag{6.1}$$

Using the unit set employed in NUMODIS, and considering that the length scale of our thin foil is approximately 1μm with a desired total strain of at least 1%, the time duration we have to simulate is given by:

$$t = \frac{x}{v} = \frac{(0.01 \times 1 \times 10^{-6}\,\text{m})}{(3 \times 10^{-7}\,\text{m/s})} \approx 0.03\,\text{s} \tag{6.2}$$

With this context in mind, we adjusted the limiting simulation parameters, including the timestep (Δt), maximum displacement (d_{max}), and minimum discretization length (l_{min}) between two nodes. To maintain stability, d_{max} is constrained to not exceed 10% of l_{min}, which we set to a maximum value of 100 Å(the thickness of dislocations in WBDF conditions), thus restricting d_{max} to 10 Å. Furthermore, the relationship between d_{max} and the timestep (Δt) was evaluated through the maximum displacement velocity. Incremental increases in the timestep, from 0.5 ns to 50 ns, were examined to ensure consistent simulations, with an

additional test focused on the interactions between two dislocations, utilizing a timestep of 5 ns. The resulting maximum velocity using the final time step $\Delta t = 50$ ns is:

$$v_{\mathsf{max}} = \frac{d_{\mathsf{max}}}{\Delta t} = \frac{10\,\text{Å}}{50\,\mathsf{ns}} = 0.2\,\text{Å}/\mathsf{ns} \tag{6.3}$$

This approach appears reasonable, given that our average deformation velocity is five orders of magnitude lower than the maximum displacement velocity. An effect we have to account for is the non-uniform dislocation velocity in our specimen. As the tomography analysis discussed in Mussi et al. (2014), the microstructure in this olivine specimen shows many screw dislocation segments, which is linked to a high lattice friction for screw (due to the core structure). Non-screw characters exhibit a higher intrinsic mobility. To overcome this problem, a constant ratio is taken between the velocities of the both fast and slow segments. All slip systems have the same ratio. This ratio between edge and screw is in the range 100-1000 according to Durinck et al. (2007b). Despite this, we are still at least two orders of magnitude lower than the maximum velocity. Thus, even if we encounter velocity peaks due to local stress concentrations, our approach should still yield meaningful results.

6.1.2 Simulation Parameters

Employing the code outlined in Section 3.3.2, we converted our tomography data into input for the DD simulations. The microstructure orientation is converted via Bunge Euler angles, from experiment to the simulation box reference frame. The applied stress in the simulation was aligned with the experimental conditions. We applied the maximum differential stress of 754 MPa. This stress is oriented along $[502]$, which corresponds to an a applied stress tensor:

$$\sigma_{app}(\mathsf{MPa}) = \begin{pmatrix} -601.6 & 0 & -302.8 \\ 0 & 0 & 0 \\ -302.8 & 0 & -152.4 \end{pmatrix}$$

The initial simulation box was set up to match the outline of our thin section. Subsequently, we extended it to account for the effect of curvature as described in Section 2.1.3 where the radius of curvature R is inversely proportional to the applied stress τ. Figure 58 shows how strong this effect can be: an artificial edge dislocation is simulated with variation in length, applied stress and the segmentation length. Due to the limitations imposed by the thin foil's thickness, approximately 500 nm, our dislocations are truncated to a certain length. To address this limitation, we extended all large dislocations (to double their lengths) under

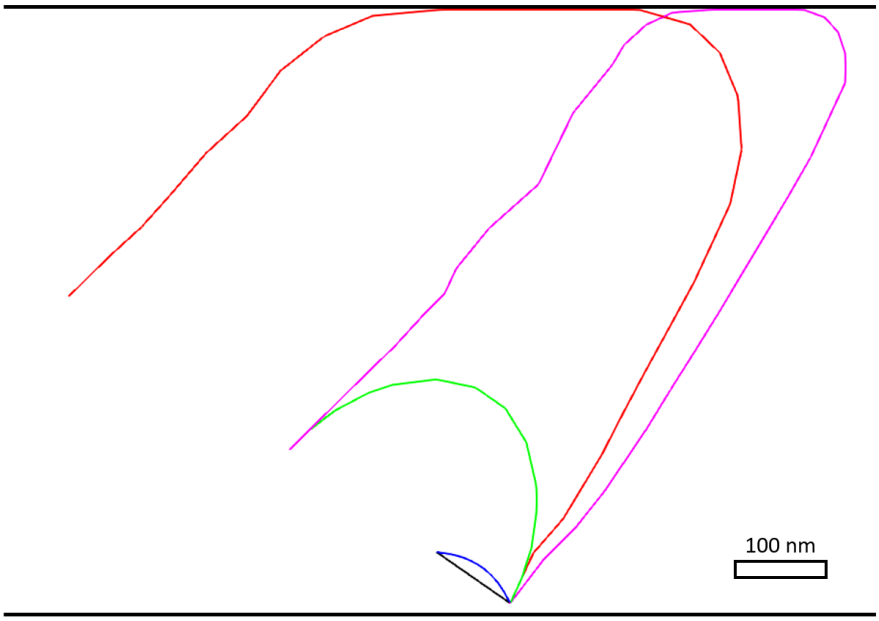

Figure 58: Simulation of an edge dislocation changing different starting parameters: Small blue dislocation with a minimum segment length l_{min} of 1 nm and a total length l_{total} of 100 nm; black dislocation with identical length, but with $l_{min} = 10\,nm$, which is used for all the others; green with $l_{total} = 300\,nm$ the same for pink but with double the stress; red with the same stress as green, but with $l_{total} = 600\,nm$.

the assumption of a consistent continuation into the bulk specimen, alongside enlarging the simulation box size (refer to Figure 59). However, a few strongly curved segments remain problematic and kept therefore in their original length. An additional reason to extend dislocation segments is to reduce the effect of mirror forces on the simulation boundaries, which is stronger the closer the dislocation segments are to the boundaries. A reason why we pinned all dislocations at their extremities even at the surface of the simulation box.

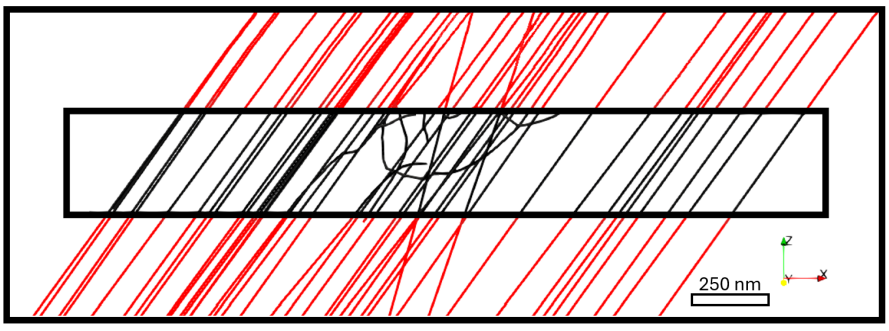

Figure 59: Extension of the simulation box, with the initial dislocation microstructure in black inside the thin foil (inner box), and the extension of the microstructure inside the larger volume.

6.1.3 Velocity law

At the experimental temperature ($806°C$) we are in a low temperature regime for olivine, were a kink pair mechanism is active. At the current state, we try to implement a velocity law for the thermally activated kink-pair mechanism (see eq. 2.20). However, we encounter persistent stability challenges associated with the thermal approach, discussed further in Section 6.4. For the mean time, we are employing a modified version of the athermal law (see eq. 2.21), adjusted with distinct dragging coefficients for edge and screw dislocations to accommodate their inherent differences, as previously noted:

$$B(\theta) = B_{edge} sin^2(\theta) + B_{screw} cos^2(\theta) \tag{6.4}$$

Here, the dragging coefficient for edge B_{edge} is set lower than the dragging coefficient for screw B_{screw} (see Table 6.1). To align with experimental temperatures, we optimize B_{screw} using values derived from the kink-pair velocity study of Durinck et al. (2007b).

Table 6.1: Simulation parameters used in NUMODIS, dragging coefficients are adjusted based on Durinck et al. (2007b)

Parameter	**Symbol**	**Value**
Time step	Δt	50 ns
Maximum displacement	d_{max}	10 Å
Minimum discretization length	l_{min}	100 Å
Maximum discretization length	l_{max}	1000 Å
Edge dragging coefficient	B_{edge}	5×10^4
Screw dragging coefficient	B_{screw}	2×10^7

6.1.4 Material

Olivine crystallizes in the orthorhombic system (space group, P*bnm*), the corresponding lattice parameters are given in Table 6.2. Even though olivine is anisotropic, NUMODIS only takes isotropic elastic behaviour into account (see Section 3.3.2). Consequently, the elasticity of olivine is estimated with Lame coefficients (Isaak et al. 1989). For our simulation we consider three active slip systems: [001](100), [001](110) and [001]($1\bar{1}0$) observed experimentally by Mussi et al. (2015b). Based on a study of Tommasi et al. (2000), all three slip systems have approximately the same CRSS, why we assume an identical activation behaviour.

To account for the distance at which it is considered that two dislocations collide, NUMODIS defines a capture radius. In a first approximation, we adopted a preset value for the capture radius in NUMODIS, set at 2 Å. However, this capture radius proved insufficient to initiate

elastic dislocation interactions. To refine our estimation of the core radius, we referenced the findings of Durinck et al. (2007a) and Mahendran et al. (2021). Their studies revealed that screw dislocations along [001] are dissociated in (100) and $\{110\}$ planes, with a separation distance between the two partials of less than 15 Å. In (010) plane, [001] screw dislocations are un-dissociated and presents a narrow core, with the half-width below 6 Å. Given that dissociation is not experimentally observable for us due to resolution limitations of the diffraction contrast in TEM, we used the half-width of the narrow core for each slip system. Thus, for all simulations, we employed a core radius of c/2 (3Å). Nevertheless, we conducted tests using various core radius values ranging from c/2 to c. Despite this variation, consistent behavior and results were observed, validating the choice of c/2 as the core radius.

Table 6.2: **Lattice parameters** and **Lame coefficients** (isotropic assumption) of olivine at $P = 300\,MPa$ and $T = 1079\,K$ based on (Isaak et al. (1989))

a (Å)	b (Å)	c (Å)	λ(GPa)	μ(GPa)
4.7535	10.1843	5.9807	77.4	78

6.1.5 Refinements

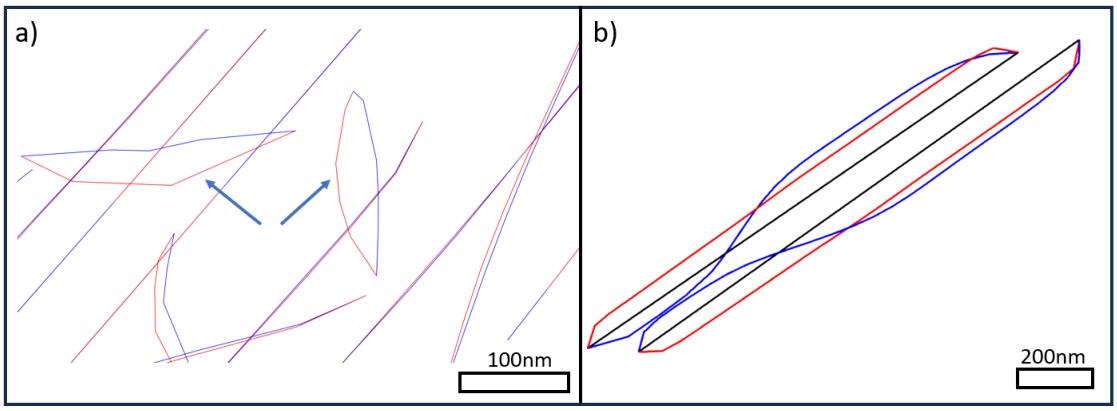

Figure 60: Refinement of the dislocation microstructure: (a) Initial line direction in blue showed incorrect bending direction; red inverse line directions for the tiny dislocations indicated by the arrow, agreed with bending visible in the thin foil; an effect of the change on the surrounding microstructure is also clearly visible. (b) Change of habit planes for two dislocations; black line starting condition; blue line plane initially used, showing a strange interaction behavior; dislocation with change plane in red, showing regular translation behavior similar to the original microstructure.

In the examination of pure screw dislocations, all three active slip systems were tested and then assigned to reflect the most stable configuration. Instances of instability were addressed by adjusting the plane to achieve stability, as depicted in Figure 60 (b). For the a few small dislocations the line direction was unclear. To put it in correct order, we tested every permutation and chose the one that best represents the original microstructure (see Figure

60 (a)). For part of dislocations that are in climb configuration we assigned a non-active glide plane, to keep them immobile. The final refinement was to reduce the visible part of the volume to the initial thin foil size.

6.2 Results

An overview of the final simulation at different time steps is presented in Figures 61 and 62. The simulation represents a total simulated deformation time of 0.1 s.

Notably, the motion of screw dislocations appears slow, contrasting with the rapid velocities observed for edge segments. Due to the simplicity of the microstructure, only one type of interaction is observed throughout the simulation. A collinear annihilation takes place close to 18 ms, illustrated in Figure 63, between two dislocations with opposite Burgers vectors. One glides in [001](100) and the other in $[00\overline{1}](110)$. Both dislocations are attracted to each other along a large section before the annihilation. The annihilation occurs only locally, when the dislocations are connected. The annihilation produces a recombination in two new dislocations. One is retracting fast to surface, and for the other one the interaction produces a tip (see Figure 63 (b)). After a few milliseconds this tip disconnects from the dislocation and leaves a debris behind. It leaves a single segment behind which is an artifact from the simulation, from the relaxation of the debris.

Towards the later stages of the simulation, at significantly high time steps (see Figure 62 (b)), an anomalous phenomenon emerges: the screw segments undergo uncharacteristic bending. This deviation is attributed to the pinning of dislocations at the surface of the extended box, leading to this nonphysical behavior.

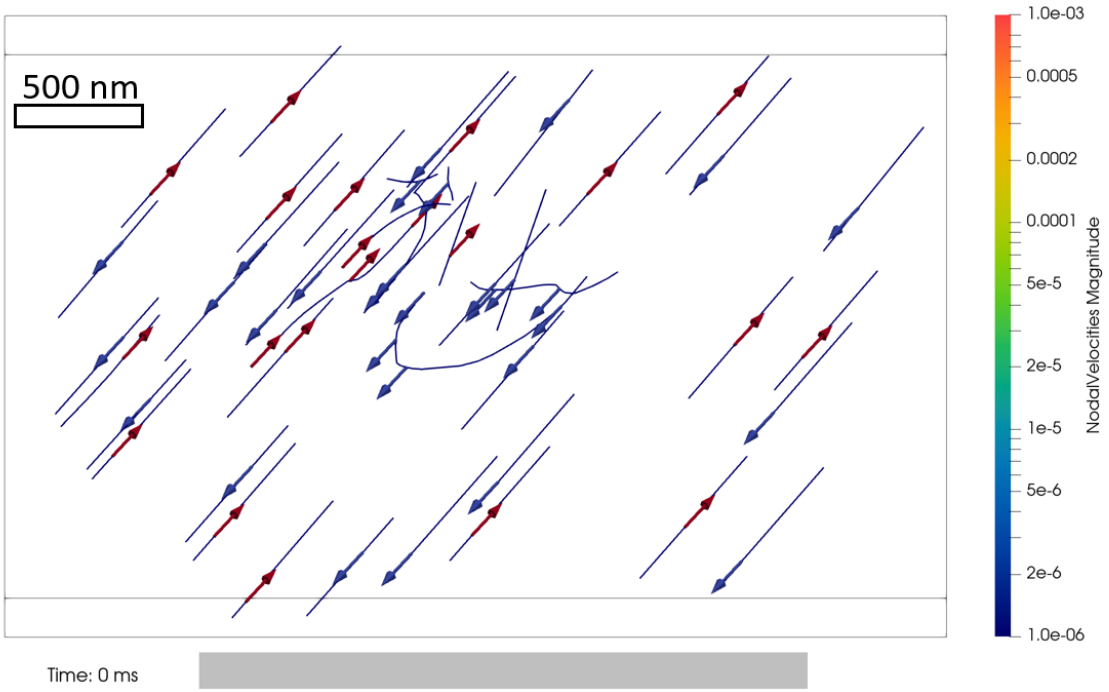

(a)

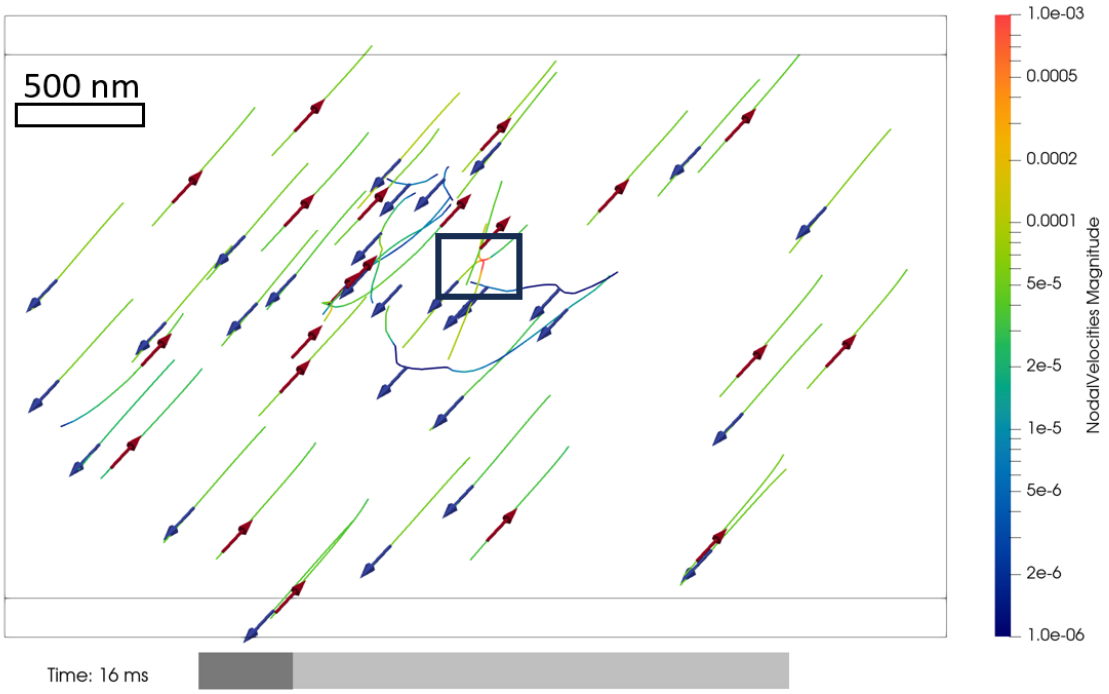

(b)

Figure 61: Simulation of the microstructure at different time steps. The lines are colored according to the velocity in Å/ns, in addition the Burgers vector directions are indicated with the colored arrows. (a) Starting microstructure; (b) microstructure after 16 ms, black box indicates interaction detailed in Figure 64.

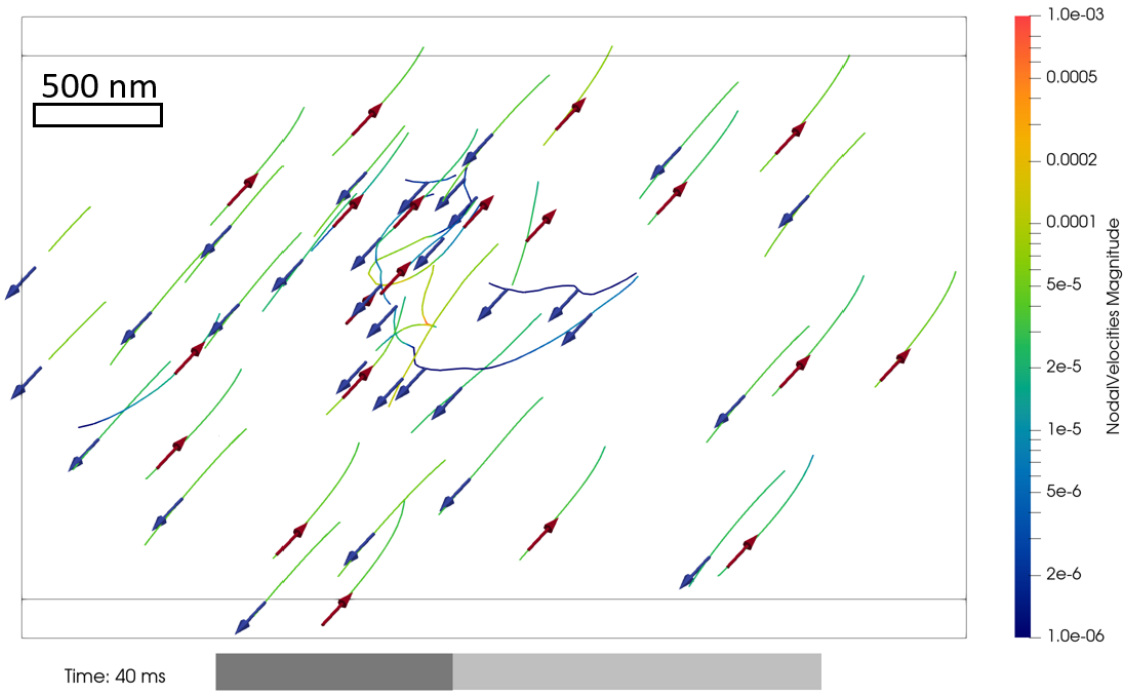

(a)

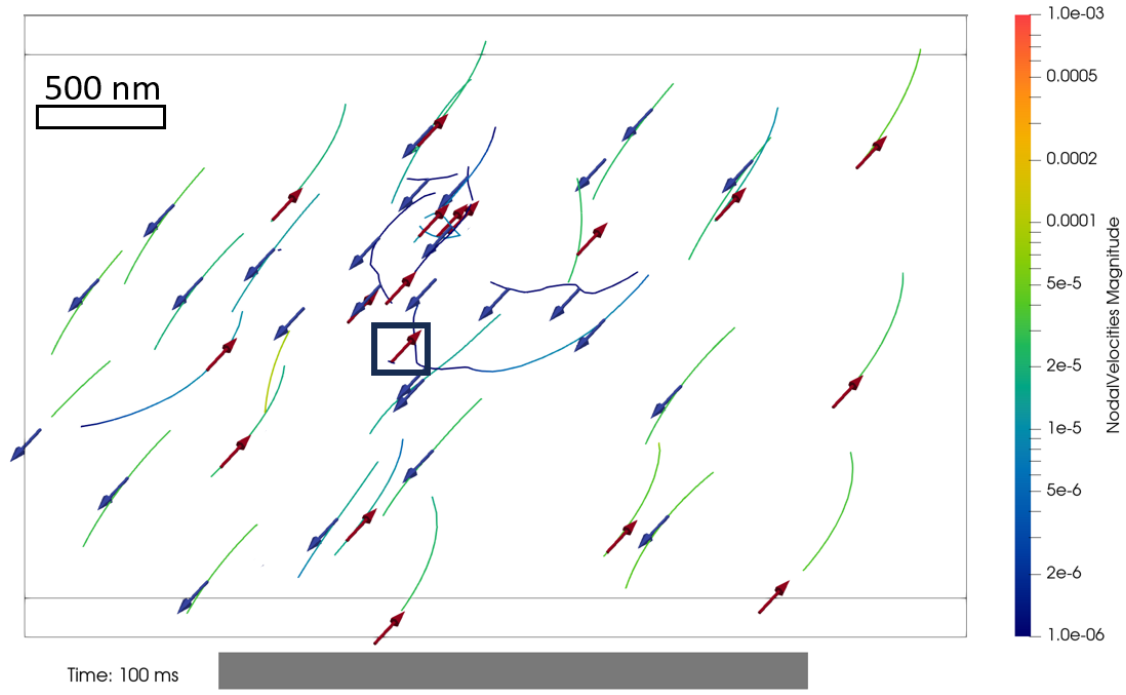

(b)

Figure 62: Simulation of the microstructure at different time steps. The lines are colored according to the velocity in Å/ns, in addition the Burgers vector directions are indicated with the colored arrows. (a) dislocation microstructure after 40 ms; (b) final microstructure after 100 ms, black box indicates the debris left behind from the annihilation shown in Figure 63.

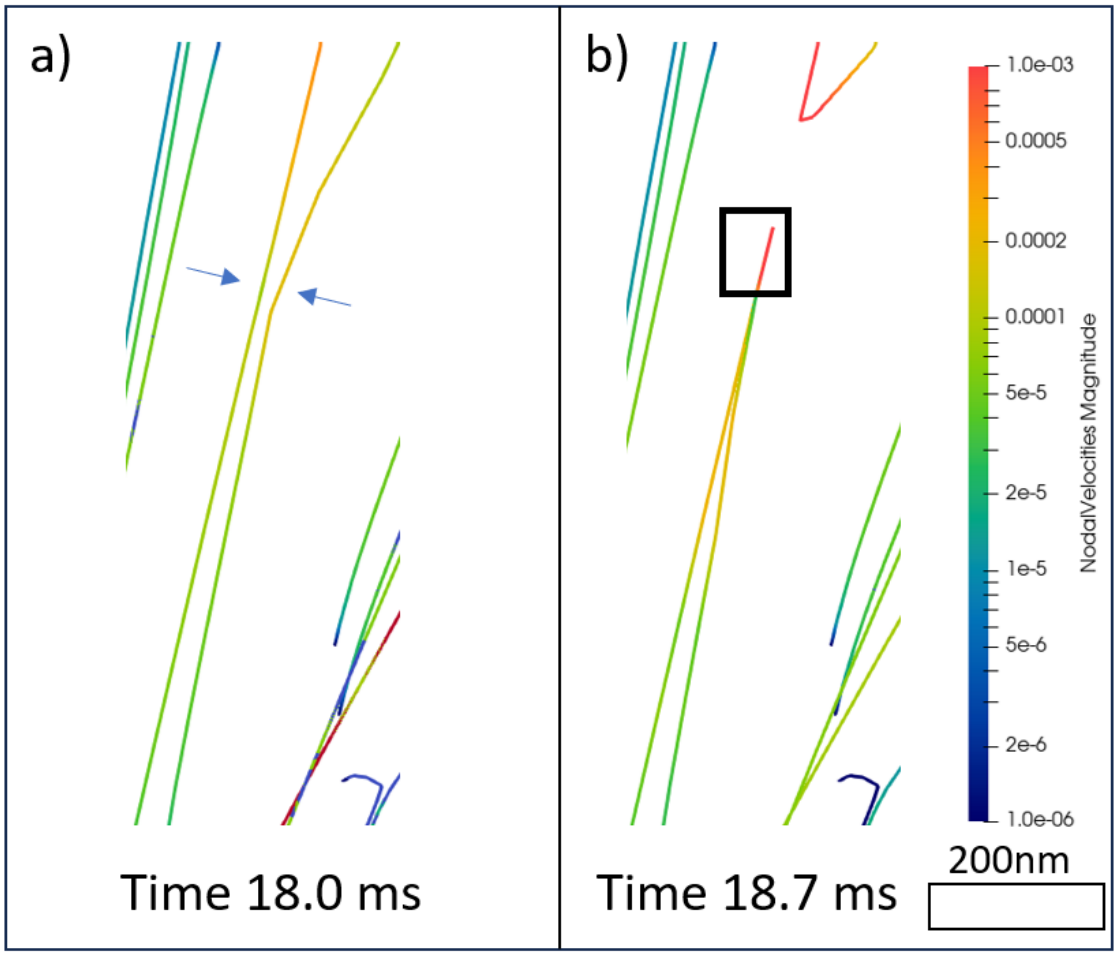

Figure 63: Observed collinear annihilation: The lines are colored according to the velocity in $\text{Å}/ns$. (a) Shows dislocations and the surrounding microstructure directly before the annihilation happens at the position indicated by the two arrows. (b) State after the annihilation, with the top part retracting to the surface of the simulation box; the black box shows the entangled segments, that later separate and form a debris as shown in Figure 62 (b).

6.3 Discussion

We had to cope with several challenges regarding the thin foil boundaries. It had influence regarding the curvature of dislocations and created mirror forces due to the boundary conditions. We accounted this problem by artificially enlarging the simulation volume. But therefore, we had to make the hypothesis to extrapolate of the dislocations as straight screw segments. This assumption was grounded in the observation of the general microstructure, which exhibited long, extended loops predominantly characterized by large screw segments, attributed to high lattice friction. For the straight non screw dislocations, we assumed a straight continuation as well, since their curvature seems to be negligibly small compared to the increase in length. We pinned the surface nodes of dislocation to mitigate the influence of mirror forces on the internal evolution of the structure. In the normal case these surface

nodes are allowed to move freely. The pinning created back stresses at high strain due to the resulting curvature. (see Figure 62 (b)).

The study also delved into the dynamics of dislocation movement, noting the velocity for screw dislocations could be well adapted based on the work of Durinck et al. (2007b). The general behavior which would rely on a thermal kink pair mechanism is still in development, but even with our simple approach, we could recreate certain mechanism that would have been expected in this specimen. Collinear interaction is observed during the simulation.

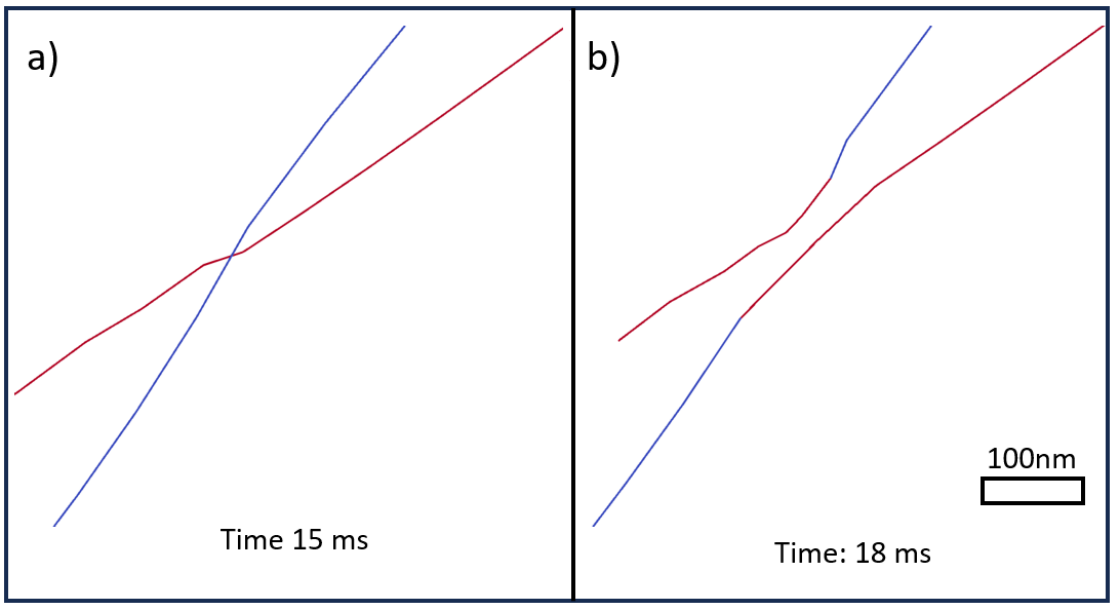

Figure 64: Interaction between two dislocation with collinear planes, (110) in red and (100) in blue; (a) approaching dislocations; (b) dislocations after an exchange of arms, both dislocations consists now with an upper part in one plane and a lower part in another plane.

Experimentally, collinear interaction has been observed in the same specimen but in different area (Mussi et al. 2015a).

Notably, a non-physical interaction occurs after around 15 ms, which is further elucidated in Figure 64. This interaction occurs between two dislocations with the same Burgers vector, but in different planes: one screw configuration in [001](100) and another one mixed configuration in [001](110). Close to 15 ms both dislocations start to interact repulsively (Figure 64 (a)). The mixed dislocation, which has the higher velocity, catches up to the one in screw configuration and creates some oscillations, due to a problem of stability in the code. These oscillations related to interplay with the repulsive forces create a state where two segments are in opposite sign. This instability allows annihilation. Both dislocations glide afterwards in two different planes (Figure 64 (b)). This artefact of the simulation has been difficult to remove at this point.

A crucial aspect of our analysis was the emphasis on the simplicity of our microstructure. With most dislocation in simple screw glide configuration, it provided the clarity for a proof of concept study. Especially since the involving orientations and loading conditions where known. Despite its simplicity, the model facilitated direct comparisons with previous studies on olivine, notably Durinck's work, enhancing the relevance and applicability of our findings. However, the study's simplicity also introduced significant constraints, particularly in capturing complex interactions and the diversity of interactions, which were limited by the unique Burgers vector, screw dislocations, and glide mechanisms across only three predominant slip systems. Notably, the model's current iteration did not incorporate climb and cross-slip mechanisms. Both are important to represent the full dynamic behavior in the microstructure especially under conditions of high strain. Unfortunately, it's a challenging task to incorporate in DDD modeling.

6.4 Conclusion

Throughout this proof of concept study, we encountered numerous challenges in bridging the gap between experimental results from tomography and simulation at mesoscale. We had to extract the positions of the image of the dislocation cores from the DET and link them precisely with the orientation and deformation conditions from the experiment to be able to simulate them. Since, in this study, we worked with a real microstructure and not with virtual dislocations. We had also to account for the velocity law in the regime of the experiment, which is to this point only partly resolved, since the values are reasonable to alignment with previous studies, but the actual mechanism is not yet incorporated. Then there where parts of the microstructure that could not be transferred due to missing information from the reconstruction. One of the key hurdles we encountered involved managing dislocations in odd or unknown configurations. For instance, identifying the habit planes or line directions for certain dislocations within the microstructure was initially problematic. However, our simulations ultimately provided clarity, helping to resolve these ambiguities. We are also still missing some mechanisms, namely cross-slip and climb, which are at currently not incorporated in our simulation, but would help to allow for more possible interactions inside the microstructure. Still the findings we had, as the collinear interaction, demonstrated that complex interaction need several no screw dislocations.

Looking ahead, we want to enhance the accuracy and robustness of our simulation framework. To do this, we want to better reflect the velocity mechanism in our microstructure. We try to incorporate an approach by Amodeo et al. (2011) in MicroMegas, which tries to reproduce a

kink pair mechanism. We slightly adjusted the velocity law used for the screw dislocation to be consistent with the work of Durinck et al. 2007b, with a velocity law (Kocks et al. 1975) (as described in section 2.3.2.1). It is worth noting that this velocity law is non-local, since it correlated with the entire length of the segment, that is in screw configuration. It therefore requires some criteria to detect this length of the screw part of a dislocation. This special implementation is so far unstable. We had particular problems in mitigating effects associated with the thickness of thin foils in simulations, particular mirror forces. This could be overcome with EL NUMODIS, a coupled code that integrates a finite element model with NUMODIS, as recently developed (Gonzalez-Joa et al. 2023). Although more computationally demanding, this approach promises significant advancements, handling the surface effects. In the near future, we anticipate finalizing the conversion from DDD output files to FDM, which will enable us to observe the evolution of various fields over the simulation's timespan. It would for example give the option to look at the stress and strain fields related to the interaction, which then could be compared to the same kind of interactions from other experiments.

This work is critical for advancing our understanding of dislocation dynamics beyond the limitations of simple modelling by comparing it with the experiment.

7 Side Project - Modeling creep in periclase (MgO) under lower mantle conditions

This is work finds its origin during my master program and continued over to the first year of my PhD thesis, where the finalized simulations were performed, and the paper was constructed and later published in Nature[1]. My personal contribution to this work correspond to the 2.5 D modelling of creep of periclase (MgO), which I worked on together with K. Gouriet.

Transport of heat from the interior of the Earth drives convection in the mantle, which involves the deformation of solid rocks over billions of years. The lower mantle of the Earth is mostly composed of iron-bearing bridgmanite and approximately 25% volume periclase (also with some iron). It is commonly accepted that ferropericlase is weaker than bridgmanite (Yamazaki and Karato 2001). Considerable progress has been made in recent years to study assemblages representative of the lower mantle under the relevant pressure and temperature conditions (Girard et al. 2016; Miyagi and Wenk 2016). However, the natural strain rates are 8 to 10 orders of magnitude lower than in the laboratory, and are still inaccessible to us. Once the deformation mechanisms of rocks and their constituent minerals have been identified, it is possible to overcome this limitation thanks to multiscale numerical modelling, and to determine rheological properties for inaccessible strain rates. In this work we use 2.5-dimensional dislocation dynamics to model the low-stress creep of MgO periclase at lower mantle pressures and temperatures.

7.1 Periclase deforms slower than bridgmanite at lower mantle conditions

This work aims to model steady-state creep of periclase under lower mantle conditions, with an emphasis on the role of extremely low strain rates. It is based on the extensive knowledge we have of the deformation of this oxide following (1) the large number of experimental studies

[1] Cordier, P., K. Gouriet, T. Weidner, J. Van Orman, O. Castelnau, J. M. Jackson, and P. Carrez (2023). "Periclase deforms more slowly than bridgmanite under mantle conditions". In: *Nature 613.7943, pp. 303–307*.

carried out on this ceramic since the 1970s, including the more recent mineral physics studies taking into account the effect of pressure, and (2) the important modelling effort carried out in recent years. At room pressure, periclase is easily deformed by glide of $\frac{1}{2}<110>$ dislocations on $\{110\}$ planes. The thermal activation of this mechanism can now be modelled from the atomic scale (Amodeo et al. 2011), even at low strain rates (Cordier et al. 2012). Pressure strongly affects this mechanism and induces a transition of glide towards the $\{100\}$ planes above 50 GPa (Amodeo et al. 2012; Girard et al. 2012; Immoor et al. 2018; Marquardt and Miyagi 2015). At high temperature, dislocations glide without friction (athermal regime) and the flow stress results from dislocation interactions, leading, at large strains and strain rates to a pronounced hardening (Amodeo et al. 2014). At low strain rates, ionic diffusion can enhance recovery mechanisms and allow steady-state creep (Reali et al. 2017). In this study, we model the influence of mantle pressures on steady-state creep of periclase by 2.5-dimensional (2.5D) dislocation dynamics (DD). We focus on four pressures: 30, 60, 90 and 120 GPa, which, along the geotherm (Stacey and Davis 2004), correspond to 2,000, 2,300, 2,500 and 2,800 K respectively, at around depths of 800, 1,500, 2,100 and 2,700 km respectively.

7.1.1 Diffusion coefficients

Dislocation climb in MgO is enabled by diffusion of Mg and O atoms, and the climb rate is controlled by the slower diffusing species. Diffusion in MgO has been studied for decades, and the mechanisms and rates of cation and anion diffusion are well established (Van Orman and Crispin 2010). Mg and O diffuse using vacant sites on the cation and anion sublattices, respectively. Because the concentration of cation vacancies is much higher than that of anion vacancies, in both nominally pure synthetic and natural periclase samples, O diffusion is orders of magnitude slower than Mg diffusion, and is the rate-limiting step in dislocation climb. Whereas Mg diffusion is controlled by extrinsic vacancies, produced to charge-balance trivalent (and tetravalent) cation impurities, O diffusion is intrinsic, enabled by thermally produced Mg and O vacancy pairs (Schottky defects).

To calculate the oxygen self-diffusion coefficient, $D^{\mathrm{sd}}_{\mathrm{Ox}}$, over the full range of temperatures and pressures relevant to Earth's mantle, we use the expression presented by Ita and Cohen (Ita and Cohen 1997), which is derived from their theoretical results on vacancy formation and migration:

$$\ln D^{\mathrm{sd}}_{\mathrm{Ox}} = \ln \alpha^2 \nu_a + \frac{S_0 + PS'_0}{k_B} - \frac{E_0 + PV_0 + P^2V'_0}{k_B T} \tag{7.1}$$

Table 7.1: Oxygen self-diffusion parameters for MgO global fit as a function of pressure and temperature (Ita and Cohen 1997)

Parameter	Symbol	Value
Attempt frequency	ν_a	5.4 THz
Activation entropy at $P = 0$	S_0	4 k_B
S_0 pressure derivative	S_0'	0.02 k_B GPa^{-1}
Activation energy	E_0	0.4 $\times 10^{-19}$ J
Activation volume at $P = 0$	V_0	16.7 Å^3
V_0 pressure derivative	V_0'	-0.038 Å^3 GPa^{-1}

where P and T are in GPa and K respectively, a is the lattice constant and k_B is the Boltzmann constant. The other parameters are listed in Table 7.1. The enthalpies are obtained by inverting the Arrhenius equation of diffusion coefficient:

$$D_{\mathrm{Ox}}^{\mathrm{sd}} = D_0 \exp\left(-\frac{\Delta H^{sd}}{k_B T}\right) \tag{7.2}$$

where $D_0 = 7.2 \times 10^{-4}\,\mathrm{m^2\,s^{-1}}$ and ΔH^{sd} are, respectively, the exponential prefactor and the activation enthalpy (Reali et al. 2017). The activation enthalpies for each set of pressure/temperature and the diffusion coefficients are given in Table 7.2.

Table 7.2: Oxygen self-diffusion coefficients ($m^2 s^{-1}$) from equation 7.1 and activation enthalpy (eV) for MgO obtained from equation 7.2

P (GPa)	T (K)	$\mathbf{D_{Ox}^{sd}}$	$\mathbf{\Delta H}$
30	2000	6.61×10^{-27}	9.15
60	2300	3.05×10^{-29}	11.59
90	2500	3.46×10^{-31}	13.56
120	2800	5.26×10^{-31}	15.09

This expression produces values of $D_{\mathrm{Ox}}^{\mathrm{sd}}$ that are in agreement with the most reliable experimental results on intrinsic O diffusion from Yang and Flynn (1994) (see Figure 65). Higher values of $D_{\mathrm{Ox}}^{\mathrm{sd}}$ determined by Van Orman et al. (2003) at high pressure are considered to reflect the contribution of dislocations (Dos Reis et al. 2022) and/or other extended defects, as in most other studies of oxygen diffusion in MgO (Van Orman and Crispin 2010). The results of Ita and Cohen (1997) are also similar to those presented in several later theoretical studies (Ammann et al. 2010; Karki and Khanduja 2006; Runevall and Sandberg 2011).

7.1.2 Modelling dislocation creep of periclase

To model plasticity of periclase under mantle conditions, we use a 2.5D DD simulation approach (see section 3.3.4) already benchmarked for periclase at ambient pressure (Reali et

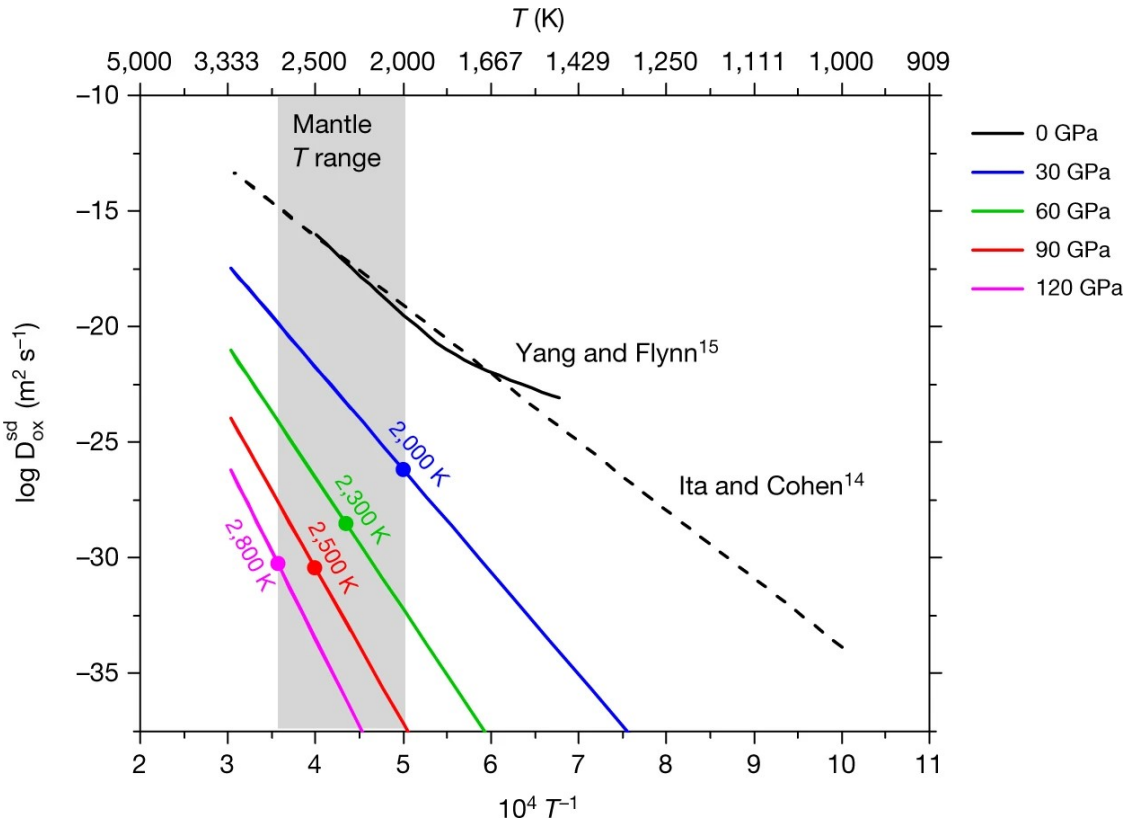

Figure 65: Oxygen diffusion coefficients in periclase:The solid black line represents the diffusion coefficients of Yang and Flynn (1994). The black dashed line corresponds to the diffusion coefficients of Ita and Cohen (1997) at 0 GPa. The other lines (blue, green, red, and magenta) correspond to Equation 7.1 at 30, 60, 90, and 120 GPa respectively. The range of temperatures considered in this study $[2000\,\text{K} : 2800\,\text{K}]$ is shown with the grey shading. The symbols (filled circles) correspond to the (P,T) conditions along the geotherm considered in the present study (Stacey and Davis 2004) (Table 7.2).

al. 2017). Our creep results are presented in Figure 66(a), which shows the creep strain rates obtained from the 2.5D DD simulations as a function of the creep stress for the four (P,T) conditions selected. A constant slope is found for all these strain rate–stress curves, which gives the value of the power law stress exponent, $n = 3.1$. A strong pressure dependence is found between $(30\,\text{GPa}, 2,000\,\text{K})$ and $(90\,\text{GPa}, 2,500\,\text{K})$, whereas creep rates at $(90\,\text{GPa}, 2,500\,\text{K})$ and $(120\,\text{GPa}, 2,800\,\text{K})$ are very close due to very similar values for the diffusion coefficients (Figure 65 and Table 7.2). On Figure 66(a) we compare the creep rates of periclase with those of bridgmanite at the same depths. For bridgmanite, we use the results of Reali et al. (2019b) for pure climb creep (PCC) with a vacancy concentration $X_v = 1 \times 10^{-5}$; these results were shown to be in good agreement with empirical geophysical constraints on the viscosity profile of Earth's lower mantle. Bridgmanite and periclase exhibit similar stress exponents. However, we see that these calculations lead to bridgmanite having higher creep rates than periclase at any depth. To better illustrate this difference, we report, on Figure 66(b), the viscosity contrast between those two phases, taken as the ratio

$\eta_{\text{Per}}/\eta_{\text{Bdm}}$. We see that under lower mantle conditions, bridgmanite creep rates are 10^3 to 10^7 greater than periclase creep rates. This result reflects the fact that in the lower mantle, anionic diffusion in periclase is much slower than cationic diffusion in bridgmanite (see Figure 67).

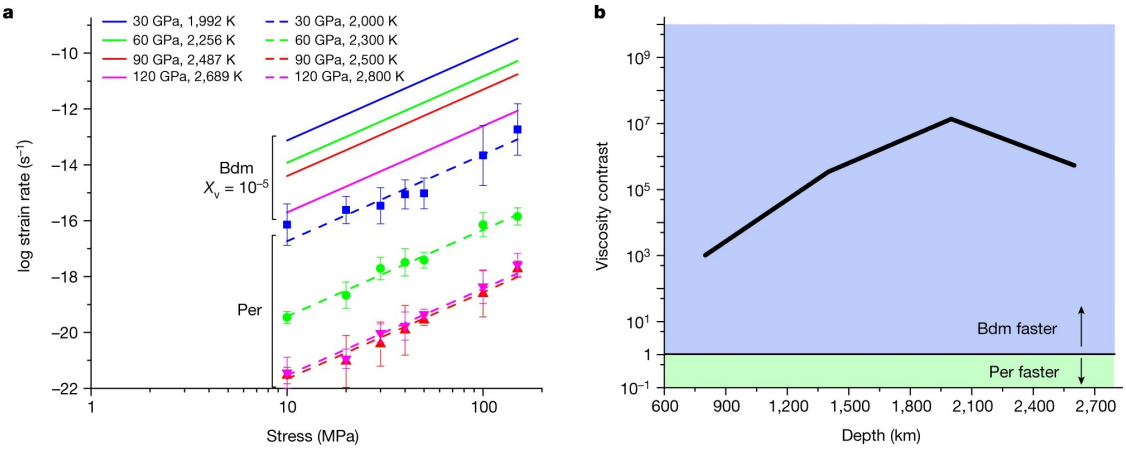

Figure 66: Creep rate modelling: (a) Creep strain rates as a function of applied stress of bridgmanite (Bdm; solid line) and periclase (Per; symbols) at 30 GPa (blue), 60 GPa (green), 90 GPa (red), and 120 GPa (magenta). (b) Viscosity contrast $\eta_{\text{Per}}/\eta_{\text{Bdm}}$ (calculated at 10 MPa) between the two pure phases, periclase and bridgmanite, as a function of depth.

7.1.3 Laboratory versus nature

In this paragraph, we address the influence of strain rate on deformation mechanisms. Our calculations showing that bridgmanite deforms faster than periclase under mantle conditions seem to contradict the common intuition that the silicate is stronger than the oxide. Beyond general considerations (Yamazaki and Karato 2001) or studies of analogous compounds (Kaercher et al. 2016; Wang et al. 2013), Girard et al. (2016) conducted experiments under mantle conditions of pressure and temperature that show very clearly that ferropericlase accommodates most of the strain compared to bridgmanite. We show here that there is no fundamental opposition between modeling and experiments and that our models are able to account equally for natural and experimental conditions. The experiments of Girard et al. (2016) are conducted at a strain rate of $3 \times 10^{-5}\,\text{s}^{-1}$ and under very high stresses. Under these laboratory conditions, dislocation glide is expected as the dominant deformation mode. For bridgmanite, dislocation glide is thermally activated under these conditions, and a model based on the Orowan equation can be built (Orowan 1934). The stress values predicted by this model are reported in Figure 68. They are close to the experimental values (slightly lower as this model was constructed for single crystals and does not involve grain boundaries). At $30\,\text{GPa}$ and $2,000\,\text{K}$, dislocations in periclase glide in the athermal regime (Amodeo et al.

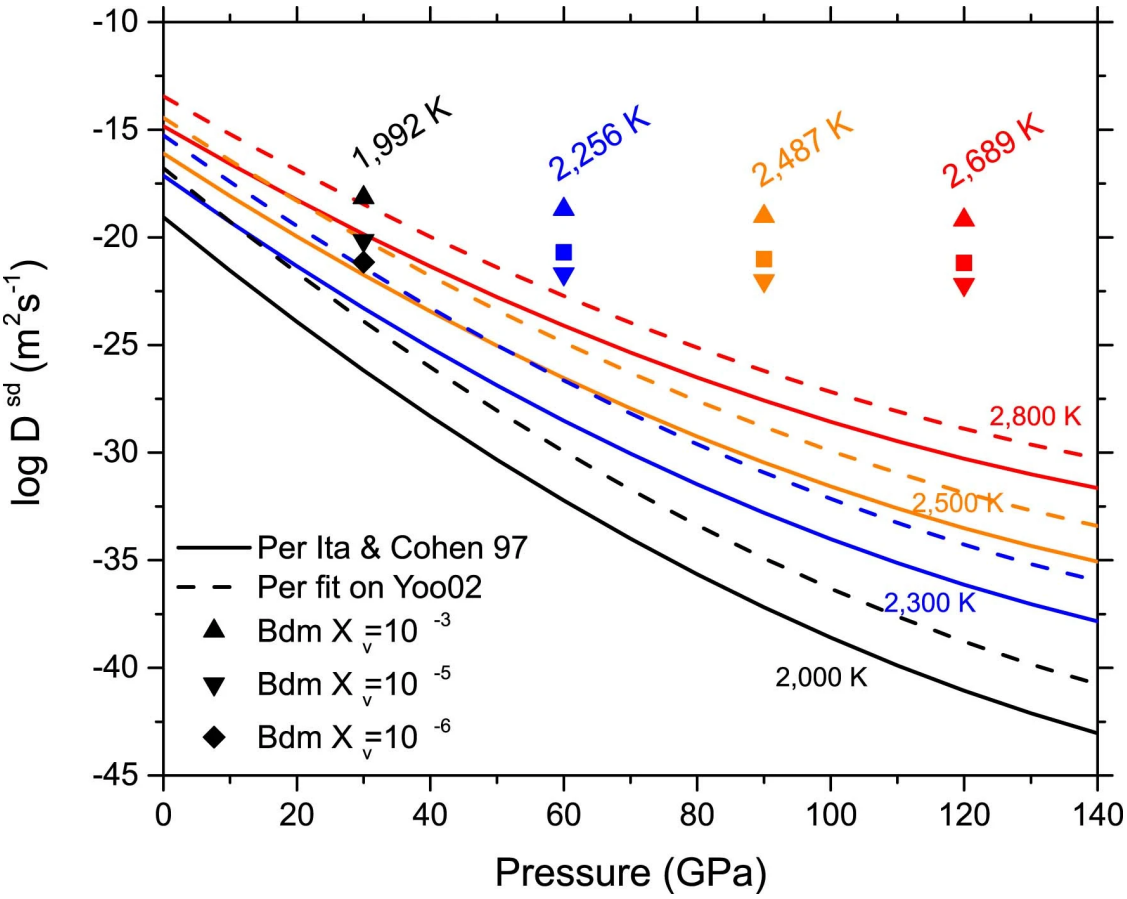

Figure 67: Pressure dependence of ionic diffusion: The lines represent oxygen diffusion coefficients in periclase (Per). We compare the data of Ita and Cohen (1997) (solid lines) to those obtained from the pressure dependence of Ita and Cohen (1997) but anchored on data from Yoo et al. (2002) (dotted lines). The symbols correspond to magnesium diffusion in bridgmanite (Bdm) considering a range of vacancy concentrations from 10^3 to 10^6

2012). Several deformation experiments of periclase report that in the athermal regime, no steady state is reached, and strain hardening occurs (Copley and Pask 1965; Hulse and Pask 1960; Routbort 1979) under the influence of dislocation–dislocation interactions. The origin of this strain hardening has been studied and modeled by Amodeo et al. (2014). It is well described by the Taylor mechanism, and the athermal stress τ_f required to overcome the forest dislocation network is given by:

$$\tau_f = \mu b \frac{\ln\left(1/b\sqrt{\beta\rho_{\mathrm{f}}}\right)}{\ln\left(1/b\sqrt{\beta\rho_{\mathrm{ref}}}\right)} \sqrt{\beta\rho_{\mathrm{f}}} \tag{7.3}$$

where μ is the shear modulus, b the modulus of the Burgers vector, β is a forest strengthening coefficient calibrated by Amodeo et al. (2014), ρ_{f} is the forest dislocation density, and ρ_{ref} is the reference dislocation density. Transmission electron microscopy observations (Nzogang et al. 2018) on the specimens of Girard et al. (2016) confirm this view and show a very

large dislocation density estimated at over $10^{15}\,\mathrm{m}^{-2}$. Using this dislocation density and Equation 7.3 leads to an excellent description of experimental values for the deformation of ferropericlase under shallow lower mantle P, T conditions at laboratory strain rates (Figure 68). Our modeling approach allows us to reproduce very well the experimental data of Girard et al. (2016) and confirm that, under laboratory conditions, bridgmanite is indeed expected to be stronger than ferropericlase. It should be noted that the flow stress value for ferropericlase corresponds to very high hardening, and that under more 'gentle' laboratory deformation conditions (that is, smaller strains or more recovery), the rheology contrast under laboratory conditions should be even larger. At $30\,\mathrm{GPa}$, oxygen diffusion is already slow, and strain rates much lower than those obtainable in laboratory experiments would be required for climb to become active and promote the recovery necessary for steady-state creep.

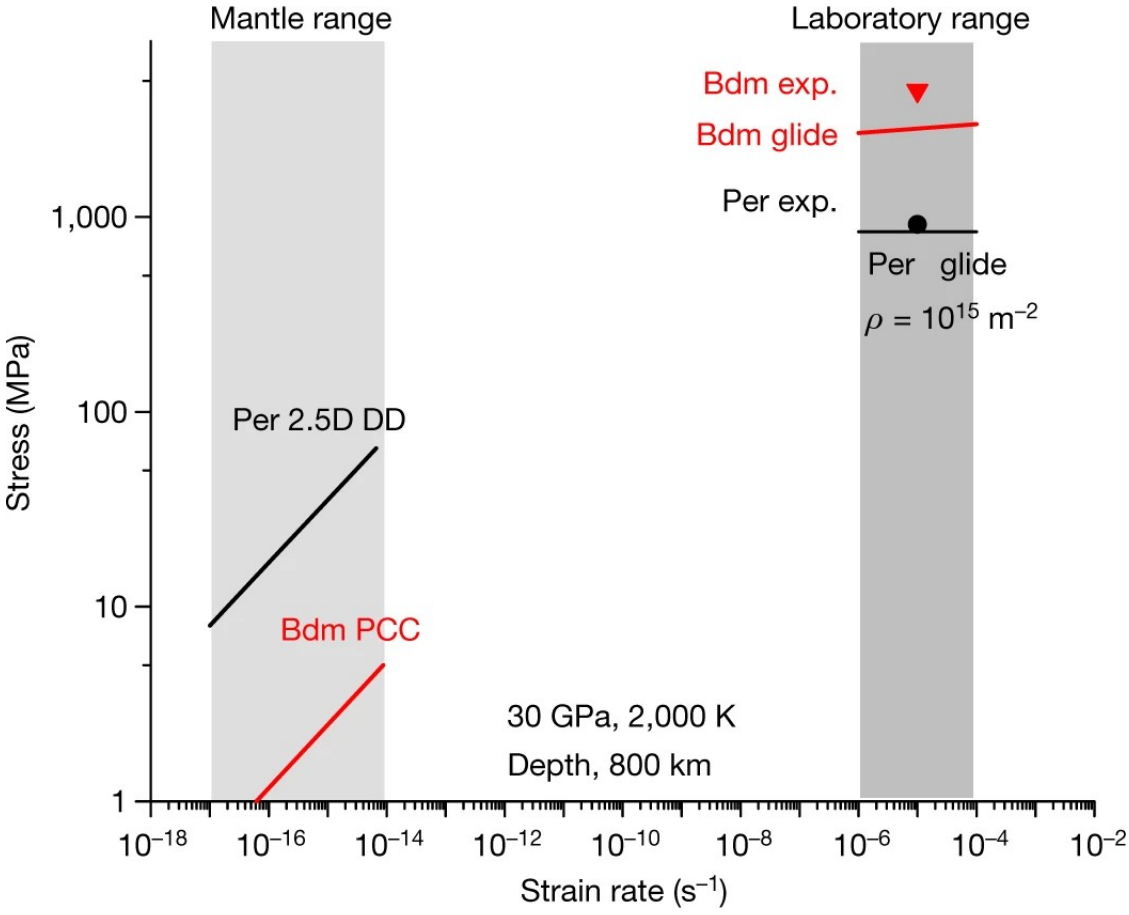

Figure 68: Influence of strain rate on deformation mechanisms: This figure corresponds to approximately $30\,\mathrm{GPa}, 2,000\,\mathrm{K}$, where the experimental (exp.) data of Girard et al. (2016) (symbols) can be compared to numerical models (lines). At laboratory stresses and strain rates numerical models based on dislocation glide are in fair agreement with experimental data and show that bridgmanite (Bdm) is stronger than periclase (Per). At mantle strain rates, creep (Weertman creep modeled by 2.5D DD in periclase (see text) and pure climb creep (PCC) in bridgmanite) is controlled by ionic diffusion, which leads to an inversion of rheology, with periclase deforming more slowly than bridgmanite.

8 General Discussion

8.1 Dislocation Electron Tomography

8.1.1 Analysis Possibilities

Up to this point, only a handful of laboratories have published work on dislocation electron tomography. The first contribution was made by the group of Midgley in Cambridge (Barnard et al. 2006). The most prolific laboratories are the group of Hata,in Japan which up to now published 11 articles (e.g. Hata et al. 2020a) and in the US the group of Kacher with a total of 9 articles (e.g. Kacher and Robertson 2014). The number of publications of this specific scientific approach up to this day reached 63, it is a "niche". Despite being in the early stages of development, the potential applications of DET are significant, heralding a promising future for in-depth dislocation analyses. However, it's important to recognize that much work remains to be done to fully realize its capabilities.

We have decided to develop DET, because it can help us access fundamental mechanisms of plastic deformation. The slip systems are the first characterization needed. It can be accessed with the Burgers vector and the line direction.

To retrieve the Burgers vector multiple techniques are known. The first method developed is known as the extinction criteria, which is time consuming. Later the thickness fringes method (Ishida et al. 1980) allow us to reduce the micrographs needed. The most efficient approach to indexing Burgers vectors is through LACBED, where only a single pattern is required. Consequently, the Burgers vector characterization has been optimized by the community.

The situation to access glide planes is more difficult. The usual way to characterize glide planes is via stereographic projection, but it is laborious and limited by accessible orientations. For that reason we have decided to extend the development of DET at Lille. DET analysis expands the scope beyond slip system indexations, which will be discussed in the next section.

8.1.2 Advanced characterization with DET

DET allowed us to characterize slip systems in various materials. In quartz we have characterized <a> prismatic and <a> pyramidal as well as <c> prismatic, which have been previously found in literature (Baeta and Ashbee 1969; Hobbs 1968; Mainprice et al. 1986; Morrison-Smith et al. 1976). In addition we found less common systems like glide in <c+a> prismatic and <c+a> pyramidal. For olivine we have characterized <a> in (010) and <c> in (010) , {110} and (100) which have all been found previously (Durham et al. 1985; Miyajima et al. 2009).

Tomography provides complete access to the 3D microstructure, which gives the possibility to observe annihilation and collinear interaction (Stach et al. 2000). DET can also reveal double cross slip, which leads to interactions that creates loops in sessile planes (Mussi et al. 2017).

Finally and above all, DET reveals dislocation motion in non-glissile planes, or in other words climb planes. We could index dislocations in pure climb of <a> in (100) for olivine, as well as <a> prismatic in quartz. Mixed climb, a newly recognized strain mechanism, it occurs when climb and glide velocities are comparable, questions traditional dislocation motion models. Despite its potential significance, accurately quantifying its impact remains a challenge, requiring an advanced characterization technique like DET. The first mention of this mechanism has been proposed by Malaplate et al. (2004) in a TiAl alloy. They propose a mixed climb mechanism generated by high frictional forces in glide planes (probably linked to specific dislocation core structures). In a later study (Galy et al. 2023) they then confirmed similar velocities for both mechanisms in TiAl at a temperature of $790°C$. This could be done by in-situ TEM deformation, with a direct measurement by stereographic projection.
In our study we could characterized a <a> (210) mixed climb configuration in a natural deformed olivine specimen (see figure 50 in Section 4.2). The angle between mixed climb and pure climb is of $13.12°$, which is closer to a pure climb configuration.

For natural deformed quartz specimens we even did quantitative studies, considering dislocation length in two samples. The work on quartz showed a high amount of mixed climb contribution, with over half of the dislocation length was in a mixed climb configuration, distributed in the whole angle range between, glide and pure climb. The actual glide velocities are very hard to estimate in this case, in the absence of direct (e.g. in situ in the TEM) measurements of dislocation mobility. To estimate the climb velocity we would need accurate self-diffusion values which are also missing. However, these statistics suggest that disloca-

tion climb might act as a deformation mechanism in its own right capable of contributing significantly to the deformation of rocks, and not just as a recovery mechanism.

It is worth noting that the identification of mixed climb begins to spread thank to tomography. The first study was published in 2004 on TiAl alloy, in minerals from 2017 to present and very recently on UO_2 (Onofri et al. 2024).

In summary, I am now able to conduct DET analyses on various materials, minerals and a MAX-phase (in early progress). It can be done in conventional form or in fast way (tilt series acquisition with few images). To go further we have decided to associated tomography with continuum mechanics. We will discuss this association improving the resolution from spatial scale to time scale.

8.2 Dislocation Electron Tomography: Association with Continuum Mechanics and Dislocation Dynamics

8.2.1 Association of DET with Continuum Mechanics at the Grain Scale

To associate DET with strain tensor, we have extracted the habit plane normal of each dislocation segment, each linked with a corresponding Burgers vector for quartz in natural conditions. It is noteworthy that this study has been conducted both quantitatively and accurately. It is the first analysis of its kind up to this day. The powerful tool of tomography gives us the possibility to get access not only to strain tensor but also to stress tensor.

We have to emphasis that due to the plastic response of the material, the dimensionless stress tensor is not simply obtained by a Hook's law, but via a minimization method. Likewise, we can obtain relative CRSS, which are very difficult to measure and even more in geological conditions.

It has to be mentioned that the model is based on significant approximations (particular for modeling climb) to facilitate the calculations. The study was a first attempt to test the limits of this model, which must be refined. It showed success for one of the two grains but did not give relevant results for the other one.

To achieve a truly quantitative analysis of strain tensor, it is essential to capture the full dislocation microstructure of a whole grain. To characterize the complete 3D dislocation microstructure, several diffraction vectors might be needed. But even worse the necessity to characterize a whole grain from a thin foil is incompatible. Generally, TEM thin foils have a thickness ranging from 50nm to 500nm. On the other hand, representative grain sizes have

an order of magnitude of several micrometers. It could work in the case of materials with very fine grain sizes, which makes it difficult to perform DET analysis.

Going from grain scale we will now go to spatial resolution of WBDF (few nanometers).

8.2.2 Association of DET with Continuum Mechanics at the Scale of WBDF Resolution

As outlined in 3.1, we can extract the dislocation line direction from tomography analyses. Associating these line directions with their respective Burgers vectors enables us to access the local Nye tensor. This allows us to simulate the mechanical fields of the thin foil with the resolution of the WBDF micrograph. To conduct such a study, we have to keep in mind that it relies on obtaining the sign of the Burgers vectors, which is challenging. It can be achieved using the LACBED technique, but it is difficult to identify each dislocation due to shadow image problems and it gets impossible for thick specimens due to multi scattering events. Therefore, we usually rely on the thickness fringes method, where the sign is linked with the termination direction. However, if dislocations lie parallel to the thickness fringes the termination direction is hard to access. In the case of a more or less flat specimen, the thickness fringes are far from each other. This is generally the case far from the wedge. To bring them close we need to increase the excitation error s, which exponentially decreases the micrograph contrast.

The sign of the Burgers vector is linked with the asymmetry of the contrast intensity at dislocation extremities, but it depends on the material. It could be linked with the structure factor and the anisotropy of the crystal. In some material it is strongly visible, in others no such signature can be seen. In conclusion, this represents the primary limitation of the technique.

An advantage of this method is that we can resolve continuum mechanics at high spatial resolution. A DET study has been performed on a TEM device with a X-FEG filament (high brightness), which allows a high signal over noise ratio even at a high excitation error (Mussi et al. 2021a). Consequently, high resolution WBDF could be achieved, resulting in a reconstruction resolution of 4 nm.

It is possible to improve the resolution even further. A WBDF image by Douin (Morniroli 2001) shows a resolution below 1 nm (see Figure 69), therefore a reconstruction resolution near 1 nm could be reached.

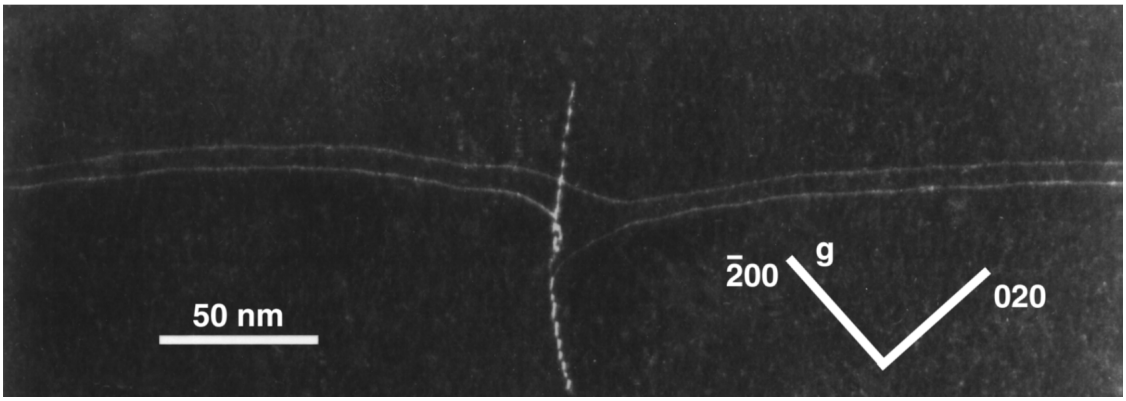

Figure 69: WBDF micrography of a superdislocation [110] dissociated into two identical partials 1/2[110] in Ni_3Al, showing a resolution below 1 nm (unpublished results from Douin, Morniroli 2001).

A validation of our technique has to be done, by directly comparing it to elastic field maps on the surface from direct analyses like HR-EBSD. This will be further discussed in the conclusion.

The association of tomography gives the opportunity to locally anticipate fundamental mechanisms of plastic deformation: collinear interaction, cross slip, dislocation climb and more.

To go even further, we can investigate the evolution of the microstructure with time. To accomplish this, we therefore naturally use DD to associate DET with time.

8.2.3 Association of DET with Time by Dislocation Dynamics

Generally DD uses virtual microstructures to study a specific behavior. In the present state of knowledge, it is the first time, that a real microstructures is incorporated in a DD model. The idea is to bring life back to real dislocation microstructure.

The results are a proof of concept and therefore the extend of the simulations are limited. We needed a specimen with only few slip systems and minimal sessile configurations. It is important to be able to trace back the orientation of applied stress to reactivate the microstructure in the same experimental conditions. Of course, we need to consider all experimental conditions as well (temperature, strain rate, etc.). From the point of view of tomography, the access to the Burgers vector signs is necessary, we encounter the same problem as previously. In all materials we studied, only one tilt series in PoEM9 fulfilled all the required conditions for this proof of concept. First of all, the microstructure contains only three slip systems with one Burgers vector and only few climb configurations. The biggest advantage of this specimen is that most parameters relevant for dislocation dynamic modelling are known (thermal kink pair mechanism parameters (Durinck et al. 2007b), core

width (Mahendran et al. 2021), etc.). Finally, the dislocation microstructure contains mainly straight screw segments. In this particular specimen we have high asymmetric contrast of dislocation extremities, consequently we can easily get access to most of the Burgers vector signs. However, this specimen possesses flaws that are intrinsic to its characteristics. As much as the simplicity of the microstructure helps us to perform a proof of concept, it also introduces some limitations.

The simplicity makes it impossible to obtain complex interactions. To increase the complexity, it is necessary to rise the amount of active slip systems. The majority of the segments are screw with the same Burgers vector which on their own can create dipoles or interactions between [c] dislocations of opposite signs gliding in different family planes. Which such a configuration, only collinear interactions can be observed. Moreover, to create entangled zones, we need obstacles. Collinear interactions are the only obstacles created during DD simulation, except sessile segments, coming from the initial microstructure. To accumulate entangled zones, we need high strain (several dozen %), which it not reachable in DD (usually up to several %).

In addition, we had to make hypotheses for the habit planes of the straight screw dislocations. Tomography revealed three preferential slip systems. We have decided to address only those three slip systems as possible gliding planes. Then, based on interaction behavior in the relaxed condition, we have eliminated odd dislocation configurations (Figure 60). Finally, it is possible to predict the supposed activated slip system.

Olivine has an orthorhombic structure. This crystallographic structure shows anisotropy in its elastic behavior. Unfortunately, DDD codes rely on isotropic elasticity for interactions between dislocation segments. The calculations of stress fields and displacements of dislocation in anisotropic domains are still challenging and have high numerical calculation costs.

The main problem occurring in our simulation is linked with the boundaries of the thin foil. Consequently, all hidden dislocation microstructures are not considered. Limiting the simulation to the geometry of a thin foil is a large approximation, since the elastic fields of dislocations occur at long distances. All dislocations near the surface are strongly affected by mirror forces from the boundary of the thin foil. To avoid those forces, we extended the simulation box and pined the end nodes of the emerging dislocations. For this reason, we had to make an assumption on the shape of the extrapolated dislocations. We have decided to make the hypothesis that extrapolation of the dislocations are straight screw segments. To resolve these problems, a coupled code between a finite element model and NUMODIS has been recently developed, El-NUMODIS (Gonzalez-Joa et al. 2023). It is more computational

demanding and would go too far for a simple proof of concept study. But it is promising since computational capability will increase in future and should be incorporated in a next study.

Another problem concerns the occurrence of cross-slip and climb. Both occurrences have been observed in PoEM8 and PoEM9 respectively. Cross-slip and more precisely double cross-slip mechanism has been identified in PoEM8 (see Figure 4 in Mussi et al. (2017)). Climb mechanism has been observed in PoEM9 through the occurrence of string of small loops. Indeed, it can be explained by the shrinkage of dislocation dipoles by climb. The problem in NUMODIS is that cross-slip is not well adapted for this study and climb is not included yet.

9 Conclusion: Advancing Dislocation Analysis through Electron Tomography

This work has highlighted the capabilities of dislocation electron tomography (DET) as a tool to connect experimental data to modeling. In concluding this work, we have emphasized two significant insights. First, the detection of mixed climb mechanisms in minerals via DET and in general the importance of climb in geodynamics, undermined by the Dislocation Dynamics (DD) the study on the rheology of the lower mantle. Second, the successful association of DET with mechanics, enhanced by incorporating time evolution through DD.

9.1 On the Importance of Climb in Geodynamics

In the course of this thesis, several studies have helped to highlight the importance of the climb mechanism in geodynamics, where we often deal with high temperature and low strain rates.

At first, it appeared indirectly, in the study of periclase creep initiated during my Master's degree (Section 7). In this study, dislocation dynamics modeling of creep highlighted the rate-controlling role played by climb. As anionic diffusion is virtually inhibited in MgO under pressure, this mineral does not deform at mantle strain rates. Climb therefore played the role traditionally considered as a recovery, rate-controlling mechanism. Indirectly, however, my modelling has led to the proposition that it is bridgmanite, which deforms by pure climb, that controls mantle rheology. In this way, I have helped to confirm Boioli et al. (2017) and Reali et al. (2019b)'s proposal that dislocation climb plays the leading role in deep mantle rheology. This work has highlighted the importance of climb, particularly at high temperature and low strain rates. Starting by its role as a rate-controlling mechanism for periclase in the lower mantle, revealed by 2.5D DD modeling. And when looking at the bigger picture, we found that it deforms slower than bridgmanite under lower mantle condition, contrary to previous suggestions. Within bridgmanite, climb is suggested to serve as a strain-producing mechanism through pure climb.

This study on periclase was purely numerical. My thesis project, essentially based on dislocation tomography, contributed to shed light on the climb in an unexpected way. What stands out in our study is the detailed characterization of dislocation microstructures in samples deformed in nature, something that is rarely done today. Compared with the previous project, this has necessarily led to a shift of interest towards more superficial geodynamic contexts. But natural samples are the only ones that retain traces of deformation that took place at very low tectonic strain-rates.

The main study therefore focused on quartz, following the preliminary observation of mixed climb in a Bohemian granulite (Mussi et al. 2021c).

Our investigation with DET of quartz from two highly sheared mylonites has revealed complex dislocation configurations beyond the standard glide planes. It uncovered the pervasive occurrence of climb in natural deformed samples. We have shown that the contribution of glide to the strain produced by observed dislocations is sufficient to meet the von Mises-Taylor criterion, indicating that while climb's activation is not necessary for additional strain components, it however significantly contributes to the magnitudes of strains observed. Indeed, the plastic strains produced by climb are on par with, if not greater than, those produced by glide. This demonstrates that relying solely on glide for the analysis of strain does not offer a complete picture of quartz deformation at natural strain rates.

More interestingly, we showed that approximately half the dislocations length was in mixed climb configuration. Such evidence explains why climb does not just play a role in recovery, but also actively contributes to strain. Activation of mixed climb shows that glide and climb mechanisms exhibit similar mobilities in natural conditions. The reason is that under low stress and strain rate, glide (which is stress driven) is slowed down while climb (which is diffusion controlled) has time to operate. The deformation mechanisms activated in nature are thus probably, at least in quartz, very different than those activated in the laboratory. This calls for care in extrapolation laboratory data to nature. In particular since most analyses are based on crystal preferred orientations which only capture the kinematics resulting from glide.

Furthermore, we hypothesize that the activation of mixed glide and climb could facilitate the activation of glide on additional planes. This hypothesis, grounded in preliminary observations, calls for further empirical and theoretical exploration.

Following the work on quartz, we also report some preliminary observations of mixed climb in an olivine from Oman ophiolite. This observation is too preliminary to draw general conclusions, but calls for further investigations to assess the potential importance of dislocation

climb in the lithospheric or asthenospheric mantle. However, it is clear that the DET is and will be the preferred tool for carrying out these investigations.

9.2 An Association with Continuum Mechanics and Dislocation Dynamics

In the work on quartz, I contributed to associate DET with mechanics by looking at mechanical field on grain scale resolution, but to get a better view of the intrinsic behavior between the individual dislocations, we have to go beyond, involving local analysis.

To do so, I helped to linked DET, which provides a 3D reconstruction of dislocation lines, with continuum mechanics to analyze stress and strain at the nanoscale. This was accomplished by transforming the observed dislocation microstructure into a continuum field using FDM. To achieve this, we computed local Nye tensors at the resolution provided by the dislocation contrast of WBDF imaging, effectively bridging the gap between the localized, discrete nature of dislocations and the continuous framework of material deformation. This integration enhances our understanding of the mechanical fields within a thin foil, providing a richer view of material behavior from the microstructural level to macroscopic properties.

This methodology allowed me to reveal significant local variations in stress fields and Resolved Shear Stresses (RSSs) in various slip systems in olivine. These variations are critical for understanding the pronounced plastic anisotropy of materials like olivine and for identifying the activation mechanisms of different dislocation slip systems. Consequently, this analysis allows us to explore processes such as kinematic hardening at the nanometer scale within a thin foil, marking a significant progression in the nanoscale characterization of plastic deformation mechanisms.

Moreover, by incorporating microstructure from DET into DDD simulations, I have introduced a temporal dimension to our analysis, allowing us to observe how dislocation networks might evolve over time. Incorporating real microstructures into DD models brings life back to our microstructure, transforming static images into dynamic scenarios that reflect the complex interactions and evolution of dislocations under various conditions. The incorporation of DET into DD models represents a novel methodological advancement, allowing for the simulation of dislocation behavior based on real dislocation microstructure instead of virtual.

Incorporating DET with continuum mechanics and DD simulations represents a frontier in materials science, offering a powerful toolkit for unraveling the intricacies of plastic deforma-

tion. From the point of view to connect DET to FDM and DDD, the access to the Burgers vector signs is necessary, which might be still the biggest challenge.

Although this approach is in a proof of concept stage, with challenges related to incomplete data from DET and the missing models for complex mechanisms especially in DD, it marks a significant stride towards a deeper understanding of dislocation mechanics.

9.3 Perspectives

In the journey ahead, our research aims to deepen the understanding of mixed climb and climb in general, by looking at other specimens with low deformation rate and at high temperatures, which favors deformation by climb. Low strain rates in most natural deformed minerals, combined with often high temperatures during their deformation makes them good candidates to further explore. Applying FDM for more detailed strain tensor analysis in similar specimens, potentially can help revealing new aspects of mixed climb and associated deformation mechanisms. Also looking at in situ tomography like it was performed by Mussi et al. (2021b), should give insides into the mobility of the dislocations. For this DET with few projected images is important to faster perform tomography. In this regard a comparison with other techniques like stereo pair (e.g.Oveisi et al. 2018), which relies on only two micrographs, has to be done to compare advantages and disadvantages of the techniques to others. A even more reasoned approach by Niermann et al. (2024) based on 4D STEM, proposes a reconstruction without tilting. This method analyzes changes in electron Bloch wave bands resulting from scattering in the strain field of dislocations within the crystal. This approach appears promising and deserves further comparison and development to be able to classify its capabilities correctly.

Another point is the improvement of the reconstruction quality with the help of machine learning, and a more automatic reconstruction.

Then a direct validation of association between tomography and FDM has to be performed by techniques like HR-EBSD (Ernould et al. 2022). For a TEM experiment this could be done with ASTAR. A first work conducted by Despres gave access to strain fields on Al precipitates. This work has been presented in a conference in 2023 and another work on MAX phases Cr_2AlC on emerging edge dislocations, was presented at Plasticite 2023 and CMJ 2023.

Regarding DD with NUMODIS, there is still the development to incorporate a more accurate velocity law, and at some point, to incorporate additional mechanisms. One of the biggest

issues when associated it with DET, is the aspect of the thin foil boundaries, which should be improve with coupled codes like El-NUMODIS (Gonzalez-Joa et al. 2023).

After the proof of concept has been done, it should also be interesting to work with a less anisotropic sample with a more interesting microstructure (e.g. a fcc multi-glide metallic specimen), that primarily is in glide to use the full capabilities of the code. Even though there seems to be first approaches to incorporate anisotropy in to DD (Forghani and Khaji 2022).

A final dream would be to study a specimen, where both 4D DET and DDD would be possible to be performed under the same conditions, which would then allow to directly compare the modeling with the experiment and afterwards to analyze the mechanical field, to see the effect of interactions. As we look to the future, I think I can say that the association of DET with other techniques opens new avenues in understanding and analyzing dislocation microstructure, despite the challenges that still exist.

A Appendix

A.1 Analysis on straight line dislocations

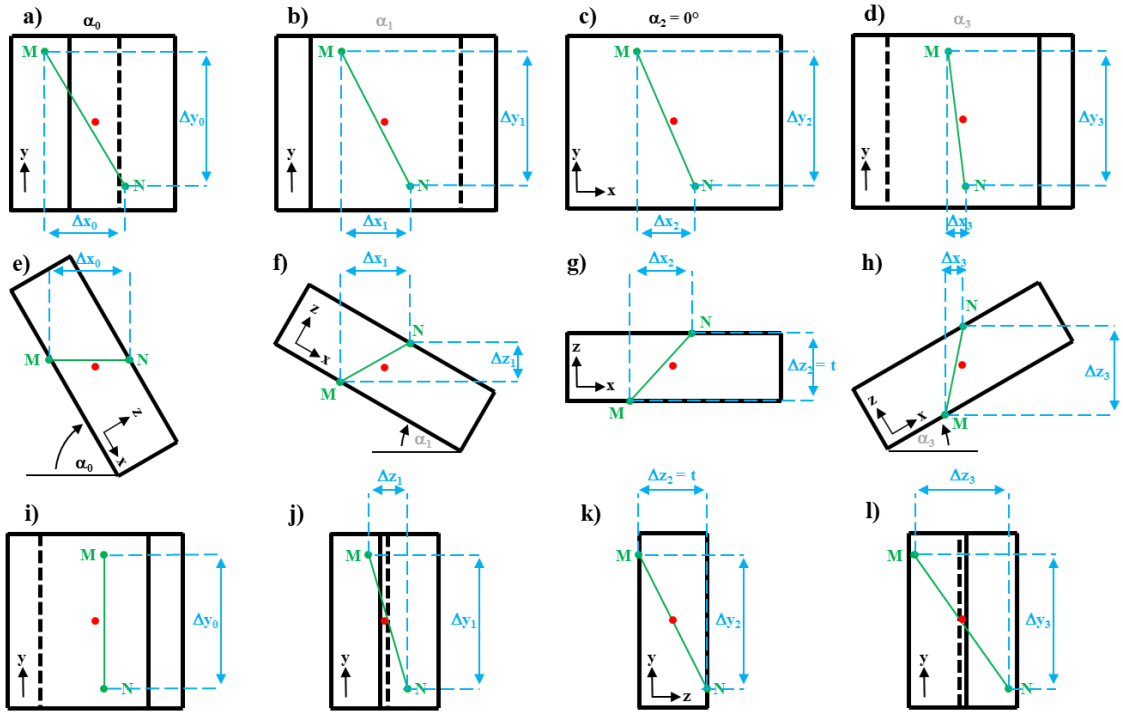

Figure 70: Sketch of a straight line dislocation represented with four projection angles ($\alpha_0, \alpha_1, \alpha_2,$ and α_3) delimited by two points (M and N colored in green): (a)-(d) Observations along the electron beam axis. (e)-(h) Observations along the $(0, y)$ axis. (i)-(l) Observations along the axis that is perpendicular to the electron beam axis and to the $(0, y)$ axis.

Here I describe the manual reconstruction of straight line dislocations, that was applied in in our study on quartz (see section 4.1). Let's consider $(0, x, y, z)$ the direct orthonormal reference frame where the thin-foil is laid horizontally, and four projection angles:

- α_0, where the dislocation is laid horizontally,
- α_1, the angle of the micrograph obtained with the maximum negative angle, shown in grey in Figure 69 (α is the angular difference between α_1 and α_0),
- α_2, where the thin-foil is laid horizontally ($\alpha_2 = 0°$),

- α_3, the angle of the micrograph obtained with the maximum positive angle, shown in grey in Figure 69 ($\Delta\alpha$ is the angular difference between α_3 and α_1).

The tilt-axis is along the $(0, y)$ axis and passes through a small detail (usually a small dislocation loop, indicated by a red dot in Figure 69) used to align the tilt-series.

Note that:

- The $\Delta y_i (= \Delta y)$, Δx_1 and Δx_3 deviations can be obtained from micrographs acquired at the two extreme angles of the tilt-series,
- The Δz_2 deviation is simply the thickness of the thin plate ($\Delta z_2 = t$),
- The Δx_0, Δy_0 and Δz_0 deviations give us access to the line vector of the rectilinear dislocation in the reference frame where the dislocation is laid horizontally (projection angle α_0), a simple change of reference frame allows us to find the dislocation in the reference frame where the thin-foil is laid horizontally,
- The Δx_0, Δy_0 and Δz_0 deviations also give us access to the length of the straight line segment: $L = \sqrt{\Delta x_0^2 + \Delta y_0^2 + \Delta z_0^2}$,
- When the dislocation is laid horizontally, $\Delta z_0 = 0$, then $L = \sqrt{\Delta x_0^2 + \Delta y^2}$,
- The aim is to find Δx_0.

Method for finding Δx_0:

$$\frac{\Delta x_1}{\Delta x_0} = \cos(\alpha_1 - \alpha_0) = \cos(\alpha) \tag{A.1}$$

Similarly:

$$\frac{\Delta x_3}{\Delta x_0} = \cos(\alpha_3 - \alpha_0) \tag{A.2}$$

This can also be written:

$$\frac{\Delta x_3}{\Delta x_0} = \cos(\Delta\alpha + \alpha) \tag{A.3}$$

Therefore:

$$\frac{\Delta x_3}{\Delta x_0} = \cos[\Delta\alpha + \arccos(\frac{\Delta x_1}{\Delta x_0})] \tag{A.4}$$

We deduce Δx_0:

$$\Delta x_0 = \sqrt{[1 + \cot^2(\Delta\alpha)]\Delta x_1^2 - 2\cot(\Delta\alpha)\frac{\Delta x_1 \Delta x_3}{\sin(\Delta\alpha)} + \frac{1}{\sin^2(\Delta\alpha)}\Delta x_3^2} \tag{A.5}$$

We obtain the length of the straight line segment:

$$L = \frac{1}{\sin(\Delta\alpha)}\sqrt{\Delta x_1^2 - 2\cos(\Delta\alpha)\Delta x_1 \Delta x_3 + \Delta x_3^2 + \sin^2(\Delta\alpha)\Delta y^2} \tag{A.6}$$

Knowing Δx_0, we deduce α_0:

$$\alpha_0 = \alpha_1 - \arccos(\frac{\Delta x_1}{\Delta x_0}) \tag{A.7}$$

To find the coordinates of the line vector $\vec{t}$, simply rotate the reference frame by an $\alpha_2 - \alpha_0$ angle along the $(0, y)$ axis. We know $\vec{t}$ in the reference frame for the α_0 projection angle:

$$\vec{t} = \begin{bmatrix} \Delta x_0 \\ \Delta y \\ 0 \end{bmatrix} \tag{A.8}$$

To obtain $\vec{t'}$ in the reference frame for the α_2 projection angle, we simply need to change the reference frame using the following rotation matrix:

$$R_y(\alpha_2 - \alpha_0) = \begin{bmatrix} \cos(\alpha_2 - \alpha_0) & 0 & \sin(\alpha_2 - \alpha_0) \\ 0 & 1 & 0 \\ -\sin(\alpha_2 - \alpha_0) & 0 & \cos(\alpha_2 - \alpha_0) \end{bmatrix} \tag{A.9}$$

Thus:

$$\vec{t'} = \begin{bmatrix} \Delta x_0 \cdot \cos(\alpha_0) \\ \Delta y \\ \Delta x_0 \cdot \sin(\alpha_0) \end{bmatrix} \tag{A.10}$$

Finally:

$$\vec{t'} = \begin{bmatrix} \Delta x_1 \cos(\alpha_1) + \frac{\sin(\alpha_1)}{\sin(\Delta\alpha)} \sqrt{\cos^2(\Delta\alpha)\Delta x_1^2 - 2\cos(\Delta\alpha)\Delta x_1 \Delta x_3 + \Delta x_3^2} \\ \Delta y \\ \Delta x_1 \sin(\alpha_1) - \frac{\cos(\alpha_1)}{\sin(\Delta\alpha)} \sqrt{\cos^2(\Delta\alpha)\Delta x_1^2 - 2\cos(\Delta\alpha)\Delta x_1 \Delta x_3 + \Delta x_3^2} \end{bmatrix} \tag{A.11}$$

Bibliography

Acharya, A. (2001). "A model of crystal plasticity based on the theory of continuously distributed dislocations". In: *Journal of the Mechanics and Physics of Solids* 49.4, pp. 761–784.

Ahrens, J., B. Geveci, C. Law, C. Hansen, and C. Johnson (2005). "36-paraview: An end-user tool for large-data visualization". In: *The visualization handbook* 717, pp. 50038–1.

Altingövde, O., A. Mishchuk, G. Ganeeva, E. Oveisi, C. Hebert, and P. Fua (2022). "3D reconstruction of curvilinear structures with stereo matching deep convolutional neural networks". In: *Ultramicroscopy* 234, p. 113460.

Ammann, M., J. Brodholt, J. Wookey, and D. Dobson (2010). "First-principles constraints on diffusion in lower-mantle minerals and a weak D layer". In: *Nature* 465.7297, p. 462.

Amodeo, J., P. Carrez, B. Devincre, and P. Cordier (2011). "Multiscale modelling of MgO plasticity". In: *Acta Materialia* 59.6, pp. 2291–2301.

Amodeo, J., P. Carrez, and P. Cordier (2012). "Modelling the effect of pressure on the critical shear stress of MgO single crystals". In: *Philosophical Magazine* 92.12, pp. 1523–1541.

Amodeo, J., B. Devincre, P. Carrez, and P. Cordier (2014). "Dislocation reactions, plastic anisotropy and forest strengthening in MgO at high temperature". In: *Mechanics of Materials* 71, pp. 62–73.

Appel, F. and B. Wielke (1985). "Low temperature deformation of impure MgO single crystals". In: *Materials science and engineering* 73, pp. 97–103.

Arsenlis, A., W. Cai, M. Tang, M. Rhee, T. Oppelstrup, G. Hommes, T. G. Pierce, and V. V. Bulatov (2007). "Enabling strain hardening simulations with dislocation dynamics". In: *Modelling and Simulation in Materials Science and Engineering* 15.6, p. 553.

Bachmann, F., R. Hielscher, and H. Schaeben (2010). "Texture analysis with MTEX–free and open source software toolbox". In: *Solid state phenomena* 160, pp. 63–68.

Baeta, R. and K. Ashbee (1969). "Slip systems in quartz: I. Experiments". In: *American Mineralogist: Journal of Earth and Planetary Materials* 54.11-12, pp. 1551–1573.

Baeta, R. and K. Ashbee (1973). "Transmission electron microscopy studies of plastically deformed quartz". In: *physica status solidi (a)* 18.1, pp. 155–170.

Bakker, R. J. and J. B. H. Jansen (1990). "Preferential water leakage from fluid inclusions by means of mobile dislocations". In: *Nature* 345.6270, pp. 58–60.

Bakker, R. J. and J. B. H. Jansen (1994). "A mechanism for preferential H2O leakage from fluid inclusions in quartz, based on TEM observations". In: *Contributions to Mineralogy and Petrology* 116.1-2, pp. 7–20.

Bakó, B., E. Clouet, L. M. Dupuy, and M. Blétry (2011). "Dislocation dynamics simulations with climb: kinetics of dislocation loop coarsening controlled by bulk diffusion". In: *Philosophical Magazine* 91.23, pp. 3173–3191.

Ball, A. and S. White (1978). "On the deformation of quartzite". In: *Physics and Chemistry of Minerals* 3, pp. 163–172.

Ball, A. and G. Glover (1979). "Dislocation climb deformation in quartz". In: *Bulletin de Minéralogie* 102.2, pp. 188–194.

Barnard, J., J. Sharp, J. Tong, and P. Midgley (2006). "High-resolution three-dimensional imaging of dislocations". In: *Science* 313.5785, pp. 319–319.

Basinski, Z. and S. Basinski (1964). "Dislocation distributions in deformed copper single crystals". In: *Philosophical magazine* 9.97, pp. 51–80.

Behrmann, J. and D. Mainprice (1987). "Deformation mechanisms in a high-temperature quartz-feldspar mylonite: evidence for superplastic flow in the lower continental crust". In: *Tectonophysics* 140.2-4, pp. 297–305.

Bertin, N. (2019). "Connecting discrete and continuum dislocation mechanics: A non-singular spectral framework". In: *International Journal of Plasticity* 122, pp. 268–284.

Blacic, J. (1975). "Plastic-deformati on mechanisms in quartz: the effect of water". In: *Tectonophysics* 27.3, pp. 271–294.

Boioli, F., P. Carrez, P. Cordier, B. Devincre, K. Gouriet, P. Hirel, A. Kraych, and S. Ritterbex (2017). "Pure climb creep mechanism drives flow in Earth's lower mantle". In: *Science advances* 3.3, e1601958.

Boioli, F., P. Carrez, P. Cordier, B. Devincre, and M. Marquille (2015a). "Modeling the creep properties of olivine by 2.5-dimensional dislocation dynamics simulations". In: *Physical Review B* 92.1, p. 014115.

Boioli, F., A. Tommasi, P. Cordier, S. Demouchy, and A. Mussi (2015b). "Low steady-state stresses in the cold lithospheric mantle inferred from dislocation dynamics models of dislocation creep in olivine". In: *Earth and Planetary Science Letters* 432, pp. 232–242.

Bulatov, V. and W. Cai (2006). *Computer simulations of dislocations*. Vol. 3. OUP Oxford.

Cai, W., A. Arsenlis, C. R. Weinberger, and V. V. Bulatov (2006). "A non-singular continuum theory of dislocations". In: *Journal of the Mechanics and Physics of Solids* 54.3, pp. 561–587.

Caillard, D. and J.-L. Martin (2003). *Thermally activated mechanisms in crystal plasticity*. Elsevier.

Carrez, P., A. Mussi, and P. Cordier (2024). "On Dislocation Climb as an Important Deformation Mechanism for Planetary Interiors". In: *Annual Review of Earth and Planetary Sciences* 52.

Castelnau, O., K. Derrien, S. Ritterbex, P. Carrez, P. Cordier, and H. Moulinec (2020). "Multiscale modeling of the effective viscoplastic behavior of Mg2SiO4 wadsleyite: Bridging atomic and polycrystal scales". In: *arXiv preprint arXiv:2012.00823*.

Cherns, D. and A. Preston (1986). "Convergent beam diffraction studies of crystal defects". In: *Proceedings of the XIth International Congress on Electron Microscopy, Kyoto*. Vol. 1. Japanese Society of Electron Microscopy, Tokyo, pp. 721–722.

Christie, J. and A. Ardell (1974). "Substructures of deformation lamellae in quartz". In: *Geology* 2.8, pp. 405–408.

Christie, J. and A. Ardell (1976). "Deformation structures in minerals". In: *Electron microscopy in mineralogy*. Springer, pp. 374–403.

Christie, J., H. Heard, and P. LaMori (1964). "Experimental deformation of quartz single crystals at 27 to 30 kilobars confining pressure and 24 degrees C". In: *American Journal of Science* 262.1, pp. 26–55.

Cockayne, D., I. Ray, and M. Whelan (1969). "Investigations of dislocation strain fields using weak beams". In: *Philosophical Magazine* 20.168, pp. 1265–1270.

Cooper, D., N. Bernier, and J.-L. Rouvière (2015). "Combining 2 nm spatial resolution and 0.02% precision for deformation mapping of semiconductor specimens in a transmission electron microscope by precession electron diffraction". In: *Nano letters* 15.8, pp. 5289–5294.

Copley, S. M. and J. A. Pask (1965). "Plastic deformation of MgO single crystals up to 1600 C". In: *Journal of the American Ceramic Society* 48.3, pp. 139–146.

Cordier, P., J. Doukhan, X. Buisson, and O. Bignon (1989). "Growth defects in cultured quartz: a microscopic investigation". In: *Proceedings of the 43rd Annual Symposium on Frequency Control*. IEEE, pp. 459–469.

Cordier, P. (2013). *Characterization of dislocations and deformation processes by Transmission Electron Microscopy*. Mineralogical Society of Great Britain and Ireland.

Cordier, P., J. Amodeo, and P. Carrez (2012). "Modelling the rheology of MgO under Earth's mantle pressure, temperature and strain rates". In: *Nature* 481.7380, pp. 177–180.

Cordier, P., B. Boulogne, and J. C. Doukhan (1988). "Water precipitation and diffusion in wet quartz and wet berlinite AlPO4". In: *Bulletin de minéralogie* 111.2, pp. 113–137.

Cordier, P. and J. C. Doukhan (1991). "Water speciation in quartz: a near infrared study". In: *American Mineralogist* 76.3-4, pp. 361–369.

Cotton, J., M. Kaufman, and R. Noebe (1991). "A simplified method for determining the number of independent slip systems in crystals". In: *Scripta metallurgica et materialia* 25.10, pp. 2395–2398.

Couret, A. (2010). "Low and high temperature deformation mechanisms in TiAl alloys". In: *Journal of Physics: Conference Series*. Vol. 240. 1. IOP Publishing, p. 012001.

De Rosier, D. and A. Klug (1968). "Reconstruction of three dimensional structures from electron micrographs". In: *Nature* 217.5124, pp. 130–134.

Demouchy, S. (2021). "Defects in olivine". In: *European Journal of Mineralogy* 33.3, pp. 249–282.

Demouchy, S., A. Mussi, F. Barou, A. Tommasi, and P. Cordier (2014). "Viscoplasticity of polycrystalline olivine experimentally deformed at high pressure and 900 C". In: *Tectonophysics* 623, pp. 123–135.

Demouchy, S., A. Tommasi, T. B. Ballaran, and P. Cordier (2013). "Low strength of Earth's uppermost mantle inferred from tri-axial deformation experiments on dry olivine crystals". In: *Physics of the Earth and Planetary Interiors* 220, pp. 37–49.

Després, A. and M. Veron (2023). "Elastic strain field measurements in the TEM for metallurgical applications". In: *Materials Characterization* 202, p. 113012.

Devincre, B., R. Madec, G. Monnet, S. Queyreau, R. Gatti, and L. Kubin (2011). "Modeling crystal plasticity with dislocation dynamics simulations: the 'microMegas' code". In: *Mechanics of Nano-objects*, pp. 81–100.

Devincre, B. (1993). "Simulations dynamiques des dislocations a une echelle mesoscopique: Une etude de la deformation plastique". PhD thesis. Paris 11.

DeWit, G. and J. Koehler (1959). "Interaction of dislocations with an applied stress in anisotropic crystals". In: *Physical Review* 116.5, p. 1113.

Djaka, K. S., A. Villani, V. Taupin, L. Capolungo, and S. Berbenni (2017). "Field dislocation mechanics for heterogeneous elastic materials: a numerical spectral approach". In: *Computer Methods in Applied Mechanics and Engineering* 315, pp. 921–942.

Dos Reis, M. L., Y. Giret, P. Carrez, and P. Cordier (2022). "Efficiency of the vacancy pipe diffusion along an edge dislocation in MgO". In: *Computational Materials Science* 211, p. 111490.

Doukhan, J. C. and M. Paterson (1986). "Solubility of water in quartz. A revision". In: *Bulletin de minéralogie* 109.3, pp. 193–198.

Doukhan, J. C. and L. Trépied (1985). "Plastic deformation of quartz single crystals". In: *Bulletin de minéralogie* 108.1, pp. 97–123.

Drouet, J., L. Dupuy, F. Onimus, F. Mompiou, S. Perusin, and A. Ambard (2014). "Dislocation dynamics simulations of interactions between gliding dislocations and radiation induced prismatic loops in zirconium". In: *Journal of Nuclear Materials* 449.1-3, pp. 252–262.

Durham, W., D. Ricoult, and D. Kohlstedt (1985). "Interaction of slip systems in olivine". In: *Point defects in minerals* 31, pp. 185–193.

Durinck, J. (2005). "Modélisation de la plasticité de la forsterite par calculs à l'échelle atomique et par dynamique des dislocations". PhD thesis. Lille 1.

Durinck, J., P. Carrez, and P. Cordier (2007a). "Application of the Peierls-Nabarro model to dislocations in forsterite". In: *European Journal of Mineralogy* 19.5, pp. 631–639.

Durinck, J., B. Devincre, L. Kubin, and P. Cordier (2007b). "Modeling the plastic deformation of olivine by dislocation dynamics simulations". In: *American Mineralogist* 92.8-9, pp. 1346–1357.

Edelin, G. and J. Poirier (1973). "Study of Dislocation Climb by Means of Diffusional Creep Experiments in Mg. Pt. 1. Deformation Mechanism". In: *Phil. Mag.* 28.6, pp. 1203–1210.

Eftink, B. P., G. T. Gray, and S. A. Maloy (2017). "Stereographic methods for 3D characterization of dislocations". In: *Microscopy and Microanalysis* 23.S1, pp. 210–211.

Ernould, C., V. Taupin, B. Beausir, J.-J. Fundenberger, N. Maloufi, J. Guyon, and E. Bouzy (2022). "Characterization of a nanopipe dislocation in GaN by means of HR-EBSD and field dislocation mechanics analysis". In: *Materials Characterization* 194, p. 112351.

Faleiros, F. M., R. d. Moraes, M. Pavan, and G. A. d. C. Campanha (2016). "A new empirical calibration of the quartz c-axis fabric opening-angle deformation thermometer". In: *Tectonophysics* 671, pp. 173–182.

Feng, Z., R. Fu, C. Lin, G. Wu, T. Huang, L. Zhang, and X. Huang (2020). "TEM-based dislocation tomography: Challenges and opportunities". In: *Current Opinion in Solid State and Materials Science* 24.3, p. 100833.

Fliervoet, T. F., S. H. White, and M. R. Drury (1997). "Evidence for dominant grain-boundary sliding deformation in greenschist-and amphibolite-grade polymineralic ultramylonites from the Redbank Deformed Zone, Central Australia". In: *Journal of Structural Geology* 19.12, pp. 1495–1520.

Foreman, A. and M. Makin (1966). "Dislocation movement through random arrays of obstacles". In: *Philosophical magazine* 14.131, pp. 911–924.

Forghani, S. and N. Khaji (2022). "An anisotropic multi-scale method for slipping dislocations". In: *International Journal of Plasticity* 148, p. 103130.

Francsis, M. K. (2012). "Piezometry and Strain Rate Estimates Along Mid-Crustal Shear Zones". PhD thesis. Virginia Tech.

Frenkel, J. (1926). "Zur theorie der elastizitätsgrenze und der festigkeit kristallinischer körper". In: *Zeitschrift für Physik* 37.7-8, pp. 572–609.

Friedel, J. (1964). *Dislocations, Pergamon Press LTD*.

Friedrich, H., P. E. De Jongh, A. J. Verkleij, and K. P. De Jong (2009). "Electron tomography for heterogeneous catalysts and related nanostructured materials". In: *Chemical reviews* 109.5, pp. 1613–1629.

Fukuda, J.-i., C. W. Holyoke III, and A. K. Kronenberg (2018). "Deformation of fine-grained quartz aggregates by mixed diffusion and dislocation creep". In: *Journal of Geophysical Research: Solid Earth* 123.6, pp. 4676–4696.

Galy, B., M. Musi, M. Hantcherli, G. Molénat, A. Couret, P. Spoerk-Erdely, H. Clemens, and J.-P. Monchoux (2023). "Glide and mixed climb dislocation velocity in γ-TiAl investigated by in-situ transmission electron microscopy". In: *Scripta materialia* 228, p. 115333.

Gerretsen, J., M. Paterson, and A. McLaren (1989). "The uptake and solubility of water in quartz at elevated pressure and temperature". In: *Physics and Chemistry of Minerals* 16, pp. 334–342.

Gevers, R. (1962). "On the kinematical theory of diffraction contrast of electron transmission microscope images of edge dislocations". In: *The Philosophical Magazine: A Journal of Theoretical Experimental and Applied Physics* 7.73, pp. 59–66.

Girard, J., G. Amulele, R. Farla, A. Mohiuddin, and S.-i. Karato (2016). "Shear deformation of bridgmanite and magnesiowüstite aggregates at lower mantle conditions". In: *Science* 351.6269, pp. 144–147.

Girard, J., J. Chen, and P. Raterron (2012). "Deformation of periclase single crystals at high pressure and temperature: Quantification of the effect of pressure on slip-system activities". In: *Journal of Applied Physics* 111.11.

Gómez-Garcıa, D., B. Devincre, and L. Kubin (1999). "Forest hardening and boundary conditions in 2-D simulations of dislocations dynamics". In: *MRS Online Proceedings Library Archive* 578.

Gómez-Garcıa, D., B. Devincre, and L. Kubin (2006). "Dislocation patterns and the similitude principle: 2.5 D mesoscale simulations". In: *Physical review letters* 96.12, p. 125503.

Gonzalez-Joa, J. A., L. Dupuy, P. Råback, M. Fivel, M. Perez, and J. Amodeo (2023). "El-Numodis: a new tool to model dislocation and surface interactions". In: *Modelling and Simulation in Materials Science and Engineering* 31.5, p. 055003.

Green, H. (1976). "Plasticity of olivine in peridotites". In: *Electron microscopy in mineralogy*. Springer, pp. 443–464.

Griggs, D. (1967). "Hydrolytic weakening of quartz and other silicates". In: *Geophysical Journal International* 14.1-4, pp. 19–31.

Griggs, D. (1974). "A model of hydrolytic weakening in quartz". In: *Journal of Geophysical Research* 79.11, pp. 1653–1661.

Griggs, D. and J. Blacic (1965). "Quartz: Anomalous weakness of synthetic crystals". In: *Science* 147.3655, pp. 292–295.

Gueguen, Y. and M. Darot (1980). "Microstructures and stresses in naturally deformed peridotites". In: *Tectonic Stresses in the Alpine-Mediterranean Region: Proceedings of the Symposium Held in Vienna, Austria, September 13–14, 1979*. Springer, pp. 159–172.

Haruta, K. (1965). "New Method of Obtaining Stereoscopic Pairs of X-Ray Diffraction Topographs". In: *Journal of Applied Physics* 36.5, pp. 1789–1790.

Hata, S., T. Honda, H. Saito, M. Mitsuhara, T. Petersen, and M. Murayama (2020a). "Electron tomography: An imaging method for materials deformation dynamics". In: *Current Opinion in Solid State and Materials Science* 24.4, p. 100850.

Hata, S., H. Miyazaki, S. Miyazaki, M. Mitsuhara, M. Tanaka, K. Kaneko, K. Higashida, K. Ikeda, H. Nakashima, S. Matsumura, et al. (2011). "High-angle triple-axis specimen holder for three-dimensional diffraction contrast imaging in transmission electron microscopy". In: *Ultramicroscopy* 111.8, pp. 1168–1175.

Hata, S., H. Furukawa, T. Gondo, D. Hirakami, N. Horii, K.-I. Ikeda, K. Kawamoto, K. Kimura, S. Matsumura, M. Mitsuhara, et al. (2020b). "Electron tomography imaging methods with diffraction contrast for materials research". In: *Microscopy* 69.3, pp. 141–155.

Heard, H. C. and N. L. Carter (1968). "Experimentally induced'natural'intragranular flow in quartz and quartzite". In: *American Journal of Science* 266.1, pp. 1–42.

Heggie, M. (1992). "A molecular water pump in quartz dislocations". In: *Nature* 355.6358, pp. 337–339.

Heggie, M. and R. Jones (1986). "Models of hydrolytic weakening in quartz". In: *Philosophical Magazine A* 53.5, pp. L65–L70.

Heggie, M., R. Jones, and M. Nylén (1985). "Electronic structure of a-quartz, the [10 1 0] surface and perfect stoichiometric dislocations". In: *Philosophical Magazine B* 51.6, pp. 573–580.

Herman, G., A. Lakshminarayanan, and A. Naparstek (1976). "Convolution reconstruction techniques for divergent beams". In: *Computers in biology and medicine* 6.4, pp. 259–271.

Hirsch, P. (1981). "Plastic deformation and electronic mechanisms in semiconductors and insulators". In: *Le Journal de Physique Colloques* 42.C3, pp. C3–149.

Hirsch, P., R. Horne, and M. Whelan (1956). "LXVIII. Direct observations of the arrangement and motion of dislocations in aluminium". In: *Philosophical Magazine* 1.7, pp. 677–684.

Hirsch, P. and M. Whelan (1960). "A kinematical theory of diffraction contrast of electron transmission microscope images of dislocations and other defects". In: *Philosophical*

Transactions of the Royal Society of London. Series A, Mathematical and Physical Sciences 252.1017, pp. 499–529.

Hirth, G., C. Teyssier, and J. W. Dunlap (2001). "An evaluation of quartzite flow laws based on comparisons between experimentally and naturally deformed rocks". In: *International Journal of Earth Sciences* 90, pp. 77–87.

Hirth, G. and J. Tullis (1992). "Dislocation creep regimes in quartz aggregates". In: *Journal of structural geology* 14.2, pp. 145–159.

Hobbs, B. (1968). "Recrystallization of single crystals of quartz". In: *Tectonophysics* 6.5, pp. 353–401.

Hobbs, B. (1984). "Point defect chemistry of minerals under a hydrothermal environment". In: *Journal of Geophysical Research: Solid Earth* 89.B6, pp. 4026–4038.

Hobbs, B. E. (1981). "The influence of metamorphic environment upon the deformation of minerals". In: *Tectonophysics* 78.1-4, pp. 335–383.

Hodges, K. V. (2000). "Tectonics of the Himalaya and southern Tibet from two perspectives". In: *Geological Society of America Bulletin* 112.3, pp. 324–350.

Holyoke III, C. W. and A. K. Kronenberg (2010). "Accurate differential stress measurement using the molten salt cell and solid salt assemblies in the Griggs apparatus with applications to strength, piezometers and rheology". In: *Tectonophysics* 494.1-2, pp. 17–31.

Hulse, C. O. and J. A. Pask (1960). "Mechanical properties of magnesia single crystals corn pression". In: *Journal of the American Ceramic Society* 43.7, pp. 373–378.

Immoor, J., H. Marquardt, L. Miyagi, F. Lin, S. Speziale, S. Merkel, J. Buchen, A. Kurnosov, and H.-P. Liermann (2018). "Evidence for $\{100\}< 011>$ slip in ferropericlase in Earth's lower mantle from high-pressure/high-temperature experiments". In: *Earth and Planetary Science Letters* 489, pp. 251–257.

Isaak, D. G., O. L. Anderson, T. Goto, and I. Suzuki (1989). "Elasticity of single-crystal forsterite measured to 1700 K". In: *Journal of Geophysical Research: Solid Earth* 94.B5, pp. 5895–5906.

Ishida, H., N. Miyamoto, and K. Kohra (1976). "Determination of the Burgers vector of a dislocation from equal-thickness fringes observed with a plane wave of X-rays". In: *Journal of Applied Crystallography* 9.3, pp. 240–241.

Ishida, Y., H. Ishida, K. Kohra, and H. Ichinose (1980). "Determination of the Burgers vector of a dislocation by weak-beam imaging in a HVEM". In: *Philosophical Magazine A* 42.4, pp. 453–462.

Ita, J. and R. E. Cohen (1997). "Effects of pressure on diffusion and vacancy formation in MgO from nonempirical free-energy integrations". In: *Physical review letters* 79.17, p. 3198.

Jácome, L. A., K. Pöthkow, O. Paetsch, and H.-C. Hege (2018). "Three-dimensional reconstruction and quantification of dislocation substructures from transmission electron microscopy stereo pairs". In: *Ultramicroscopy* 195, pp. 157–170.

Johnson, M., S. Kelley, G. Oliver, and D. Winter (1985). "Thermal effects and timing of thrusting in the Moine thrust zone". In: *Journal of the Geological Society* 142.5, pp. 863–873.

Kacher, J. and I. M. Robertson (2014). "In situ and tomographic analysis of dislocation/grain boundary interactions in α-titanium". In: *Philosophical Magazine* 94.8, pp. 814–829.

Kacher, J. and I. Robertson (2012). "Quasi-four-dimensional analysis of dislocation interactions with grain boundaries in 304 stainless steel". In: *Acta Materialia* 60.19, pp. 6657–6672.

Kacher, J., G. Liu, and I. Robertson (2011). "Visualization of grain boundary/dislocation interactions using tomographic reconstructions". In: *Scripta Materialia* 64.7, pp. 677–680.

Kaercher, P., L. Miyagi, W. Kanitpanyacharoen, E. Zepeda-Alarcon, Y. Wang, D. Parkinson, R. Lebensohn, F. De Carlo, and H. Wenk (2016). "Two-phase deformation of lower mantle mineral analogs". In: *Earth and Planetary Science Letters* 456, pp. 134–145.

Karki, B. B. and G. Khanduja (2006). "Vacancy defects in MgO at high pressure". In: *American Mineralogist* 91.4, pp. 511–516.

Kekulawala, R., M. Paterson, and J. Boland (1978). "Hydrolytic weakening in quartz". In: *Tectonophysics* 46.1-2, T1–T6.

Kekulawala, R., M. Paterson, and J. Boland (1981). "An experimental study of the role of water in quartz deformation". In: *Mechanical Behavior of Crustal Rocks: The Handin Volume* 24, pp. 49–60.

Keller, L. and M. Stipp (2011). "The single-slip hypothesis revisited: Crystal-preferred orientations of sheared quartz aggregates with increasing strain in nature and numerical simulation". In: *Journal of Structural Geology* 33.10, pp. 1491–1500.

Keralavarma, S. M., T. Cagin, A. Arsenlis, and A. A. Benzerga (2012). "Power-law creep from discrete dislocation dynamics". In: *Physical Review Letters* 109.26, p. 265504.

Kirby, S. and J. McCormick (1979). "Creep of hydrolytically weakened synthetic quartz crystals oriented to promote (2110) less-than-0001-greater-than slip-brief summary of work to date". In: *BULLETIN DE MINERALOGIE* 102.2-3, pp. 124–137.

Kirby, S. H. and M. W. Wegner (1978). "Dislocation substructure of mantle-derived olivine as revealed by selective chemical etching and transmission electron microscopy". In: *Physics and Chemistry of Minerals* 3.4, pp. 309–330.

Kocks, U. F., A. AS, and A. MF (1975). "Thermodynamics and kinetics of slip". In.

Kohnert, A. A. and L. Capolungo (2022). "The kinetics of static recovery by dislocation climb". In: *npj Computational Materials* 8.1, p. 104.

Koster, A., U. Ziese, A. Verkleij, A. Janssen, and K. De Jong (2000). "Three-dimensional transmission electron microscopy: a novel imaging and characterization technique with nanometer scale resolution for materials science". In: *The Journal of Physical Chemistry B* 104.40, pp. 9368–9370.

Kronenberg, A. K., S. H. Kirby, R. D. Aines, and G. R. Rossman (1986). "Solubility and diffusional uptake of hydrogen in quartz at high water pressures: Implications for hydrolytic weakening". In: *Journal of Geophysical Research: Solid Earth* 91.B12, pp. 12723–12741.

Kronenberg, A. K., K. T. Ashley, M. K. Francsis, C. W. Holyoke III, L. Jezek, J. A. Kronenberg, R. D. Law, and J. B. Thomas (2020). "Water loss during dynamic recrystallization of Moine thrust quartzites, northwest Scotland". In: *Geology* 48.6, pp. 557–561.

Kronenberg, A. K., H. F. Hasnan, C. W. Holyoke III, R. D. Law, Z. Liu, and J. B. Thomas (2017). "Synchrotron FTIR imaging of OH in quartz mylonites". In: *Solid Earth* 8.5, pp. 1025–1045.

Kröner, E. (1959). "Allgemeine kontinuumstheorie der versetzungen und eigenspannungen". In: *Archive for Rational Mechanics and Analysis* 4, pp. 273–334.

Kruhl, J. (1996). "Prism-and basal-plane parallel subgrain boundaries in quartz: A microstructural geothermobarometer". In: *Journal of metamorphic Geology* 14.5, pp. 581–589.

Kukta, R. V. and L. B. Freundt (1998). "Three-Dimensional Numerical Simulation of Interacting Dislocations in a Strained Epitaxial Surface Layer". In: *MRS Online Proceedings Library* 538.1, pp. 99–105. ISSN: 1946-4274.

Lang, A. (1959). "Studies of Individual Dislocations in Crystals by X-Ray Diffraction Microradiography". In: *Journal of Applied Physics* 30.11, pp. 1748–1755.

Laue, M. v. (1913). "Eine quantitative Prüfung der Theorie für die Interferenzerscheinungen bei Röntgenstrahlen". In: *Annalen der Physik* 346.10, pp. 989–1002.

Law, R. (2014). "Deformation thermometry based on quartz c-axis fabrics and recrystallization microstructures: A review". In: *Journal of structural Geology* 66, pp. 129–161.

Law, R., M. Casey, and R. Knipe (1986). "Kinematic and tectonic significance of microstructures and crystallographic fabrics within quartz mylonites from the Assynt and Eriboll regions of the Moine thrust zone, NW Scotland". In: *Earth and Environmental Science Transactions of the Royal Society of Edinburgh* 77.2, pp. 99–125.

Law, R., D. Mainprice, M. Casey, G. E. Lloyd, R. Knipe, B. Cook, and J. Thigpen (2010). "Moine thrust zone mylonites at the Stack of Glencoul: I–microstructures, strain and influence of recrystallization on quartz crystal fabric development". In: *Geological Society, London, Special Publications* 335.1, pp. 543–577.

Law, R., D. Stahr Iii, M. Francsis, K. Ashley, B. Grasemann, and T. Ahmad (2013). "Deformation temperatures and flow vorticities near the base of the Greater Himalayan Series, Sutlej Valley and Shimla Klippe, NW India". In: *Journal of Structural Geology* 54, pp. 21–53.

Lebensohn, R. A., C. S. Hartley, C. N. Tomé, and O. Castelnau (2010). "Modeling the mechanical response of polycrystals deforming by climb and glide". In: *Philosophical Magazine* 90.5, pp. 567–583.

Lepinoux, J. and L. Kubin (1987). "Dynamic organization of dislocation structures: A simulation". In: *Scr. Metall.;(United States)* 21.6.

Li, Y., C. Robertson, M. Shukeir, and L. Dupuy (2018). "Screw dislocation interaction with irradiation defect-loops in α-iron: evaluation of cross-slip effect using dislocation dynamics simulations". In: *Modelling and Simulation in Materials Science and Engineering* 26.5, p. 055009.

Lister, G. and B. Hobbs (1980). "The simulation of fabric development during plastic deformation and its application to quartzite: the influence of deformation history". In: *Journal of Structural Geology* 2.3, pp. 355–370.

Liu, B., P. Eisenlohr, F. Roters, and D. Raabe (2012). "Simulation of dislocation penetration through a general low-angle grain boundary". In: *Acta Materialia* 60.13-14, pp. 5380–5390.

Liu, G., S. House, J. Kacher, M. Tanaka, K. Higashida, and I. Robertson (2014). "Electron tomography of dislocation structures". In: *Materials characterization* 87, pp. 1–11.

Liu, G. and I. Robertson (2011). "Three-dimensional visualization of dislocation-precipitate interactions in a Al–4Mg–0.3 Sc alloy using weak-beam dark-field electron tomography". In: *Journal of Materials Research* 26.4, pp. 514–522.

Longsworth, M. and M. Fivel (2021). "The effect of stress on the cross-slip energy in face-centered cubic metals: A study using dislocation dynamics simulations and line tension models". In: *Journal of the Mechanics and Physics of Solids* 148, p. 104281.

Ludwig, W., P. Cloetens, J. Härtwig, J. Baruchel, B. Hamelin, and P. Bastie (2001). "Three-dimensional imaging of crystal defects bytopo-tomography'". In: *Journal of applied crystallography* 34.5, pp. 602–607.

Madec, R., B. Devincre, L. Kubin, T. Hoc, and D. Rodney (2003). "The role of collinear interaction in dislocation-induced hardening". In: *Science* 301.5641, pp. 1879–1882.

Madec, R., B. Devincre, and L. Kubin (2002). "Simulation of dislocation patterns in multislip". In: *Scripta materialia* 47.10, pp. 689–695.

Mahendran, S., P. Carrez, and P. Cordier (2021). "The core structure of screw dislocations with [001] Burgers vector in Mg _2 SiO _4 olivine". In: *Comptes Rendus. Physique* 22.S3, pp. 7–18.

Mainprice, D., J.-L. Bouchez, P. Blumenfeld, and J. M. Tubià (1986). "Dominant c slip in naturally deformed quartz: implications for dramatic plastic softening at high temperature". In: *Geology* 14.10, pp. 819–822.

Malaplate, J., D. Caillard, and A. Couret (2004). "Interpretation of the stress dependence of creep by a mixed climb mechanism in TiAl". In: *Philosophical Magazine* 84.34, pp. 3671–3687.

Marquardt, H. and L. Miyagi (2015). "Slab stagnation in the shallow lower mantle linked to an increase in mantle viscosity". In: *Nature Geoscience* 8.4, pp. 311–314.

McElfresh, C., N. Bertin, S. Aubry, and J. Marian (2022). "A parallel discrete dislocation dynamics/kinetic Monte Carlo method to study non-conservative plastic processes". In: *Computational Materials Science* 209, p. 111332.

McLaren, A., J. Fitz Gerald, and J. Gerretsen (1989). "Dislocation nucleation and multiplication in synthetic quartz: relevance to water weakening". In: *Physics and chemistry of minerals* 16.5, pp. 465–482.

McLaren, A. and B. Hobbs (1972). "Transmission electron microscope investigation of some naturally deformed quartzites". In: *Washington DC American Geophysical Union Geophysical Monograph Series* 16, pp. 55–66.

Messaoudil, C., T. Boudier, C. O. S. Sorzano, and S. Marco (2007). "TomoJ: tomography software for three-dimensional reconstruction in transmission electron microscopy". In: *BMC bioinformatics* 8, pp. 1–9.

Midgley, P. and M. Weyland (2011). "STEM Tomography". In: *Scanning Transmission Electron Microscopy: Imaging and Analysis*. Ed. by S. Pennycook and P. Nellist. New York, NY: Springer New York, pp. 353–392.

Miller, W. H. (1839). *A treatise on crystallography*. Printed at the Pitt Press, for J. & JJ Deighton.

Mises, R. v. (1928). "Mechanik der plastischen Formänderung von Kristallen". In: *ZAMM-Journal of Applied Mathematics and Mechanics/Zeitschrift für Angewandte Mathematik und Mechanik* 8.3, pp. 161–185.

Miyagi, L. and H.-R. Wenk (2016). "Texture development and slip systems in bridgmanite and bridgmanite+ ferropericlase aggregates". In: *Physics and Chemistry of Minerals* 43, pp. 597–613.

Miyajima, N. and N. Walte (2009). "Burgers vector determination in deformed perovskite and post-perovskite of CaIrO3 using thickness fringes in weak-beam dark-field images". In: *Ultramicroscopy* 109.6, pp. 683–692.

Miyajima, N., T. Yagi, and M. Ichihara (2009). "Dislocation microstructures of MgSiO3 perovskite at a high pressure and temperature condition". In: *Physics of the Earth and Planetary Interiors* 174.1-4, pp. 153–158.

Morales, L. F., G. E. Lloyd, and D. Mainprice (2014). "Fabric transitions in quartz via viscoplastic self-consistent modeling part I: Axial compression and simple shear under constant strain". In: *Tectonophysics* 636, pp. 52–69.

Morales, L. F., D. Mainprice, G. E. Lloyd, and R. D. Law (2011). "Crystal fabric development and slip systems in a quartz mylonite: an approach via transmission electron microscopy and viscoplastic self-consistent modelling". In: *Geological Society, London, Special Publications* 360.1, pp. 151–174.

Morniroli, J. (2001). "École thématique: Microscopie des défauts cristallins". In: *Société Française des Microscopies* 45, p. 46.

Morniroli, J., D. Vankieken, and L. Winter (1994). "Electron diffraction". In: *Dedicated Software to Interpret LACBEDPatterns USTL, Lille, France*.

Morrison-Smith, D., M. Paterson, and B. Hobbs (1976). "An electron microscope study of plastic deformation in single crystals of synthetic quartz". In: *Tectonophysics* 33.1-2, pp. 43–79.

Mott, N. F. (1951). "The Mechanical Properties of Metals". In: *Proceedings of the Physical Society. Section B* 64.9, p. 729.

Moulin, A., M. Condat, and L. Kubin (1997). "Simulation of Frank-Read sources in silicon". In: *Acta materialia* 45.6, pp. 2339–2348.

Mussi, A., A. Addad, and F. Onimus (2021a). "Dislocation electron tomography: A technique to characterize the dislocation microstructure evolution in zirconium alloys under irradiation". In: *Acta Materialia* 213, p. 116964.

Mussi, A., P. Carrez, K. Gouriet, B. Hue, and P. Cordier (2021b). "4D electron tomography of dislocations undergoing electron irradiation". In: *Comptes Rendus. Physique* 22.S3, pp. 67–81.

Mussi, A., P. Cordier, and S. Demouchy (2015a). "Characterization of dislocation interactions in olivine using electron tomography". In: *Philosophical Magazine* 95.4, pp. 335–345.

Mussi, A., P. Cordier, S. Demouchy, and B. Hue (2017). "Hardening mechanisms in olivine single crystal deformed at 1090 C: an electron tomography study". In: *Philosophical Magazine* 97.33, pp. 3172–3185.

Mussi, A., P. Cordier, S. Demouchy, and C. Vanmansart (2014). "Characterization of the glide planes of the [001] screw dislocations in olivine using electron tomography". In: *Physics and Chemistry of Minerals* 41, pp. 537–545.

Mussi, A., J. Gallet, O. Castelnau, and P. Cordier (2021c). "Application of electron tomography of dislocations in beam-sensitive quartz to the determination of strain components". In: *Tectonophysics* 803, p. 228754.

Mussi, A., M. Nafi, S. Demouchy, and P. Cordier (2015b). "On the deformation mechanism of olivine single crystals at lithospheric temperatures: an electron tomography study". In: *European Journal of Mineralogy* 27.6, pp. 707–715.

Nabarro, F. (1967). "Steady-state diffusional creep". In: *Philosophical Magazine* 16.140, pp. 231–237.

Niermann, T., L. Niermann, and M. Lehmann (2024). "Three dimensional classification of dislocations from single projections". In: *Nature Communications* 15.1, p. 1356.

Nye, J. F. (1953). "Some geometrical relations in dislocated crystals". In: *Acta metallurgica* 1.2, pp. 153–162.

Nzogang, B. C., J. Bouquerel, P. Cordier, A. Mussi, J. Girard, and S. Karato (2018). "Characterization by scanning precession electron diffraction of an aggregate of bridgmanite and ferropericlase deformed at HP-HT". In: *Geochemistry, Geophysics, Geosystems* 19.3, pp. 582–594.

Okudaira, T., T. Takeshita, I. Hara, and J.-i. Ando (1995). "A new estimate of the conditions for transition from basal< a> to prism [c] slip in naturally deformed quartz". In: *Tectonophysics* 250.1-3, pp. 31–46.

Onofri, C., J. Monchoux, J. Amodeo, R. Madec, C. Sabathier, H. Palancher, J. Fouet, D. Drouan, and M. Legros (2024). "Versatility of dislocation motions in polycrystalline UO2 deformed at 1550 °C investigated by TEM". In: *Scripta Materialia* 244, p. 116034.

Ord, A. and J. Christie (1984). "Flow stresses from microstructures in mylonitic quartzites of the Moine Thrust zone, Assynt area, Scotland". In: *Journal of Structural Geology* 6.6, pp. 639–654.

Orowan, E. (1934). "Zur kristallplastizität. III: Über den mechanismus des gleitvorganges". In: *Zeitschrift für Physik* 89.9-10, pp. 634–659.

Oveisi, E., A. Letouzey, S. De Zanet, G. Lucas, M. Cantoni, P. Fua, and C. Hebert (2018). "Stereo-vision three-dimensional reconstruction of curvilinear structures imaged with a TEM". In: *Ultramicroscopy* 184, pp. 116–124.

Paterson, M. (1990). "Rock deformation experimentation". In: *The brittle-ductile transition in rocks* 56, pp. 187–194.

Peierls, R. (1940). "The size of a dislocation". In: *Proceedings of the Physical Society* 52.1, p. 34.

Pettersen, E. F., T. D. Goddard, C. C. Huang, G. S. Couch, D. M. Greenblatt, E. C. Meng, and T. E. Ferrin (2004). "UCSF Chimera—a visualization system for exploratory research and analysis". In: *Journal of computational chemistry* 25.13, pp. 1605–1612.

Phakey, P., G. Dollinger, and J. Christie (1972). "Transmission electron microscopy of experimentally deformed olivine crystals". In: *Washington DC American Geophysical Union Geophysical Monograph Series* 16, pp. 117–138.

Polanyi, M. (1934). "Über eine Art Gitterstörung, die einen Kristall plastisch machen könnte". In: *Zeitschrift für Physik* 89.9-10, pp. 660–664.

Pollock, T. M. and R. LeSar (2013). "The feedback loop between theory, simulation and experiment for plasticity and property modeling". In: *Current Opinion in Solid State and Materials Science* 17.1, pp. 10–18.

Radon, J. (1917). "On the determination of functions from their integrals along certain manifolds". In: *Mathematisch-Physische Klasse* 69, pp. 262–277.

Reali, R., F. Boioli, K. Gouriet, P. Carrez, B. Devincre, and P. Cordier (2017). "Modeling plasticity of MgO by 2.5 D dislocation dynamics simulations". In: *Materials Science and Engineering: A* 690, pp. 52–61.

Reali, R., J. M. Jackson, J. Van Orman, D. J. Bower, P. Carrez, and P. Cordier (2019a). "Modeling viscosity of (Mg, Fe) O at lowermost mantle conditions". In: *Physics of the earth and planetary interiors* 287, pp. 65–75.

Reali, R., J. A. Van Orman, J. S. Pigott, J. M. Jackson, F. Boioli, P. Carrez, and P. Cordier (2019b). "The role of diffusion-driven pure climb creep on the rheology of bridgmanite under lower mantle conditions". In: *Scientific Reports* 9.1, p. 2053.

Rebled, J., L. Yedra, S. Estrade, J. Portillo, and F. Peiro (2011). "A new approach for 3D reconstruction from bright field TEM imaging: Beam precession assisted electron tomography". In: *Ultramicroscopy* 111.9-10, pp. 1504–1511.

Routbort, J. (1979). "Work hardening and creep of MgO". In: *Acta Metallurgica* 27.4, pp. 649–661.

Runevall, O. and N. Sandberg (2011). "Self-diffusion in MgO—a density functional study". In: *Journal of Physics: Condensed Matter* 23.34, p. 345402.

Rutter, E. and K. Brodie (2004). "Experimental grain size-sensitive flow of hot-pressed Brazilian quartz aggregates". In: *Journal of Structural Geology* 26.11, pp. 2011–2023.

Sato, F. and K. Sumino (1980). "The yield strength and dynamic behaviour of dislocations in MgO crystals at high temperatures". In: *Journal of Materials Science* 15.7, pp. 1625–1634.

Sauzay, M. and L. Kubin (2011). "Scaling laws for dislocation microstructures in monotonic and cyclic deformation of fcc metals". In: *Progress in Materials Science* 56.6. Festschrift Vaclav Vitek, pp. 725–784.

Sharp, J., J. Barnard, K. Kaneko, K. Higashida, and P. Midgley (2008). "Dislocation tomography made easy: A reconstruction from ADF STEM images obtained using automated image shift correction". In: *Journal of physics: conference series*. Vol. 126. 1. IOP Publishing, p. 012013.

Sills, R. B. and D. L. Medlin (2022). "Semi-Automated, Object-Based Tomography of Dislocation Structures". In: *Microscopy and Microanalysis* 28.3, pp. 633–645.

Sokolnikoff, I. (1966). "RM Redheffer". In: *Mathematics of Physics and Modern Engineering New York*.

Srinivasan, M. and T. Stoebe (1974). "Temperature dependence of yielding and work-hardening rates in magnesium oxide single crystals". In: *Journal of Materials Science* 9.1, pp. 121–128.

Stacey, F. and P. Davis (2004). "High pressure equations of state with applications to the lower mantle and core". In: *Physics of the Earth and Planetary interiors* 142.3-4, pp. 137–184.

Stach, E., R. Hull, R. Tromp, F. Ross, M. Reuter, and J. Bean (2000). "In-situ transmission electron microscopy studies of the interaction between dislocations in strained SiGe/Si (001) heterostructures". In: *Philosophical Magazine A* 80.9, pp. 2159–2200.

Stipp, M., H. StuÈnitz, R. Heilbronner, and S. M. Schmid (2002a). "The eastern Tonale fault zone: a 'natural laboratory'for crystal plastic deformation of quartz over a temperature range from 250 to 700 C". In: *Journal of structural geology* 24.12, pp. 1861–1884.

Stipp, M., H. Stünitz, R. Heilbronner, and S. M. Schmid (2002b). "Dynamic recrystallization of quartz: correlation between natural and experimental conditions". In: *Geological Society, London, Special Publications* 200.1, pp. 171–190.

Stipp, M., J. Tullis, and H. Behrens (2006). "Effect of water on the dislocation creep microstructure and flow stress of quartz and implications for the recrystallized grain size piezometer". In: *Journal of Geophysical Research: Solid Earth* 111.B4.

Strachan, R., M. Smith, A. Harris, and D. Fettes (2002). "The northern Highland and Grampian terranes". In.

Sylvester, A. G. (1969). "SA microfabric study of calcite, dolomite, and quartz around Papoose Flat pluton, California". In: *Geological Society of America Bulletin* 80.7, pp. 1311–1328.

Tanaka, M., K. Higashida, K. Kaneko, S. Hata, and M. Mitsuhara (2008). "Crack tip dislocations revealed by electron tomography in silicon single crystal". In: *Scripta Materialia* 59.8, pp. 901–904.

Taylor, G. I. (1934). "The mechanism of plastic deformation of crystals. Part I.—Theoretical". In: *Proceedings of the Royal Society of London. Series A, Containing Papers of a Mathematical and Physical Character* 145.855, pp. 362–387.

Taylor, G. I. (1938). "Plastic strain in metals". In: *J. Inst. Metals* 62, pp. 307–324.

Tokle, L., G. Hirth, and W. M. Behr (2019). "Flow laws and fabric transitions in wet quartzite". In: *Earth and Planetary Science Letters* 505, pp. 152–161.

Tommasi, A., D. Mainprice, G. Canova, and Y. Chastel (2000). "Viscoplastic self-consistent and equilibrium-based modeling of olivine lattice preferred orientations: Implications for the upper mantle seismic anisotropy". In: *Journal of Geophysical Research: Solid Earth* 105.B4, pp. 7893–7908.

Trépied, L. and J. C. Doukhan (1982). "Evidence of< a+ c> dislocations in synthetic quartz single crystals compressed along the c axis". In: *Bulletin de Minéralogie* 105.2, pp. 176–180.

Tullis, J., J. M. Christie, and D. T. Griggs (1973). "Microstructures and preferred orientations of experimentally deformed quartzites". In: *Geological Society of America Bulletin* 84.1, pp. 297–314.

Tullis, J. and R. A. Yund (1989). "Hydrolytic weakening of quartz aggregates: The effects of water and pressure on recovery". In: *Geophysical Research Letters* 16.11, pp. 1343–1346.

Van Orman, J. A. and K. L. Crispin (2010). "Diffusion in oxides". In: *Reviews in Mineralogy and Geochemistry* 72.1, pp. 757–825.

Van Orman, J. A., Y. Fei, E. H. Hauri, and J. Wang (2003). "Diffusion in MgO at high pressures: Constraints on deformation mechanisms and chemical transport at the core-mantle boundary". In: *Geophysical Research Letters* 30.2.

Vernooij, M. G. (2005). "Dynamic recrystallisation and microfabric development in single crystals of quartz during experimental deformation". PhD thesis. ETH Zurich.

Vincent, R. and P. Midgley (1994). "Double conical beam-rocking system for measurement of integrated electron diffraction intensities". In: *Ultramicroscopy* 53.3, pp. 271–282.

Vitek, V. (1968). "Intrinsic stacking faults in body-centred cubic crystals". In: *Philosophical Magazine* 18.154, pp. 773–786.

Voisin, T., J.-P. Monchoux, M. Thomas, C. Deshayes, and A. Couret (2016). "Mechanical properties of the TiAl IRIS alloy". In: *Metallurgical and Materials Transactions A* 47, pp. 6097–6108.

Volterra, V. (1907). "Sur l'équilibre des corps élastiques multiplement connexes". In: *Annales scientifiques de l'École normale supérieure*. Vol. 24, pp. 401–517.

Wallis, D., L. N. Hansen, K. M. Kumamoto, C. A. Thom, O. Plümper, M. Ohl, W. B. Durham, D. L. Goldsby, D. E. Armstrong, C. D. Meyers, et al. (2020). "Dislocation interactions during low-temperature plasticity of olivine and their impact on the evolution of lithospheric strength". In: *Earth and Planetary Science Letters* 543, p. 116349.

Wallis, D., L. N. Hansen, A. J. Wilkinson, and R. A. Lebensohn (2021). "Dislocation interactions in olivine control postseismic creep of the upper mantle". In: *Nature Communications* 12.1, p. 3496.

Wallis, D., A. J. Parsons, and L. N. Hansen (2019). "Quantifying geometrically necessary dislocations in quartz using HR-EBSD: Application to chessboard subgrain boundaries". In: *Journal of Structural Geology* 125, pp. 235–247.

Wang, Y., N. Hilairet, N. Nishiyama, N. Yahata, T. Tsuchiya, G. Morard, and G. Fiquet (2013). "High-pressure, high-temperature deformation of CaGeO3 (perovskite)±MgO aggregates: Implications for multiphase rheology of the lower mantle". In: *Geochemistry, Geophysics, Geosystems* 14.9, pp. 3389–3408.

Weathers, M. S., J. M. Bird, R. F. Cooper, and D. L. Kohlstedt (1979). "Differential stress determined from deformation-induced microstructures of the Moine Thrust Zone". In: *Journal of Geophysical Research: Solid Earth* 84.B13, pp. 7495–7509.

Weertman, J. (1968). "Diffusion Law for the Dispersion of Hard Particles in an Ice Matrix that Undergoes Simple Shear Deformation". In: *Journal of Glaciology* 7.50, pp. 161–165.

Weertman, J. (1955). "Theory of steady-state creep based on dislocation climb". In: *Journal of Applied Physics* 26.10, pp. 1213–1217.

Wenk, H.-R., G. Canova, A. Molinari, and U. Kocks (1989). "Viscoplastic modeling of texture development in quartzite". In: *Journal of Geophysical Research: Solid Earth* 94.B12, pp. 17895–17906.

Wenk, H.-R., R. Yu, S. Vogel, and R. Vasin (2019). "Preferred orientation of quartz in metamorphic rocks from the Bergell Alps". In: *Minerals* 9.5, p. 277.

White, S. (1977). "Geological significance of recovery and recrystallization processes in quartz". In: *Tectonophysics* 39.1-3, pp. 143–170.

Williams, D. and C. Carter (2009). *Transmission Electron Microscopy*. springer publication.

Wu, K., G. Liu, P. Yu, C. Ye, J. Shi, and Y. Shen (2022). "Prediction of hardening effect by irradiation-induced vacancy clusters with dislocation dynamics". In: *International Journal of Plasticity* 149, p. 103160.

Yamazaki, D. and S.-I. Karato (2001). "Some mineral physics constraints on the rheology and geothermal structure of Earth's lower mantle". In: *American Mineralogist* 86.4, pp. 385–391.

Yang, M. and C. Flynn (1994). "Intrinsic diffusion properties of an oxide: MgO". In: *Physical review letters* 73.13, p. 1809.

Yoo, H.-I., B. J. Wuensch, and W. T. Petuskey (2002). "Oxygen self-diffusion in single-crystal MgO: secondary-ion mass spectrometric analysis with comparison of results from gas–solid and solid–solid exchange". In: *Solid state ionics* 150.3-4, pp. 207–221.

Yuan, S., M. Huang, Y. Zhu, and Z. Li (2018). "A dislocation climb/glide coupled crystal plasticity constitutive model and its finite element implementation". In: *Mechanics of Materials* 118, pp. 44–61.

Abstract: The study of dislocation microstructures (linear defects) enables us to identify the fundamental mechanisms of plastic deformation in materials. These defects are defined by their Burgers vectors, line vectors and habit planes (slip and climb planes). TEM is the most suitable tool for characterizing these vectors and planes, but the main drawback of this technique is access to projected images, a source of interpretation errors. Dislocation electron dislocations (DET) has been developed to observe these microstructures in 3D, and thus better decipher them. As part of my thesis, I pursued the development of DET. I improved 3D reconstruction techniques and carried out fast tomography (tomography with a low number of projected images). This enabled me to characterize the 3D microstructures of dislocations in natural quartz and olivine samples. DET revealed an original dislocation climb mechanism: mixed climb. This mechanism, intermediate between pure climb and glide, is the signature of an equivalent balance between the mobility of dislocations in glide and in climb. This mechanism, a priori singular, turns out to be particularly common in high lattice friction microstructures loaded at high temperatures. In order to go beyond simple characterizations by indexing the line directions and habit planes of dislocation segments, we undertook an approach aimed at combining tomography with continuum mechanics. A first study enabled us to obtain the strain tensor of a grain in a natural quartz sample from characterizations of the Burgers vectors associated with the normals to the habit planes of dislocation segments reconstructed in 3D using DET. This quantitative study (the lengths of the dislocation segments were considered in the calculations) enabled us to verify that the von Mises criterion was respected (the plastic deformation of the quartz polycrystal occurred with more than five independent slip systems, which explains the absence of damage). We were also able to access the stress tensor and the relative critical resolved shear stress. The characterization of line vectors and Burgers vectors, identified using tomography, also enables us to derive the Nye tensor for each dislocation segment. This tensor is obtained by the dyadic product of the Burgers vectors and their line vectors. By applying the laws of continuum mechanics, we were able to determine, in a second study, the strain tensor and stress tensor fields from a real 3D microstructure of dislocations. We then linked DET to dislocation dynamics (DD). The NUMODIS nodal DD software, developed at CEA Saclay, enables dislocation segments to be delimited by nodes in space. Its nodal nature makes it ideal for use with DET. The principle is to bring dislocations back to life if modeling is carried out under the same mechanical stress conditions as during mechanical testing. We looked for a sample with perfectly known mechanical stress axes and the simplest possible dislocation microstructure: gliding dislocations, a single type of Burgers vector, a majority of straight screw dislocations and few gliding mechanisms. An olivine sample deformed in a Paterson press at 800°C, under a confining pressure of 300 MPa, satisfies all conditions. The DD simulations undertaken in this study are the first to be derived from a real dislocation microstructure obtained by tomography. We were able to characterize annihilation and collinear interaction mechanisms.

Résumé: L'étude des microstructures de dislocations (défauts linéaires) permet d'identifier les mécanismes fondamentaux de déformation plastique des matériaux. Ces défauts sont définis par leurs vecteurs de Burgers, leurs vecteurs lignes et leurs plans d'habitat (plans de glissement et de montée). La MET est l'outil le plus adapté pour caractériser ces vecteurs et ces plans, mais le principal inconvénient de cet instrument est l'accès à des images projetées, sources d'erreurs d'interprétation. La tomographie électronique des dislocations (TED) a été développée pour observer en 3D et donc mieux déchiffrer ces microstructures. Dans le cadre de ma thèse, j'ai poursuivi le développement de la TED. J'ai amélioré les techniques de reconstruction 3D et effectué de la tomographie rapide (tomographie à faible nombre d'images projetés). Les microstructures 3D de dislocations d'échantillons naturels de quartz et d'olivine ont ainsi pu être caractérisées. La TED a permis de révéler un mécanisme de montée de dislocations original : la montée mixte. Ce mécanisme, à l'intermédiaire entre la montée pure et le glissement, est la signature d'une pondération équivalente entre la mobilité de dislocations en glissement et en montée. Ce mécanisme, a priori singulier, se révèle particulièrement commun dans les microstructures à fortes frictions de réseaux sollicitées à hautes températures. Pour dépasser les simples caractérisations par indexations de directions de lignes et de plans d'habitat des segments de dislocations, nous avons entrepris une démarche visant à associer la tomographie à la mécanique. Une première étude nous a permis d'obtenir le tenseur des déformations d'un grain dans un échantillon naturel de quartz à partir des caractérisations des vecteurs de Burgers associés aux normales aux plans d'habitat des segments de dislocations reconstruits en 3D grâce à la TED. Cette étude quantitative (les longueurs des segments de dislocation ont été prise en compte dans les calculs) nous a permis de vérifier que le critère de von Mises était respecté (la déformation plastique du polycristal de quartz s'est produit avec plus de cinq systèmes de glissement indépendants qui explique l'absence d'endommagement). Nous avons également pu accéder au tenseur des contraintes et au contraintes critiques résolues relatives. Les caractérisations des vecteurs de lignes et des vecteurs de Burgers, identifiées grâce à la tomographie, permettent également d'obtenir le tenseur de Nye pour chaque segment de dislocation. Ce tenseur s'obtient par le produit dyadique des vecteurs de Burgers par leur vecteurs lignes. En appliquant les lois de la mécanique des milieux continus, nous avons pu déterminer, dans une seconde étude, les champs de tenseurs de déformation et de tenseurs de contrainte à partir d'une microstructure réelle et 3D de dislocations. Nous avons, par la suite, associé la TED à la dynamique des dislocations (DD). Le logiciel de DD nodal NUMODIS, mis au point au CEA à Saclay, permet de délimiter des segments de dislocations par des nœuds dans l'espace. Son caractère nodal fait qu'il s'associe idéalement avec la TED. Le principe consiste à redonner vie aux dislocations si la modélisation est effectuée dans les mêmes conditions de sollicitations mécaniques qu'au cours de l'essai mécanique. Nous avons cherché un échantillon dont les axes de sollicitations mécaniques sont parfaitement connus et avec la microstructure de dislocations la plus simple qui soit : dislocations en glissement, un seul type de vecteur de Burgers, une majorité de dislocations vis rectilignes et peu de mécanismes de glissement. Un échantillon d'olivine déformé sous presse Paterson à 800°C, sous une pression de confinement de 300 MPa, cochait toutes les cases. Les simulations de DD, entreprises dans cette étude, sont les premières tirées d'une microstructure réelle de dislocations obtenues par tomographie. Nous avons pu caractériser des mécanismes d'annihilations et d'interactions colinéaires.